BỘ GIÁO DỤC VÀ ĐÀO TẠO
VIỆN HÀN LÂM KHOA HỌC VÀ CÔNG NGHỆ VIỆT NAM

HỌC VIỆN KHOA HỌC VÀ CÔNG NGHỆ

TRẦN THỊ THÁI

THE SOURCES OF COSMIC REIONIZATION AS SEEN BY MUSE/VLT

LUẬN ÁN TIẾN SĨ VẬT LÝ

Hà Nội – 2023

BỘ GIÁO DỤC VÀ ĐÀO TẠO
VIỆN HÀN LÂM KHOA HỌC VÀ CÔNG NGHỆ VIỆT NAM

HỌC VIỆN KHOA HỌC VÀ CÔNG NGHỆ

TRẦN THỊ THÁI

THE SOURCES OF COSMIC REIONIZATION AS SEEN BY MUSE/VLT

LUẬN ÁN TIẾN SĨ VẬT LÝ

Chuyên ngành: Vật lý nguyên tử và Hạt nhân
Mã số chuyên ngành: 9 44 01 06

Xác nhận của cơ sở Đào tạo **Thầy hướng dẫn 2** **Thầy hướng dẫn 1**

TS. ROSER PELLO **TS. PHẠM TUẤN ANH**

Hà Nội - 2023

Affidavit

I, undersigned, Thi Thai TRAN, hereby declare that the work presented in this manuscript is my own work, carried out under the scientific supervision of Roser PELLO and Tuan-Anh PHAM, in accordance with the principles of honesty, integrity and responsibility inherent to the research mission. The research work and the writing of this manuscript have been carried out in compliance with both the french national charter for Research Integrity and the Aix-Marseille University charter on the fight against plagiarism.

This work has not been submitted previously either in this country or in another country in the same or in a similar version to any other examination body.

Marseille, September 13 2023

Acknowledgement

This thesis has been done under a cotutelle programe between the Laboratoire d'Astrophysique de Marseille/Aix-Marseille University (LAM/AMU) and Graduate University of Science and Technology, Department of Astrophysics of Vietnam National Space Center (DAP/VNSC) under supervision of Dr. Roser Pello and Dr. Pham Tuan-Anh, respectively. I spent one year in total in Marseille/France to work directly with Dr. Roser Pello, and colleagues in LAM, Lyon, and MUSE consortium. The rest of the time was in Hanoi/Vietnam working with Dr. Pham Tuan-Anh.

First of all, I would like to express my gratitude to Dr. Roser Pello and Dr.Pham Tuan-Anh for affording me the opportunity to work with them. Their unwavering encouragement, support, listening to me, and believing in me even when my own belief wavered.

I would like to thank my collaborators: Johan Richard, Adelaide Claeyssens, Ilias Goovaerts, Thibault Garel, and the MUSE consortium for their guidance, constructive feedback, and valuable advice in helping me successfully complete the thesis.

I am grateful to everyone who has been working at DAP, Prof. Pierre Darriulat, Assoc Prof. Pham Ngoc Diep, Dr. Pham Tuyet Nhung, Dr. Do Thi Hoai, Dr. Nguyen Thi Phuong, PhD student Nguyen Thi Bich Ngoc, Bcs Mai Nhat Tan for their help in the work, creating a great working environment as well as their experiment sharing in life.

The support from my beloved friends played an invaluable role throughout my thesis journey. I am deeply thankful to my LAMmates, Lise-Marie, Meriam, Diana, Martin, and Mathilde, who have been by my side since the day I arrived in Marseille. Their immense assistance and sharing of their experiences helped me to adapt to the new environment. Additionally, I am especially grateful to my Vietnamese friends who have been with me since my first day of pursuing the thesis, through the challenges of the COVID-19 pandemic together until this very day.

I would like to seize this moment to express my heartfelt gratitude to Jean-Michel and Dominique for their unwavering material and spiritual support during these three years. Their genuine care and concern made me extremely moved and felt like I had a new family during my time in France.

The financial support from the French Embassy Excellence Scholarship Programme (for foreign students), the VINgroup Innovation Foundation, Vietnam National Foundation for Science and Technology Development (grant no. 103.99-2019.325), the Laboratoire d'Astrophysique de Marseille, Vietnam National Space Center, the World Laboratory, and the Odon Vallet scholarship are acknowledged.

I thank the lecturers at the Graduate University of Science and Technology (GUST), Vietnam Academy of Science and Technology.

Lastly, I extend my sincere gratitude to my parents, who let me freely choose my interests and support my decisions. Hence I was able to go through all the challenges of life and pursue my dreams.

Hanoi & Marseille

Contents

List of Figures

List of Tables

List of acronyms

AGN

Active Galactic Nuclei. 7, 8, 15, 18, 36

AO

Adaptive Optic. 19, 24–26, 36, 38, 39, 59

BCG

Bright Cluster Galaxy. 36, 38

Bp

Brightest pixel. 59, 60, 62

CCD

Charge Coupled Device. 19

CGM

Circum Galactic Medium. v, 4–6, 8, 9

CLASH

Cluster Lensing And Supernova Survey. 33, 35, 36, 38, 43

CMB

Cosmic Microwave Background. 1

DEC

Declination. 30, 43

DM

Dark matter. 34, 44, 45

EoR

Epoch of Reionization. 7, 13–15, 27, 96, 104

ESO

European Southern Observatory. 24, 25, 30, 36

EW

Equivalent Width. v, 4, 9–12, 19, 27

FF

Frontier Fields. 32, 33, 36, 43

FIR

Far Infrared. 36

FoV

Field of View. 33, 35, 48, 50

FWHM

Full Width at Half Maximum. 41, 53, 54

GALACSI

Ground Atmospheric Layer Adaptive Corrector for Spectroscopic Imaging. 26, 36

GLASS

Grism Lens Amplified Survey from Space. 32

GTO

Guarantee Time of Observation. 22, 24, 27, 30, 31, 36, 38

HDFS

Hubble Deep Field Survey. 11

HST

Hubble Space Telescope. v, vi, 18, 22, 27–37, 39, 44, 48–50, 52, 53

IFU

Integral Field Unit. 19, 24

IGM

Intergalactic Medium. 6–8, 10, 13–16, 21, 27, 53, 96

ISM

Interstellar Medium. 8, 9, 13, 16, 96

JWST

James Web Space Telescope. iv, 7, 102, 104, 105

LAE

Lyman Alpha Emitter. iii–vi, 1, 8–13, 18–24, 26–28, 35, 36, 41, 43, 48, 50–56, 58, 70, 74, 76, 77, 79, 84, 85, 88, 90, 99, 101–105

LBG

Lyman Break Galaxy. iii, 1, 9, 13, 16, 17, 27, 41, 104

LF

Luminosity Function. iv–viii, 7, 20–23, 27, 50, 51, 56, 58, 70, 74, 77–91, 93–99, 101–104

LLAMAS

Lensed Lyman Alpha MUSE Arc Sample. 104

MACS

MAssive Cluster Survey. v, vi, 30, 35–40, 43, 53, 54, 59, 61–63, 65, 68, 73

MCMC

Markov Chain Monte Carlo. vi, 53, 79, 80, 82, 83, 90

MPDAF

MUSE Python Data Analysis Framework. 48

MUSE

Multi Unit Spectroscopic Explorer. iii–vi, viii, 9, 11, 19, 22–44, 48–53, 56, 59, 61, 62, 65, 68, 69, 74–76, 88, 102–105

MUSELET

MUSE Line Emission Tracker. iii, 24, 48, 51

NB

Narrow Band. v, 10, 18–20, 28, 48–50, 54, 59, 74–77

NE

North East. 36

NFM

Narrow Field Mode. 19, 24, 26

OB

Observation Blocks. 35, 36

PSF

Point Spread Function. 28

QSO

Quasi-Stellar Object. 5, 8, 15

RA

Right Ascension. 30, 43

RMS

Root Mean Square. vi, 48, 59, 62, 63, 65

SB

Surface Brightness. 28, 41

SED

Spectral Energy Distribution. v, 8, 17, 18, 36

SFR

Star formation Rate. 5, 35, 36

SFRD

Star Formation Rate Density. vii, 8, 21, 23, 98–101, 103, 104

SIE

Singular Isothermal Ellipsoid. 34

SIS

Single Isothermal Sphere. 34

SMBH

Super Massive Black Hole. 26

SN

Signal to Noise. 50, 51, 76

SNR

Signal to Noise Ratio. 48, 84

SW

South West. 36

UV

Ultra Violet. v, 2, 5, 8, 9, 11–14, 22, 28, 96, 104

VLT

Very Large Telescope. iii, v, viii, 9, 11, 19, 24–26, 30, 36, 40, 43, 48, 49, 51, 88, 102–104

WFM

Wide Field Mode. 19, 24, 26, 27, 34, 39

1 Introduction

Contents

After the Big Bang, the temperature of the Universe was so hot that protons and electrons could not combine together to form neutral hydrogen atoms. As the Universe expanded, its temperature cooled down. At ~ 3000 K, it is cool enough for the formation of neutral hydrogen, marking the beginning of the dark age. The Universe became transparent and the radiation from the Big Bang referred as Cosmic Microwave Background (CMB), could freely travel. This happened roughly half a billion years before the first stars and first galaxies started lighting up our Universe. In this stage, the dark matter particles collapse to form halos. As time passes, these halos become more massive, and the thermal pressure inside tends to prevent the gas from collapsing into the halo. However, the gas can continue collapsing if the dark matter halos which have been formed reach a threshold where the gravity force overcomes the thermal pressure. This threshold can be treated as compensation for the thermal pressure of the gas called the Jeans mass and is defined as follow:

$$M_J = \frac{\pi^{2.5} c_s^3}{6(G^3\rho)^{0.5}} \tag{1.1}$$

in which ρ is the density of the gas, G is the gravitational constant, c_s is the sound speed identified by $c_s = \left(\frac{\gamma k_b T}{\mu m_p}\right)^{0.5}$ (γ is the adiabatic index, T is the gas temperature, μ is the mean molecular weight, m_p is the mass of the proton, and k_b is the Boltzmann constant). During this stage, the mean gas density can be computed using the following form:

$$\overline{\rho_b} = \rho_c \Omega_b (1+z)^3 \tag{1.2}$$

where ρ_c is the critical density of the Universe, the baryon density parameter and redshift are Ω_b, and z, respectively. Peebles 1993 have shown that at redshift $z_t = 136$, the temperature can be estimated as $T = 2.73(1+z_t) = 374$ K. At this point, the thermal coupling of CMB blackbody and other objects is no longer significantly affected by the Compton scattering, so the gas will undergo adiabatic cooling, and its temperature will

decrease by a factor of a^{-2}, where a is expanding factor. The minimum halo mass needed for the gas to collapse, when ignoring streaming velocities, can be estimated at redshift $z = 30$, $M_J \sim 3.2 \times 10^4$ $M_\odot$ and its temperature decreases as $a^{-1.5}$ (Barkana et al. 2001). Note that streaming velocity is the relative velocity of the gas that was already coupled to radiation before the recombination process happened (Tseliakhovich et al. 2010). This calculation allows us to evaluate the spatial fluctuations of the lower mass limit for the halos that are able to bind gas.

The second major phase of transition happened when the first objects inside hydrogen clouds in the massive dark matter halos collapsed under gravity to form the first stars and galaxies. Properties of galaxies in the early Universe have been identified and quantified up to a few hundred million years after the Big Bang. These intense star-forming galaxies (SFGs) often host very massive and short lifetimes stars (O, B types). Their intense stellar UV emissions easily ionize the neutral hydrogen atoms, marking the end of the Dark Age. This important process happened at redshift $z \sim 12$ and completed at redshift $z \sim 6$ owing to observations of the Gunn-Peterson trough from measured quasars' spectra (R. H. Becker et al. 2001; Fan et al. 2006) (see Figure 1.1).

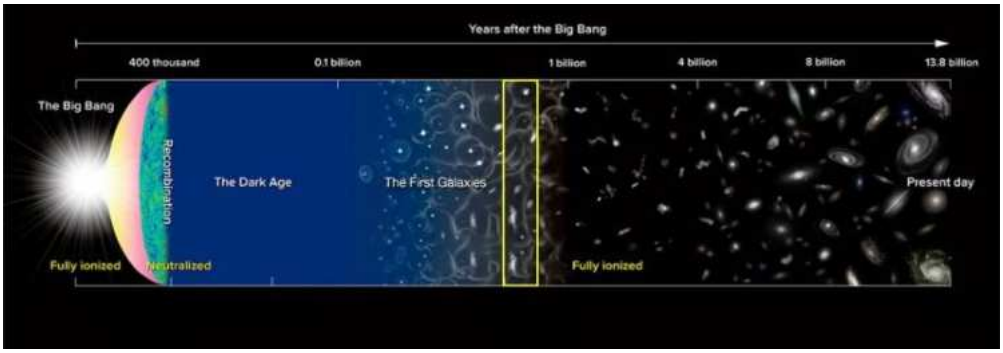

Figure 1.1: A brief history of the Universe from the Big Bang. The horizontal axis traces back time (top). The evolution phases of the Universe are shown from the time when the matter was fully ionized right after the Big Bang; after 380'000 years the recombination happened, at a redshift of 1100; after a few hundred million years the formation of the first structures (first stars, and galaxies) at the redshift of ~ 10, marked the end of the dark ages; the re-ionization was completed at redshift ~ 6. Credit: NAOJ.

1.1 The first structures

The primordial stars are formed mostly from hydrogen and helium atoms, and then the heavier elements are formed by nucleosynthesis. The gas formed from metal-poor stars is less effective than from metal-rich stars for cooling environment, which leads to the formation of more massive stars than nowadays (V. Bromm et al. 2001; Abel et al. 2002). The atomic cooling mechanism allows the gas temperature to decrease to 10 K. For this reason, the halos with a mass over 10^8 $M_\odot$ will have their thermal pressure compensated by gravity. However, for the halos with a mass below 10^8 $M_\odot$, the stars formed in this region will require another mechanism to cool down the gas temperature below 10^4 K. This mechanism is called molecular cooling caused by the formation of H_2 molecules:

$$H + e^- \rightarrow H^- + \gamma$$
$$H + H^- \rightarrow H_2 + e^-$$

Considering feedback of H_2 formation combined with simulations until the end of reionization, Wise et al. 2012 found a constant rate of metal-free stars at 3×10^{-5} $M_\odot$ yr^{-1} Mpc^{-3}. Such metal-free stars are believed more massive than nowadays stars (Volker Bromm et al. 1999; Abel et al. 2002; Hirano et al. 2014) and they efficiently create radiation during their time (3-10 Myr) (D. Schaerer 2002a). At the end of their life, these stars explode as supernovae, outflowing a large quantity of chemical elements into their surrounding environment on a scale of 10-100 ckpc (co-moving kpc). This process also expels most of the gas from their host halo, partially halting the formation of other stars. Finally, some metal elements are included in the stars, forming a different type of star.

For the first galaxies, the dark matter halos keep increasing their mass, where stars and larger structures can be formed. Such stars gather into clusters and eventually form proto-galaxies that are efficient for atomic line cooling. However, as mentioned above, the supernovae from stars at the end of their life deplete the gas in their host halos, delaying the star formation process. This can be continuous at the order of $sSFR = \frac{\dot{M}_*}{M_*} \sim 10^{-8}yr^{-1}$ if halo mass is higher than the atomic cooling limit (Kimm and Cen 2014; Kimm, Katz, et al. 2017). Of course, the value of special star formation rate can vary from one halo to another depending on the feedback from supernovae explosions. Some recent research has shown that the first galaxies can contain a range of 10^{6-7} $M_\odot$ of metal-poor stars and their host halos can contain a dark matter at a mass of 10^9 $M_\odot$ (Xu et al. 2016).

The galaxies reside in the halos of dark matter formed from both dark matter and baryons (gas, dust, and stars). This makes galaxies sensitive to physical processes that do not affect the cold dark matter. For example, stellar feedback or black hole physics can play a role in the formation and evolution of galaxies. Galaxies are composed of several components of gas, dust, and dark matter. For this reason, their morphology, mass, and size can vary widely. The most massive galaxy contains 10^{12} stars while the smallest one has only 10^7 stars. Depending on their morphology, galaxies are classified into four types:

- Spiral galaxies are the most common type of galaxy. They have a spiral shape, with a central bulge and a disk of stars, dust, and gas. The spiral arms are made up of denser gas, which makes them more likely to form stars. The stars in the spiral arms are usually young and hot, while the stars in the bulge are older and cooler.

- Elliptical galaxies have a smooth, elliptical shape and a very old stellar population. They usually include very little or even no stars due to the very low amount of gas and dust. As a result, the populations of stars are therefore older.

- Lenticular galaxies are the intermediate galaxies between spiral and elliptical phases with a large massive bulge, around which revolves a disk that is not quite active in the sense of stellar formation and in which we could not discern a spiral structure.

- Irregular galaxies with a complicated morphology. They often show chaotic shapes, including young stars and large amounts of gas.

1.2 Circum galactic medium

In the mid-1950s, while observing spectra of hot stars at high galactic latitudes, Guido Munch observed absorption of neutral sodium (NaI) and single ionized calcium (CaII). The appearance of these lines has been integrated by Spitzer 1956 as evidence for diffuse, extraplanar hot gas ($T \sim 10^6$K). In 1956, Lyman Spitzer introduced the concept of the "galactic corona", an encompassing region that surrounds galaxies for up to 1500 pc. After 7 years, when Schmidt discovered the first quasar, analysis of extragalactic gas progressed rapidly within the sense of the intervening absorption lines by spectroscopy (Bahcall 1968; Burbidge et al. 1967). Bahcall and Spitzer 1969 confirmed the presence of absorption

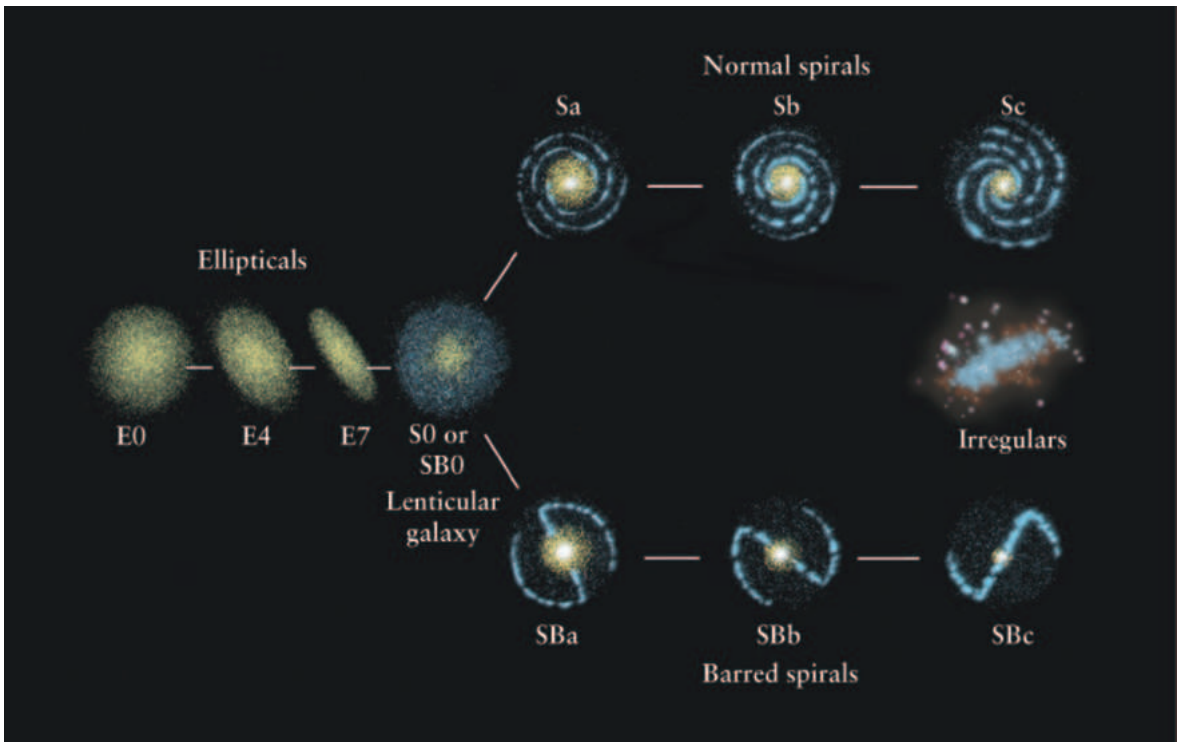

Figure 1.2: Four categories of morphology galaxies. https://sites.ualberta.ca/~pogosyan/teaching/ASTRO_122/lect23/lecture23.html

lines in observations caused by the extended gas around galaxies at redshift between 1 to 3. By the time, during the COPAS meeting in Canada in 2008, the term circumgalactic medium went back to Greg Bryan. Until now, there is no clear definition of CGM caused by its complicated environment, and multiple phases with a large number of physical phenomena, Rudie et al. 2012 introduced CGM as a region surrounding a galaxy within a radius of 300 kpc. Nowadays, we have investigated four big issues implicated in the evolution of the CGM: the difference in formation and evolution of galaxies may relate to the different massive dark matter halos; there is a small fraction of baryons and metals in the galaxies; the inflow and outflow of the regular gas passed into/through the CGM.

In the following paragraphs, I will present five approaches that have been employed to investigate this intriguing phenomenon.

- Transverse absorption line studies. Observing the CGM in absorption against a luminous background source, such as a quasar has three advantages over other methods. i) it can be used on the extremely low column densities $N \sim 10^{12}\mathrm{cm}^{-2}$ due to high sensitivity ii) one can access a wide density range iii) it is not affected by the redshift or luminosity of the host galaxy. However, there is one drawback to using transverse absorption lines, we can only measure gas surface density and are usually limited to one sightline per galaxy due to lacking background quasars. At the scale level of the local Universe (a few Mpc), it is possible to use multiple sightlines (Lehner et al. 2015). The method can be extended to the high redshift galaxies by using multiple lensed images of background quasars to constrain the size of absorbed sources (Rauch et al. 2011; Kate H. R. Rubin et al. 2015). In general, the CGM map made from absorption lines detected from many galaxies is obtained from statistical sampling of gas. For the massive optical spectroscopic surveys, the sample in low ions MgII and CaII have grown to hundreds or thousands (Zhu et al. 2013). This sample may extend out to $z \sim 4$ for quasar/galaxy pairings (Turner et al. 2014). It's also interesting to study HI column density regimes using different approaches. For example, lines up to $\log N \sim 15$ could be probed with Voigt profile fitting or Equivalent Width (EW). This value is

quite low for the CGM but is a bit high for the Lyα forest within a region of 100 kpc in which HI is not seen (Tumlinson, Thom, et al. 2013; S. D. Johnson et al. 2014). At $\log L \sim 16$ the absorption becomes a major factor, and robust column densities have to be obtained from profile fitting or higher Lyα series lines if the system is redshifted enough. This value is quite close to the Lyman limit system $N_{HI} > 10^{16}\mathrm{cm}^{-2}$. If the limitation is covered ($z > 0.24$ for Hubble), the decreasing of flux at $\lambda = 912(1+z)$ Å allows us to measure precisely $\log N_{HI}$ and metallicity properties. At the higher level, i.e. $\log N_{HI} \sim 18$, where N_{HI} is the HI column density, the Lyman limitation is completely opaque, the Lyman series is saturated so the true column density has to be computed by fitting the Lyman profile for the Lyman limit systems and damped Lyα series.

- Stacking analyses: A novel method for the investigation of halo gas could be conducted by massive spectroscopic surveys. The faint signal of the absorption line dataset could be extracted by stacking, which requires a catalog of redshifts for either absorbers or foreground galaxies. For this reason, spectra of background sources could be shifted to their rest frame and be continuum-normalized and then co-added together. The addition reduces statistical noise, allowing low absorption signals to be measured at the cost of averaging over the individual absorption profiles. The stack can be performed to examine the variation of mean profiles of input parameters such as mass, Star formation Rate (SFR), color, orientations, and radius, which are included in the subsets of the data (York, Khare, et al. 2006; Bordoloi et al. 2011). Due to the appearance of a large amount of dust in the CGM of galaxies (Ménard et al. 2010; Peek et al. 2015), the stacking may relate to the reddening of quasars. In addition, the stacking method can help exploit more faint sources by stacking spectra of background galaxies as the one was conducted in Steidel et al. 2010 to characterize the CGM of galaxies at redshift $z \sim 3$.

- Down-the-barrel is another method that is efficient for studying the inflow and outflow of galaxies (A. Henry et al. 2015; Heckman et al. 2015), as well as accretion (Kate H. R. Rubin et al. 2012) by using data collected from spectroscopy of star-forming galaxies. The main idea of the method is to use the starlight of our own galaxy as a background source for detecting absorption lines, such as CaII, NaI, MgII, and FeII. The down-the-barrel measurements are important for understanding the CGM because we can directly trace the outflow gas at galactocentric radii that are inefficiently covered by background sources. However, one disadvantage of this method is that it does not constrain the galactocentric radius of any detected absorption which will be anywhere along the light of sight.

- Emission line map: An emission line map is a method that aims to search for the photons emitted from the CGM gas. However, this method is still a challenge due to the measurement being scaled by a factor of n^2, where n is the number density of the gas and the CGM has $n_H \sim 10^{-2}$, which makes it very difficult to detect emission lines from the gas. At the UV/optical wavelength range, M. Hayes, Melinder, et al. 2016 detected an extended O, VI halo with a radius of 20 kpc surrounding a low redshift starburst galaxy. An extended Lyα emission has been observed out to ~ 100 kpc way from galaxies and Quasi-Stellar Object (QSO)s at redshift $z \sim 2.5$ (Cantalupo et al. 2014). The emission lines map can constrain the morphology, density profile, and physical extent of gas more than aggregated pencil beam sightlines (Corlies et al. 2016).

- Hydrodynamic simulations: Besides using data from observations to examine CGM, one can build models providing information on the environments, physical properties such as histories, and the future of gas. One can simulate the evolution of the cosmic web and galaxies by including the effects of dark matter, gravity, and hydrodynamics. These methods included smoothed particle hydrodynamics (Ford et al. 2013; Oppenheimer et al. 2016), adaptive mesh refinement (Hummels et al. 2013), moving mesh (Suresh et al. 2016), etc.

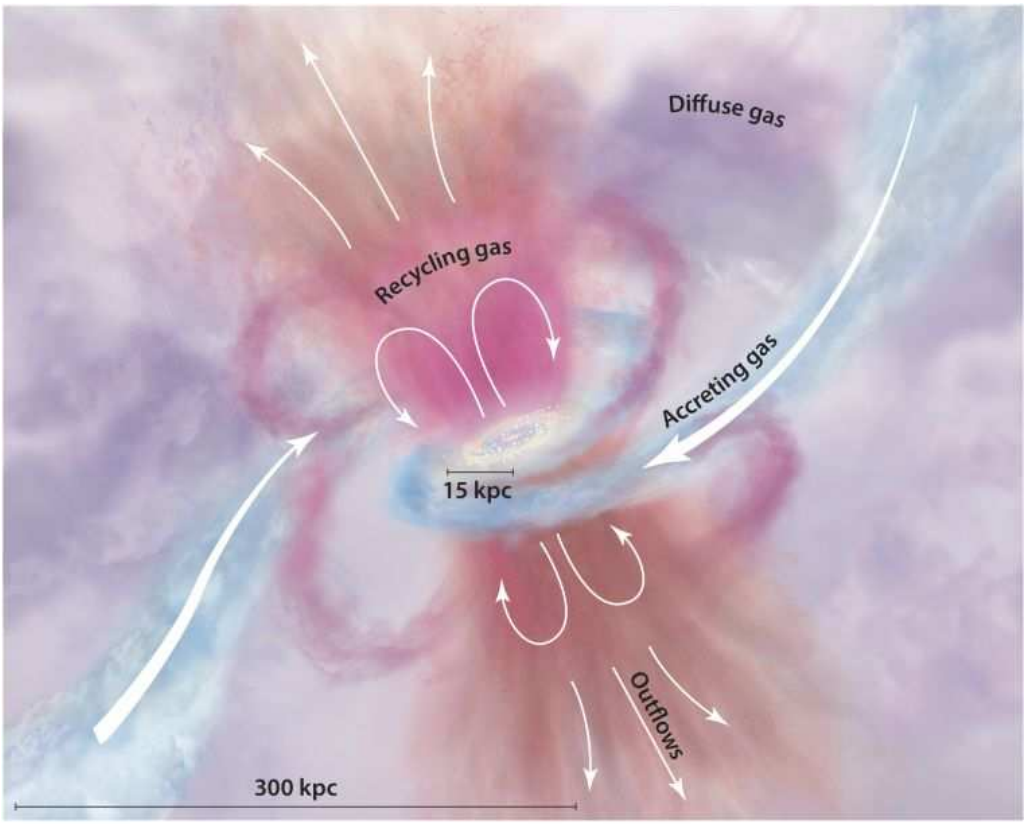

Figure 1.3: A schematic of the CGM showing outflow and recycle gas. The center volume and the gas disk are fed by the filamentary accretion from the Intergalactic Medium (IGM) (blue). The outflows have been marked pink and orange colors. The gas that was rejected previously is being recycled. The diffuse gas halo is marked by purple, its probability is contributed by these sources and mixed together over the time. Credit: Tumlinson, Peeples, et al. 2017.

1.3 Epoch of re-ionization

When the first structures of the Universe were formed, its radiation would ionize their surrounding environment. This stage starts between 0.1 and 0.2 Gyrs after the Big Bang. The ionized photons from such structures can travel freely in the neutral intergalactic medium (IGM) before being absorbed. This distance is called the mean free path, and expressed in the form:

$$l = \frac{1}{\sigma(\lambda) n_H(z)} \tag{1.3}$$

where $\sigma(\lambda)$ is the hydrogen cross-section for a photo-ionizing photon at a given redshift z, $n_H(z)$ is the average hydrogen number density with respect to a given redshift. Planck Collaboration: et al. 2013 estimated the mean free path in the IGM at redshift $z = 20$ was about l ~0.2 ckpc at redshift $z = 20$ and l=1.7 ckpc at redshift $z = 10$. Such results are much shorter than the normal size of the halo (100 ckpc), suggesting that the ionizing photon can not significantly travel in the neutral regions and will be absorbed by the neutral hydrogen atom at the boundary of the regions that have already ionized. For this reason, most of the ionized regions have a spherical shape which, is called of ionization bubble. Such a bubble always starts at a source and keeps growing with a sharp ionization front beyond. The ionizing process has been shown to have a negative feedback effect. Once the ionization happens, the gas inside the halo can not cool down as efficiently as before

because the cooling is done by the atomic cooling mechanism. When the neutral hydrogen content decreases, the probability for the collision excitation also decreases significantly (Wiersma et al. 2009). In addition, this ionizing process heats the gas up to 10^4K, efficiently photo-evaporating proto-halos of virial temperature below 10^4K.

The sources responsible for cosmic re-ionization are still under debate. Many candidates have been invoked to explain this major phase transition, but the evidence is still inconclusive. Massive population III stars were first thought to be the main contributors, but their short lifetimes prevented them from contributing much to the process (M. Ricotti et al. 2004; J. .-. Paardekooper et al. 2013). Other sources, such as X-ray binaries and Active Galactic Nuclei (Active Galactic Nuclei (AGN)), were then considered, but their abundance prevented them from making a significant contribution (Massimo Ricotti et al. 2004; McGreer, Jiang, et al. 2013). There is a minimum contribution to the ionizing budget coming from AGN (L. L. Cowie et al. 2009; Madau and Haardt 2015; Trebitsch et al. 2021). This is because the number density of AGN decreases dramatically at redshift $z > 3$ (Masters et al. 2012), and the escape fraction from ionizing photons seems not to be as high as needed (Micheva et al. 2017). The contribution of AGN to the Epoch of Reionization (Epoch of Reionization (EoR)) becomes significant for a large number of AGN having a low luminosity. This was proposed by Giallongo et al. 2015; Grazian et al. 2018, and has been confirmed by recent observations conducted with JWST (Kocevski et al. 2023; Übler et al. 2023; Harikane et al. 2023). In addition, the contribution of AGN to the EoR can be discussed via its contribution to the LyC emission at the redshift range $z = 2-3$ (G. D. Becker, Bolton, et al. 2015; Madau and Haardt 2015; Trebitsch et al. 2021). Until now, the question related to the contribution of AGN to the reionization of the Universe has not been answered yet and needs to be debated.

Quasars were once thought to be of importance, but it soon turned out that they are responsible mostly for the ionization of helium, not hydrogen atoms. The recent research (Matsuoka et al. 2018) shows that the ionizing photons created from quasars is only $\dot{n_{ion}} = 10^{48.8\pm0.1}$ s^{-1}Mpc^{-3}. This is only 10% less than the critical rate needed to keep the IGM ionized, but it suggests that quasars are not the main contributor to cosmic reionization.

Recently, there have been several observational results that suggest that star-forming galaxies may be the best candidates for the contribution of the ionization photons to the EoR (Robertson, Furlanetto, et al. 2013; Finkelstein et al. 2015; Onoue et al. 2017; Naidu et al. 2022; Matthee et al. 2022; Hakim Atek, Labbé, et al. 2023). These galaxies have low masses but high densities, which makes them likely to become dominant in driving the reionization process. However, the lack of observational data, in particular in the faint luminosity regime, makes the role of this population still uncertain. The luminosity function (LF), defined as the number of galaxies per given cosmic co-moving volume, is of importance in helping to quantify their role in the ionization process.

1.4 Recombination

In addition to studying the ionization of neutral hydrogen, there is another process that needs to be considered to model the reionization process: recombination. Recombination occurs when an electron in an excited state decays to the ground state, emitting a photon. If this photon is absorbed by another hydrogen atom, it can ionize that atom. The probability of recombination is determined by the number density of electrons and protons, as well as the temperature of the gas. The recombination coefficient α_A is a measure of the probability of recombination per unit volume per second. At a temperature of $T \sim 10^4$ K, the recombination coefficient for hydrogen is: $\alpha_A(H^0, 10^4 K) = 4.2 \times 10^{-13}$ cm^3 s^{-1}. This

value is much larger than the typical value of 10^{-14} cm^3 s^{-1} because of the Coulomb focusing of the incoming electron. It is significant at the lower temperature environment in which the recombination coefficient will be proportional to $T^{-0.7}$. There are two main channels for recombination: direct recombination, in which the electron decays to the ground state, and indirect recombination, in which the electron decays to a higher excited state before decaying to the ground state. The recombination coefficient being discussed includes both channels. However, in the case of direct recombination, the photon that is emitted can be reabsorbed by another hydrogen atom, ionizing that atom. This means that the effective recombination coefficient is actually lower than the value mentioned above. A correction factor has been calculated for this effect, and the resulting recombination coefficient is $\alpha_B(H^0, 10^4 K) = 2.6 \times 10^{-13}$cm^3 s^{-1}.

There are two main cases of recombination: case A, in which the hydrogen atom can move to many different excited states before decaying to the ground state, and case B, in which the atom decays directly from the first excited state to the ground state. The recombination time can be estimated from the recombination coefficient α as follows: $t_{rec}(T,z) = (\alpha(T) n_H(z))^{-1}$, where α is the recombination coefficient found from one of the two cases above at a given temperature. The recombination time for case B is about half that of case A, so it is often used in numerical simulations to reduce the computational time. However, this is only valid for the mean density of the IGM. In reality, the IGM is clumpy, with small neutral clumps that have a higher number density than the mean. These clumps have a high recombination rate, which can slow down the ionization process (McQuinn et al. 2011; Haardt et al. 2012). The clumping factor is a measure of the deviation from the mean density, and it can be used to estimate the effective recombination rate. The effective recombination rate is then used to calculate the recombination time. The effect of clumping on the Star Formation Rate Density (SFRD) will be discussed later in Section 5 of the thesis.

1.5 Spectral features of star-forming galaxies

1.5.1 The Lyman alpha line

The Lyα line is a spectral line of hydrogen atoms that is emitted when an electron transits from the excited state (n=2) to the ground state (n=1), where n is the quantum principal number. Due to the spin-orbit interaction, the line is split into a fine structure having two components, referred to as the Lyα doublet. Three states $2S_{1/2}$, $2P_{1/2}$, and $2P_{3/2}$ are associated with n=2 but only two transitions between 2P and 1S states can produce Lyman-alpha photons because of the quantum selection rule, which states that the total angular momentum of the initial and final states must be the same (Fig. 1.4).

Lyα emission may come from various sources. Young massive stars and AGN in the central regions of Interstellar Medium (ISM) are for example the sources of ionized hydrogen atoms. At larger scales, in CGM, the outflows from galaxies cause the excitation of HI region via shock heating. The infalling gas towards the galaxy center in cold accretion mode releases a large amount of gravitational energy via collisional excitation. The fluorescence light from hydrogen in the CGM and IGM photoionized by UV radiation background from QSOs may also contribute to ionized hydrogen clouds. Figure 1.5, from Ouchi, Ono, et al. 2020, illustrates the conceptual figure of an LAE.

Lyα line is one of the important probes to study early star-forming galaxies. Neutral hydrogen is the most abundant element in the Universe, making up about 70% of the mass, and exists at temperature ranges of 3000 – 7000 K. Most of the data observed in the SEDs of starburst galaxies show that the Lyα emission lines are formed through the combination

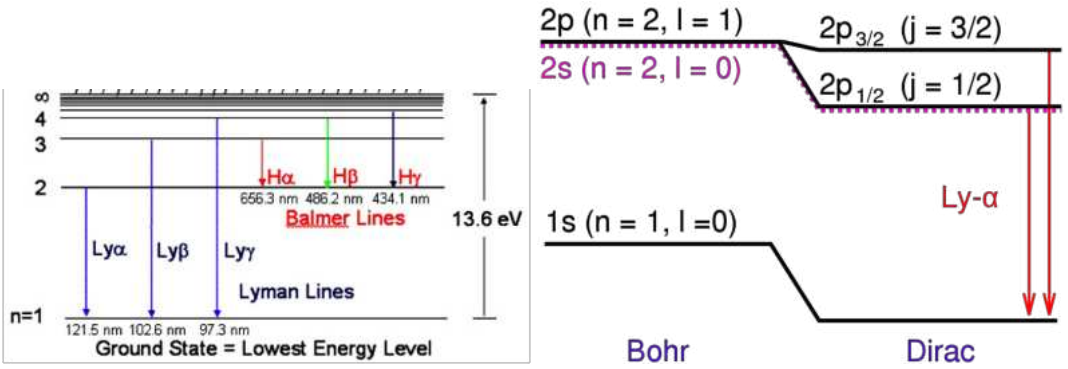

Figure 1.4: Lyman-alpha and other lines are shown together with the Lyman and Balmer series of hydrogen atom (left, credit: https://www.daviddarling.info/encyclopedia/L/Lyman-alpha.html). Lyman-alpha doublet (right, credit: https://en.wikipedia.org/wiki/Lyman-alpha_line).

of hydrogen atom inside the numerous HII region surrounding the most massive and hottest stars of these galaxies (O & B stars). At ~ 10,000K or so, stars emit a large amount of ionizing photons blueward the Lyα limit, allowing them to ionize the surrounding ISM neutral hydrogen gas and to emit Lyα emission lines. The wavelength of the Lyα photon at the rest frame is 121.6 nm. The expansion of the Universe makes the light from high-z star-forming galaxies redshifted and can be observed with a ground-based telescope in the visible and near-infrared ranges. This is one of the brightest emission lines of high-z galaxies and therefore is an important tool to probe the early Universe. In the environment of CGM, one can study the diffused Lyα emission extended over 10 kpc, or even more. The intrinsic Lyα luminosity in HII regions can be computed, based on the number of ionizing photons emitted from stars (D. Schaerer 2002b): $L(Ly\alpha) = 2/3(1 - f_{esc})h\nu_0 Q_H$ erg s^{-1}, where Q_H is total flux of ionizing photons, f_{esc} is fraction of Lyα photons which do not ionize hydrogen atoms, ν_0 is frequency of Lyα photons in the rest frame. Under the optical thick assumption, which is typical of HII regions, all Lyα photons emitted by recombination of hydrogen atoms are likely to be re-absorbed. All three states $2S_{1/2}$, $2P_{1/2}$ and $2P_{3/2}$ of neutral hydrogen atoms are equally populated, namely 2/3 of the recombination in HII regions converts to Lyman-alpha photons (Donald E. Osterbrock 1989).

The Lyα line is one of the brightest lines from star-forming galaxies (Partridge et al. 1967; Charlot et al. 1993; Malhotra et al. 2002), and it can be observed in the far-UV range. Galaxies that are identified by using the Lyman-alpha emission line are called Lyman Alpha Emitters (LAEs). They are in the early stage of their evolution, having masses ranging from 10^8 to $10^9 M_\odot$, more compact in physical size with radii of ~1 kpc, and less dusty than other types of high-z star forming LBGs (Taniguchi et al. 2009). Thanks to both the prominent strength of the Lyman-alpha emission and the advent of modern spectrographs such as MUSE/VLT, properties of host galaxies can be studied in some detail such as their Lyman-alpha luminosity, their EW, star formation rate by Lyα photons, the time scale of the Lyα emission.

The intrinsic Lyα line is very bright, and its contribution is up to 7% of the total bolometric luminosity of a star-forming galaxy (Partridge et al. 1967). However, as a resonant line, the radiative transfer of the Lyα photon is very complex. As these photons travel through the ISM, they are subject to being absorbed and/or scattered by neutral hydrogen atoms. The excited atoms then re-emit Lyα photons with slightly different frequencies in random directions, which is referred to as the resonant radiation process. In high-density regions of neutral hydrogen in the ISM of a star-forming galaxy, the resonant scattering increases the path lengths of the Lyα photons and hence their probability to be

absorbed by dust grain. As a result, the transportation of the Lyα photon depends very much on the mass of neutral hydrogen clouds, its dynamics, and the dust content of the IGM. These interactions leave strong imprints on the measured features of the Lyα line such as its line strength, its shape, its EW, etc. All the factors mentioned above must be taken into account when interpreting the observed Lyα profile and the intrinsic properties of high-z star-forming galaxies.

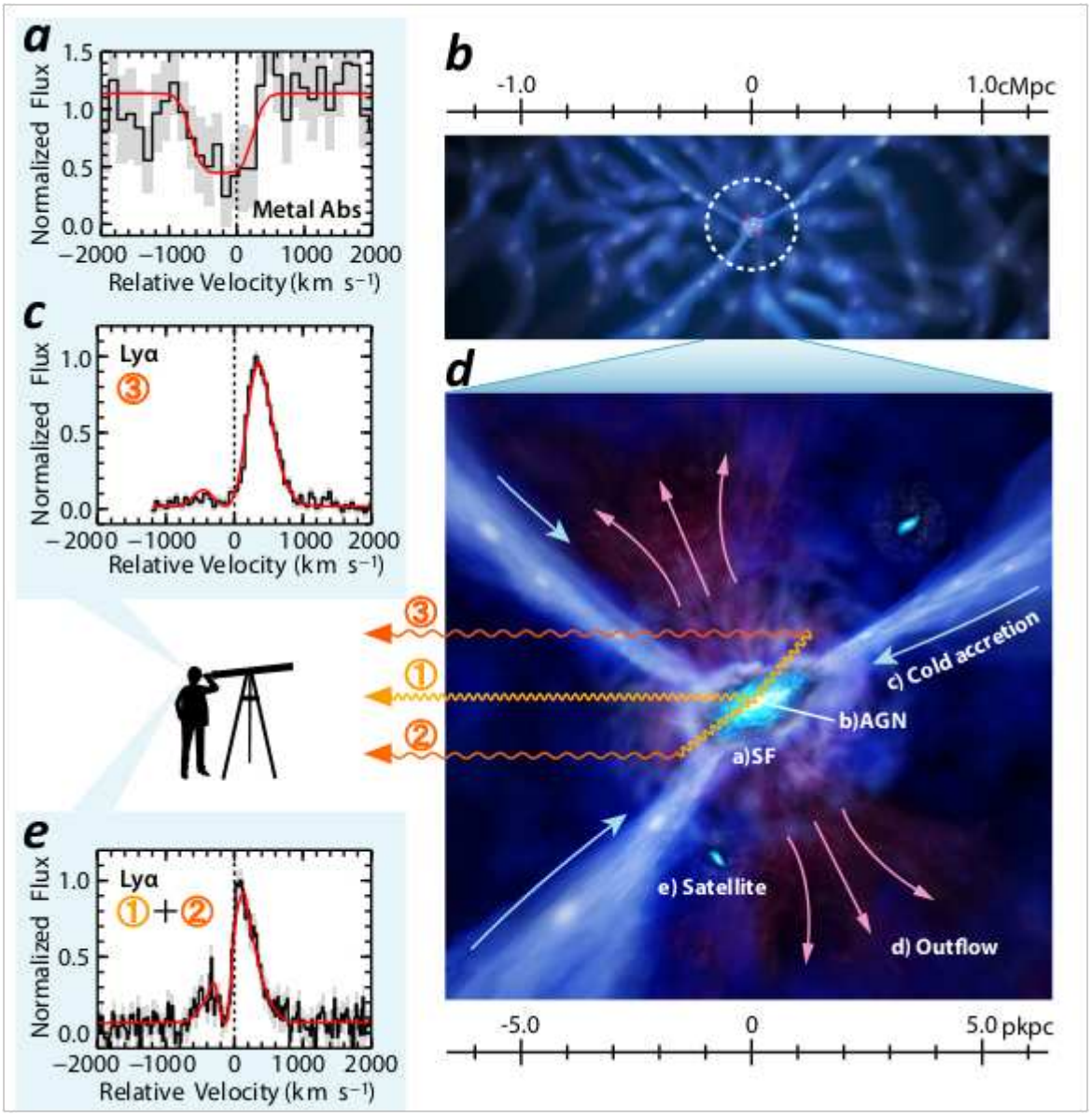

Figure 1.5: Conceptual figure of an LAE, located at the node of the filament (panel b). The zoom-in of an LAE is shown in panel d). Spectra of light paths 1, 2, and 3 are shown in panels c) and e). Credit: Ouchi, Ono, et al. 2020.

In addition to the high brightness of the Lyα line, the other feature of Lyman EW has been also studied. The EW is the ratio between the integrated luminosity of the line and the monochromatic luminosity of the continuum: EW = $L_{\rm line}/L_{\rm continuum}$ (Duval 2014). $L_{\rm line}$, $L_{\rm continuum}$ and EW are in units of erg s^{-1}, erg s^{-1} Å^{-1}, and Å, respectively. The EW of LAEs could reach 240 Å for normal stellar metallicities and 360 Å for metal-poor stars (Charlot et al. 1993). The EW declines with stellar populations aging and depends also on star formation activity. Its evolution is displayed in Fig. 1.7 (left). The lower limit of their EW is ~20 Å obtained from the samples using narrowbands (NBs) having a transmission

width ~ 1% of the central wavelength. Fig. 1.7 (right) displays the average fraction of Lyα emitting galaxy having EW > 25 Å for faint galaxies (M_{UV}>−20.25) and bright ones (M_{UV} < −20.25). This fraction increases with redshift between 4 and 6, then decreases at higher redshift, implying that the opacity of Lyα and the cosmic neutral hydrogen fraction do increase beyond 6. It implies also that the detection of LAEs at the middle and early epoch of re-ionization becomes more challenging.

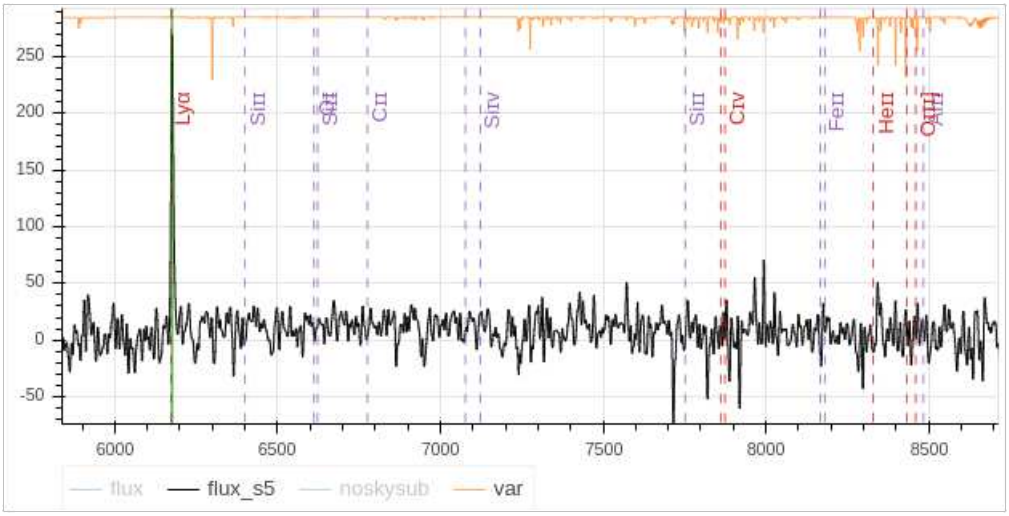

Figure 1.6: An LAE spectrum obtained from Multi Unit Spectroscopic Explorer/ Very Large Telescope (MUSE/VLT).

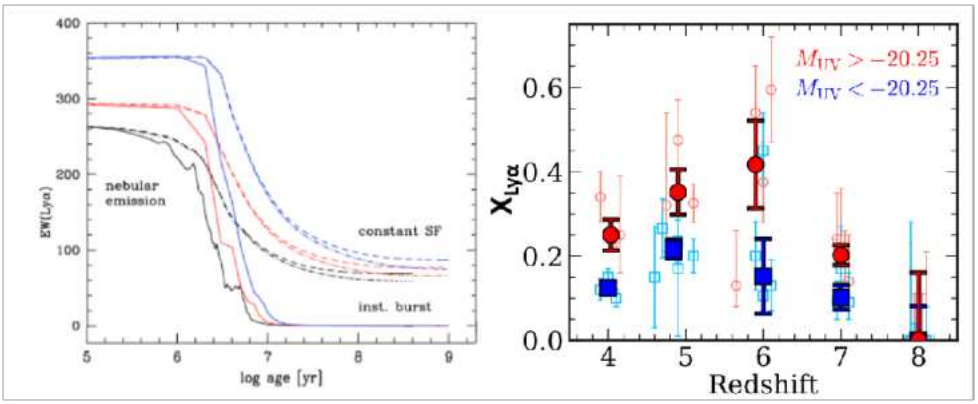

Figure 1.7: Left: The evolution of Lyman-alpha EW of instantaneous burst (solid lines) and constant star formation (dashed lines). Credit: Schaerer, D. et al. 2008. Right: Fraction of Lyman-alpha emitting galaxies having EW > 25 A° as a function of redshift. Credit: Ouchi, Ono, et al. 2020 (Figure 18)

Wisotzki et al. 2016a presented a sample of 26 galaxies that were observed by MUSE in the Hubble Deep Field Survey (HDFS), six of them showed an appearance of halos. In the Lyα analysis, such halos may be extended by a factor of 5 to 15 compared to the UV emission. By dividing Lyα emission into two components, one is close to the size of UV emission, and the other is more extended, they were able to investigate the properties of the central emission from those of the extended halo. The Lyα emission distribution may follow an exponential law with a characteristic length of a few kiloparsecs and most of them come from the extended component of the halo. One year later, Leclercq, Floriane et al. 2017 studied a larger sample of LAEs with 145 Lyα halos and found a correlation

between extended Lyα emission component and UV properties of galaxies in both size and magnitude.

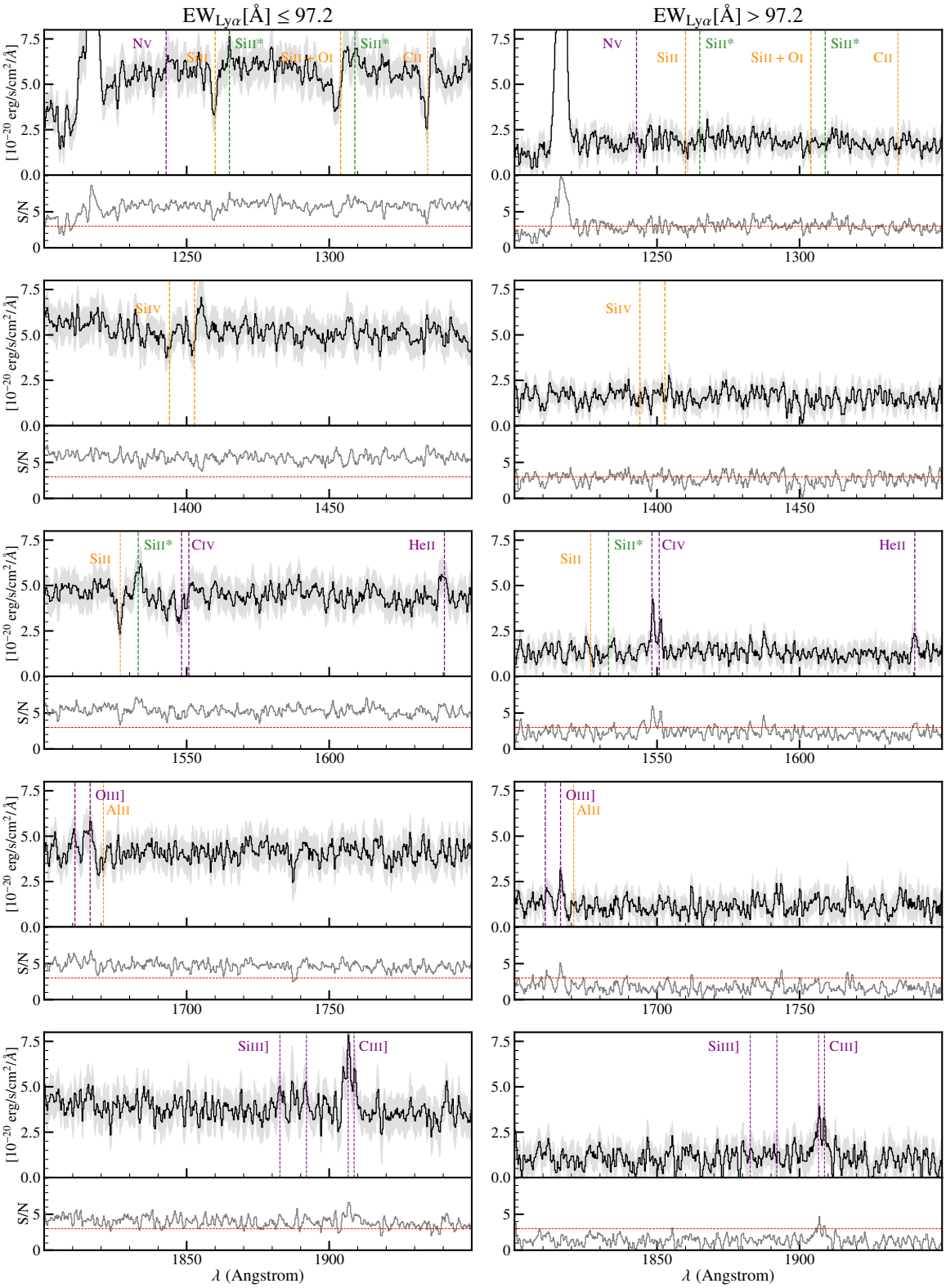

Figure 1.8: Mean spectra of LAEs with Lyα EW < 97.2 and > 97.2 (left and right, respectively). The median values of the Lyα EW for the two subsamples are 54.7 and 163.1, respectively. Credit: Feltre, Maseda, et al. 2020.

1.5.2 The Lyman Break galaxies

Lyman Break galaxies (LBGs) are star-forming galaxies detected by using the traditional technique. They are identified by comparing their fluxes in different broad-band filters. Surrounding neutral gas both in the interstellar environment ISM and IGM absorb completely radiation photons having energy higher than the Lyman limit of 912 Å, making galaxies "drop-out" bluewards with respect to this limit. The method has been extensively used and has become the traditional way to look for high-z galaxies in the early universe.

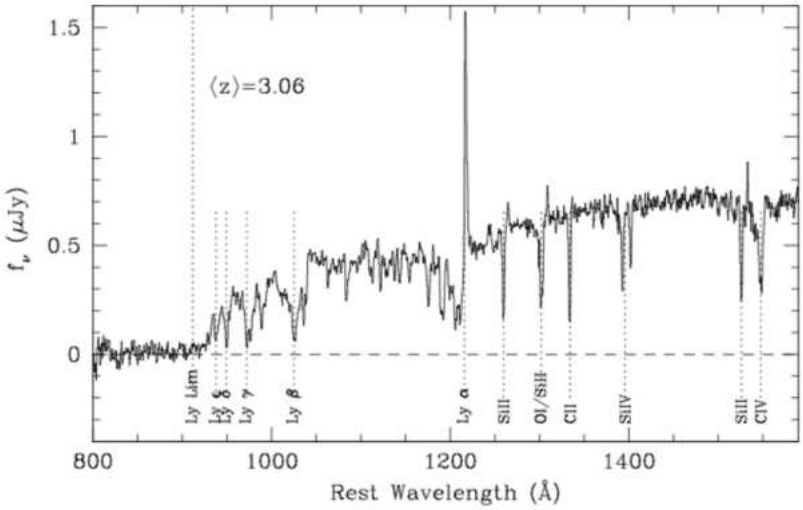

Figure 1.9: A spectrum at rest frame of a star-forming galaxy at redshift $z \sim 3$ (Shapley, Steidel, Pettini, et al. 2006) in the wavelength range of (800 – 1500 Å). The break of the UV continuum flux can be seen in the interval of 912 – 1215 Å.

The properties of these LBGs depend strongly on the host galaxies (UV luminosity, neutral hydrogen mass fraction, etc.). The less massive galaxies tend to have fainter UV luminosities and lower HI masses. Such properties make them difficult to be detected in the UV continuum. LBGs are often found in more massive galaxies having larger HI masses and are associated with active star-forming galaxies. As a result, LBGs emit a bright UV continuum making them easy to be identified. In addition, this effect also can be seen from the observed profile of the Lyα line. The UV continuum flux in the blue part of the Lyα line is lower than that of the red one. This can be explained as the foreground neutral IGM hydrogen clouds absorb significant UV radiation making the observed continuum level in the blue part of the Lyman-alpha line reduced accordingly. For galaxies at the early EoR, the observed UV continuum flux toward the blue of Lyα lines is expected to be zero, namely, they are completely absorbed. This is the so-called Gunn-Peterson effect (Gunn et al. 1965).

Many thousands of LBGs have been found. Their properties are summarized as follows, in comparison with those of LAEs. They often have a high star formation rate from 10 to 100 $M_\odot yr^{-1}$ at the redshift $z \sim 3$ (Porciani et al. 2002). They are a bit older than LAEs, typically ~300 Myrs at redshift $z \sim 3$ (Shapley, Steidel, Adelberger, et al. 2001), more massive, 10^{8-11} $M_\odot$ with $z \sim 1-4$ (Shapley, Steidel, Adelberger, et al. 2001; Elsner, F. et al. 2008), dustier (Gawiser, van Dokkum, et al. 2006; Gawiser, Francke, et al. 2007; Kornei et al. 2010), more extended in size, R ~1.8 kpc at $z \sim 3$ and decrease to R ~0.8 at $z \sim 6$ (M. Akiyama et al. 2008; R. Bouwens et al. 2006).

1.5.3 Lyα forest

Spectra of high-z galaxies in the early Universe often display a series of absorption lines that are related to the Lyα line of the neutral hydrogen atom, which is at 121.6 nm in the UV range. The absorption feature is caused by the presence of neutral clouds in the IGM along the line of sight. The appearance of the Lyα series is treated as a post-reionization version of the Gunn-Peterson trough so it can not be used directly to study the EoR. They are usually used to quantify the inhomogeneous properties (i.e.: the gas cloud's physical and chemical states) of neutral fraction after EoR with a lower limit of neutral fraction $n_{HI} > 0.94$ at redshift $z = 5.9$ (Mesinger 2010; Greig et al. 2017). The lower column density region $N_{HI} \sim 10^{12-16}$ cm^{-2} is an ideal environment to observe Lyα forest as these clouds are very sensitive to photo-ionization and photo-heating from UV background. Based on these properties one can estimate ionization rate and temperature after EoR, those help us have a deeper understanding of the behaviors during the reionization.

An example of using Lyα forest to study reionization rate could be mentioned in the research of York and Adelman 2000; G. D. Becker, Hewett, et al. 2013 showing a constant value within a range of redshift $z = 2-5$, and starts increasing at a higher redshift. One also uses Lyα forest to investigate a typical temperature of IGM at $z = 5$, which is about $T \sim 10^4$ K (Schaye et al. 2000; G. D. Becker, Hewett, et al. 2013).

The very first confirmation of the presence of Lyα series from the mostly absorption of HI Lyα was done in Lynds 1970. After that, hundreds of individual absorption lines of quasars at redshift $z > 2$ could be resolved using a higher resolution spectrograph, its appearance gave raising to the label of the Lyα forest (Weymann et al. 1981). However, there are some missing lines in the forest coming from UV transitions of common metal or heavy element ions such as the ionization stages of Fe, Si, Mg, Al, C, and O which are usually seen in the spectral observations. Such lines always appear with a strong Lyα line.

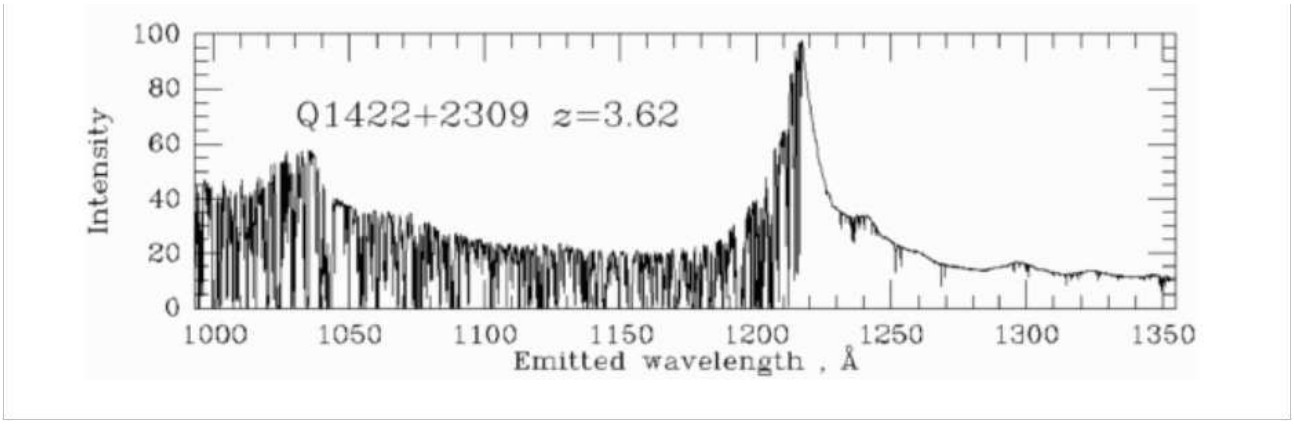

Figure 1.10: Observed spectral energy distributions of a quasar at redshift $z \sim 3.6$ in the rest-frame. The series of absorption lines (Lyα forest) due to the presence of IGM neutral hydrogen clouds at different redshifts along the line of sight, is clearly seen. The appearance of hundreds of absorption lines in the measured spectra is then referred as Lyα forest. Credit: http://www.astr.ua.edu/keel/agn/forest.html.

1.5.4 The Gunn – Peterson effect

It is already known that the Lyα line is formed from a transition between the ground state and the first excited state at a wavelength of 1215 Å. This only happens to the neutral hydrogen which can undergo such a transition (absorption and emission properties), so

it's a clue for the existence of neutral hydrogen along the line of sight. In addition, the quasars are known to have a continuum emission of the same order magnitude as the Lyα line. In some observations of quasars at redshift $z > 6$, one usually sees a strong absorption pattern blueward of the Lyα line or redward of the Lyman beta line (Fan et al. 2006; McGreer, Mesinger, et al. 2014). This feature is called a Gunn-Peterson trough from the very first observation made in Gunn et al. 1965. The existence of this effect is shown in Fig. 1.11 as the very latest observation on the quasar spectrum at redshift $z = 6.13$ showing a clear Gunn- Peterson trough obtained by G. D. Becker, Bolton, et al. 2015 and others observations (see Fig. 1.12).

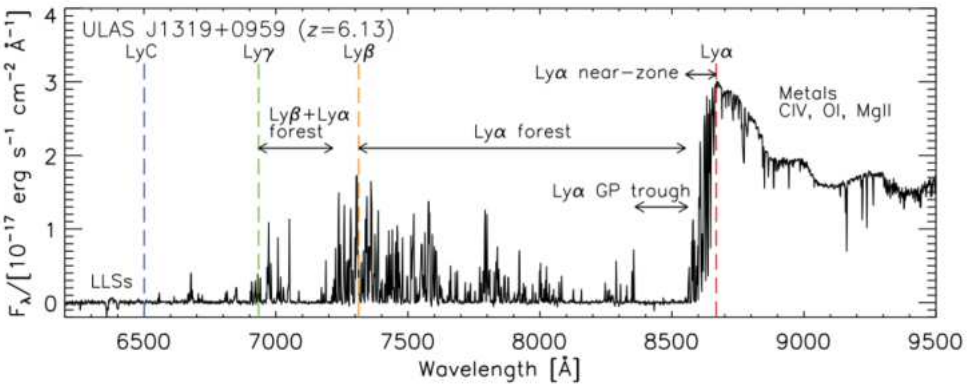

Figure 1.11: Spectrum of a quasar at redshift $z = 6.13$ (ULAS J1319+0959) taken from G. D. Becker, Bolton, et al. 2015 simulation for the existence of Lyα forest and Gunn-Peterson effect.

In general, from such a spectrum, one can access the position of neutral hydrogen clouds and find the local neutral fraction along the line of sight as well. However, there is a problem of this reconstruction method related to the optical depth at the Lyα wavelength. The increase of neutral hydrogen gas of the Universe at the higher redshift was confirmed in many previous results, so when the neutral fraction $x_{HI} > 10^{-4}$ exists in the environment of IGM, this region will become optically thick to the Lyα photon leading a total absorption and limitation the reconstruction process to the very end of EoR. However, there are still some other affect a depth observation of the EoR. Firstly, using the radiations from QSO shows that the hydrogen vicinity of AGN regions seems to be more ionized than the normal IGM. It means that the radiation towards the blueward of Lyα is more weakly absorbed suggesting that one can study further on the ionized regions surrounding the quasars. In addition, for a given width of the Lyα line, the photons can be absorbed at the wing of the line with an even lower probability. Even at the lowest level, when the neutral hydrogen column density may reach up to $N_{HI} = 10^{20}$ cm^{-2}, the absorption property can be observed in the wing.

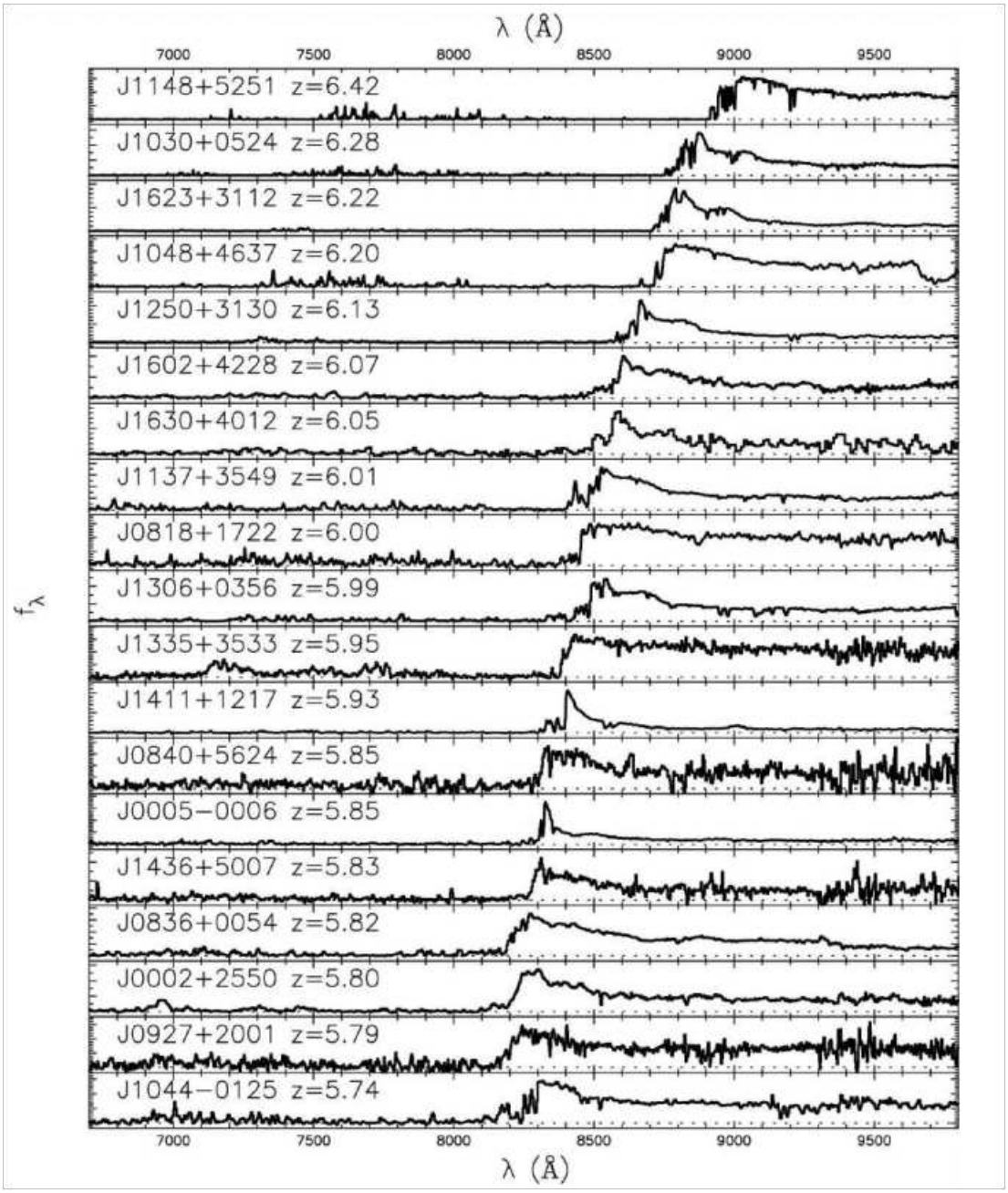

Figure 1.12: Measured quasar's spectra at different redshifts. The Gunn – Peterson trough is observed for quasar spectra having $z > 6$. Credit: Fan et al. 2006.

1.6 LBG technique and photometric redshifts

The typical spectrum of a high redshift star-forming galaxy (Fig. 1.13) leads to the LBG selection method. An emitted photon having a wavelength less than 912 Å is completely absorbed by neutral hydrogen gas in the ISM and IGM to make the Lyman break in the observed spectrum. At redshift $z > 3$, the Lyman break is shifted to the visible range making high-z galaxies become accessible to ground-based optical telescopes. To identify a high-z LBG, three traditional broadband filters (U, G, R) have been used to look for variations of colors of a galaxy. Nearby galaxies show their appearance in all three filters but if sources disappear in the bluestone, they are high-z candidates. This is illustrated in Fig. 1.14. This technique has been proven to be very efficient in detecting high-z star-forming galaxies, even up to $z \sim 12-13$ (Pacucci et al. 2022). Following up on spectroscopy observations

of these sources, which is time-consuming, will help to confirm their redshifts. Many thousands of LBGs have been identified using this selection method.

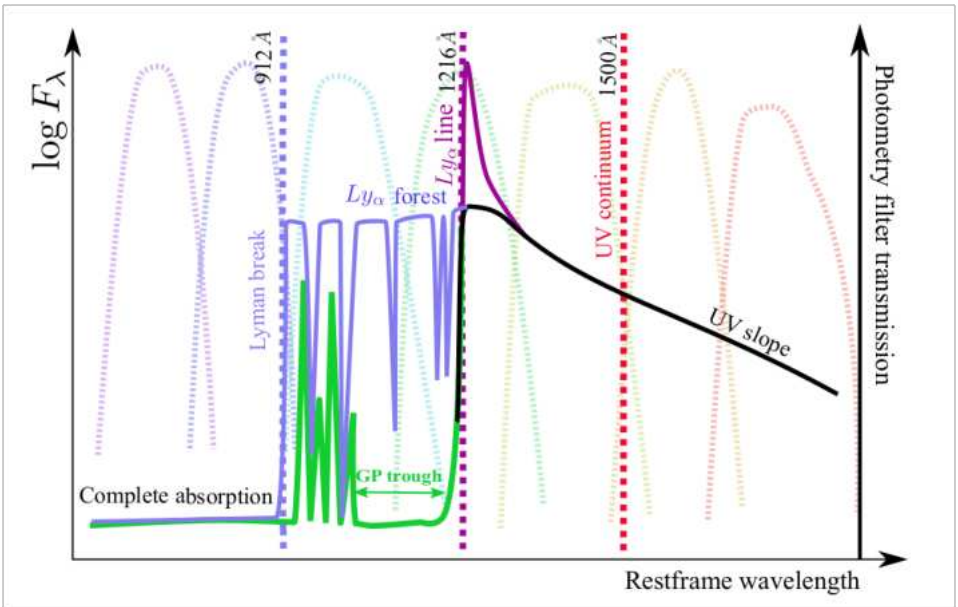

Figure 1.13: Typical spectrum of a high redshift galaxy. Credit: Vieuville 2019.

In addition to this color–color selection, which is relatively fast and simple to implement, a more advanced technique using SED-fitting has been used to estimate more precise photometric redshift (Bolzonella et al. 2000). The fit procedure makes use of photometric measurements and template spectra having a wide range of parameters such as star formation, metallicity, initial mass functions, etc. An example of the SED fitting technique is illustrated in Fig. 1.15.

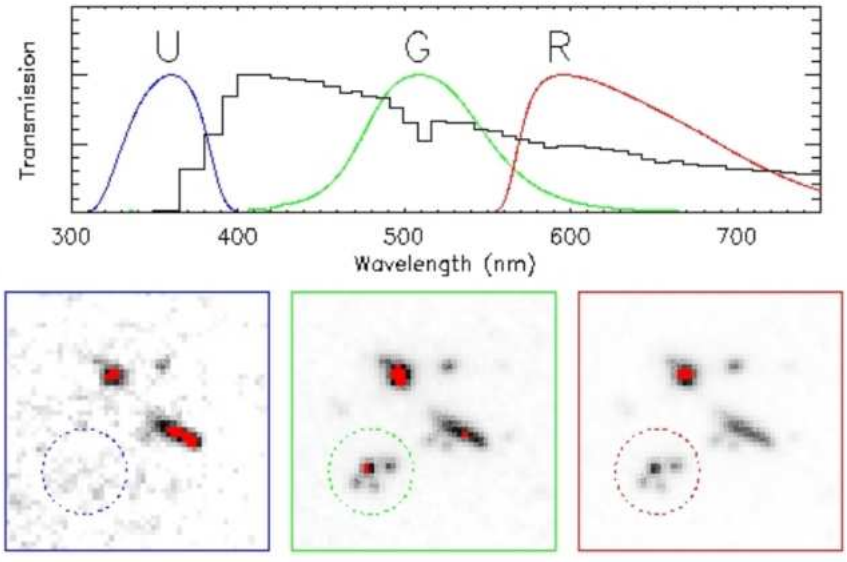

Figure 1.14: Lyman break technique method. Upper panel: SED model of a star-forming galaxy at redshift $z \sim 3$ is shown together with three broadband filters U, G, R. Lower panel: Galaxy appearances at different filters. The galaxy is detected both in R and G bands but disappears in the U band. Credit: Burgarella, D. et al. 2006.

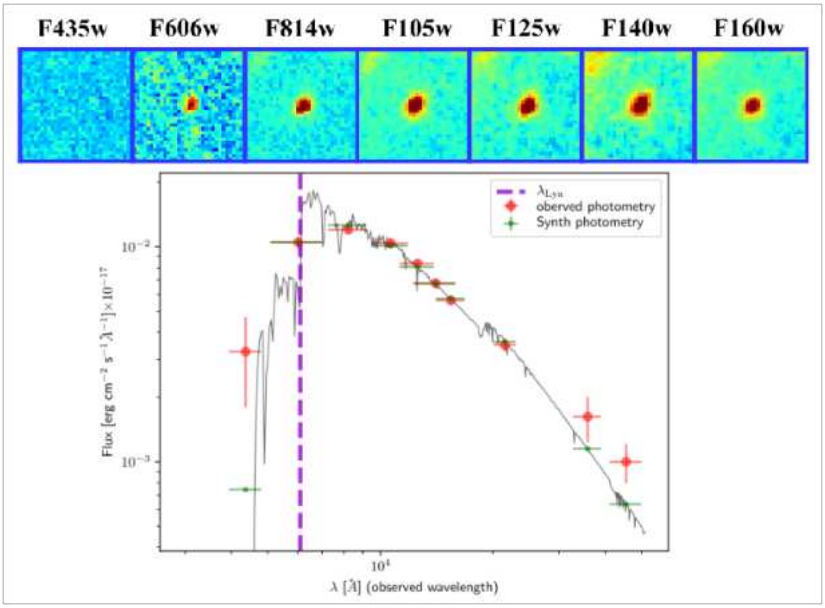

Figure 1.15: Upper panel: HST filters show a drop-out of a galaxy at short wavelength filters (Lotz et al. 2017). Lower panel: SED fitting technique using HST photometry. Credit: Vieuville 2019.

The photometric technique has been developed for a long time (since ~1960) and has become spectacular in recent years because of deep multicolor photometric surveys. The technique allows us to study a large number of objects that could not be accessed by spectroscopic observations or that would have required a long time for the available instruments. This tool allows users to estimate the redshift of galaxies, quasars, AGN, etc. using the input values as magnitude/flux measured from long/medium band photometry and identify the spectral break as well. This method provides less accurate results than the one obtained from spectroscopic owing to being dependent on the filters.

To measure the photometric redshift of sources, there is a very popular method is being applied named SED fitting method (Lanzetta et al. 1996; Fernández-Soto et al. 1999). It is a combination of the observed values obtained from filters at the range of 912-4000 Å and several reference spectra obtained from theoretical research aiming to find a minimum difference χ^2 which is performed as the one proposed by Bolzonella et al. 2000:

$$\chi^2(z) = \sum_{i=1}^{N_{filters}} \left[\frac{F_{obs,i} - b \times F_{temp,i}(z)}{\sigma_i} \right]^2 \tag{1.4}$$

where $F_{obs,i}$, $F_{temp,i}$ and σ_i is the observed flux/AB magnitude, template flux, and its uncertainty with respect to the filter i and b is a normalization constant.

The most advantage of this method is easy to use and does not require any spectral sample. The user can be flexible to modify some parameters/choose several models to get the best fitting values. However, this is also the disadvantage of the method as we have to choose a few representative models valid for all objects in the present sample.

1.7 Selection of LAEs: narrow-band technique

In the rest frame, the wavelength of the Lyα line emission is 1215 Å. When emitted by high-redshift galaxies, the line is shifted to the optical and near IR ranges. With the advent of modern optical telescopes and filters, one now uses the Narrow Band (NB) technique to

detect high redshift star-forming galaxies, using both a NB filter displaying a flux excess on the line and broadband filters overlapping with it or redder. Fig. 1.16 shows an example of the detection of an LAE at $z = 6.96$ using the Lyα emission line (Iye et al. 2006). A measure of the quality of identification of a Lyα line is the so-called rest-frame Equivalent Width (EW) defined as the ratio between the line flux and the continuum spectral flux density; one usually retains lines having EW in excess of 20 Å.

Thousands of LAEs at various redshifts, up to $z = 8$, have been identified using large telescopes such as KECK, VLT, and Subaru, equipped with very sensitive Charge Coupled Device (CCD) cameras, which started operation in the late 1990s (Hu et al. 1998; Ouchi, Shimasaku, Furusawa, et al. 2010). With the advent of MUSE/VLT, an integral field spectrograph, associated with high performance Adaptive Optic (AO), major progress has been achieved in the search for LAEs having redshifts in the range from 2.9 to 6.7 (see Chapter 2).

The availability of a large sample of high-redshift detected LAEs made it possible to study their physical properties in some detail. They are often found to be very compact, with a typical effective radius of 0.6 ± 0.1 kpc at $z \sim 6$ (Dow-Hygelund et al. 2007). They have low stellar masses ranging from 10^8 to 10^9 $M_\odot$ at $z \sim 3$, and from 10^6 to 10^{10} $M_\odot$ at $z \sim 5$ (Gawiser, Francke, et al. 2007; Pirzkal et al. 2007). They host young stellar populations (< 90 Myrs at $z \sim 3$) and have moderate star formation rates. Their EW can reach 200 Å (Shimasaku et al. 2006).

1.8 Selection of LAEs: Integral Field Units

A normal spectrograph usually captures data from a line through an image and provides spectral data over one spatial dimension. However, the new technique known as Integral Field Units allows a spectrograph with a slit opening to collect data across a two-dimensional field. The signal in each pixel is fed into a spectrograph to generate a spectrum for that pixel. After this stage, the result will be arranged into a datacube with 2D entire FoV and 1D drawn from the spectrograph. This technique is associated in the second generation of VLT instruments aiming at producing high-quality images with a large Field of View ($1' \times 1'$ in Wide Field Mode (WFM) and $7" \times 7"$ in Narrow Field Mode (NFM)). It has excellent spectroscopic capabilities, covering a large wavelength range (475 – 935 nm) with spectral resolution $R \sim 3000$. It is equipped with powerful AO to correct for atmospheric turbulence and is well suited for spectroscopy studies of crowded fields such as lensing clusters. The AO-corrected field of view is split into 24 sub-fields, each fed into a spectrograph called Integral Field Unit (IFU). An image slicer in front of each IFU serves as entrance slit, thus producing a spatially resolved spectrum of the whole sub-field. Wide-field narrow-band surveys using the MUSE pencil beam provide a direct measure of the redshift and the practical procedure to select LAEs is presented in Section 2.4.

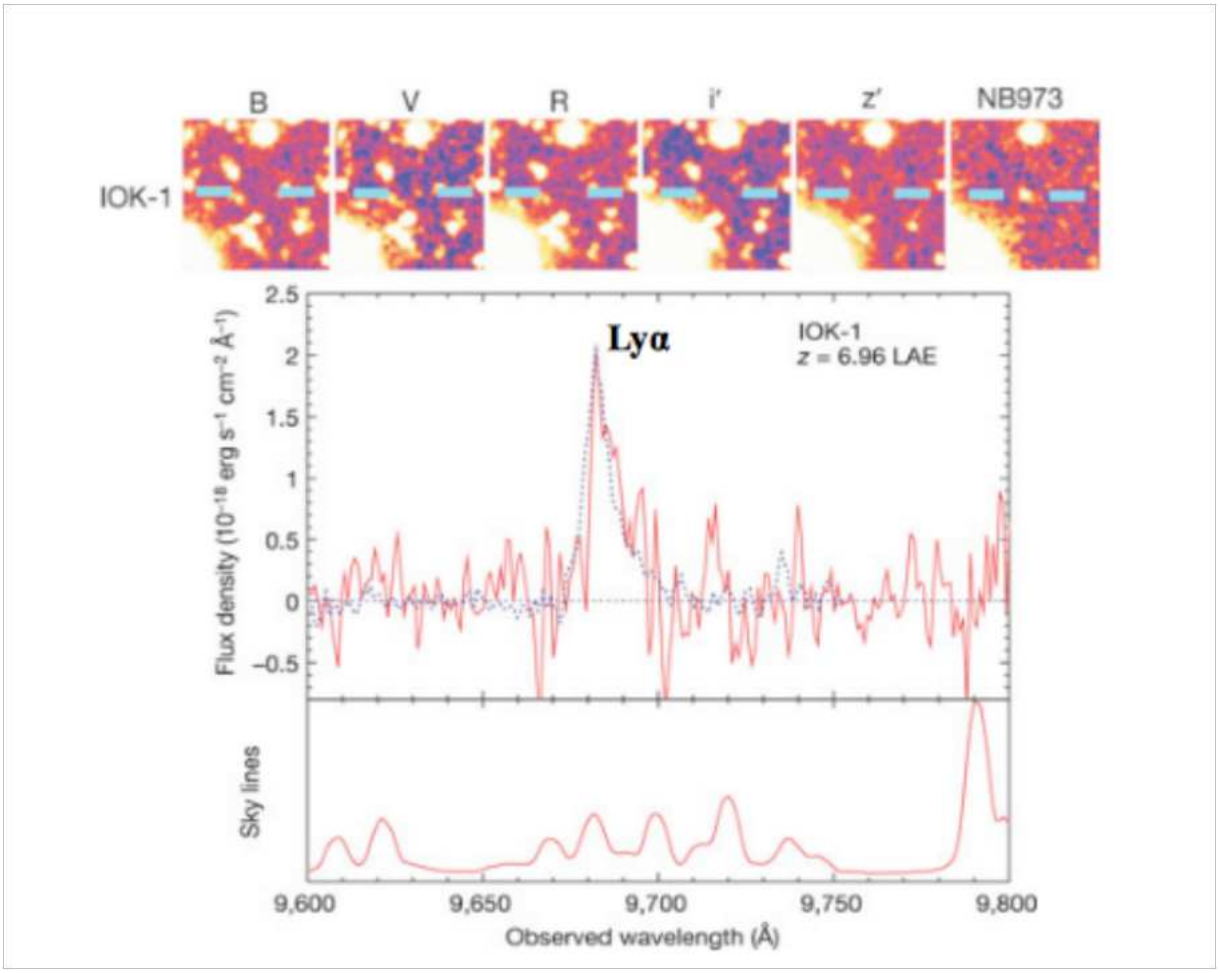

Figure 1.16: Illustration of LAE detection at redshift $z = 6.96$ using the NB technique. In this case, the Lyα emission line is detected using the NB973 filter, but not using the other 5 broadband filters (B, V, R, i', and z') blueward of the line. Credit: Iye et al. 2006.

1.9 The galaxy luminosity function

The Luminosity Function (LF) is defined as the dependence on luminosity of the number of galaxies detectable in a given co-volume, called number-density. It is measured in units of $(\mathrm{erg\,s^{-1}\,Mpc^3})^{-1}$. It is one of the most fundamental quantities used in the study of the evolution of galaxies in the early Universe. The LF usually displays a transition between high values toward its faint-end at low luminosities and low values toward its bright end from a power-law to an exponential decline. One refers to it as the turnover or knee. The position of the knee and the values taken by the slope are characteristic parameters of the LF. In the present work, we limit the study to luminosities smaller than the knee in order to secure the reliability of the evaluation of the LF. In the study of the evolution of LAEs, one usually uses a parameterization of the LF called Schechter function, of the form (Schechter 1976):

$$\phi(L_{Ly\alpha})dL_{Ly\alpha} = \phi* \left(\frac{L_{Ly\alpha}}{L_{Ly\alpha}*}\right)^{\alpha} \exp\left(-\frac{L_{Ly\alpha}}{L_{Ly\alpha}*}\right) d\left(\frac{L_{Ly\alpha}}{L_{Ly\alpha}*}\right) \tag{1.5}$$

where $L_{Ly\alpha}$ is the LAE luminosity, $\phi*$ a normalization factor, $L_{Ly\alpha*}$ is the value taken by the LF at the knee, α the value of the slope at the faint end. The Schechter function may be

re-written in logarithmic form:

$$\phi(\log L_{Ly\alpha}) = (\ln 10)\phi * 10^{(\alpha+1)(\log L_{Ly\alpha} - \log L_{Ly\alpha *})} \exp(-10^{(\log L_{Ly\alpha} - \log L_{Ly\alpha *})}) \quad (1.6)$$

In order to reveal the evolution of galaxies, one needs to study the dependence on redshift of the LF. Two decades ago, Loveday 2004, using data from the SDSS Data Release 1, and found a significant evolution of galaxies in r-band, corresponding to a range of redshifts $z = 0 - 0.3$. It could be interpreted in terms of an evolution of the density, of the luminosity, of an intrinsic change of shape, or of any combination of these. Recent studies have given evidence for an increase of Lyα LF at low redshifts ($z = 0-3$) as shown by Deharveng et al. 2008, a moderate evolution at intermediate redshifts ($z = 3-6$) as shown by Ouchi, Shimasaku, Masayuki Akiyama, et al. 2008, and a sudden and strong decrease beyond $z \sim 6$ as shown by Kashikawa et al. 2011. At redshifts in the $z = 2.2 - 3.3$ interval, at high luminosities $L_{Ly\alpha} > 10^{43.3}$ erg s^{-1}, Spinoso et al. 2020 measured $\alpha = -1.35 \pm 0.84$ from observations of the Javalambre Photometric Local Universe Survey (J-PLUS) covering a region of ~ 1000 deg^2. Konno, Ouchi, Shibuya, et al. 2018 examined 1266 LAEs at redshift $z = 5.7$ and $z = 6.6$ using data of Subaru/Hyper Suprime Cam Survey with luminosity in the range of $\log L = 10^{42.8-43.8}$ erg s^{-1} measured $\alpha = -2.6^{+0.6}_{-0.4}$ and $\alpha = -2.5^{+0.5}_{-0.5}$, respectively. Itoh et al. 2018 compared LAEs with other galaxies at higher redshift ($z \sim 7.0$) in a field of view ~ 3.1 deg^2 observed with Subaru Telescope and measured $\alpha = -2.5$. The same value was found by Konno, Ouchi, Ono, et al. 2014 for sources at redshift $z \sim 7.3$. These previous studies suffer from a clear lack of deep enough observations of Lyα emissions. To cope with it, the fits were made with a fixed value of $\alpha = -2.5$ at the faint end, providing a satisfactory picture of the overall evolution of the LF of LAEs. Figure 1.17 shows an evolution of LF at different redshifts of these works. Yet, some questions are still unanswered, as concerning the contribution to Lyα emission from low mass dark matter halos surrounding SFGs. The best fit Schechter function, providing an estimate of the LAE luminosity density, is an essential input for understanding the evolution of galaxies during the epoch of cosmic reionization, including evaluations of the SFRD and of the fraction of hydrogen ionizing photons that escape from galaxies into the IGM. It is therefore important to obtain as precise as possible a shape of the LF. In particular, this requires a good understanding of the impact of having fixed the slope at the faint end, where a turnover (Liu et al. 2016) is expected to be caused by the efficiency of gas cooling in SFG halos (Hakim Atek, Johan Richard, et al. 2018; R. J. Bouwens, G. Illingworth, et al. 2022).

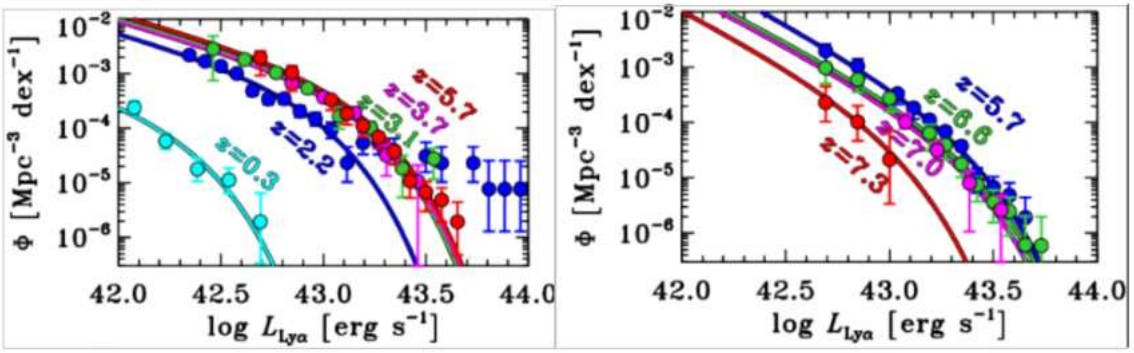

Figure 1.17: Evolution of Lyα LF from $z = 0.3$ to $z = 5.7$ (left) and from $z = 5.7$ to $z = 7.3$ (right). The curves are the best-fit Schechter functions obtained by Lennox L. Cowie et al. 2010; Konno, Ouchi, Nakajima, et al. 2016; Ouchi, Shimasaku, Masayuki Akiyama, et al. 2008; Konno, Ouchi, Shibuya, et al. 2018; Itoh et al. 2018

Recently, MUSE has made it possible to detect fainter LAEs in a redshift interval covering $z = 2.9 - 6.7$ and has provided a more complete picture of the LF evolution. Drake et al. 2017 explored a blank field using blind IFS of MUSE and detected 604 LAEs with luminosities down to $\log L < 41.5$ erg s^{-1} in the redshift interval $z = 2.9 - 6.7$. They measured a slope of $-2.03^{+1.42}_{-0.07}$ at $z = 3.44$ and $\alpha = -2.86^{+0.76}_{\infty}$ at $z = 5.48$. Herenz et al. 2019, using observations covering 22 arcmin^2 in the CANDELS/GOODS-S field measured the LF of 237 LAEs in a luminosity interval of $42.2 < \log L$ [erg s^{-1}] < 43.5 using three different non-parametric methods. They obtained a slope $\alpha = -1.84^{+0.42}_{-0.41}$ with a characteristic luminosity value of $\log L*$ [erg s^{-1}] $= 42.2^{+0.22}_{-0.16}$.

Lately, major progress has been achieved in exploring the very faint part of the Lyα LF by taking advantage of gravitational lensing. MUSE observations over regions of the sky covered by four lensing clusters have been very recently analysed by Vieuville et al. 2019 (hereafter DLV 2019), in the same redshift range as explored by (Drake et al. 2017; Herenz et al. 2019). Gravitational lensing enables the detection of sources which could not be seen previously, but the complex relation between the source and its images implies intricate and computer-time-expensive calculations for the evaluation of the LF. The data used by DLV 2019 include 156 LAEs reaching faint luminosities, $\log L = 10^{39-43}$ erg s^{-1}. The evolution of the LF is studied in four redshift ranges, $2.9 < z < 6.7$, $2.9 < z < 4.0$, $4.0 < z < 5.0$, and $5.0 < z < 6.7$; the measured values of the slope are $-1.69, -1.58, -1.72$, and -1.87, respectively.

1.10 Overview of this work

Taking advantage of the availability of new MUSE Guarantee Time of Observation (GTO) observations of regions of the sky covering seventeen lensing clusters, the present thesis studies LAEs detected behind these in the range of redshifts $2.9 < z < 6.7$ and measures their LF. Much attention is paid to the evaluation of the dependence of the LF on redshift, in particular toward faint luminosities. The results give an important contribution to the current progress in this field, which keeps asking for improved statistics. We proceed as follows: The first step is the selection of detected LAE images behind the lensing clusters. We need to calculate the LF in the source plane, implying a measurement of the number of sources detected in a given covolume as a function of luminosity. This requires transforming from the image plane to the source plane and evaluating for each source its probability of having been detected, its luminosity distribution corrected for various instrumental effects and the volume in which it could have been detected. These evaluations are not independent and require to proceed by iterations in a complex sequence of calculations. In addition to the complication resulting from the production of multiple images from a single source by gravitational lensing and the need to know the values taken by the associated magnifications, we need to account for the effects of noise and of seeing.

The selection of LAEs images in each of the 17 MUSE datacubes uses standard procedures: looking for line emissions in the spectral distribution (integrated over the whole field of view), subtracting continuum contribution, evaluating for each line a region of the sky containing most of the line emission. In addition, we associate each obtained image with UV HST images in the same region of the sky, providing a much more precise knowledge of the position of the image and telling us which LAE source (listed in an available catalog) it is the image of. The ~ 1400 images detected at this stage, are in fact associated with only ~ 600 different sources, because some images are associated with a same source. The next step consists, for each image, in evaluating its probability of having been detected and the volume to be used in evaluating the luminosity density. To start with, we select, for each source, one of its detected images (when there is more

than one) as considered the cleanest based on reasonable criteria. For each of the 600 selected images, we evaluate, in each of the 17 MUSE intensity maps, what is the map of the probability for this particular image to have been detected above noise (we call it a mask). The masks obtained in the image planes need to be de-projected onto the source planes. This procedure is heavy in terms of computer time and requires particular care in dealing with faint sources. Accounting for noise level leads to the introduction of the concept of completeness, measuring the probability of successfully detecting the source. Accounting for seeing leads to the concept of convolution/deconvolution using the PSF associated with it.

The selection of LAEs behind the 17 lensing clusters, with MUSE directly providing the associated datacube, differs from the method adopted in blank field observations, where the telescope is made to point toward a previously observed source. The main difficulty is to account for the lensing effect in the best possible way. This requires a proper evaluation of the magnification associated with each image of a given source as well as of the dependence on redshift of the effective surveyed volume. We start with the identification of multiple-image systems observed in the cluster cores, for which we select the best images of a given source. Lensing effects are carefully taken into account when computing the effective volume associated with each source and evaluating its incompleteness. This is presented in Chapters 3, and 4.

In order to evaluate the LF of a given source we use an approach originally developed by DLV 2019and referred to as the $V_{\rm max}$ method. Here, $V_{\rm max}$ is a measure of the maximum volume of the survey in which an individual source could have been detected. One needs to estimate the incompleteness affecting each individual source in order for its statistical weight in the LF to be properly obtained. We have introduced some improvements to the original $V_{\rm max}$ method in order to better account for the effect of lensing. These improvements made it possible, in order to include as many sources as possible in the final sample, to lower the completeness threshold down to 1%. Together with the enlarged sample of lensing clusters (17 compared to 4 in DLV 2019) they make this work a unique study of the faintest end of the Lya LF.

Having applied the improved $V_{\rm max}$ method and corrected for completeness, we are in a position to calculate the value of LF in each luminosity bin of in a given redshift range and fit the result to a Schechter function. In practice, we ignored particularly high magnification contributions to very faint luminosity bins, associated with large uncertainties, and used a modified Schechter function to account for the presence of a turnover in the faintest luminosities at the highest redshifts. The best-fit values of the parameters of the Schechter function measured in each redshift interval are then used to compute the SFRD as a function of redshift and estimate the escape fraction of Lyα photons. These results are presented and discussed in Chapter 5. They have been published in three refereed articles and presented at international conferences.

2 The MUSE Lensing Project: from observations of massive clusters to LAE sample selection

Contents

2.1 General

VLT stands for Very Large Telescope located on the Paranal of the Atacama Desert in the Northern part of Chile, at 2635 m above sea level. This system consists of 4 telescopes, 8.2-metre in diameter, mostly working in optical and infrared modes (see Fig. 2.1). It can be operated for individual observations, in visitor mode, or remotely. Sometimes, when the weather is good enough, the system is used for interferometry for a limited number of nights each year. The auxiliary telescopes of the system having a mirror of 1.8 metre can be operated every night with a maximum baseline in interferometer mode up to 140-metre. The four names of the main telescopes are Antu, Kueyen, Melipal, and Yepun.

MUSE stands for Multi Unit Spectroscopic Explorer (R. Bacon, Accardo, et al. 2010). It is the second generation VLT panoramic integral-field spectrograph developed by the European Southern Observatory (European Southern Observatory (ESO)) for the VLT. This system is associated with AO to correct for atmospheric turbulence on the surface of the Earth. There are seven big institutes in the MUSE consortium: AIP Potsdam, CRAL Lyon, ESO, ETH Zurich, IRAP Toulouse, Leiden, and IAG Gottingen. The data used in this work come from the Guaranteed Time Observations (GTO) granted to the consortium by ESO as a reward for building MUSE. The information presented in the following sections is provided by the ESO MUSE User Manual. This project has been started since 2000 and the instrument was commissioned in 2014 by its current PI, R. Bacon. MUSE is an Integral Field Unit (IFU), a spectrograph providing one spectrum per spatial element with a field of view of $1' \times 1'$ sampled at 0.2" × 0.2" in Wide Field Mode (WFM) and 7.5" × 7.5" in Narrow Field Mode (NFM). A MUSE datacube contains 2048 × 2048 spatial pixels and 4096 wavelength channels spanning a range from 4650 Å to 9300 Å with a spectral resolution varying between R=2000 to R=4000. A simulation for the MUSE cube is shown in Fig. 2.2.

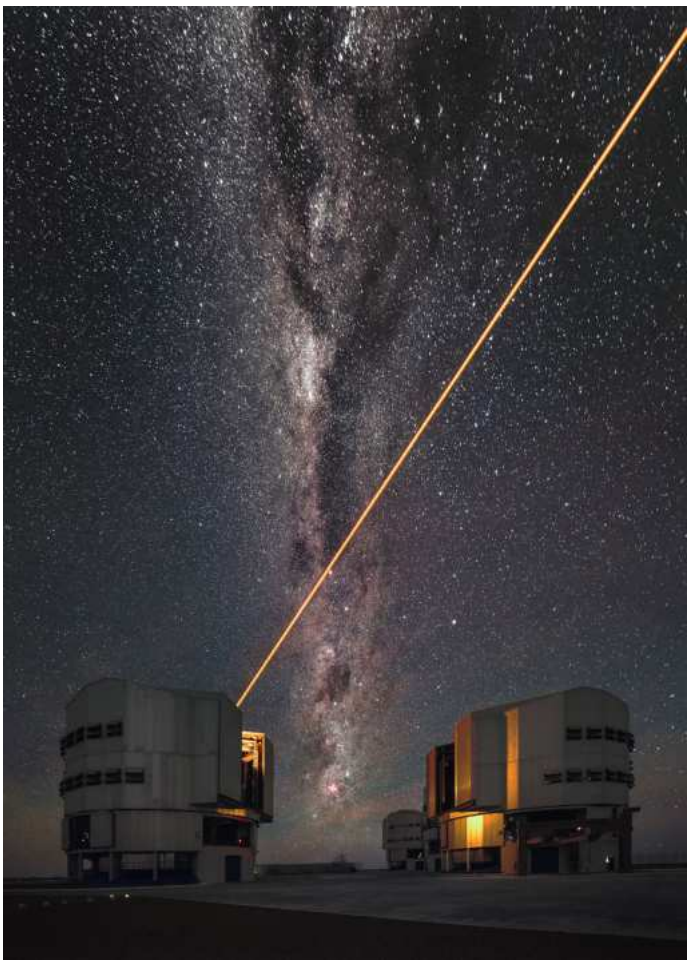

Figure 2.1: The orange glow light of a Laser Guide Star emanates from one of the Very Large Telescope with details of the Milky Way revealed. Credit: ESO/A.Ghizzi Panizza (www.albertoghizzipanizza.com).

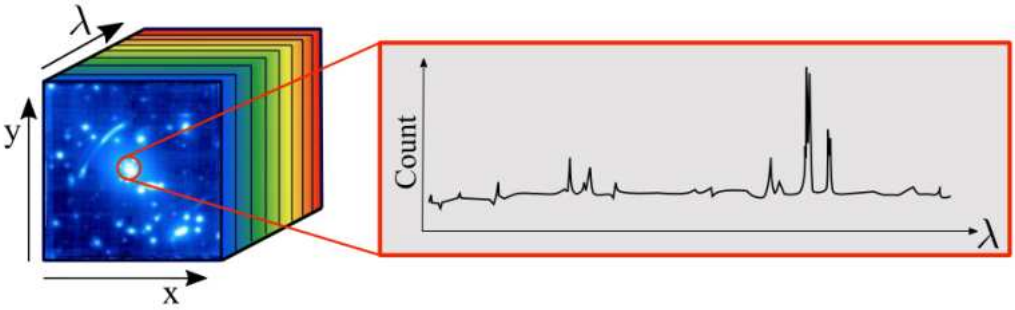

Figure 2.2: The MUSE cube structure with 2 spatial dimensions and one wavelength dimension. Credit: Vieuville 2019.

When the light from an astronomical object reaches the Earth's atmosphere, the turbulence of the atmosphere may make the image distort and move in various ways. MUSE overcomes this disadvantage by using AO to compensate for the blurring caused by the Earth's atmosphere. The MUSE project went through long planning, construction, and testing before its installation at the VLT. After a decade of preparation, the first light came to MUSE, capturing high quality images of planetary and galaxy in January 2014. MUSE has been coupled with the powerful AO system between 2017 and 2018, using four 22-watt

lasers that shine into the sky to make sodium atoms in the upper atmosphere glow. They produce spots of light in the sky that mimic stars (artificial guiding stars). The Sensor of the AO module Ground Atmospheric Layer Adaptive Corrector for Spectroscopic Imaging (GALACSI) (Ground Atmospheric Layer Adaptive Corrector for Spectroscopic Imaging) uses these signals as an artificial guide star to capture the changes in the atmospheric conditions. The signal is sent to the AO a thousand times per second to calculate the correction and then move the shape of the telescope's deformable secondary mirror to compensate for blurring caused by the Earth's atmosphere. The combination of an optimal site for the VLT facilities and the use of AO makes MUSE images sharper, resulting in twice the contrast achieved by previous facilities. For this reason, MUSE is particularly well suited to study faint sources in great detail.

There are three modes for MUSE running: NFM using AO, WFM with and without using AO. The difference between them is using AO and spatial sampling. NFM coupled with AO allows to correct for atmospheric turbulent above the telescope helping to have sharper images but over a small region for observations (`http://www.ens-lyon.fr/en/article/research/supersharp-images-new-vlt-adaptive-optics`). In particular, the system associated with the fore optics is used to select the observing mode, for instance, to change the spatial sampling from 0.2" (in the WFM) to 0.025" (in the NFM) with a reduced field of view of 7.5" × 7.5". Especially, this mode is more significant when working on studying a single object at a very high spatial resolution. For example: studying supermassive black holes, young stellar objects, or the Solar system, etc. Using WFM which has a relatively large field of view allows us to study more extended objects. This mode coupled with AO permits to correct for the effect of atmospheric turbulence up to 1km above the telescope over a wide region of the sky ($1' \times 1'$ with a spatial sampling of 0.2" × 0.2"). MUSE has been used extensively in this mode to detect up to 15000 sources by setting up nested surveys of different areas and depths. To date, one of the deepest surveys of MUSE has required a long observing time of around 141 hours reaches a $3-\sigma$ limiting flux of 1×10^{-19} erg s^{-1} cm^{-2} (Bacon, Roland et al. 2017; R. Bacon, J. Brinchmann, et al. 2023). These observations can help us solve one of the most challenging studies nowadays in the identification and characterization of the faintest objects formed during the very first billion years in the history of the Universe. For example, studying LAEs redshifted to the wavelength observed by MUSE $2.9 < z < 6.7$.

2.2 Main scientific goals of MUSE

Using AO with the possibility to use WFM and NFM makes MUSE become efficient in many different scientific fields since the commission was started, which permits the community to analyze individual sources with high angular spectral resolution such as planetary, small object science to the stellar population in nearby and high redshift galaxies. The main scientific purposes of the MUSE instrument can be listed as follows based on the observing mode.

- Using NFM, which is known to be highly efficient in the analysis of individual sources with very high resolution makes it possible to:

+ Study Super Massive Black Hole (SMBH)s with several issues that can be addressed on the merging of galaxies, SMBHs sinking to the bottom of the potential well, and the formation of binary systems, etc. In addition, it is also possible to study the accretion of the matter to form black holes. However, such observations are rare and difficult to interpret. Therefore, further investigation is necessary to understand the physical properties in these regions.

+ Young stellar objects: Thanks to MUSE we may have the opportunity to study the formation and structure of jets in great detail.

+ Solar system: There are multiple objects within our Solar system that can be observed with the same spatial resolution compared to many space telescopes.

- In contrast, we use WFM to detect multiple faint sources, which may be 100 times fainter than those observed with narrow-band imaging to address some scientific goals such as:

+ Study intrinsically faint galaxies at high redshift. This is the main driver for the development of MUSE. It is intended to identify and study the properties of faint high z galaxies observed both in blank and lensing fields. In the latter case, we use massive clusters to study the background population of galaxies by taking advantage of the magnification provided by gravitational lensing (Kneib et al. 2011).

+ Detect Lyman alpha emission out to the EoR, the origin of re-ionization.

+ The analysis of some physical properties of LBGs such as their wind, and feedback to the IGM. These studies require a combination of MUSE data with deep HST observations.

+ Find the late-forming population III objects.

+ Investigate active nuclei at intermediate and high redshifts.

+ Perform a map of the growth of dark matter halos.

Since 2017, the community has achieved a lot of progress in exploring the first MUSE spectroscopic survey data release (Bacon, Roland et al. 2017; Inami et al. 2017) in the Hubble Ultra deep field area (Beckwith et al. 2006). The list includes some of the early papers that discuss significant findings, such as the discovery of extended Lyα halos around individual high redshift galaxies (Wisotzki et al. 2016b), investigating the photometric redshift properties of the sample (J. Brinchmann et al. 2017), the properties of sources emitting CIII] (Maseda, Jarle Brinchmann, et al. 2017), the faint end of Lyman alpha LF (Drake et al. 2017; DLV 2019; Herenz et al. 2019), the extended Lyman alpha halos (see Fig. 2.3, Leclercq, Floriane et al. 2017), the extreme EW features of LAEs with a low stellar mass (Hashimoto et al. 2017; Maseda, Roland Bacon, et al. 2018), the evolution of the galaxy merging fraction (Ventou et al. 2017), etc.

There is a long list of results achieved by the MUSE consortium based on the GTO program. We could mention among others the study on MgII emission/absorption in star-forming galaxies (Feltre, Roland Bacon, et al. 2018), finding a systematic redshift from Lyman alpha line profiles (Verhamme et al. 2018), investigation of the strong lensing of A2744 using combined data from MUSE and Hubble Frontier Fields images see Fig. 2.4 (Mahler et al. 2018), the evolution of LAE fraction (Kusakabe et al. 2020), an ATLAS of lensing clusters (Johan Richard, Adélaide Claeyssens, et al. 2021), finding the hydrogen filament see Fig. 2.5 (R. Bacon, Mary, et al. 2021), a link between Lyman alpha halo sizes to the physical properties of the host galaxies (A. Claeyssens et al. 2022), observing more almost 400 LAEs per arcmin^2 in the deepest dataset encompassing 140 hours (R. Bacon, J. Brinchmann, et al. 2023), etc.

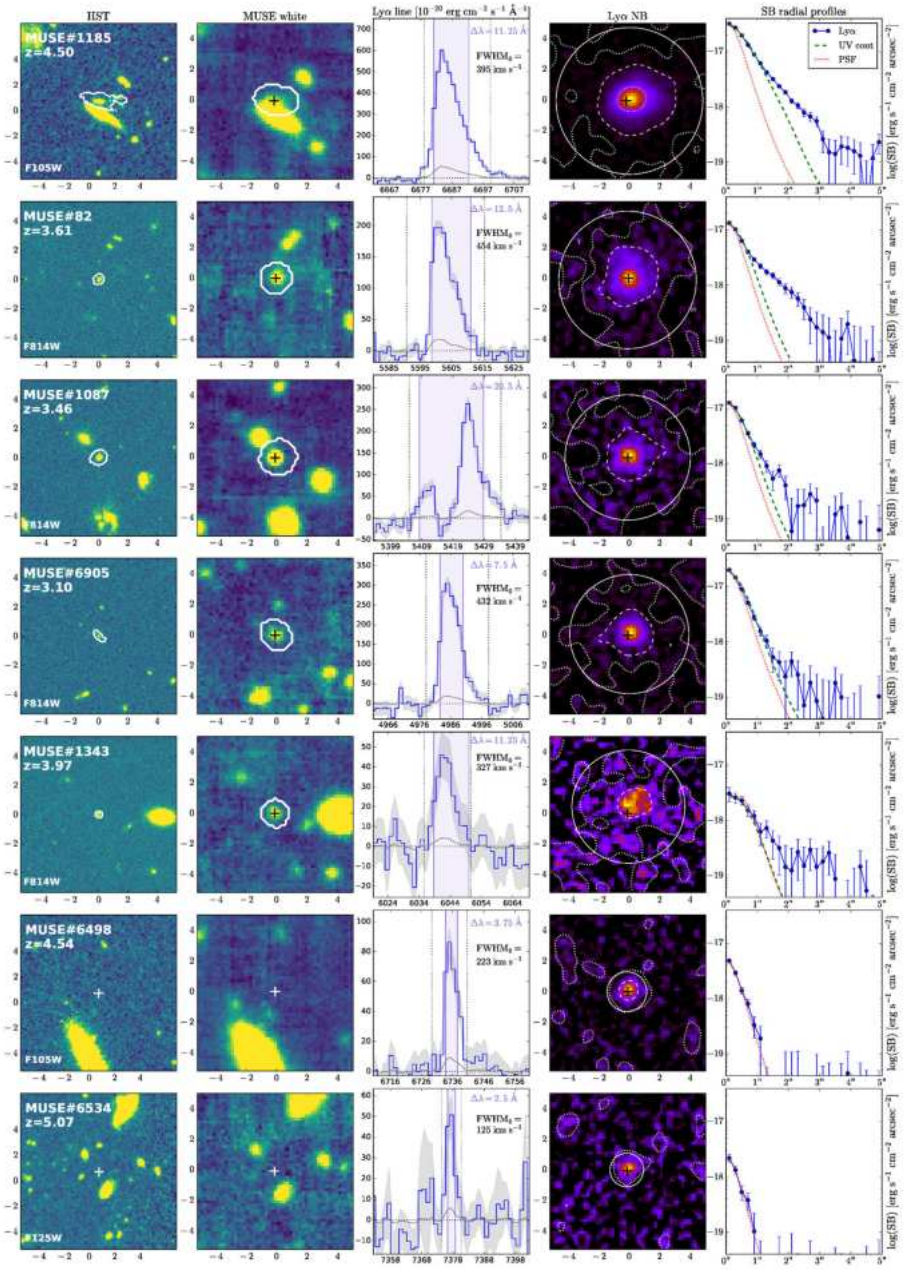

Figure 2.3: An example of finding extended Lyα haloes around high z SFGs. The first column is the HST image of LAE denoted by its contour on the HST segmentation mask. The second column is MUSE white light image of the LAE. The third column is the Lyα line extracted from the HST segmentation mask convolved with the MUSE Point Spread Function (PSF). The fourth column is NB image of the LAE with surface brightness contour at 10^{-17} erg s^{-1} cm^{-2} arcsec^{-2} (central dotted white). The last column is the radial Surface Brightness (SB) profiles of Lyα emission (blue), UV continuum (green), and the PSF (red). Credit: Leclercq, Floriane et al. 2017.

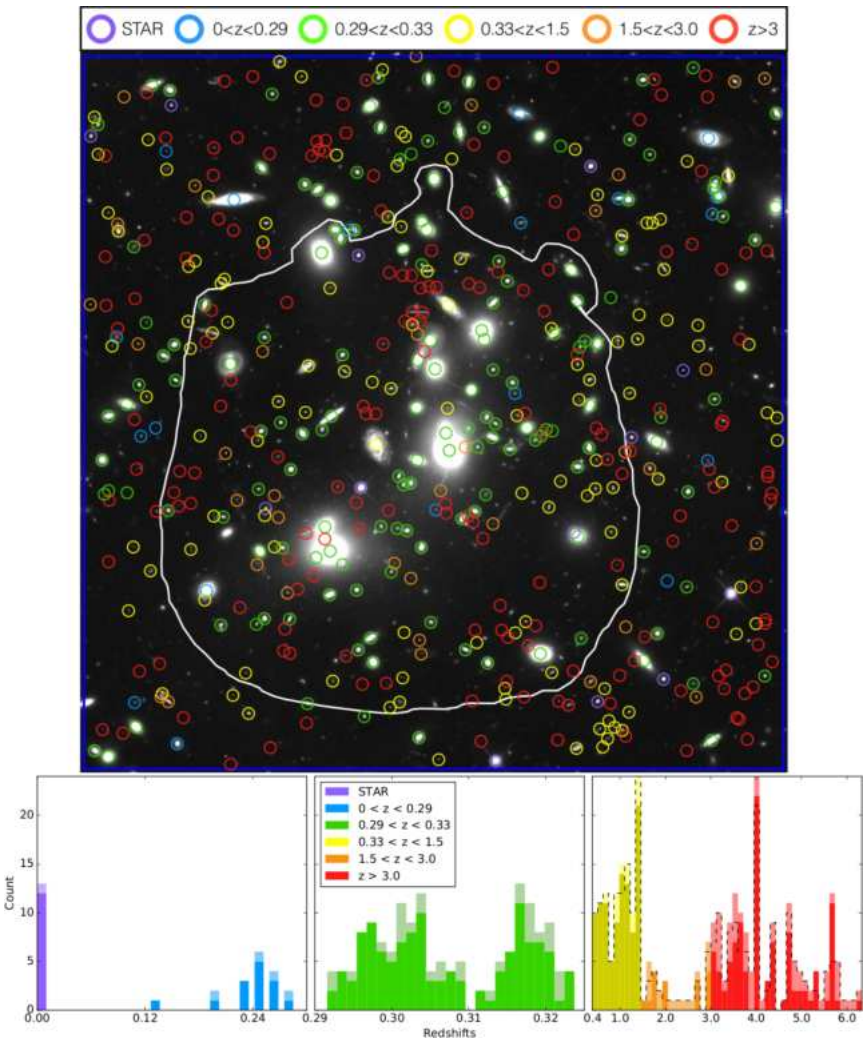

Figure 2.4: Top: The spatial distribution of sources with a secure redshift overlaid on an RGB HST image within the MUSE mosaic observation in the core of lensing cluster A2744. The lower panel shows the redshift distribution of the sources shown in the upper panel. Credit: Mahler et al. 2018.

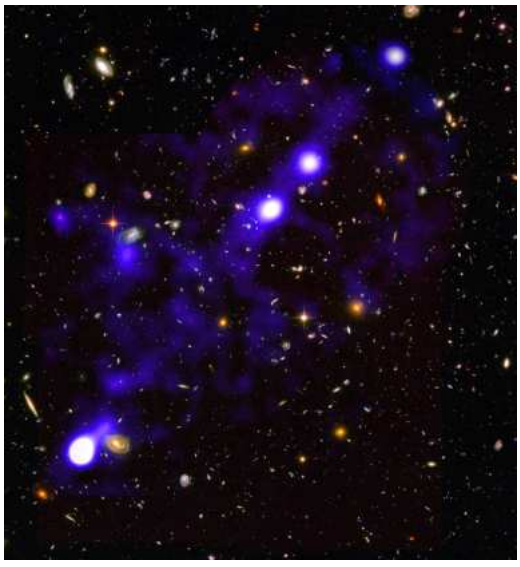

Figure 2.5: One of the recent images of hydrogen filaments (blue) observed by MUSE in the Hubble Ultra Deep Field. (R. Bacon, Mary, et al. 2021).

2.3 Lensing clusters observed with MUSE/VLT

2.3.1 General information of lensing clusters observed with MUSE/VLT

The lensing clusters used in this work were selected to be massive clusters extracted from both the MUSE Lensing Cluster GTO program and the literature, publically available from the ESO archives. All of them were known to be strong lensing clusters, having a high efficiency in terms of magnification power on the population of background sources. They were compiled from different sources. Massive X-ray luminous clusters were mainly selected from ROSAT Brightest Cluster Sample (Ebeling, Barrett, et al. 2007; Repp et al. 2016), the MAssice Cluster Survey (MACS, (Ebeling, Edge, and J. P. Henry 2001). Given the wavelength coverage of MUSE, we expect to observe the Lyα emission from background sources at redshift $2.9 < z < 6.7$.

The selected clusters have a redshift in the range of $0.2 < z_{cl} < 0.6$, some of them were taken from the Hubble Frontier Fields. Therefore, we expect to clearly identify the cluster members by using the absorption (and some emission) lines present in the MUSE spectra. This also helps include the most massive galaxies in the lensing models (see below). An additional criterion is that most of the lensing clusters have a wide Right Ascension (RA) range to adapt to the MUSE GTO observations and a low airmass at the Cerro Paranal Observatory with respect to a declination of range $-60 < Declination(DEC) < +10$ degrees. The general information of the clusters observed by MUSE and used for the thesis is presented in Table. 2.1. Taking advantage of HST observations, which are efficient in detecting bright continuum sources, the clusters in the project require at least an available high-resolution broad-band HST image, that is, it requires either F606W or F814W filter to make sure that it overlaps with the MUSE spectral range. Finally, there is a requirement for a mass model based on HST images to help us confirm the existence of at least one multiple-imaged system, that is used to estimate the total mass of the cluster core. From these, one can optimize the field of view in order to cover many of such resolved arcs together with the high magnification region.

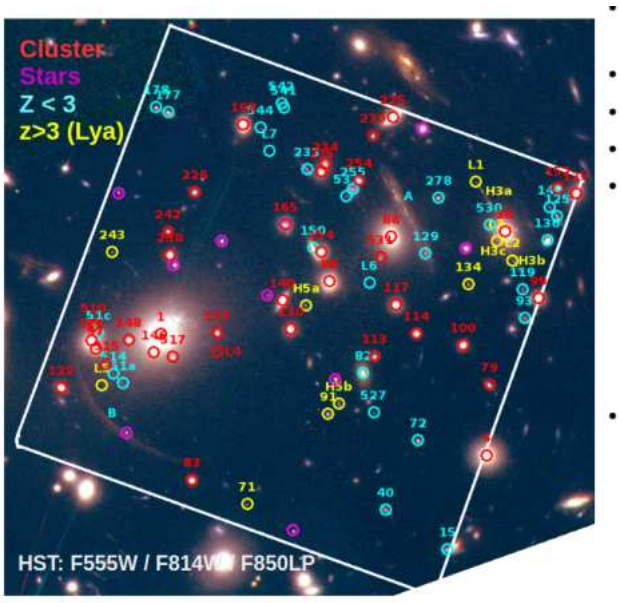

Figure 2.6: The spatial distribution of secure sources behind A2390 detected by MUSE is limited by the area inside the solid white line.

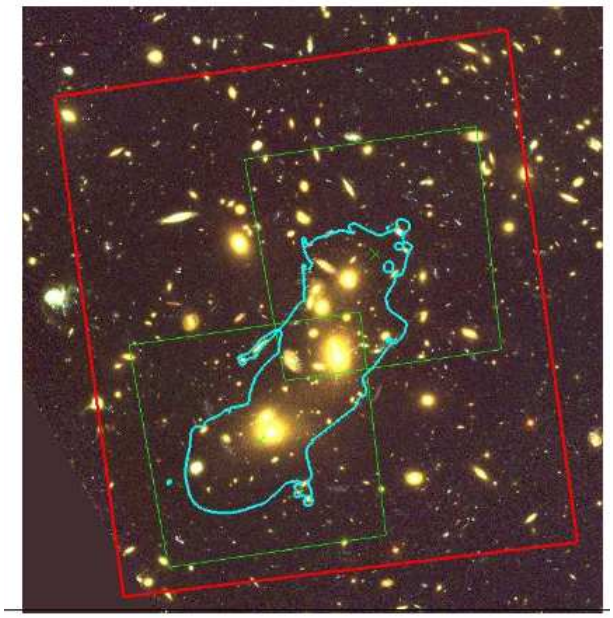

Figure 2.7: A simulation produced for MUSE proposal observation coverage of the first Hubble Frontier Field Abell A2744. The high light red area shows a deep HST coverage with ACS and WFC3. The cyan line delineates the critical line at redshift $z \sim 7$.

We briefly present below the sample of lensing clusters used in this work, with the appropriate references. A summary of the relevant information is also provided for convenience in Table. 2.1, 2.2.

- A2390 and A2667. The general information of these clusters can be found in (DLV 2019). An example of spatial image distribution behind A2390 is shown in Fig. 2.6.

- A2744 has been known to have a complex galaxy dynamics with a major merging that happens in the north-south direction (Kempner et al. 2004), hosts one of the most luminous known radio haloes within a distance of 1.8 Mpc and a large radio relic at a distance of 2 Mpc from its center (Giovannini et al. 1999; Govoni, Enßlin, et al. 2001; Govoni, Feretti, et al. 2001). It also has been known for its complex lensing properties through a combination of strong and weak lensing (Merten et al. 2011; M. Jauzac et al. 2016). This cluster was observed with MUSE under the GTO program (094.A-0115) (PI: Richard) with a 2×2 mosaic of MUSE pointings aiming to cover all the multiple image area, i.e. center at $\alpha = 00^h14^m20.952^s$ and $\delta = -30^o23^{'}53.88^{"}$. A simulation produced for the MUSE proposal to observe A2744 overlaid by the HST observation region is shown in Fig. 2.7. The quadrants observing times are 3.5, 4.0, 4.0, and 5 hours, and an extra observation time of 2 hours at the central cluster. Each pointing is divided into 30-minute individual exposures with a 90-degree rotation applied in between each exposure.

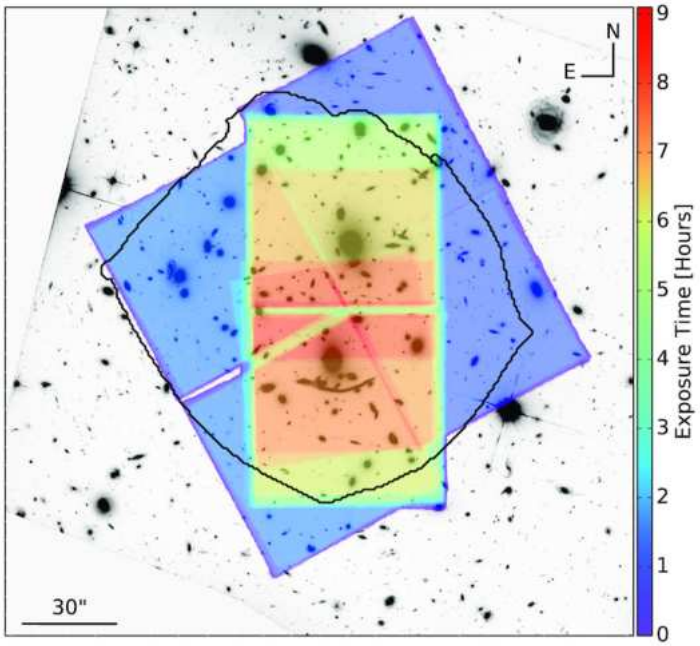

Figure 2.8: A MUSE exposure map of A370 mosaic observation. The solid black curve delineates the multiple-image zone (Lagattuta et al. 2019).

- A370 is a merging cluster at a redshift of $z \sim 0.375$ (Mellier et al. 1988). It is known to exhibit a highly elongated and efficient lens with an Einstein radius of 39" at redshift $z \sim 2$, and a mass of $M_{<250kpc} = 3.8 \times 10^{14}$ $M_\odot$ (Johan Richard, Smith, et al. 2010). This cluster is noted for the first confirmed giant gravitational arc at $z = 0.725$ (Hammer et al. 1987; Soucail et al. 1987; Patrício et al. 2018), including a very high boost zone ($\mu \sim 5-10$) twice as large as any other Frontier Fields (FF) cluster observation (Johan Richard, Mathilde Jauzac, et al. 2014). A preliminary catalog of background sources behind this cluster observed from the Grism Lens Amplified Survey from Space (GLASS) was reported in T. Treu et al. 2015. The observation was conducted with a large mosaic covering ~ 4 arcmin^2 centered on the cluster, covering almost multiple image areas (096A-0710, 094A-0115). Aiming to achieve relatively uniform line sensitivity in the presence of strong intracluster light caused the background to grow for the line searching up to a factor of 2 at the center. For this reason, we use a factor of 3 to 4 larger exposure time in the central portion of the mosaic. This was done with 2 hours on-source (one-fourth of the MUSE image), which is rotated by 28 degrees to cover the bulk of the HST WFC ~ 5 arcmin^2 footmark, 4 hours on-source spending for the two pointings centered at North-South high boost region, and 2 additional hours on-source focusing in the center. Finally, we have 18-hour observation for the A370 in mosaic mode. An exposure map is shown in Fig. 2.8. Both observations were taken in clear and photometric conditions with a DIMM seeing in a range of 0.37" and 1.09", a median airmass of 1.17 within a range of 1.09−1.42 (Lagattuta et al. 2019).

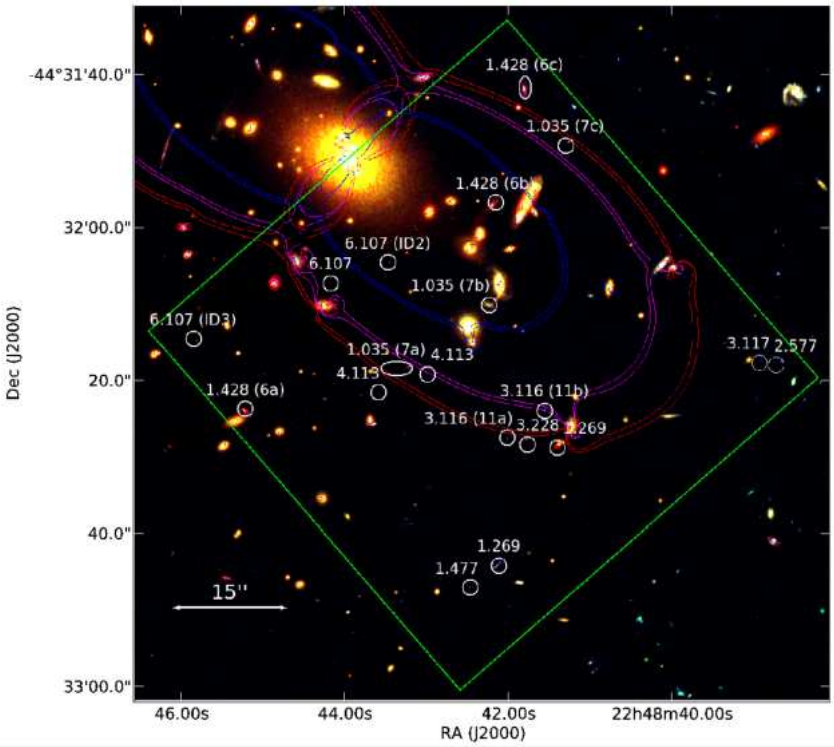

Figure 2.9: The red-green-blue HST image of the AS1063 is observed with MUSE. The green square delimits $1' \times 1'$ MUSE Field of View (FoV). The white circles and accompanying text show a redshift of the source observed by MUSE. The blue, magenta, and red contours refer to the high magnification region $\mu > 200$ at redshift $z = 1, 2$ and 4, respectively. Credit: Karman, W. et al. 2015.

- AS1063 is known as a very massive cluster at $z = 0.348$ (Karman, W. et al. 2015) containing a total mass of $(2.9 \pm 0.3) \times 10^{15}$ $M_\odot$ (Sartoris, B. et al. 2020), having a high X−ray luminosity $L_X \sim 8 \times 10^{45}$ erg s^{-1} (Gómez et al. 2012). MUSE observation (see Fig. 2.9) is centered with a position angle of 41 degrees covering the maximum magnification area following Cluster Lensing And Supernova Survey (CLASH) lensing models used for the FF Karman, W. et al. 2015. Depending on the observation condition, the data is collected two times within 1 hour for the first night at a seeing value of 1", and 3 hours for the second night having a seeing of 1.1". In order to remove cosmic rays and obtain a better noise map, a dither pattern was used with a positional offset shifted by 0.4−0.8" and a rotation by 90 degrees for every exposure was applied (Karman, W. et al. 2015).

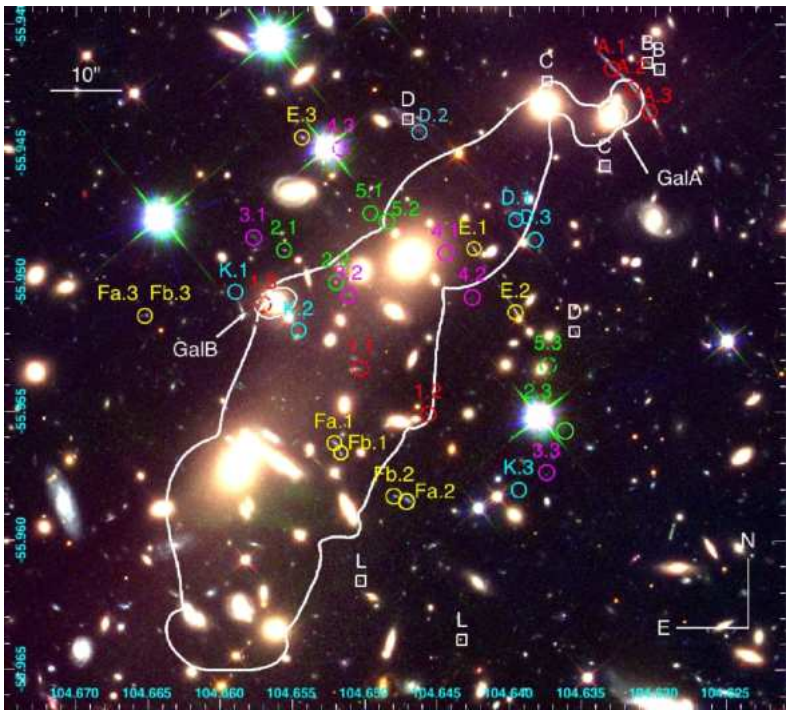

Figure 2.10: The HST observations using different filters of Bullet cluster. The color circles show the multiple images from (Mehlert et al. 2001; Gonzalez et al. 2010), (Bradač, Tommaso Treu, et al. 2009) in white squares, (Paraficz, D. et al. 2016) in red circles. The white solid line displays a critical curve at redshift $z \sim 3.24$. Credit: Paraficz, D. et al. 2016.

- BULLET is a massive cluster discovered by Tucker et al. 1998 containing two colliding galaxy clusters at $z = 0.296$ and has been known as one of the hottest galaxy clusters. The name of the cluster referred to a smaller subcluster moving away from the larger one. The majority of the baryons in the cluster is in the form of hot, diffuse X−ray emitting gas and account for a small fraction of the total lensing mass close to the center of the cluster. The mass ratio of the two components is 6:1 (Mastropietro et al. 2008) and displays a prominent bow shock preceding a cool bullet lying between the two. The first lensed model of this cluster was built by Mehlert et al. 2001 using 3 modeled Dark matter (DM) clumps as Single Isothermal Sphere (SIS) and Singular Isothermal Ellipsoid (SIE) based on 6 multiple imaged systems, one of them showing a spectroscopic redshift of $z = 3.24$. Bradač, Clowe, et al. 2006 improved the model by using 6 multiple imaged systems from Mehlert et al. 2001 combined with 4 new multiple imaged systems detected in the sub-cluster region. The new mass model helped to measure an enclosed mass at $r > 250$ kpc ($\sim 2.8 \pm 0.210^{14}$ $M_\odot$) around the main cluster and $2.3 \pm 0.2\ 10^{14}$ $M_\odot$ around the sub-cluster. Paraficz, D. et al. 2016 reconstructed the mass model by including the intra-cluster gas derived from X−ray observation, which is one with the best Bayess evidence. The new model showed a total rms value of 0.158" of imaged position difference between the predicted and observed positions and confirmed the spatial offset between X−ray mass and dark matter peaks. The fraction mass of the galaxy halo is assumed 2.5 ± 0.110^{14} $M_\odot$ within a 250 kpc radial aperture. With the MUSE observation, this cluster is observed with an Extended mode (WFM-NOAO-E) covering a bluer wavelength. Fig. 2.10 is a Bullet image observed by HST using different filters. Using different mass models helps us find multiple images of the background sources.

- MACS0257 is a special case with 25 background sources confirmed with spectroscopic redshifts, including 81 multiple image systems in total covering a field of view 1 MUSE arcmin^2. Such systems are too faint to be detected by HST but are readily revealed by MUSE observations. Fig. 2.11 displays a MUSE FoV overlaid by the HST observation. The dashed cyan line delineates the FoV of MUSE observation, the solid curve highlights the multiple image regions and the solid red line shows the critical curve at redshift $z = 4$.

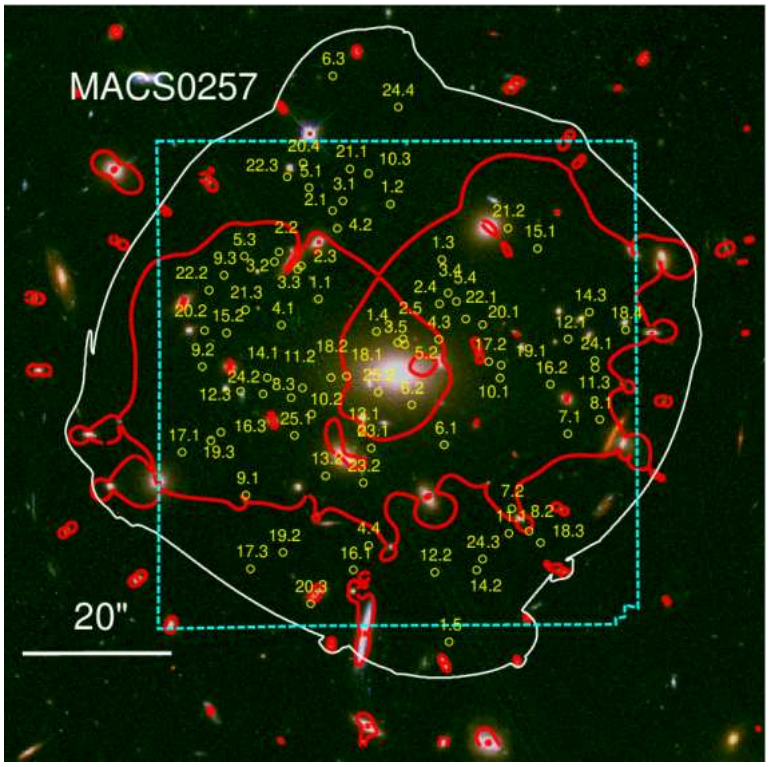

Figure 2.11: An overview of multiple image systems behind MACS0257. The dashed cyan line delineates the FoV of MUSE observation, the solid white line highlights the multiple image regions and the solid red line shows the critical curve at redshift $z = 4$. Credit: Johan Richard, Adélaide Claeyssens, et al. 2021.

- MACS0329 is a cluster found by the Massive Cluster Survey (MACS, (Ebeling, Edge, and J. P. Henry 2001; Ebeling, Edge, Mantz, et al. 2010) as an X−ray selected system. The MUSE observation was carried out with Observation Blocks (OB) consisting of ~ 1465s in both two exposures and only one pointing. The total exposure time of this cluster is 2.5 hours conducted with an angle rotation of 90 degrees with respect to the original position angle (Caminha, G. B., Rosati, P., et al. 2019). Although the data used in the present work are the same used by Caminha, G. B., Rosati, P., et al. 2019, the number of LAEs behind the lensing cluster is greater than in the previous study. This is due to the improvement of the lensing model, which helped to identify more sources (Johan Richard, Adélaide Claeyssens, et al. 2021). The locations of MUSE spectroscopic redshifts over HST F606W-F814W-F160W color composites are shown in Fig. 2.12 (bottom). Maughan et al. 2008 classified this cluster giving evidence for the presence of substructure in its X−ray surface brightness. A. Zitrin et al. 2012 studied HST/ACS/WFC3 CLASH data and found that the magnitude of the most magnified image is 24 ± 0.004 AB mag. They also discovered one of the highest redshift ($z = 6.18$) multiple imaged systems lensed into four images, with magnifications of $11.6^{+8.9}_{-4.1}$, $17.6^{+6.2}_{-3.9}$, $3.9^{+3.0}_{-1.7}$ and $3.7^{+1.3}_{-0.2}$. By analyzing the Spectral Energy Distribution using a population synthesis model, they found a demagnified stellar mass of $10^9 M_\odot$, a subsolar metallicity $Z/Z_\odot = 0.5$, low dust content, demagnified SFR of 3.2 $M_\odot$/year and a specific

SFR of 3.4 per Gyr. This suggests that it is a local dwarf galaxy.

- MACS0416 ($z = 0.397$) was discovered by MAssive Cluster Survey (MACS, (Ebeling, Edge, Mantz, et al. 2010)), has been known as a merging system with double peak X−ray surface brightness distribution (Mann et al. 2012). It was selected as one of five high magnification clusters in the Cluster Lensing And Supernova survey with Hubble (CLASH, (Postman et al. 2012)) because of its large Einstein radius. Aiming to get deep MUSE exposures of the FFs, the GTO program and ESO program are well joined. This allows the data collected from two programs to be merged. As a result, the data in the northern part of MACS0416 were added by the ESO program, while the other were collected by the GTO program. MUSE HFFs observations were conducted using 19 Observing Blocks (OBs). Sixteen of the 19 OBs were successful with an acquirement quality of A or B. Fourteen of the 16 OBs were observed with the assistance of the Ground Layer AO provided by the GALACSI module. An offset was required for each exposure, with a rotation of 90 degrees to improve the sky subtraction. All the observations were conducted under good weather conditions, with a seeing value ranging from 0.4" to 0.8". Under the GTO program, two-hour observation was split into 4 exposures (Caminha, G. B., Grillo, C., et al. 2017). Finally, these data were combined, with a total observing time on the sky of 17.1 hours within an image quality of 0".6. Caminha, G. B., Grillo, C., et al. 2017 improved the strong lensing model of MACS0416 and found 37 multiple imaged sources. Twenty-two of them are newly multiple sources found in the MUSE data set, and the rest of them were detected from previous spectroscopic measurements. They are low luminosity LAEs with redshifts ranging from 3.08 to 6.15. Johan Richard, Adélaide Claeyssens, et al. 2021 found 9 new multiple-imaged systems, raising the total number of multiple images in the MUSE cube to 22. Fig. 2.12 (upper panel) displays locations of MUSE spectroscopic redshifts over HST F606W-F814W-F160W color composites. With deeper data, more than 15 multiple systems with 33 multiple images have been found. Eleven of the 15 new systems were discovered with MUSE as faint LAEs. Recently, Vanzella, E. et al. 2021 showed a triple imaged system overlaid between two MUSE fields. They included this system, which is also listed as system 100 in (Johan Richard, Adélaide Claeyssens, et al. 2021), for completeness. Balestra et al. 2016 studied morphology and kinematic of the cluster out to 4 Mpc and showed a complex system composed of a main massive cluster with a mass of $M \sim 0.9\,10^{15}$ $M_{\odot}$ and $\sigma_{V,r200} \sim 1000$ km s^{-1} showing two main features: two central peaks separated by 1000 km s^{-1} with comparable galaxy content and velocity dispersion from the bimodal velocity histogram; and elongation of the main structures along the North East (NE)-South West (SW) direction with a sub-clump ~ 600 kpc SW of the center and a Bright Cluster Galaxy (BCG) in the middle of the center and SW clump. In addition, there is an appearance of low mass structure at $z \sim 0.390$ on the South of the cluster center.

- MACS0451: Stark et al. 2014 used data collected from spectrograph on the VLT UT1(088.A-0571, PI: Richard) to make a mass model of the cluster based on the model of T. Jones et al. 2013 and updated the multiple imaged catalog of the sources with a magnification range of 2.5 to 270, median magnification of 15.5. This cluster includes a very elongated arc and highly magnified sources ~ 49 at redshift 2.013 (T. A. Jones et al. 2010). The length of the arc is ~ 20" and is resolved up to a wavelength of 250μm. Using the Far Infrared (FIR) SED of the cluster to analyze two parts of the arc, Northern and Southern, they showed a peak at 250μm and a second at 100μm, suggesting a very high dust temperature. Further, an investigation of the infrared emission of the cluster showed an AGN component that is separate from the star-forming component.

- MACS0520: The general information of this cluster is presented in Table. 2.1 and the lens model is presented in Table. 2.2.

- MACS0940: The lensing model of the cluster can be found in (Johan Richard,

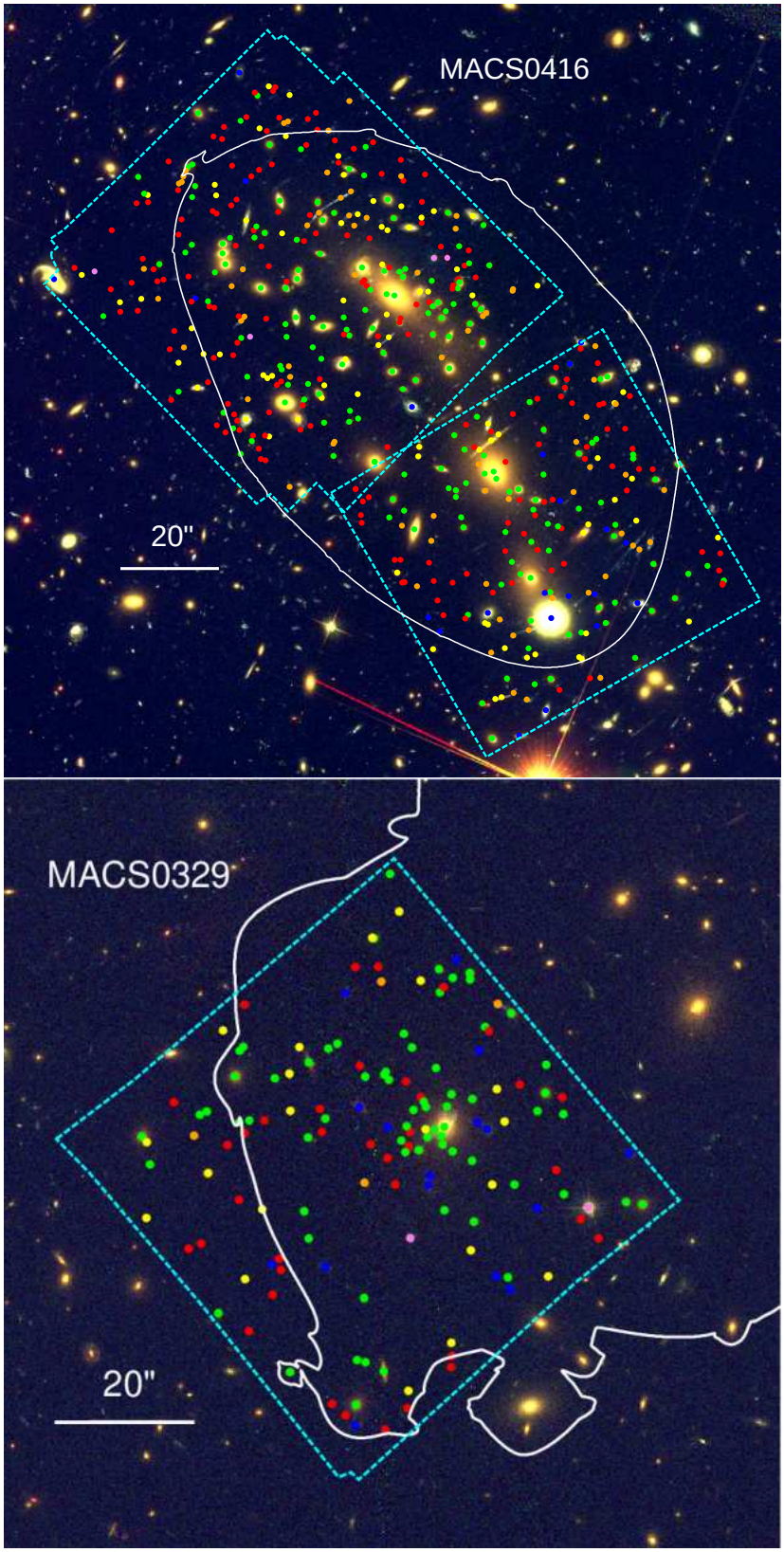

Figure 2.12: Source location of MUSE spectroscopic redshifts over HST F606W-F814W-F160W color composites for MACS0416 (top) and MACS0329 (bottom). The cyan dashed lines represent the MUSE observation regions, while the solid white line denotes the multiple imaged area. Credit: Johan Richard, Adélaide Claeyssens, et al. 2021.

Adélaide Claeyssens, et al. 2021). An overview of multiple imaged systems behind this cluster is shown in Fig. 2.13.

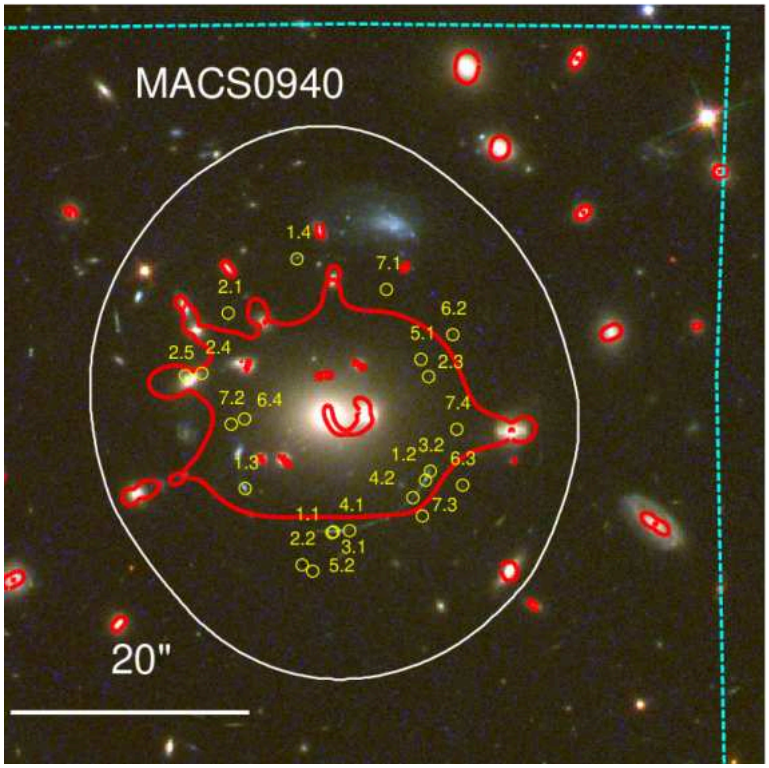

Figure 2.13: An overview of multiple image systems behind MACS0940. The dashed cyan line delineates the field of view of MUSE observation, the solid curve highlights the multiple image regions, and the solid red line shows the critical curve at redshift $z = 4$. Credit: Johan Richard, Adélaide Claeyssens, et al. 2021.

- MACS1206: It was first discovered in the ROSAT All Sky Survey (Böhringer et al. 2001) at redshift $z = 0.44$. As part of the CLASH project, the mass distribution inside the cluster has been investigated using different techniques, such as exploiting the multiple images created by lensing (A. Zitrin et al. 2012; Eichner et al. 2013), a combination of strong lensing and weak lensing to obtain information about mass distribution (Umetsu et al. 2012), etc. There is one multiple-image system with a giant arc with respect to its counter-image that was found at redshift $z = 1.036$ (Ebeling, C. J. Ma, et al. 2009). In this work, we are using data observed from GTO program 095.A-0181(A) and 097.A-0267(A) (PI: J. Richard) in April, May 2015 and April 2016, including 3 pointings, one centered on BCG with a rotation of 20 degrees and the others with an offset of 35 arcsec towards the East and West. The exposure time mode of this cluster is 26×1800 NOAO. An offset of 0.5" combined with a rotational angle of 90 degrees was applied in the different exposures to improve the removal of instrumental signatures and sky subtraction. There is a matching of redshift and multiple image systems between the catalog of (Caminha, G. B., Grillo, C., et al. 2017) and (Johan Richard, Adélaide Claeyssens, et al. 2021). The latter found eight new systems more (Johan Richard, Adélaide Claeyssens, et al. 2021). An overview of multiple imaged systems behind this cluster is shown in Fig. 2.14. Credit: Johan Richard, Adélaide Claeyssens, et al. 2021.

- MACS2214 was found from Chandra ACIS-I observation as one of the X−ray sources (Ebeling, C. J. Ma, et al. 2009). It consists of several prominent large blue arcs (Adi Zitrin et al. 2010), four of which are considered to be spiral systems. This cluster is quite close to the ecliptic plane (~ 2 degrees) allowing us to observe the passing of an asteroid

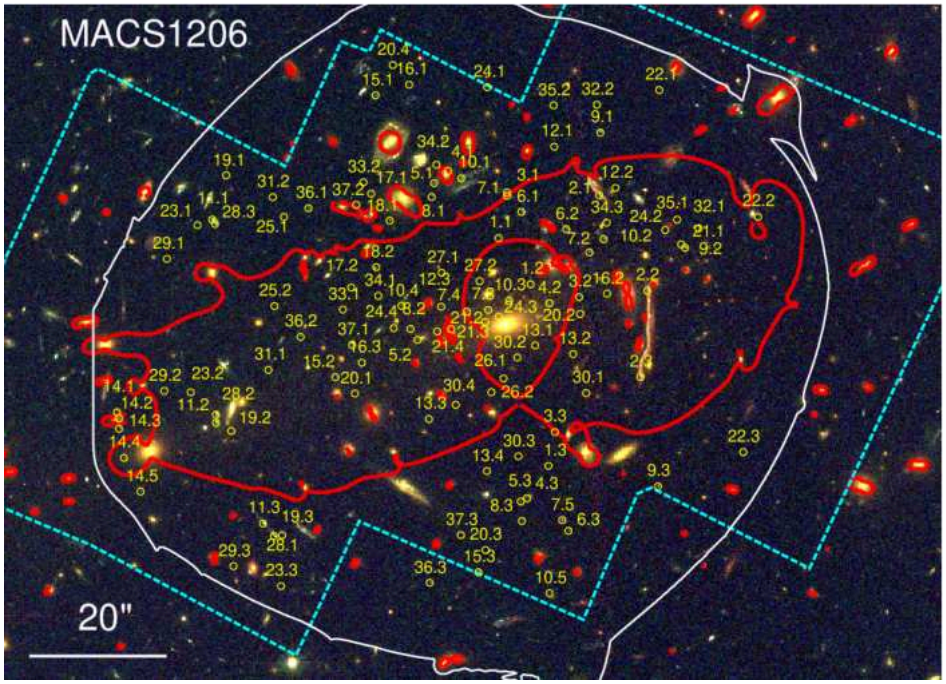

Figure 2.14: An overview of multiple image systems behind MACS1206. The dashed cyan line delineates the field of view of MUSE observations, the solid white curve highlights the multiple image regions, and the solid red line shows the critical curve at redshift $z = 4$. Credit: Johan Richard, Adélaide Claeyssens, et al. 2021.

(see Fig. 2.15 (right)). MUSE observed this lensing cluster from 2017 to 2019. During the first exposure, the passing of an object was observed in the field. This was seen again in the last poses in 2019 during the observations of the lensing cluster Claeyssens 2021.

- RXJ1347 is one of the most massive clusters with $M_{200crit} = 3.54 \pm 0.51 \times 10^{15}$ $M_\odot$ at redshift $z = 0.451$ (Caminha, G. B., Rosati, P., et al. 2019), including two very bright central galaxies. This cluster is likely to undergo an initial phase of a significant merging event with a perturbation of intra-cluster medium (Ueda et al. 2018). Based on the previous results, Caminha, G. B., Rosati, P., et al. 2019 improved the mass model and considered two smooth mass components to reproduce the positions of all the multiple images. The results showed that the addition of an external shear improved significantly the lens model with a difference of 0.36". On the other hand, R. E. Johnson et al. 2012 used multiple wavelengths in X-ray and millimeter to show evidence of merging processes in most X-ray cluster galaxies. The result showed that the core gas was undergoing turbulance of gas, which points to the primary and secondary clusters having had at least two prior strong gravitational interactions. This supports the evidence for the second cluster to have been passed by the primary cluster. An overview of multiple imaged systems observed behind this cluster is shown in Fig. 2.16. Credit: Johan Richard, Adélaide Claeyssens, et al. 2021.

- SMACS2031 ($\alpha = 20:31:47.843$, $\delta = -40:36:54.76$, $z = 0.331$) was observed with the HST as part of snapshot programs 12884 and 12166 (PI: Ebeling). This cluster has been observed as a part of the MUSE commission (60.A-9100B) with a total observing time of 10.4 hours in the nominal mode (WFM-NOAO-N), focusing on the SE cluster to cover the predicted locus of the multiple images with a small random dithering pattern of a 0.6" box. A rotational angle of 90 degrees has been applied between each exposure of 1200 sec (J. Richard et al. 2015).

Vera Patrício et al. 2016 used the MUSE data to study a young star-forming galaxy with an extended Lyman alpha halo. Using the multiple diagnostics, they found that the

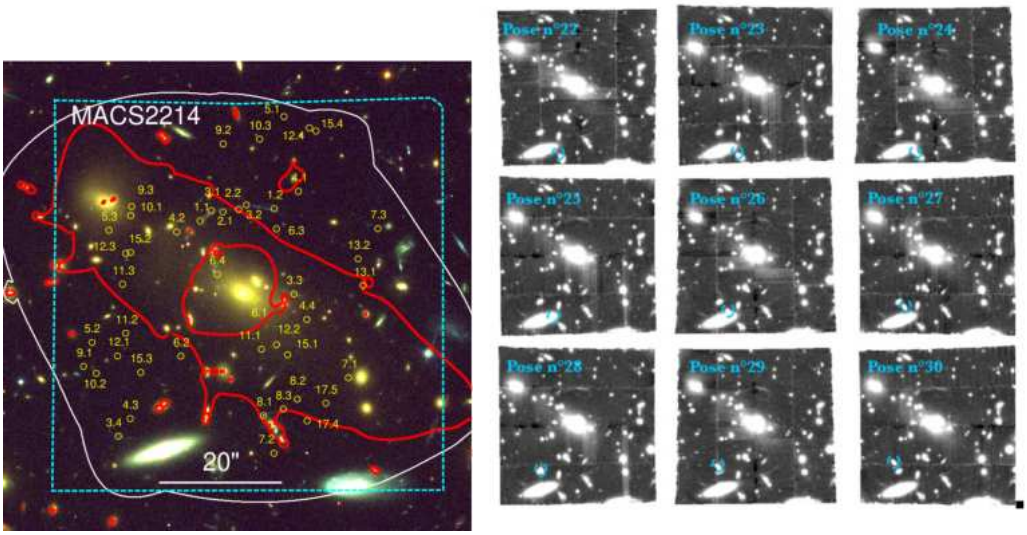

Figure 2.15: Left: MACS2214 observed by VLT/MUSE. The cyan dashed line shows the MUSE field of view, the white dashed line denotes the multiple images region, and the red solid line is the critical curve at redshift $z = 4$. Right: 9 individual exposures of the MACS2214 show the appearance of a satellite crossing the field. Credit: Claeyssens 2021.

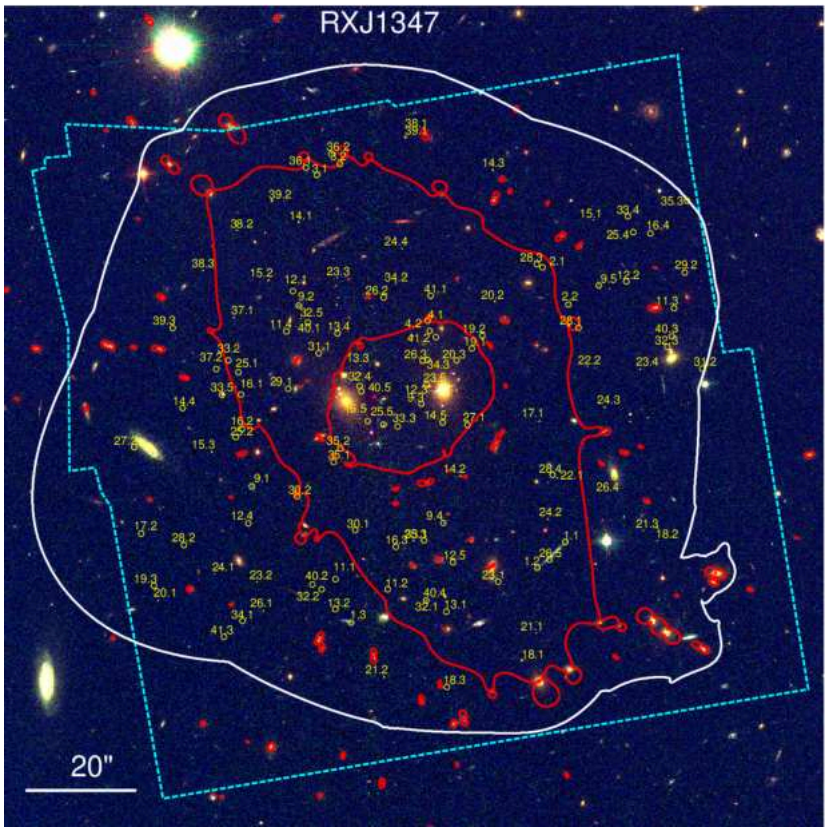

Figure 2.16: An overview of multiple image systems behind RXJ1347. The dashed cyan line delineates the field of view of MUSE observation, the solid curve highlights the multiple image regions, and the solid red line shows the critical curve at redshift $z = 4$. Credit: Johan Richard, Adélaide Claeyssens, et al. 2021.

galaxy has a temperature of T_e = 156000 K,an electron density of n_e = 300 cm^{-3}, a covering fraction of 0.4, a Lyman alpha emission extending over 10 kpc across the galaxy, and a very uniform spectral profile. The Lyman alpha extension is four times larger than the continuum emission. This makes the galaxy comparable to low-mass LAE at low redshift and more compact than the LBG.

Claeyssens et al. 2019 improved the mass model of J. Richard et al. 2015 and identified the Lyman alpha line properties in a halo out to 10 kpc. They found a mild variation of ±20 km s^{-1} in peak shift and ±20 km s^{-1} in Full Width at Half Maximum (FWHM) across the halo. There are few outer regions with low SB, a small peak shift of ~ 200 km s^{-1} comparable to the smallest value on the map. The appearance of such regions in the cluster with one of them having a distinct SB peak as in the results of Vera Patrício et al. 2016, suggests the existence of a satellite galaxy. An overview of multiple imaged systems observed behind this cluster is shown in Fig. 2.17. Credit: Johan Richard, Adélaide Claeyssens, et al. 2021.

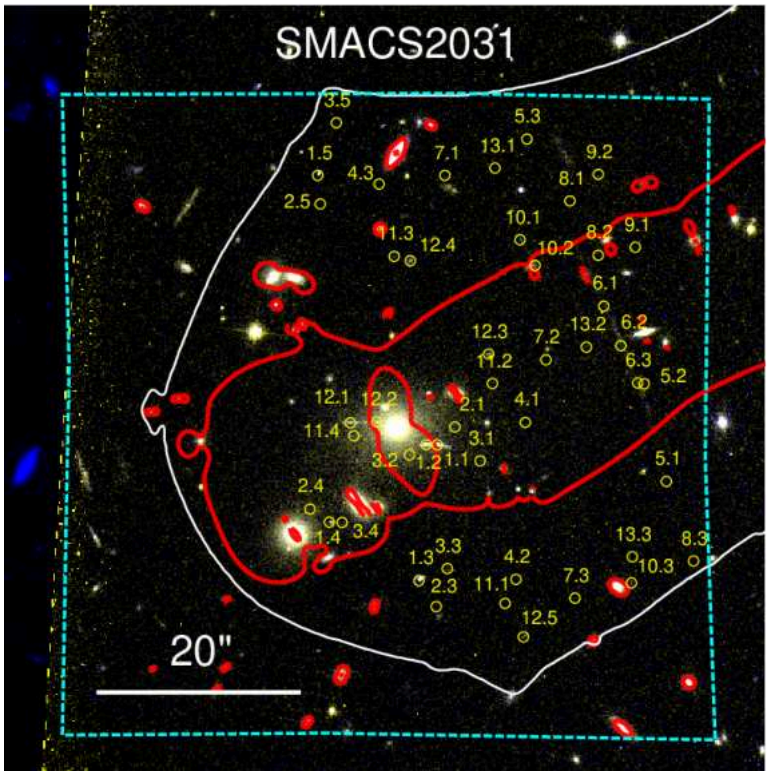

Figure 2.17: An overview of multiple image systems behind SMACS2031. The dashed cyan line delineates the field of view of MUSE observation, the solid curve highlights the multiple image regions, and the solid red line shows the critical curve at redshift $z = 4$. Credit: Johan Richard, Adélaide Claeyssens, et al. 2021.

- SMACS2131 is a galaxy cluster with a redshift of z=0.44. The general information of this cluster is summarized in Table. 2.1. The lens model of this cluster is taken from Johan Richard, Adélaide Claeyssens, et al. 2021. An overview of multiple imaged systems observed behind this cluster is shown in Fig. 2.18. Credit: Johan Richard, Adélaide Claeyssens, et al. 2021.

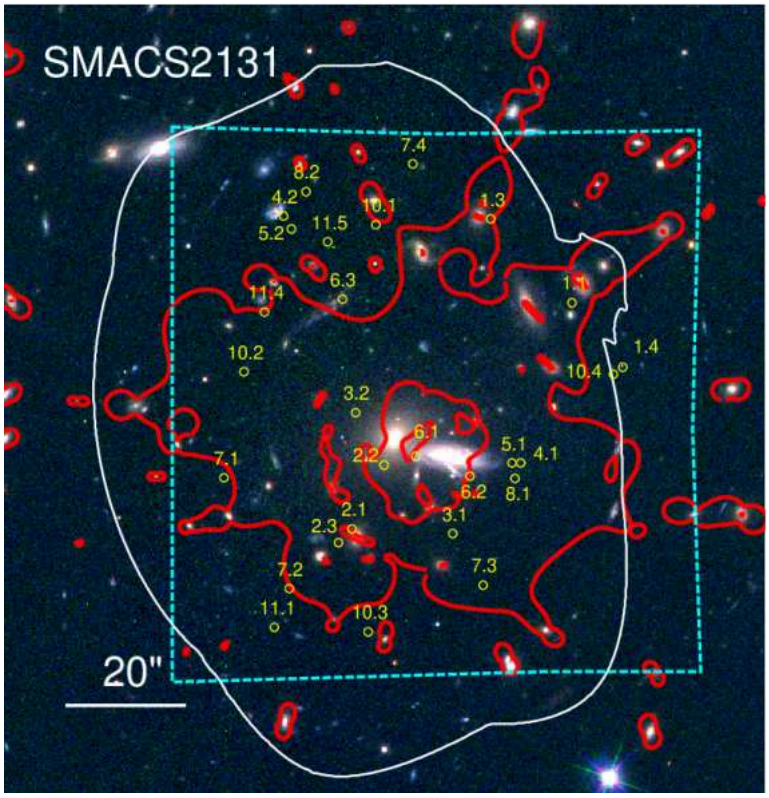

Figure 2.18: An overview of multiple image systems behind SMACS2131. The dashed cyan line delineates the field of view of MUSE observation, the solid curve highlights the multiple image regions, and the solid red line shows the critical curve at redshift $z = 4$. Credit: Johan Richard, Adélaide Claeyssens, et al. 2021.

Table 2.1: Information of 17 lensing clusters (18 fields) observed by MUSE/VLT.

Cluster	RA	DEC	z	Programme ID	Notes	Seeing value	MUSE depth (hrs)	N. LAEs
A2390	21:53:36.823	+17:41:43.59	0.228	094.A-0115		0.75	2	7
A2667	23:52:28.400	-26:05:08.00	0.233	094.A-0115		0.62	2	14
A2744	00:14:20.702	-30:24:00.63	0.308	094.A-0115, 095.A-0181	MACS, FF	0.61	3.5-7	128
A370	02:29:53.122	-01:34:56.14	0.375	094.A-0115, 096.A-0710	FF	0.66	1.5-8.5	41
AS1063	22:48:43.975	-44:31:51.16	0.348	60.A-9345, 095.A-0653	FF	1.02	3.9	20
BULLET	06:58:38.126	-55:57:25.87	0.296	094.A-0115		0.56	2	11
MACS0257	02:57:41.070	-22:09:17.70	0.322	099.A-0292, 0100.A-0249	MACS	0.52	8	24
MACS0329	03:29:41.568	-02:11:46.41	0.450	096.A-0105	MACS, CLASH	0.69	2.5	16
MACS0416N	04:16:09.144	-24:04:02.95	0.397	094.A-0115, 0100.A-0763	MACS, CLASH	0.53	17	45
MACS0416S	04:16:09.144	-24:04:02.95	0.397	094.A-0525	MACS, CLASH	0.65	11-15	32
MACS0451	04:51:54.647	+00:06:18.21	0.430	098.A-0502, 0104.A-0489	MACS	0.58	8	21
MACS0520	05:20:42.046	-13:28:47.58	0.336	098.A-0502, 0104.A-0489	MACS	0.57	8	19
MACS0940	09:40:53.698	+07:44:25.31	0.335	098.A-0502, 0101.A-0506	MACS	0.571	8	48
MACS1206	12:06:12.149	-08:48:03.37	0.438	095.A-0181, 097.A-0269	MACS, CLASH	0.521	4-9	49
MACS2214	22:14:57.292	-14:00:12.91	0.502	099.A-0292, 0101.A-0506	MACS	0.55	7	17
RXJ1347	13:47:30.617	-11:45:09.51	0.451	095.A-0525, 097.A-0909	MACS, CLASH	0.551	2-3	72
SMACS2031	20:31:53.256	-40:37:30.79	0.331	60.A-9100	MACS	0.79	10	20
SMACS2131	21:31:04.831	-40:19:20.92	0.442	0101.A-0506, 0102.A-0135	MACS	0.59	7	16
			Total:				**107-128**	**600**

2.3.2 Lens models

The signal from background galaxies in the field covered by strong lensing galaxy clusters will be magnified, with a global effect depending on the precise mass distribution within the cluster. The reader can find a detailed description of this phenomenon in Schneider et al. 1992. As a consequence of this, to measure any parameter about the intrinsic properties of the sources in their respective source planes, we have to model the mass distribution of the lensing clusters. However, the distribution in the galaxy clusters is generally complex due to the presence of dark matter halos that we can not observe directly and which account for 80% of the mass budget. To tackle this problem, one has to introduce several assumptions. One of the most popular ones, used in this work, is to assume that the total mass can be separated into a series of components without any interactions between them. In this parametric approach, the mass components can be described by analytical models, assuming a projected "flat" distribution. This is a reasonable approach given the distances involved between the observer, the lens, and the background sources. For this need, we use the well-known tool LENSTOOL as described below see Kneib et al. 2011, for more details.

In the following section, I will introduce a general picture of the mass model technique. The details of the method referrto the recent work presented in Mahler et al. 2018; Lagattuta et al. 2019, etc., with an original review performed in Schneider et al. 1992; Kneib et al. 2011.

LENSTOOL proposes several different potential profiles to be used for the fit, but the most commonly used is the PIEMD (for pseudo isothermal elliptical mass distribution) see e.g. Kassiola et al. 1993. For each potential parameter, the user can freely define a prior parameter, which can be a uniform or Gaussian distribution. Only the bright galaxies have the privilege to be optimized individually as cluster scale mass potentials, whereas the other galaxies have to be linked together by a scale relation parameter that is the only parameter being optimized. Model parameters are constrained through an interactive process, based on as many multiple images as possible, identified by their spectroscopic or photometric redshifts, sometimes with the help of high-resolution imaging (HST images). Note that the MUSE spectroscopy helps to improve the pre-existing models by the identification of new multiple images. The more images are provided, the more precise is the result of the model. For the multiple imaged systems, the images will be grouped together as a constraint factor in the same detailed observation. This step is the most important in the modeling process because a poor identification or incorrectly associated redshift can result in a distortion of the mass model. As a consequence, the excellent combination of MUSE and HST, mixing a large number of spectroscopic redshifts with highly spatially resolved images are helped us to improve lens mass modeling. The enhancements presented in the reconstruction mass distribution have been observed by J. Richard et al. 2015; Bina, D. et al. 2016; Mahler et al. 2018; Lagattuta et al. 2019, among others.

The procedure for the mass model is performed in the following steps:

+ Introduce the multiple images and their redshift as a constraint factor by users.

+ Assume a mass distribution using the visible baryonic matter and an expectation about the DM distribution.

+ Project the multiple images of the same system into the source plane using the current mass model. The quality of the model is defined by the coincidence of the source position reconstructed from the given images.

+ Lens the sources, which are found in the previous steps, back to the image plane. The quality of the model is once again estimated as the difference between the expected and observed positions of the images.

+ The procedure is repeated back and forth between source and image plane, source

by source, aiming to improve the model.

However, LENSTOOL does not take into account the morphology and flux ratio of the multiple images, only the multiple imaged positions have been used. This can be improved with two following approaches:

+ Direct reconstruction: CLEANLENS mode of LENSTOOL can be used to return values of pixels in the source plane from the image plane by inverting the lens equation. This can be done by isolating the image that we want to reconstruct. By inverting the lens equation pixel by pixel, it is possible to reconstruct the morphology of the background source.

+ Parametric reconstruction: Users can use the CLEANSET 2 function of LENSTOOL to model the background source by using the parametric light distribution. This means that information about source size, source ellipticity, and magnitude are parameters to be optimized to match with observed images. The quality of the model is measured by a chi-squared, which is defined as follows:

$$\chi^2_{tot} = \sum_{i,j} \left(\frac{(Flux_{predict}[i,j] - Flux_{observe}[i,j])}{\sigma_{ij}} \right)^2 \tag{2.1}$$

where $Flux_{predict}$, $Flux_{observe}$ are the predicted and observed flux for pixel [i, j], σ_{ij} is an estimation of flux error in the pixel [i, j]. The details of the method can be found in the thesis work of G. Mahler.

The general information on lens models used for the thesis is presented in Table. 2.2. For each cluster, we provide the position of the cluster-scale DM halos, corresponding to the largest mass distribution, together with the Mass-to-Light scaling for the cluster galaxies, as well as the reference articles where details on the lensing models can be found.

Table 2.2: Best fit parameters of mass distribution in each cluster

Cluster	ΔRA["]	ΔDEC ["]	ϵ	θ[deg]	$r_{core}[kpc]$	r_{cut}[kpc]	σ[km s^{-1}]	Reference
A2390								
DM1	$31.6^{+1.8}_{-1.3}$	$15.4^{+0.4}_{-1.0}$	$0.66^{+0.03}_{-0.02}$	$214.7^{+0.5}_{-0.3}$	$261.5^{+8.5}_{-5.2}$	[2000.0]	$1381.9^{+23.0}_{-17.6}$	Pello et al. 1991
DM2	[−0.9]	[−1.3]	$0.35^{+0.05}_{-0.03}$	$33.3^{+1.2}_{-1.6}$	$25.0^{+1.8}_{-1.1}$	$750.4^{+100.2}_{-65.5}$	$585.1^{+20.0}_{-9.7}$	Richard et al. 2010
BCG1	[46.8]	[12.8]	$0.11^{+0.10}_{-0.01}$	$114.8^{+26.8}_{-31.5}$	[0.05]	$23.1^{+3.0}_{-1.6}$	$151.9^{+5.9}_{-7.5}$	Pello et al (in prep)
$L*$ Gal					[0.15]	[45.0]	$185.7^{+5.5}_{-3.3}$	
A2667								
DM1	$0.2^{+0.5}_{-0.4}$	$1.3^{+0.5}_{-0.4}$	$0.46^{+0.02}_{-0.02}$	$-44.4^{+0.2}_{-0.3}$	$79.33^{+1.1}_{-1.1}$	[1298.7]	$1095.0^{+5.0}_{-3.7}$	Covone et al. 2006
$L*$ Gal					[0.15]	[45.0]	$91.3^{+4.5}_{-4.5}$	Richard et al. 2010
A2744								
DM1	$-2.1^{+0.3}_{-0.3}$	$1.4^{+0.0}_{-0.4}$	$0.83^{+0.01}_{-0.02}$	$90.5^{+1.0}_{-1.1}$	$85.4^{+5.4}_{-4.5}$	[1000.0]	$607.1^{+7.6}_{-0.2}$	Mahler et al. 2018
DM2	$-17.1^{+0.2}_{-0.3}$	$-15.7^{+0.4}_{-0.3}$	$0.51^{+0.02}_{-0.02}$	$45.2^{+1.3}_{-0.8}$	$48.3^{+5.1}_{2.2}$	[1000.0]	$742.8^{+20.1}_{-14.2}$	R21
BCG1	[0.0]	[0.0]	[0.21]	[−76.0]	[0.3]	[28.5]	$355.2^{+11.3}_{-10.2}$	
BCG2	[−17.9]	[−20.0]	[0.38]	[14.8]	[0.3]	[29.5]	$321.7^{+15.3}_{-7.3}$	
NGal	[−3.6]	[24.7]	[0.72]	[−33.0]	[0.1]	[13.2]	$175.6^{+8.7}_{-13.8}$	
SGal	[−12.7]	[−0.8]	[0.30]	[−46.6]	[0.1]	$6.8^{+93.3}_{-3.2}$	$10.6^{+43.2}_{-3.6}$	
$L*$ Gal					[0.15]	$13.7^{+1.0}_{0.6}$	$155.5^{+4.2}_{-5.9}$	
A370								
DM1	$2.21^{+0.12}_{-0.10}$	$1.33^{+0.05}_{-0.06}$	$0.40^{+0.03}_{-0.03}$	$-69.6^{+1.5}_{-1.3}$	$14.7^{+1.0}_{-1.5}$	[800.0]	394^{+15}_{-9}	Lagattuta et al. 2019
DM2	$2.01^{+0.10}_{-0.23}$	$11.35^{+0.31}_{-0.38}$	$0.69^{+0.02}_{-0.01}$	$-122.3^{+0.4}_{-0.6}$	$137.4^{+0.2}_{-1.3}$	[800.0]	1039^{+6}_{-14}	R21
BCG1	[−0.01]	[0.02]	[0.30]	[−81.9]	[0.1]	$57.6^{+4.1}_{-5.1}$	224^{+9}_{-6}	
BCG2	[5.90]	[37.24]	[0.20]	[−63.9]	[0.1]	$77.6^{+6.0}_{-6.8}$	388^{+6}_{-9}	
$L*$ Gal					[0.15]	$10.8^{+0.6}_{-1.2}$	152^{+2}_{-1}	
AS1063								
DM1	[0.]	[0.]	0.61	-37.5	130	[1000]	1352	Beauchesne et al. (2023)
DM2	0.0	0.03	0.27	[-35]	0.51	169	328	
L* Gal					[0.15]	[45]	99	
BULLET								
DM1	$4.8^{+0.2}_{-0.1}$	$1.2^{+0.5}_{-0.5}$	$0.68^{+0.03}_{-0.03}$	$79.5^{+0.2}_{-0.7}$	138^{+8}_{-9}	[1000]	787^{+19}_{-25}	R21
DM2	$29.9^{+0.0}_{-0.2}$	$26.3^{+0.4}_{-0.5}$	$0.64^{+0.02}_{-0.02}$	$55.8^{+0.6}_{-0.9}$	168^{+4}_{-4}	[1000]	1004^{+28}_{-21}	
GAL1	[0.0]	[0.0]	[0.26]	[43.5]	[0]	[150]	268^{+9}_{-13}	
GAL2	[24.0]	[29.1]	[0.20]	[37.4]	[0]	[112]	118^{+12}_{-10}	
$L*$ Gal					[0.15]	25^{+3}_{-2}	165^{+2}_{-3}	
MACS0257								
DM1	$-2.1^{+0.3}_{-0.2}$	$1.8^{+0.3}_{-0.2}$	$0.59^{+0.02}_{-0.02}$	$200.9^{+1.1}_{-1.2}$	62^{+2}_{-2}	1014^{+145}_{-79}	877^{+17}_{-16}	R21
DM2	$8.5^{+5.0}_{-2.4}$	$-8.4^{+0.8}_{-2.6}$	$0.87^{+0.03}_{-0.04}$	$150.1^{+2.1}_{-0.8}$	189^{+6}_{-12}	1093^{+111}_{-174}	733^{+15}_{-22}	
GAL1	[−14.1]	[15.1]	$0.39^{+0.13}_{-0.14}$	$6.8^{+35.7}_{-34.5}$	[0]	88^{+5}_{-10}	184^{+6}_{-5}	
GAL2	[−10.6]	[17.6]	[0.50]	$30.6^{+8.2}_{-12.5}$	[0]	[40]	171^{+22}_{-16}	
$L*$ Gal					[0.15]	51^{+4}_{-3}	154^{+3}_{-2}	
MACS0329								
DM1	$0.4^{+0.1}_{-0.2}$	$-0.4^{+0.2}_{-0.1}$	$0.16^{+0.02}_{-0.01}$	$64.7^{+4.1}_{-2.1}$	55^{+3}_{-4}	[1000]	959^{+14}_{-17}	R21
DM2	$43.2^{+1.5}_{-0.7}$	$17.8^{+1.2}_{-1.5}$	[0.30]	$73.1^{+5.0}_{-4.4}$	7^{+10}_{-25}	[1000]	552^{+30}_{-40}	

Continued on next page

Table 2.2 continued from previous page

Cluster	ΔRA["]	ΔDEC ["]	ϵ	θ[deg]	$r_{core}[kpc]$	r_{cut}[kpc]	σ[km s^{-1}]	Reference
GAL1	[0.0]	[0.0]	[0.19]	[−73.6]	[0]	[98]	281^{+15}_{-30}	
GAL2	[−12.7]	[−39.9]	[0.14]	[56.9]	[0]	[41]	218^{+4}_{-4}	
$L*$ Gal					[0.15]	[45]	159^{+4}_{-4}	
MACS0416								
DM1	$-2.9^{+0.3}_{-0.3}$	$1.4^{+0.3}_{-0.2}$	$0.78^{+0.01}_{-0.01}$	$142.1^{+0.4}_{-0.4}$	59^{+2}_{-2}	[1000]	731^{+10}_{-11}	R21
DM2	$22.6^{+0.3}_{-0.2}$	$-42.4^{+0.4}_{-0.6}$	$0.69^{+0.01}_{-0.01}$	$127.1^{+0.2}_{-0.3}$	92^{+2}_{-3}	[1000]	940^{+12}_{-11}	
GAL1	[31.8]	[−65.5]	[0.04]	[−40.4]	[0]	[62]	137^{+10}_{-11}	
GAL2	$-37.2^{+0.6}_{-0.8}$	$7.8^{+1.3}_{-1.1}$	$0.82^{+0.03}_{-0.03}$	$118.5^{+3.9}_{-3.8}$	[25]	[200]	252^{+10}_{-7}	
$L*$ Gal					[0.15]	36^{+3}_{-2}	137^{+2}_{-2}	
MACS0451								
DM1	4.8	1.0	0.8	-8.1	88	[1000]	763	Basto et al. (in prep)
DM2	4.0	7.3	0.78	27.8	103	[1000]	933	
GAL1	[-57]	[-7.7]	[0.22]	-12.74	[50]	[1000]	253	
L* Gal					[0.15]	[10]	99.5	
MACS0520								
DM1	2.2	1.0	0.38	7.0	78	[1000]	1186	Basto et al. (in prep)
DM2	[-0.]	[0.]	0.19	[-3.1]	0.1	6	597	
L* Gal					0.15	66.	329	
MACS0940								
DM1	$0.6^{+0.8}_{-0.7}$	$0.6^{+1.4}_{-0.2}$	$0.46^{+0.19}_{-0.04}$	$23.5^{+2.0}_{-1.2}$	31^{+79}_{-8}	1386^{+565}_{-70}	496^{+223}_{-42}	R21
GAL1	[−0.1]	[0.1]	$0.37^{+0.09}_{-0.06}$	[−7.7]	[0]	[52]	436^{+15}_{-30}	
GAL2	[−11.8]	[3.1]	$0.66^{+0.07}_{-0.29}$	$5.9^{+19.9}_{-20.9}$	[0]	[17]	195^{+17}_{-14}	
$L*$ Gal					[0.15]	62^{+62}_{-94}	162^{+28}_{-7}	
MACS1206								
DM1	$-0.1^{+0.0}_{-0.0}$	$0.7^{+0.0}_{-0.0}$	$0.63^{+0.01}_{-0.01}$	$19.9^{+0.2}_{-0.1}$	44^{+0}_{-1}	[1000]	888^{+7}_{-6}	R21
DM2	$9.5^{+0.5}_{-0.2}$	$5.7^{+0.4}_{-0.3}$	$0.70^{+0.02}_{-0.03}$	$114.7^{+0.7}_{-0.5}$	94^{+3}_{-3}	[1000]	575^{+6}_{-9}	
GAL1	[−0.1]	[0.0]	[0.71]	[14.4]	1^{+0}_{-1}	20^{+1}_{-1}	355^{+11}_{-6}	
GAL2	[35.8]	[16.1]	[0.23]	$133.8^{+69.7}_{-47.6}$	[0]	4^{+1}_{-1}	275^{+18}_{-11}	
$L*$ Gal					34^{+5}_{-1}	198^{+5}_{-6}		
MACS2214								
DM1	$-1.2^{+0.1}_{-0.2}$	$0.7^{+0.1}_{-0.1}$	$0.55^{+0.01}_{-0.01}$	$147.5^{+0.7}_{-0.8}$	38^{+1}_{-1}	[1000]	903^{+15}_{-18}	R21
DM2	$-20.8^{+0.2}_{-0.2}$	$17.2^{+0.3}_{-0.2}$	$0.70^{+0.06}_{-0.05}$	$112.0^{+3.2}_{-3.5}$	20^{+8}_{-5}	[1000]	299^{+11}_{-34}	
GAL1	[0.0]	[0.0]	[0.20]	$151.1^{+34.0}_{-45.5}$	4^{+14}_{-3}	9^{+16}_{-12}	79^{+61}_{-28}	
GAL2	[8.2]	[18.8]	$0.48^{+0.07}_{-0.04}$	[0.0]	[0]	81^{+2}_{-3}	169^{+5}_{-9}	
$L*$ Gal					[0.15]	46^{+3}_{-0}	111^{+2}_{-3}	
RXJ1347								
DM1	$0.4^{+0.1}_{-0.1}$	$5.1^{+0.4}_{-0.2}$	$0.76^{+0.02}_{-0.02}$	$111.8^{+0.5}_{-0.7}$	37^{+1}_{-1}	[1000]	638^{+24}_{-24}	R21
DM2	$-13.6^{+0.2}_{-0.1}$	$-4.5^{+0.2}_{-0.4}$	$0.78^{+0.00}_{-0.01}$	$121.4^{+0.2}_{-0.1}$	78^{+2}_{-2}	[1000]	850^{+8}_{-4}	
GAL1	[0.0]	[−0.0]	[0.23]	[−86.9]	[0]	84^{+13}_{-13}	354^{+7}_{-5}	
GAL2	[−17.8]	[−2.1]	[0.30]	[−64.1]	[0]	94^{+6}_{-4}	364^{+2}_{-3}	
$L*$ Gal					[0.15]	81^{+9}_{-9}	135^{+3}_{-4}	
SMACS2031								
DM1	$0.4^{+0.1}_{-0.1}$	$-0.7^{+0.1}_{-0.1}$	$0.31^{+0.02}_{-0.02}$	$4.4^{+1.0}_{-1.1}$	29^{+1}_{-1}	[1000]	624^{+12}_{-11}	R21
DM2	$61.2^{+0.4}_{-0.5}$	$25.3^{+0.4}_{-0.3}$	$0.46^{+0.05}_{-0.04}$	$6.4^{+2.1}_{-3.9}$	112^{+8}_{-7}	[1000]	1037^{+20}_{-19}	
GAL1	[0.1]	[−0.1]	[0.09]	[−0.4]	[0.0]	128^{+12}_{-46}	242^{+3}_{-4}	
$L*$ Gal					[0.15]	9^{+2}_{-1}	161^{+19}_{-9}	
SMACS2131								
DM1	$-3.2^{+0.4}_{-0.2}$	$3.2^{+0.1}_{-0.3}$	$0.66^{+0.01}_{-0.01}$	$155.2^{+0.2}_{-0.3}$	84^{+1}_{-1}	[1000]	866^{+15}_{-5}	R21
DM2	$21.2^{+0.9}_{-0.3}$	[17.0]	$0.53^{+0.02}_{-0.02}$	$82.7^{+6.4}_{-6.9}$	95^{+14}_{-6}	[1000]	452^{+44}_{-12}	
GAL1	[−0.0]	[0.0]	[0.11]	$59.0^{+1.4}_{-1.3}$	[0]	155^{+3}_{-14}	399^{+0}_{-1}	
GAL2	[6.7]	[−2.2]	[0.76]	$7.2^{+9.7}_{-6.4}$	[0]	96^{+8}_{-17}	93^{+18}_{-12}	
$L*$ Gal					[0.15]	93^{+6}_{-21}	202^{+4}_{-1}	

2.4 Source detection and catalog building

2.4.1 Source detection with MUSELET

Source visualization and inspection in a 3D datacube, especially when it involves executing on individual channels can be challenging. To address this issue and facilitate the analysis of the MUSE cube looking for emission-line galaxies in an automated way, there is a tool called MUSELET (for MUSE Line Emission Tracker), developed by J. Richard. MUSELET is based on Source EXtractor (Bertin et al. 1996). It is a Python package used to detect emission lines in narrow-band slices of the MUSE cubes. MUSELET is available as part of the MUSE Python Data Analysis Framework (MPDAF) suite at this address `https://mpdaf.readthedocs.io/en/latest/muselet.html`, where the interested reader can find some instructions and tutorials to run the code. By searching for emission lines, and merging all detections into a single catalog, linking them with continuum sources, the emission lines within a spatial region defined by the "radius" parameter are merged into a single source. Then, one can estimate the redshift of the source based on all the emission lines.

Aiming to obtain emission lines and a high Signal to Noise Ratio (SNR) in each channel of the MUSE cube, a NB cube can be created by subtracting the background continuum. This is done by creating two neighboring cubes of the original cube, each with a width of 5 Å on either side of the wavelength of the Lyman alpha emission line. The continuum image is defined as the average of the two mean images from the blueward and redward subcubes. Finally, the NB image of the source is created by subtracting pixel by pixel between the mean image of the central cube to the continuum image. This is called a background subtracted image or NB image. Running the Source Extractor on an NB image can provide us with several images containing information about the source that is, the RMS image is the background image, the segmentation image shows the source region, the filtered image is the background subtracted and convolved with different seeing values, etc. To judge if a group of pixels could be considered as part of a source, we usually compare pixel by pixel of the filtered image to the RMS image. During this step, we progressively loosen source detection conditions with DETECT_THRESH and MIN_AREA parameters, where MIN_AREA defines the minimum number of connected pixels in the filtered image above the threshold source detection DETECT_THRESH with respect to the RMS image.

2.4.2 Redshift determination using Source Inspector

The following part introduces a new method to identify LAEs behind lensing clusters observed with MUSE/VLT (Johan Richard, Adélaide Claeyssens, et al. 2021; R. Bacon, J. Brinchmann, et al. 2023). This work makes use of a Python-based package named MUSELET, a part of the MPDAF Python package (Piqueras et al. 2019), aiming to detect emission lines in the MUSE datacube. The datacube is in the form of ~ 300 × 300 pixels of 0.2", covering 1 arcmin^2 FoV and ~3681 frequency channels from 475 to 930nm. The package, in turn, makes use of Source EXtractor package, developed by Bertin et al. 1996, to detect source emission in NB images, created from the MUSE datacube. The main goal is to build a source catalog by detecting emission lines and associating them with the continuum emission obtained either from the MUSE white light or HST images. Using this combination, one can measure the redshift of individual LAE. This process consists of 3 main steps:

- Step 1: Source EXtractor creates the white light and the NB images from the original MUSE datacube. Each NB image is an average of 5 adjacent channels, which improves the signal-to-noise ratio of the NB. The continuum level is estimated from two

subcubes, both having the same spatial size and channel width of 25 Å one red-ward, and one blue-ward with respect to the detection line. The continuum image is then the average of the mean images of these two subcubes. NB images are continuum subtracted.

- Step 2: Source EXtractor runs in each NB image to detect source emission in that wavelength slice.

- Step 3: Source EXtractor tries to merge all sources identified from the previous step and associates the emission lines with continuum sources. The package will automatically match the spatial position of emission lines of the same source using a predefined matching radius, which is typical ~ 0.8". Based on information on these emission lines, and their features, one can measure the source redshift.

The flowchart describing the process to build the source catalog is shown in Fig. 2.19. Using this package, more than 4000 images having a wide range of redshift from 0 to 6.7 have been identified from 17 lensing clusters observed by MUSE/VLT. However, due to the nature of emission lines, some images are intrinsically bright, while others are fainter. As a result, their redshifts are then estimated at different confidence levels and will need to be discussed further later.

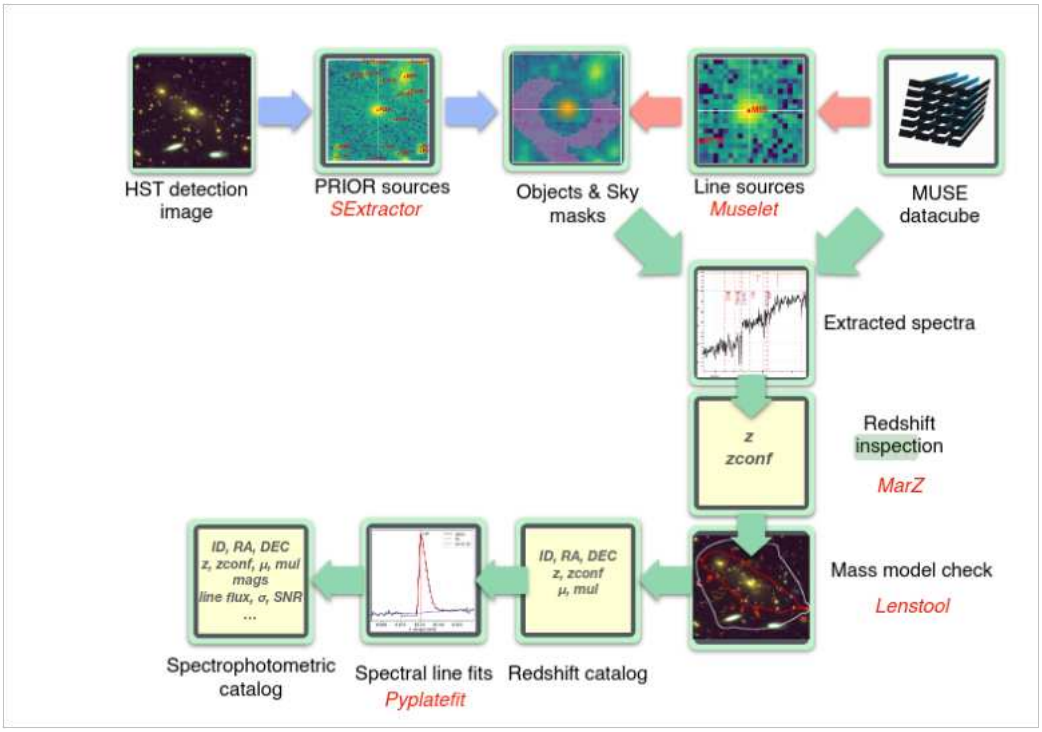

Figure 2.19: . Processing to build MUSE spectroscopic catalogs using HST images and MUSE datacubes. Credit: Johan Richard, Adélaide Claeyssens, et al. 2021.

For this work, we use all available HST images covering the same MUSE fields, aiming to create a photometric catalog of continuum sources, i.e., prior sources. This helps to locate source regions for subsequent spectral extraction. The continuum source is then associated/combined with the line emissions detected by MUSELET to form the prior source. HST images obtained using different filters sometimes help to find the dropouts of high redshift galaxies (Hakim Atek, Johan Richard, et al. 2018). During the line detection process, Source EXtractor tends to split large clumpy sources/arcs into multiple images. These are treated as separate sources with slightly different redshifts.

The MUSE consortium has developed a package named Source Inspector, (R. Bacon, J. Brinchmann, et al. 2023) to measure/estimate source redshift. This package makes use of HST, MUSE white light, and MUSE NB images to locate/guide the source position

and to extract source's spectrum. Using template spectra, Source EXtractor provides 5 best redshift solutions that match with the source extracted spectrum. Based on the spectral features, source redshift is measured, and a confidence level of redshift is assigned. Confidence 1 means that the detection is tentative, due to low Signal to Noise (SN) or ambiguous lines. These sources, however, are still being kept in the final catalog, aiming to compare with the other observations. Confidence 2 corresponds to a source that is identified based on a single emission line without any additional information or several low SN absorption lines. Confidence 3 is the case where the identification is obvious, having high SN, clear spectral features, etc. Each source should be investigated manually and independently by at least 3 experts. A reconciliation meeting among them is held to discuss and then resolve the debate cases.

An example of how to find the redshift of an LAE and its confidence level is demonstrated in Fig. 2.20. This M54 source does not show up in the HST images, and can only be identified thanks to MUSE. The Lyα line with a typical asymmetry profile is clearly visible together with an OIII emission line with high SN of ~ 5. For this case, as it is a very reliable source, we assign it the highest confidence for redshift. Only sources having confidence levels of 2 and 3 will be used later for the construction of the galaxy LF.

We often make use of features of bright emission lines to identify source redshift. Lyα usually shows an asymmetric spectral profile. Another good example is the OII doublet, which has a blue peak that is about two-third the size of the red peak. The absorption line features of CaHK, MgII, and other absorption lines are relatively easy to recognize. However, there are also some features that can be easily mistaken for others. One must identify them with much care.

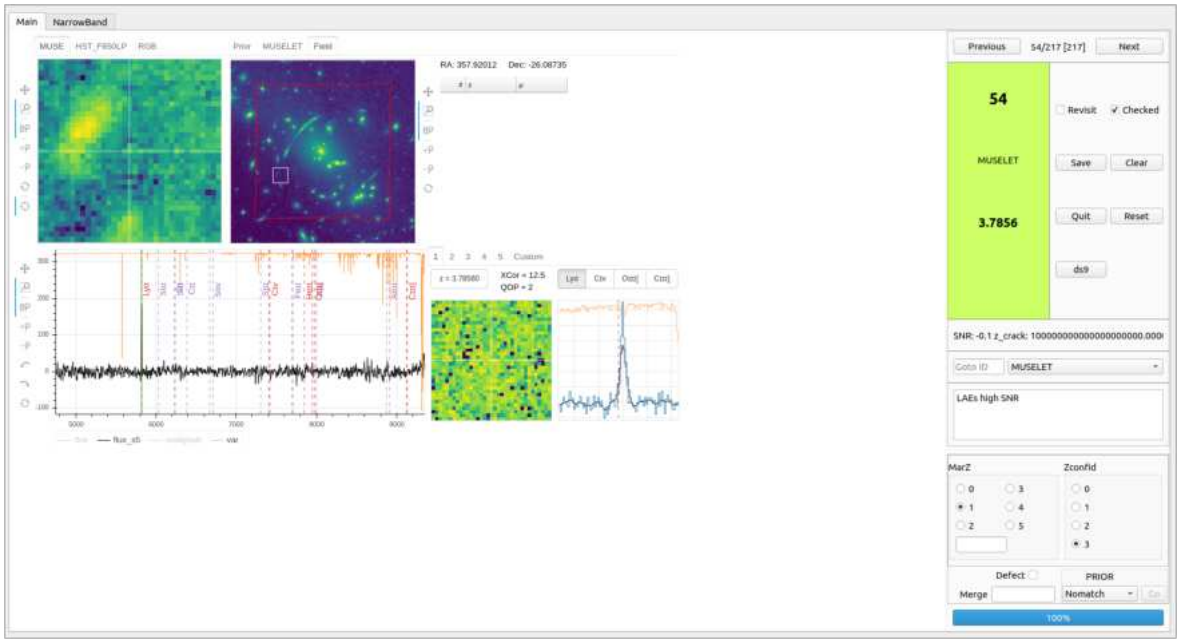

Figure 2.20: Source Inspector package interface. An example is to find an LAE from the A2667 MUSE lensing datacube and to estimate its redshift. The M54 source has no counterpart in the optical domain and only shows up in the MUSE cube. MUSE white light and its FoV are shown in the upper right. MUSE NB is shown in the upper left. The spectrum of M54 is shown in the lower left, a zoom-in spectrum is shown in the lower right.

All 17 lensing models have been built using HST images. It may happen that some of the newly identified sources belong to multiple image systems. We then use LENSTOOL

to investigate these new sources/images to find possible new counterpart which might be missed during the process described above. As the density of the source at a given redshift is quite low, it is easy to identify and match the multiple images. This helps to increase the number of detected LAEs in the final catalog.

Lensing models sometimes help to improve the source redshift confidence level. For example, if a tentative source detection is located at the position of lensed predicted multiple images, it is likely to be assigned a confidence level 2. Finding more sources/images in turn helps to constrain better the lens model. In the context of this work, we have been studying the sources of cosmic re-ionization as seen by MUSE/VLT, focusing on LAEs. MUSE datacube of 17 lensing clusters provides more than 1400 lensed images of LAEs with redshifts from 2.9 to 6.7, some of them belong to the multiple image systems. To avoid sampling in the source plane several times, only one representative image is chosen for each multiple-image system. The represented image often has high enough SN, moderate magnification error, and less contamination from nearby galaxies. Thanks to lensing clusters, signals from distant galaxies are magnified by a large factor, so one can reach the fainter sources which have not been available in the previous blank field observations. Finally, 600 LAEs have been used for the next step in computing the LF.

2.4.3 LAEs catalog

There are three quality flags for the redshift determinations indicating confidence levels, from 3 (secure redshifts) to 1 (tentative redshifts). After running MUSELET and Source Inspector to identify the redshift of the source detected in the MUSE cube, we have more than 4500 images belonging to the systems, that have a redshift confidence level $zconf > 1$ (foreground galaxies, stars, cluster galaxies, etc. at high redshift) behind 17 lensing clusters. More than ~ 40% objects in this catalog are cluster galaxies. The distribution of the sources is shown in Fig. 2.21. The figure on the left displays the redshift histogram of all the sources detected in the MUSE cube (gray), of all the images which are rated with high confident level $zconf = 2,3$ (pink), and of the representative images for each system having $zconf = 2,3$ (magenta). Fig. 2.21 (right) shows the redshift distribution of all the detected sources (gray), of sources that have been found with line emission only (pink), and of sources detected with only line emission and having a high confident level $zconf = 2,3$ (magenta). All the galaxies from these 17 clusters in the present work are located in a narrow redshift interval, with a prominent peak of an overdensity of galaxies at redshift $z \sim 0.4$. The number of sources significantly decreases in the redshift range of 1.5<z<2.9, which is known as the MUSE redshift desert (Fig. 2.21, left). At higher redshifts $z > 2.9$, LAEs are the main population in detected sources. From choosing image processing, we see that the number of multiple images is found at redshift $z > 1.8$, the "MUSE redshift desert" can be seen in a range of $(1.5 < z < 2.9)$ with a deficit in redshift, at the higher redshift $z > 2.9$ the LAEs become main contributors for the redshift distribution. In the present work, we have kept only LAEs at redshift $2.9 < z < 6.7$. For sources with a redshift confidence level of $zconf = 1$, most of them belong to the systems having one image with a small magnification (see Fig. 2.22). According to the criteria defined above, these are tentative sources that do not display a clear Lyman alpha profile, have low signal-to-noise, or lack information on association lines, etc. We will ignore them from the list.

To save time during projection back and forth between source and image planes, after having identified the LAEs redshift with source-inspector, we choose a single representative image for each multiple systems based on several criteria: high SN, more isolation compared with other multiple images of a same system, a reasonable magnification uncertainties, and less contamination from other sources. This procedure is done by

overplotting source positions on the HST images that were observed in at least two bands and overplotting on the White light image of the MUSE observation (see Fig. 2.23). Finally, there are 600 Lyman alpha lensed images kept in the final catalog. The number of LAEs behind the lensing clusters is shown in Table. 2.1.

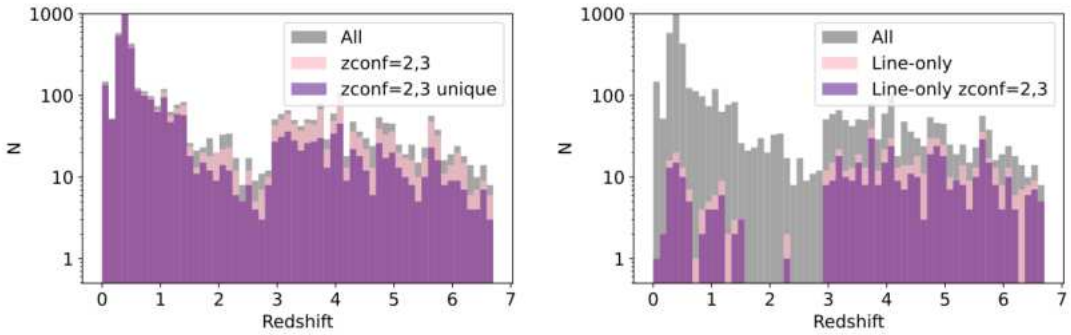

Figure 2.21: Redshift distributions of sources in the final sample. Left: the gray histogram shows the redshift distribution of all sources in the sample. The pink histogram is the redshift distribution of all sources having $zconf > 1$, and the magenta histogram is for representative images having $zconf > 1$. Right: the gray histogram is the redshift distribution of all sources in the sample, the pink histogram is the distribution of line emitters with $zconf > 1$ and the magenta histogram is for the representative line emission sources with $zconf > 1$. Credit: Claeyssens 2021.

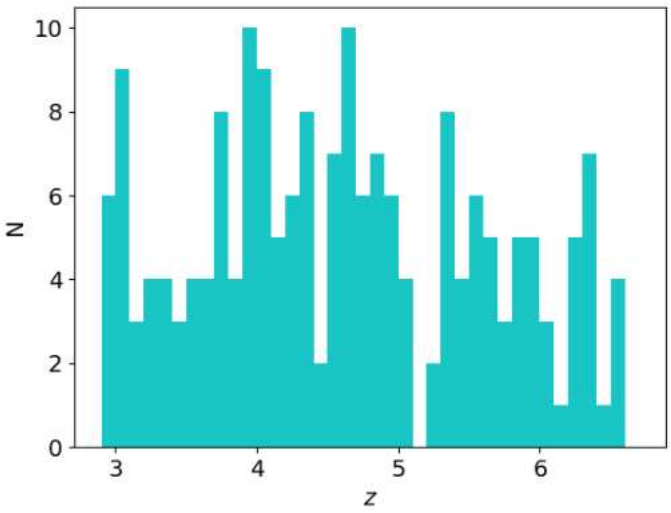

Figure 2.22: Redshift distribution of Lyman alpha sources with $zconf = 1$ behind 17 lensing clusters.

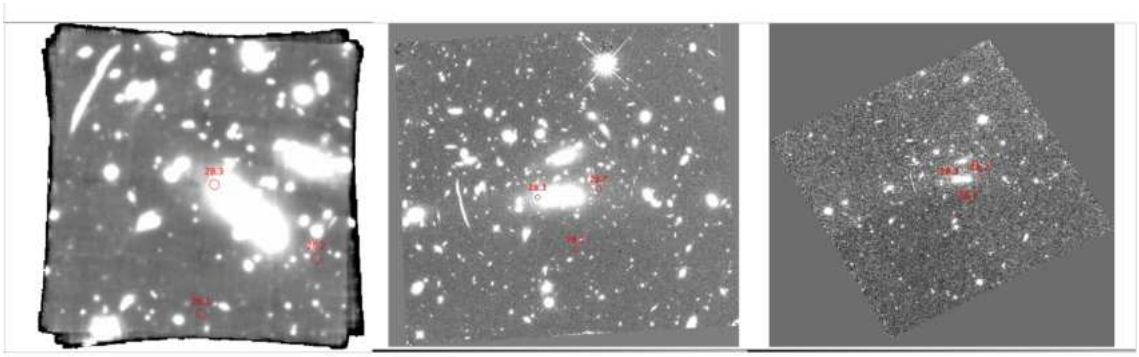

Figure 2.23: An example of choosing a representative image of multiple imaged system behind MACS0451. The image positions (red circles) are overplotted on the White Light MUSE image (left), F140W, and F814W observed by HST.

2.4.4 Lyα flux measurement

Thousands of LAEs have been observed, showing a variety of Lyα line shapes, mainly in terms of their asymmetry and number of peaks. This can be explained by the different diffusion processes that affect the Lyman alpha photons before they escape from the IGM (Verhamme, A. et al. 2006) as well as the absorption of IGM (M. J. Hayes et al. 2021). For this reason, various approaches can be employed to measure the total Lyman alpha flux emitted from the galaxies. This section introduces and discusses two methods for measuring this quantity.

- Spectral fitting: This method was developed by Shibuya et al. 2014 to use an asymmetry Gaussian profile of the Lyman alpha which follows the function below:

$$f(\lambda) = A \exp \frac{-(\lambda - \lambda_0)^2}{2(a(\lambda - \lambda_0) + d)^2} \tag{2.2}$$

where A is the amplitude of the emission line, λ_0 is the wavelength in which the Lyman alpha emission line reaches the peak and can be converted directly from the redshift of the source, a is the asymmetry parameter of the line, and d is the typical width of the line. These parameters are optimized during fitting by applying the function form above to a subcube with a size of 5" × 5" × 12.5 Å surrounding the source position. The flux value is integrated along the wavelength channel with a range of $[\lambda_0 - 6.25 : \lambda_0 + 6.25]$ Å. The mean values of FWHM and asymmetry were found are 7 Å and 0.2, respectively (A. Claeyssens et al. 2022). Fig. 2.24 shows different asymmetry Lyα line profiles, each with a different best-fit a value. The four best fit parameters were obtained by employing a MCMC fitting process using 8 walkers and 10 000 steps, combined with the median values of their posteriors distribution. The uncertainties of individual values are taken at 16th and 84th percentiles. There are 31 sources in the total of 600 that have two peaks in the present work. This pattern can be adapted by applying the function above on the red peak with a positive asymmetry value and with a negative value for the blue peak. The final flux value of a source will be summed up from the two peaks. The final median flux value is 2 $\times 10^{-18}$ erg cm^{-2} s^{-1}.

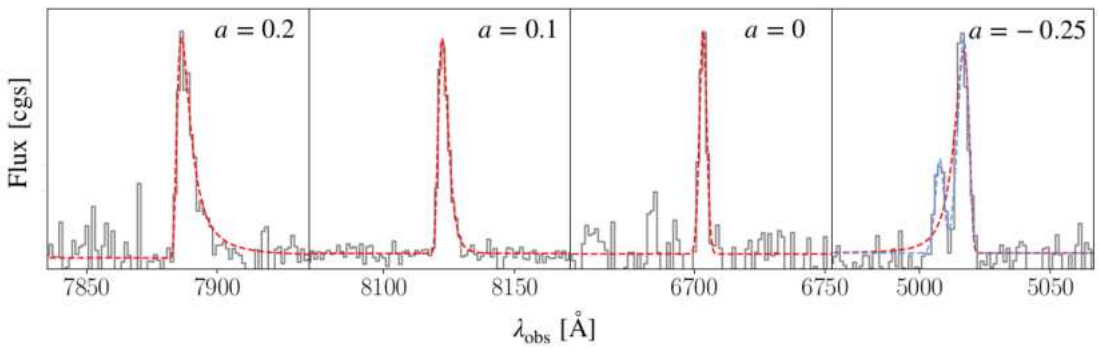

Figure 2.24: An example of asymmetry values obtained from the flux fitting method for four different LAEs behind MACS0940. The red dashed curve displays an asymmetry Gaussian fit to the observed profile (black). Right panel shows a double asymmetry Gaussian model (blue). The asymmetry value of a simple model is indicated for each line. Credit: Claeyssens 2021.

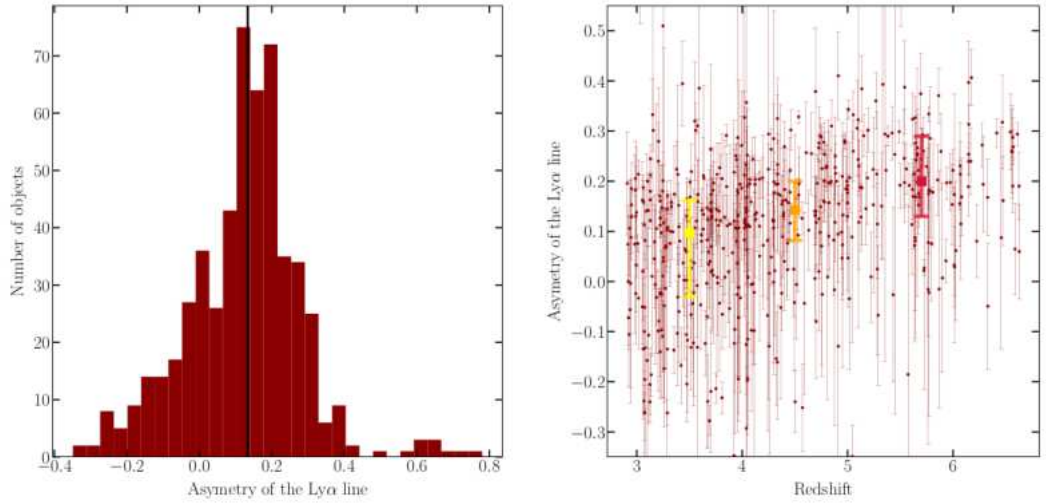

Figure 2.25: Left: Asymmetry parameter distribution of Lyman alpha profiles in the present work. A positive value of the asymmetry parameter indicates that the line profile is asymmetric towards the red, while a negative value indicates that the profile is asymmetric towards the blue. A zero value indicates a normal Gaussian profile. Right: Asymmetry parameter versus redshift of individual sources. Credit: Claeyssens 2021.

Fig. 2.25 shows the distribution of the asymmetry parameter in the present LAEs sample. 81% of LAEs exhibit an asymmetry towards the red ($a > 0$), with a medium value of 0.18. This has been confirmed in many recent studies. However, the main reason for the asymmetry of the line profile is still difficult to interpret. The asymmetry generally correlated with FWHM in an asymmetric fit.

- The second method is obtained from SExtractor. In this method, we do not assume a parametric profile for the line, instead, the total flux is directly extracted from the cube. We create a subcube with a size of 10" × 10"× width of the Lyman alpha line and its two neighbor cubes on both sides with a volume of 10" × 10" × 20 Å. We then ask SExtractor to run on NB image to obtain FLUX_AUTO value of the source and its error. This parameter is developed based on Kron's first-moment algorithm, which ensures that 90% of its flux

will be contained in the circular aperture of the Kron radius when the source is convolved with the seeing condition. To adapt to different seeing conditions, we relax SExtractor parameters (DETECT_THRESH, MIN_AREA) to ensure that the faint sources also have the opportunity to be detected. The final flux value is multiplied by the width of the emission line.

The first method is more reasonable because it takes into account the shape of line emission, whereas the second method is more efficient in measuring the flux of faint sources. In the present work, the second method is applied for sources found in A2744 due to a large number of faint sources being included, while the first method is applied for the remaining sources in the catalog. Whenever the first method fails due to a spectral extraction problem, the second method is used. In total, 425 of the 600 sources in the catalog have fluxes measured using the spectral fitting method. The remaining 128 LAEs behind A2744, plus 47 faint sources that failed from the first one, have their fluxes measured using Source Extractor.

A comparison of the difference of central flux values for individual sources using two methods is plotted in Fig. 2.26 (left). The abscissa axis displays flux values measured from SExtractor and the vertical axis is from spectral fitting, both in the unit of 10^{-18} erg s^{-1}. The solid black line shows a one-to-one ratio between the two methods, and the dashed black lines denote a ratio of 0.5 and 2.

It is worth noting that the first method, as described in A. Claeyssens et al. 2022 tended to use the central magnification value of the individual sources, while the second method used the weighted magnification to correct for the lensing effect. Fig. 2.27 shows distribution of the weighted magnifications of LAEs in the present work. A comparison of magnification values obtained from two methods are shown in Figure 2.26 (right). The flux values obtained from the first method are combined with the central magnification value to compute the luminosity. This luminosity value is then plotted against the value derived using the SExtractor and weighted magnification, as shown in Fig. 2.28. In the remaining part of the work, we will use the weighted magnification values for the computation process.

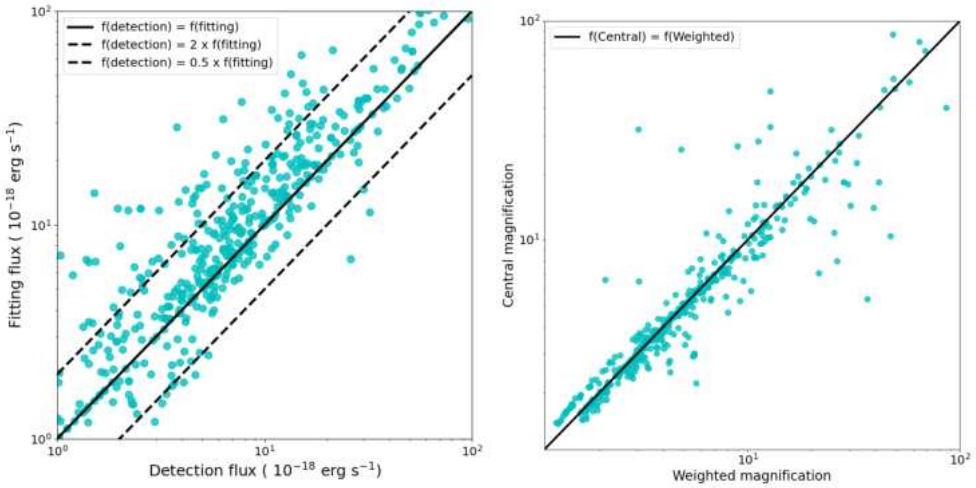

Figure 2.26: Left: Comparison between the flux values obtained from the two methods: line fitting (y-axis) versus SExtractor (x-axis). Right: Comparison of central magnification (ordinate) and weighted one (abscissa) .

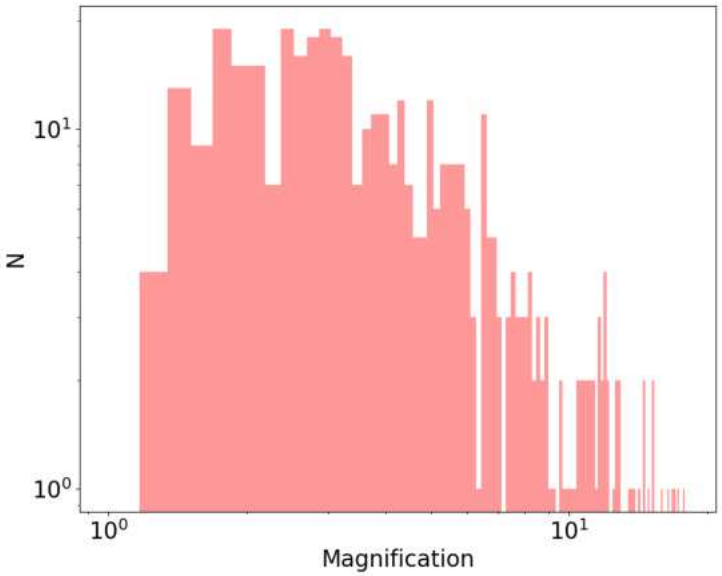

Figure 2.27: Distribution of weighted magnification in the present work.

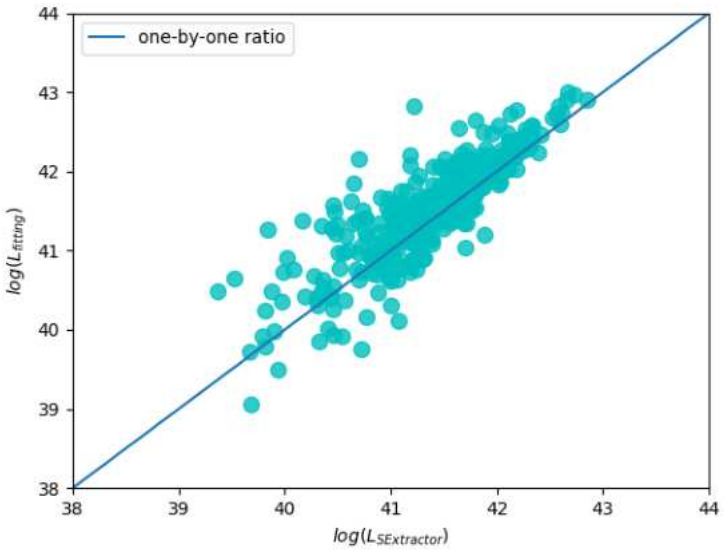

Figure 2.28: Comparison of Lyman alpha luminosity between the two methods of flux measurements and magnification computations (see text).

It is also worth mentioning that DLV 2019 studied the LF for LAEs behind four lensing clusters observed by MUSE. Fig. 2.29 displays the comparison between the two data samples. The present data sampleis denoted by magenta and the data sample behind four lensing clusters used in the DLV 2019 is shown in cyan. It's clear that the number of LAEs in this work is three times larger compared to the previous one. Using this data, we expected to have better coverage towards the faint part of the LF, as well as an improved the statistic in this domain.

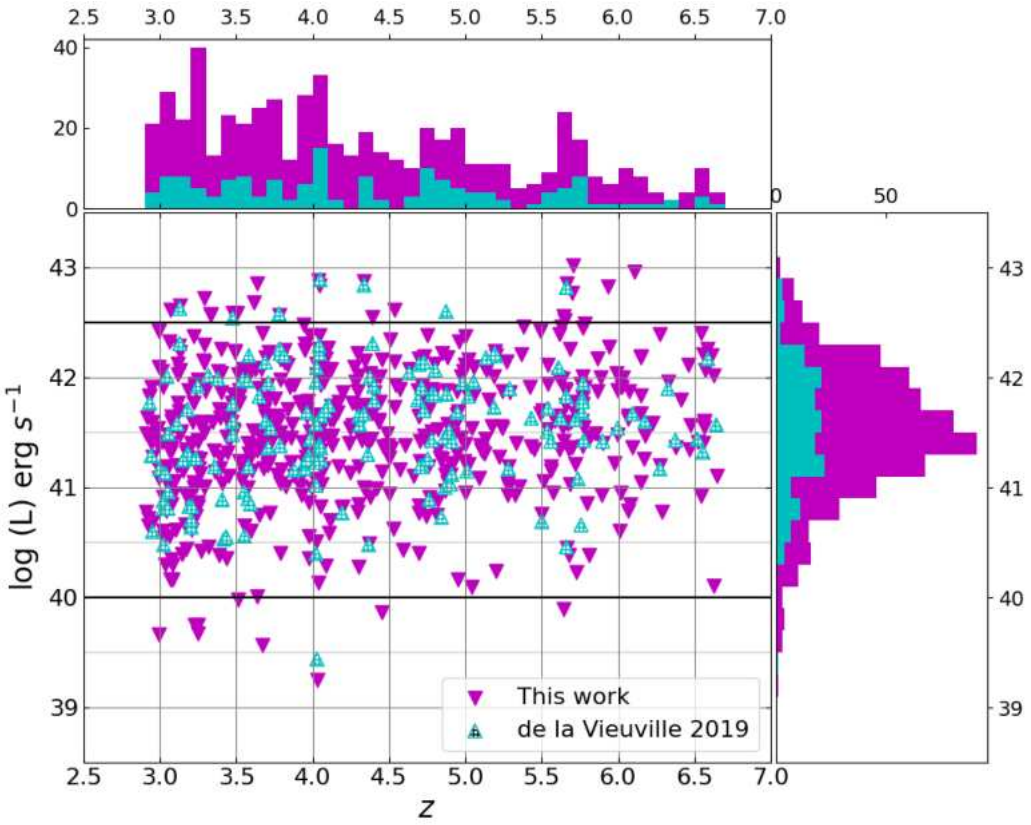

Figure 2.29: Comparison between the present data sample and the one in DLV 2019. The magenta color denotes the data used in the thesis, while the cyan color indicates the data sample in DLV 2019.

3 Computing the Luminosity Function in Lensing Clusters

Contents

To compute the LF of LAEs, we have used the non-parametric V_{max} method (Schmidt 1968) to estimate the volume of the survey in which an individual source could be detected. The contribution of the source to the density of galaxies is given by reciprocal this parameter. The present work uses data collected from 17 surveys in lensing clusters meaning that the final value of V_{max} for a given source should be computed from all the fields of the survey, including the fields where the source was present. Working in the image plane to compute the V_{max} value of individual sources may lead to an overestimate of this value. For this reason, the present work has been done in the source plane, based on the creation of a 3D cube in the source plane for each LAE using the pipeline developed in DLV 2019, including some improvements presented in this thesis. The main steps are shown in Fig. 3.1 (DLV 2019).

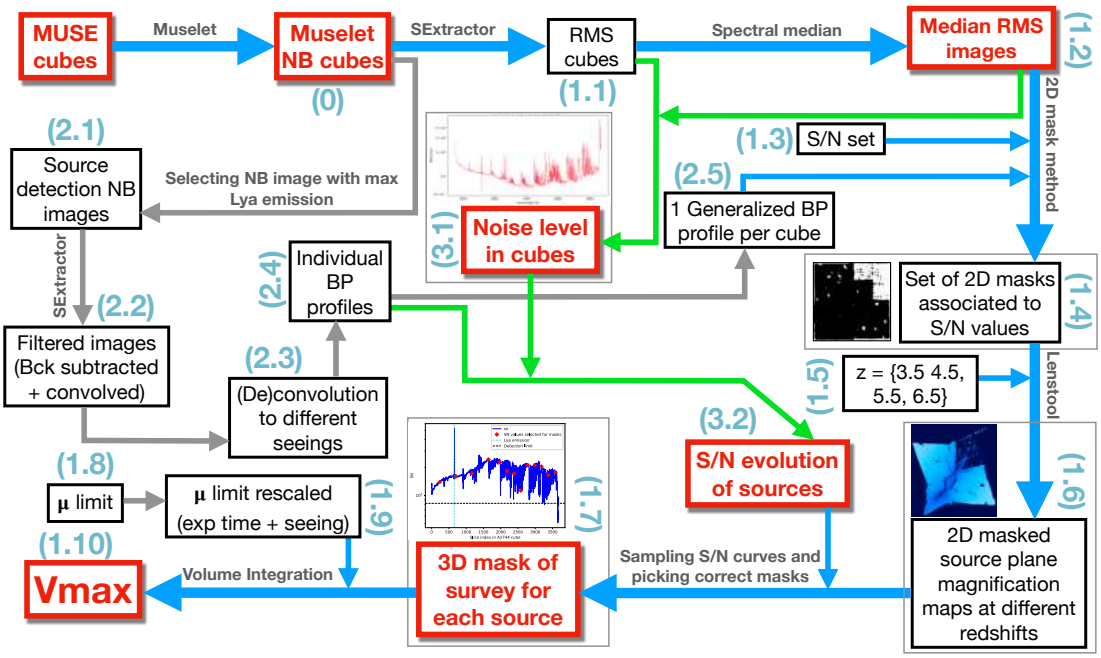

Figure 3.1: Procedure to create the 3D mask images and V_{max}. The main steps are followed by the red boxes and blue arrows. The details are given in DLV 2019.

3.1 3D mask cubes in the source plane

3.1.1 Noise level

The noise level of a given layer is computed based on its RMS image combined with the median RMS image of the cube as a normalization factor, so the noise level in the i^{th} channel is defined as:

$$\text{Noise level}_i = \text{Noise level (RMS}_i) = \frac{< RMS_i >_{x,y}}{< RMS_{\text{median}} >_{x,y}} \tag{3.1}$$

where $< RMS_i >$ is the RMS image in the i^{th} layer, $< RMS_{\text{median}} >$ is the RMS image of the median layer of the cube obtained by running the Source Extractor on the individual NB images. The signal-to-noise value reflects only the evolution of the noise level with wavelength within a given cube and could not be used to compare the noise level between the cubes. This evolution is shown in Fig. 3.2 for each of the 17 clusters. The noise levels in Fig. 3.2 are similar in all datacubes, except for MACS0257, MACS0416N, MACS0451, MACS0520, MACS0940, MACS2214, and RXJ1347. These cubes show an increase in noise level within the AO filter (around 5890 Å). This can be explained due to the shorter effective exposure time in the WFM-NOAO-N mode of the instrument, which is only 50 minutes instead of 7 or 8 hours elsewhere. However, all of the datacubes show the best sensitivity in the 6800-7800 Å wavelength range, with a detection limit of $3-\sigma$ for an unresolved emission line (R. Bacon, J. Brinchmann, et al. 2023).

3.1.2 Signal to noise of a given source

The probability of detecting a given source will be determined by comparing in each pixel the signals from the sources and RMS images. The signal of the source image is defined by a group of the 9 brightest pixels found from the filtered image obtained by running Source Extractor on the NB image of the source. They are found in a circle with a radius of 1" surrounding the source position. When the first pixel was found, we continued looking for the 8 connected pixels to find the second one. The process stops when the 9 brightest pixels of the individual source are found. This probability has been taken into account for all the fields surveyed in the present work, hence the filtered image has to be convolved/de-convolved with different seeing values. Consequently, each source will have one brightest pixel profile found from its parent cube, in which the source is presented and has 17 other brightest pixel profiles due to the convolving/de-convolving procedure. Fig. 3.3 shows the brightest pixel profiles of M39 detected in A2390 (left) and P8192 detected in A370 (right). M39 was detected under a seeing condition of 0.75" (the thick solid line). When the M39 filtered image has been de-convolved to lower seeing values producing its brightest pixel profiles (the thin solid lines above the thick solid line), better than the value found from the parent cube, while the convolving with higher seeing values will get a lower value (the thin solid lines below the thick solid line).

Fig. 3.4 illustrates the 9 Brightest pixel (Bp) that have been found from the filtered image of a source detected in the A2390 MUSE cube. This method allows us to follow the morphology of the source and its detectability without assuming any prior shape. For example, from the profile, we can partly study the spatial profile of the sources because the extended sources tend to display a flattened Bp profile, while compact sources usually show a steep slope profile. The Bp profile of the individual source behind each lensing cluster is shown as the red solid curve of Fig. 3.7.

From the definition of noise level above, the signal-to-noise of each source in a

given channel is computed based on its Bp profile and the noise level for that channel, following the equation:

$$S/N_i = \frac{\max(Bp)}{noiselevel(RMS_i)} \tag{3.2}$$

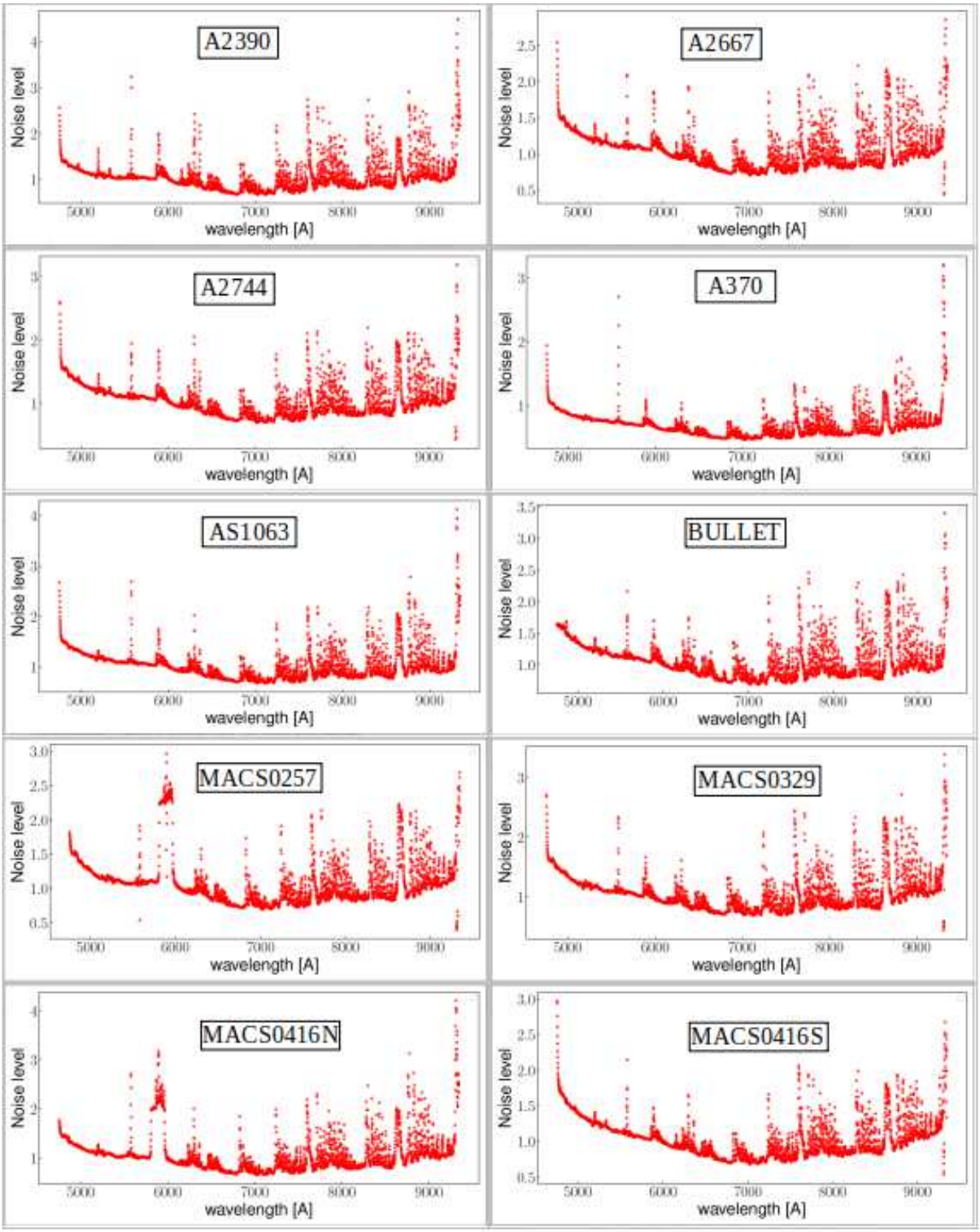

Continued on next page

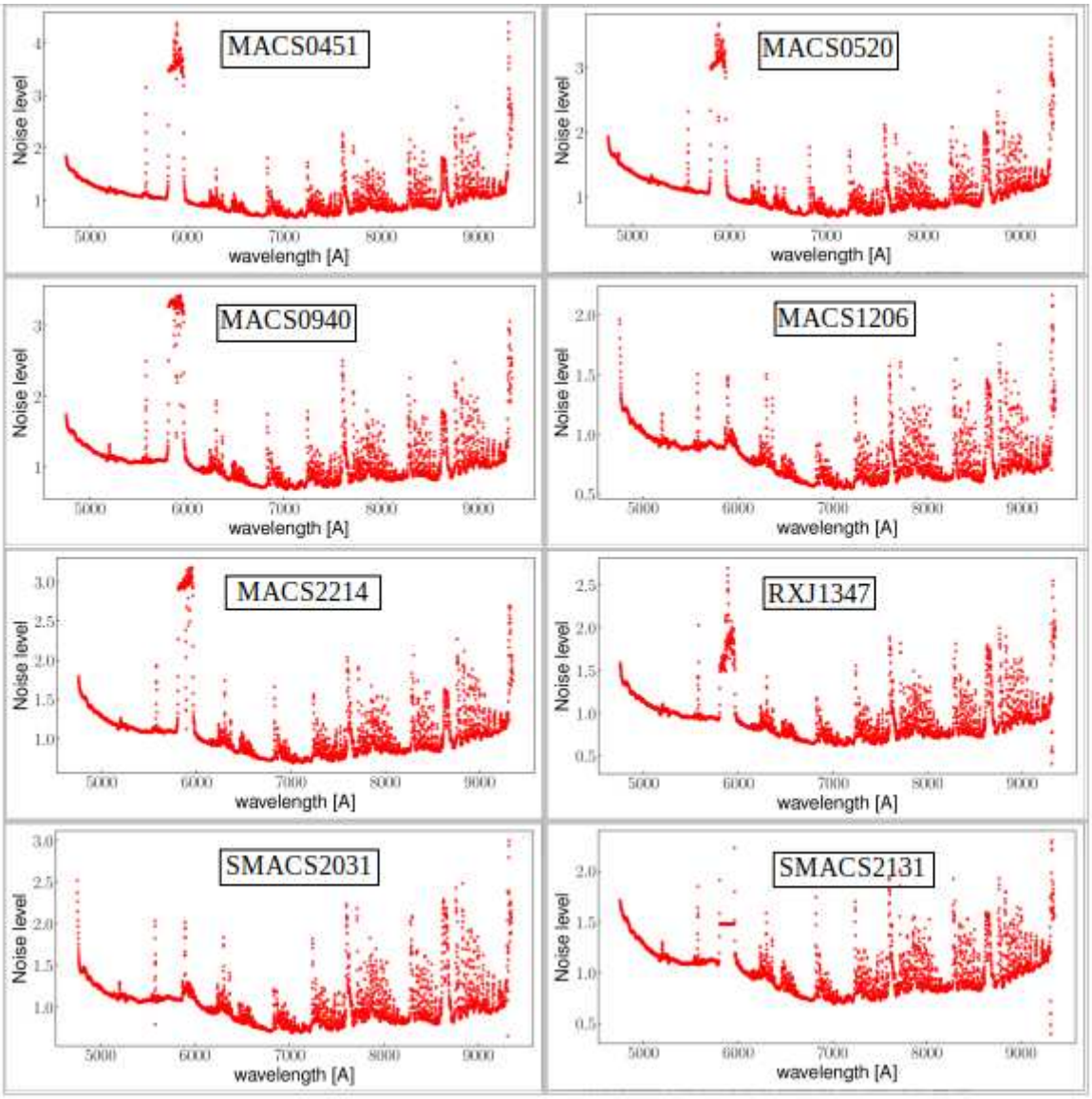

Figure 3.2: Evolution of noise with wavelength inside each MUSE cube. From left to right, up to down, the cubes are: A2390, A2667, A2744, A370, AS1063, BULLET, MACS0257, MACS0329, MACS0416N, MACS0416S, MACS0451, MACS0520, MACS0940, MACS1206, MACS2214, RXJ1347, SMACS2031, and SMACS2131.

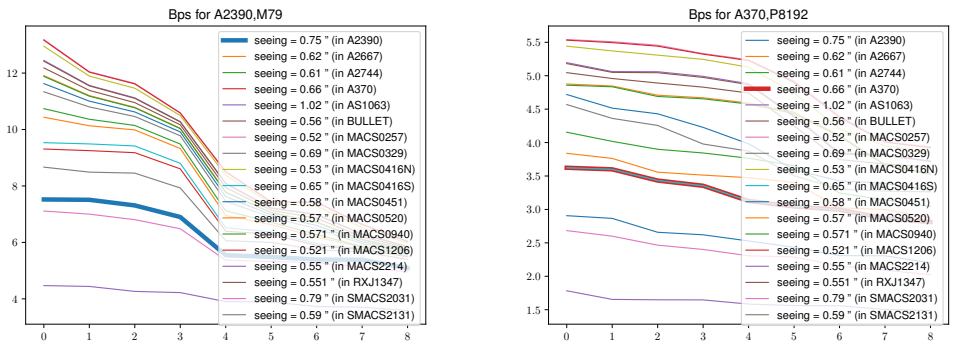

Figure 3.3: Examples of the brightest pixel profiles of M79 located inside the A2390 field (left) and P8192 inside the A370 field (right) after being convolved/de-convolved to account for the different seeing conditions in the different cubes.

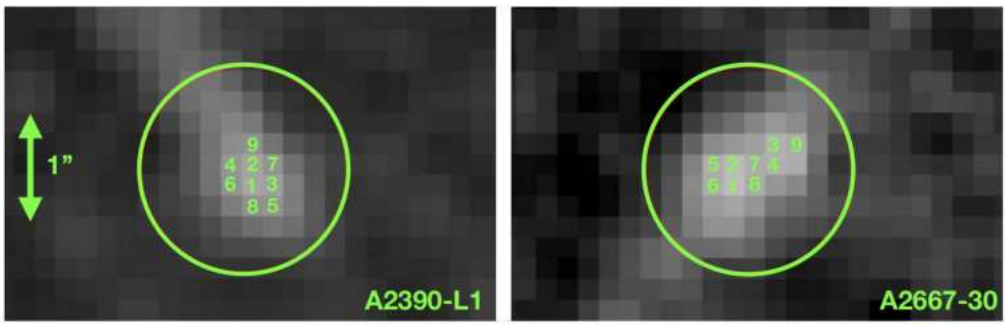

Figure 3.4: An example of the 9 brightest pixels list of 2 sources behind lensing A2667 in the catalog of (DLV 2019). The green circle is the critical region with a radius of 1" which is used to look for the first brightest pixel.

Using Eq. 3.2, a given pixel belonging to the source area could be detected and unmasked if its value satisfies the following condition:

$$Bp[MIN\_AREA-1]/DETECT\_THRESH < local\_noise[x,y] \tag{3.3}$$

where $[x, y]$ is the pixel on the RMS map and Bp[MIN_AREA-1] is the faintest value of the individual Bp profile of the source, the DETECT_THRESH is varied to make sure that the source always has the opportunity to be detected. In this case, we are using the faintest value of the Bp profile, meaning that if this value fulfills the criterion, the other bright pixels that have a higher value will also meet the same criteria at the local noise $[x, y]$. In general, the central pixel of the RMS map is unmasked. This process is applied to all the pixels of the RMS image.

When the detectability condition is applied to a given RMS image, a masked image is generated. In principle, this image has to be projected into the source plane. To avoid creating too many images for each source with respect to a given signal-to-noise, we create masked images for a given cube at various signal-to-noise values, ensuring the detection of all sources within the cube. This can be done under two simplifications introduced below:

- First, the RMS map in each channel of the MUSE cube can be modeled and reproduced by scaling from the median map. This assumption has been introduced due to a linear evolution of the pattern with the MUSE slices that have been found during studying a large number of RMS images. The evolution with channels is shown in Fig. 3.5 for A370 (upper panel) and MACS1206 (lower panel) at slice numbers 500, 1000, 2500, 3000, and its median RMS image at channel 1839 (last column image). The different patterns of the RMS maps can be explained by the difference in morphology or the variance of noise with the slices. Fig. 3.6 shows RMS median maps of 18 datacubes used for the present work, the difference in the structure of the instrument, and exposure times are clearly visible in each image, suggesting that the assumption is reasonable for all the channels of RMS cubes.

- Second, we use a general bright pixel profile, which may be the representative profile for all sources in a cube named general bright pixel profile (Bp_g). The profile is built based on individual brightest pixel profiles of a source that is already convolved/deconvolved to adapt to the seeing conditions. The deconvolution algorithm is computed

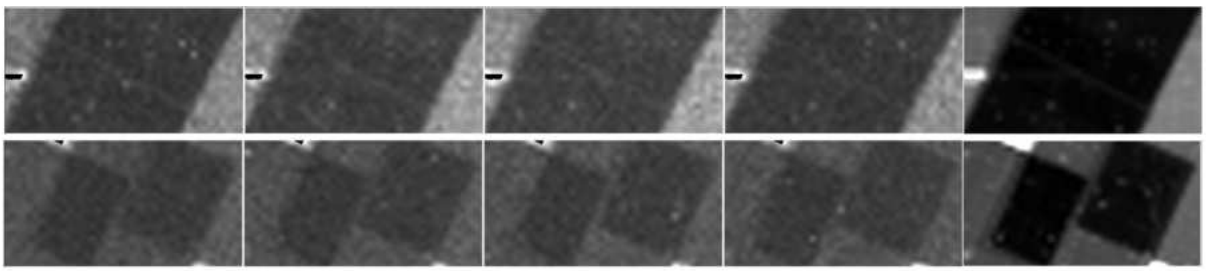

Figure 3.5: The evolution of RMS maps at different channels inside a given cube. From left to right is the evolution of RMS maps at different channels (500, 1000, 2500, 3000) and its median RMS map inside A370 (upper) and MACS1206 (lower).

based on the description of a Weiner filter which is presented in Orieux et al. 2010 combined with the Python Scikit image package in Walt et al. 2014. The final value of Bp_g in each cube is the median value of the individual bright pixel profiles contained in that cube. At this step, the normalization is presented by $max(Bp_g) = 1$, and the other general bright pixel profiles will be scaled following the value of the maximum general bright pixel profile before normalization.

Using the two assumptions, the signal-to-noise of a given source in a cube is given by the function:

$$s/n = \frac{max(C \times Bp_g)}{\text{Noise level}(RMS_{\text{median}})} \tag{3.4}$$

where:

$$\text{Noiselevel}(RMS_{\text{median}}) = \frac{< RMS >_{\text{median}}}{< RMS >_{\text{median}}} = 1 \tag{3.5}$$

C and $max(Bp_g)$ are independent, so $max(C \times Bp_g) = C \times \max(Bp_g) = C$, since $max(Bp_g)$ was previously defined as equal to 1. Consequently, the signal-to-noise of a source in a cube is found as the rescaled factor of that cube to the $max(Bp_g)$. In another way, we can write as:

$$s/n = C \tag{3.6}$$

so now 2D masked images for each cube can be produced based on its RMS median image combined with its signal-to-noise value of $s/n \times Bp_g$ as the bright pixel profile. At this step, we have presented a set of signal-to-noise values (introduced signal-to-noise value) covering a range of 0.6 to 20 with 100 steps in logarithmic scale, which have included all possible values to detect the Lyman alpha sources in the present sample. Therefore, 100 masked images are generated for each cube. In connection with a given value of the signal to noise ratio, we estimate the ratio of masked pixels to the total of pixels in each masked image, named covering fraction. If this ratio is 0, meaning that the possibility of detection happens to any location within the image, a covering fraction of 1 suggests that the input source remains undetected throughout the entire image. The covering factor can vary between 0 and 1, indicating whether the source could be found in certain parts of the image. Therefore, if several images have the same covering fraction, we keep only one of them. Our data sample shows that bright sources tend to have a covering fraction value close to 0, whereas the diffuse sources tend to be 1 in their parent cube. In addition, at a higher redshift, our observations have been affected much by the skylines reducing the number of masked images adapted to the given criteria.

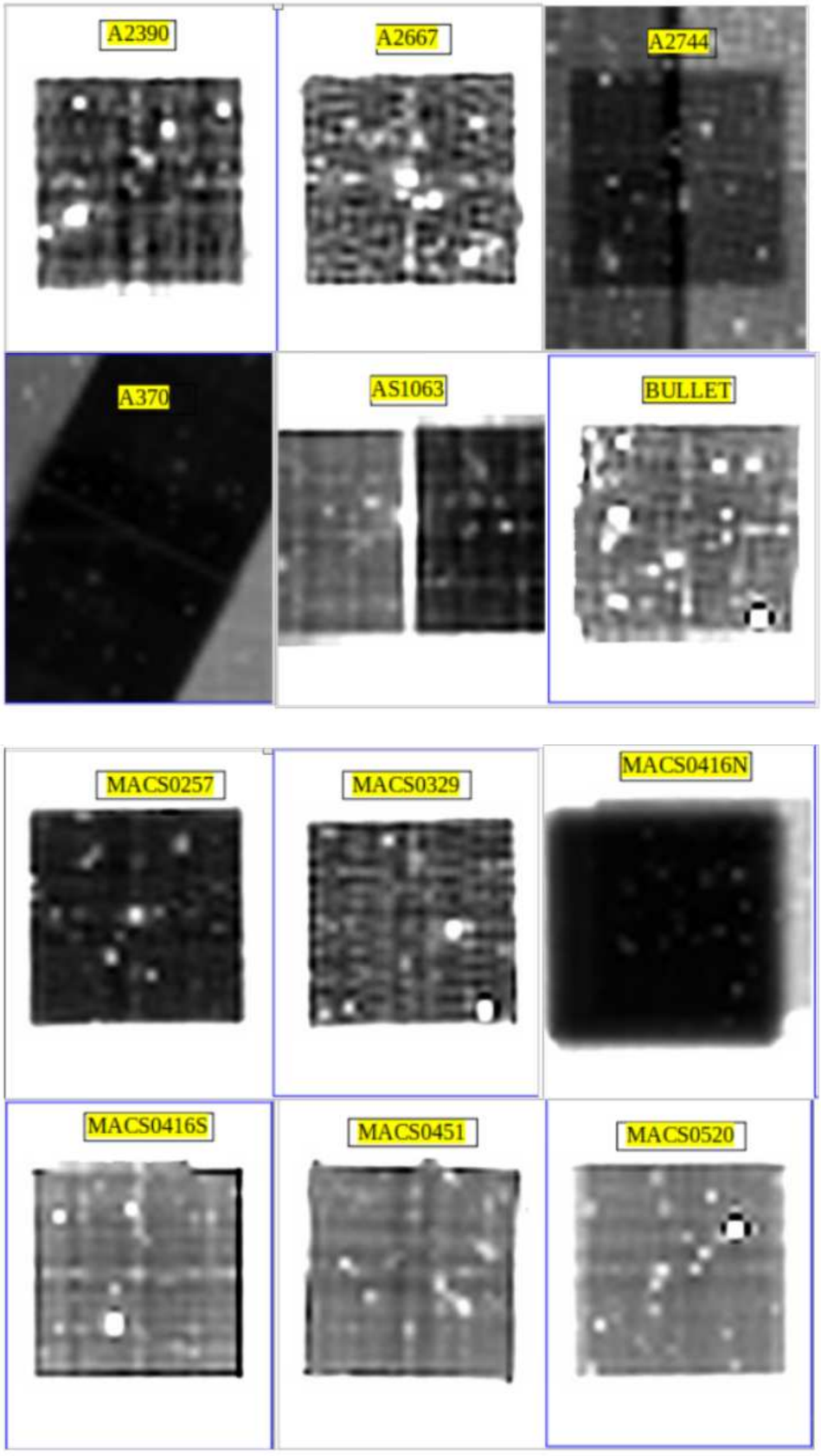

Continued on next page

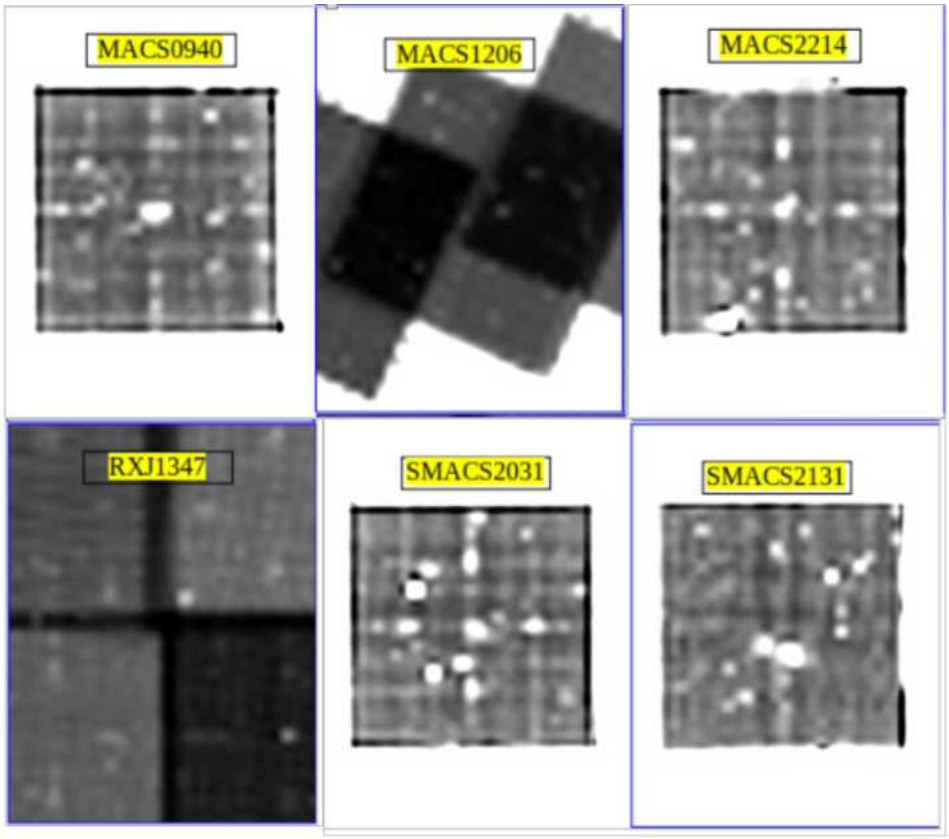

Figure 3.6: RMS median images of 18 datacubes in the present work. From left to right, up to down corresponding to A2390, A2667, A2744, A370, AS1063, BULLET, MACS0257, MACS0329, MACS0416N, MACS0416S, MACS0451, MACS0520, MACS0940, MACS1206, MACS2214, RXJ1347, SMACS2031, and SMACS2131.

3.1.3 Creating 3D masked images

The previous subsection presented a way to produce 2D masked images for a given cube, that helps us reduce the number of masked images for the source plane projection, save time for computation, and avoid overlapping regions in the computation. However, the main purpose is to compute the total co-moving volume, where individual sources could be detected. This requires 3D masked images, which are associated with individual sources. This subsection presents how to form 3D masked images both in image and source planes.

- In the image plane:

From Equation 3.2, the signal to noise of an individual source on all the layers of its cube can be estimated. They were resampled by 300 values over the MUSE cube, 100 values in the range from 4749 to 7100 Å, and 200 values in the rest. As I mentioned before, at longer wavelengths, the source detection is affected by the skylines, so the resampled signal to noise is denser in this region to achieve higher precision. The final masked images of each source are found by fetching the closest signal-to-noise value from the resampled measurement to the introduced signal-to-noise.

- In the source plane:

In this plane, we have applied the same method of constructing the individual 3D mask image of the source. The 2D masked images from the image plane are projected in the source plane at different redshifts. This is done using PYLENSTOOL, which allows us to use LENSTOOL automatically. In practise, we have realized that there is not a substantial disparity in the pattern of the images at different projected redshift values, therefore there

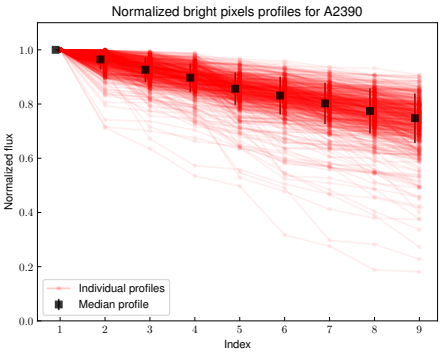

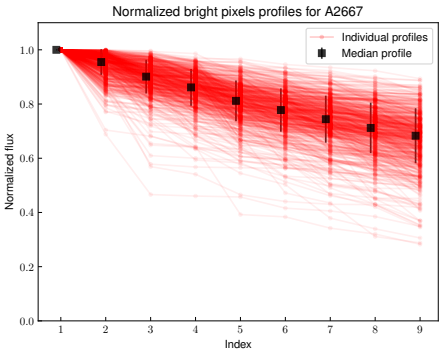

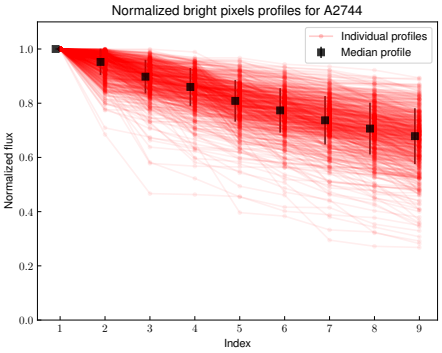

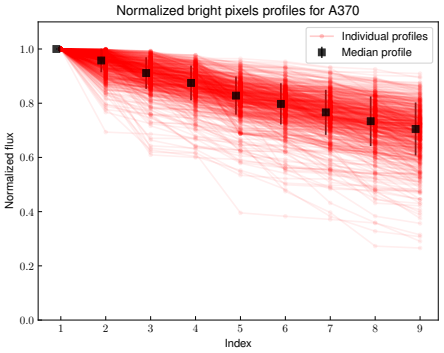

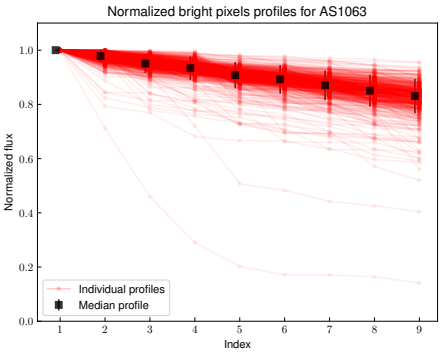

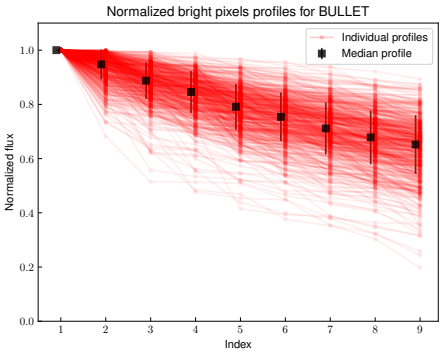

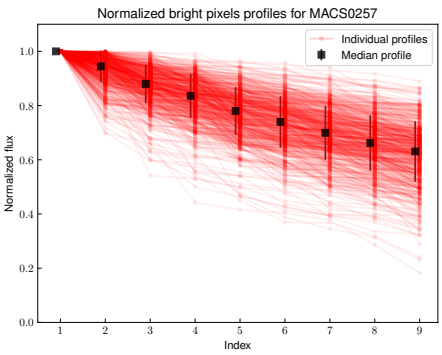

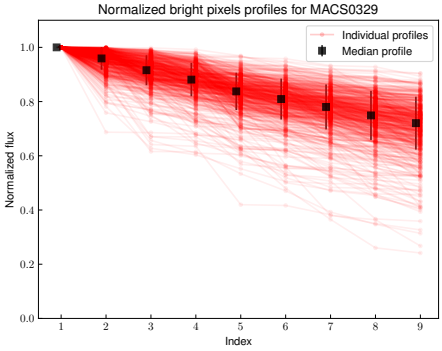

Continued on next page

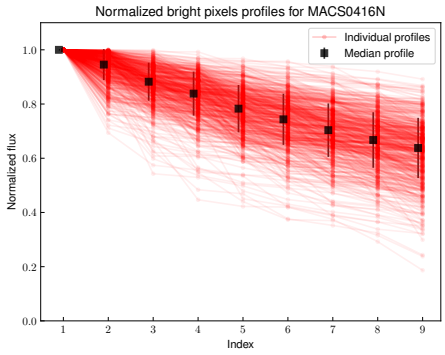

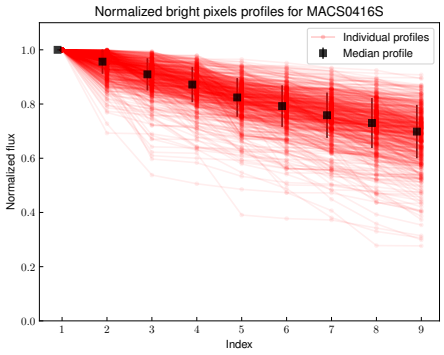

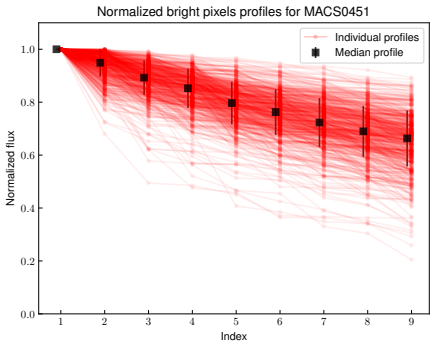

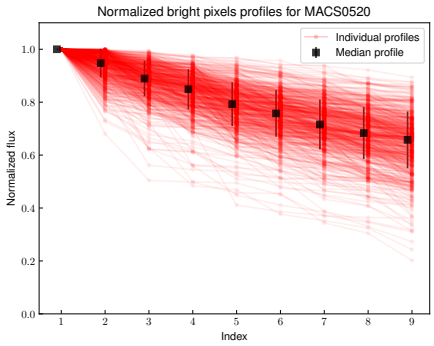

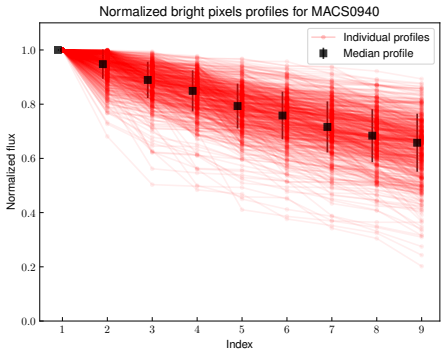

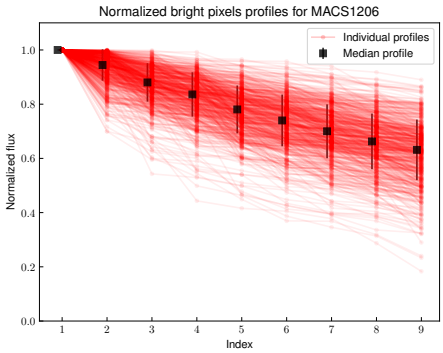

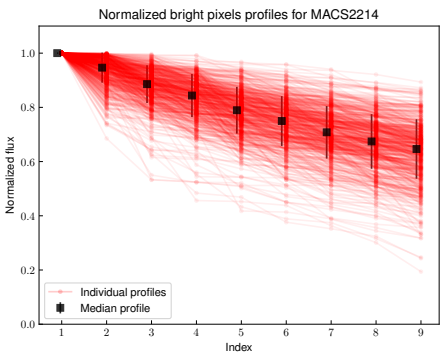

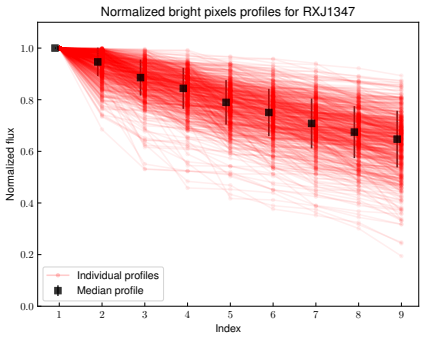

Continued on next page

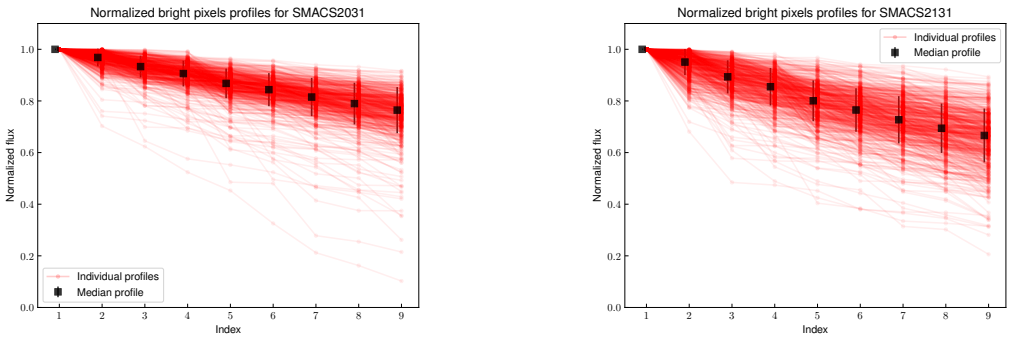

Figure 3.7: The individual brightest pixel profiles (red solid line) and general brightest pixel profile (black solid line) are represented for each MUSE cube. Clusters are labeled from left to right, up to down as A2390, A2667, A2744, A370, AS1063, BULLET, MACS0257, MACS0329, MACS0416N, MACS0416S, MACS0451, MACS0520, MACS0940, MACS1206, MACS2214, RXJ1347, SMACS2031, and SMACS2131.

are four redshift samplings chosen for the projection z_s = 3.5, 4.5, 5.5, and 6.5 (see Fig. 3.8, 3.9). At this stage, besides matching up the closest signal-to-noise value as the one in the image plane, we attempt to align the projected redshift to the MUSE resampling wavelength to make sure that the z_s is the closest value to the $(\lambda_{sampling}/\lambda_{Ly\alpha}) - 1$. The number of source plane projections depends on the number of redshift values used for the procedure, the number of MUSE cubes, and the definition of introduced signal-to-noise values. While the number of sources in the sample and the precision of the sampling signal to noise are independent.

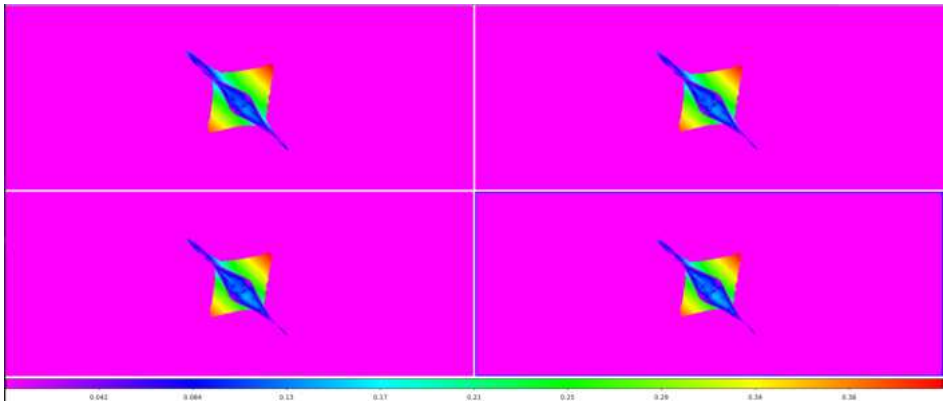

Figure 3.8: A 2D masked image of A2667 in the image plane projected into the source plane at different redshifts. From left to right, up to down, the projected redshift is z_s = 3.5, 4.5, 5.5, and 6.5.

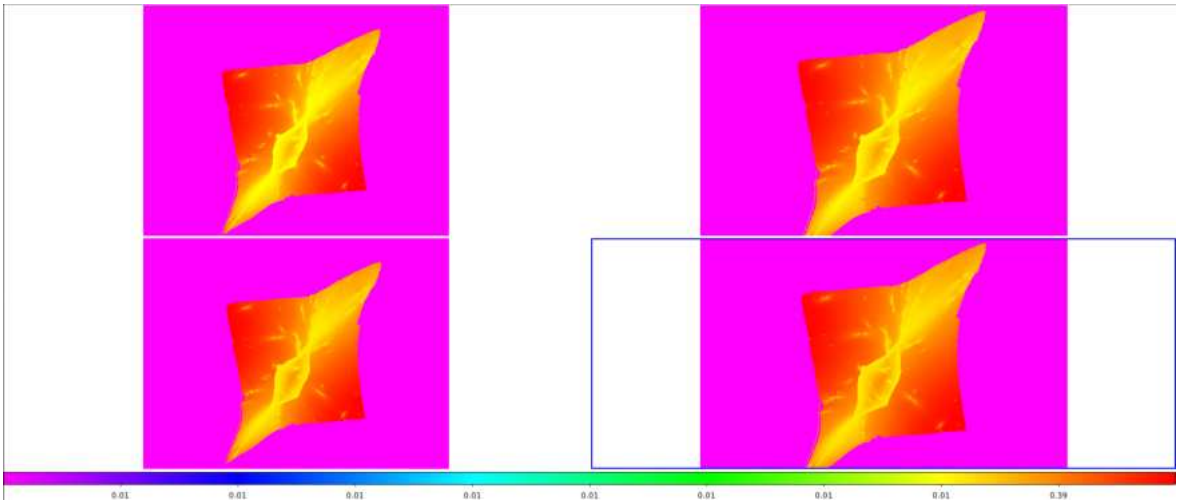

Figure 3.9: A 2D masked image of A2744 in the image plane projected into the source plane at different redshifts. From left to right, up to down, the projected redshift is z_s = 3.5, 4.5, 5.5, and 6.5.

3.2 Computing $V_{\max}$ value

After the projection of the 2D masked images onto the source plane, we compute the $V_{\max}$ value of the sources by associating the proper masks. This is done on the source plane at the pixels in which the value of the magnification exceeds the given limited magnification to make sure that the source can be detected. Therefore, the process will apply to the area with a reasonable magnification. At the parent cube, where the source is present, this limit value is defined as :

$$\mu_{lim} = \mu \frac{\delta F_d}{F_d} \tag{3.7}$$

where μ is weighted magnification, F_d is the detection flux value, δF_d is uncertainty of flux value and μ_{lim} is the limited magnification of individual source. Following the definition of limited magnification value, the source is only detected at the region in which $\mu > \mu_{lim}$, meaning that the signal we are measuring is high enough to be detected. In addition, the procedure is extended to all the other cubes with different seeing values, Eq 3.7 will be rephrased to be adapted with this condition:

$$\mu_{lim,ext} = \frac{< RMS_{ext} >_{x,y,\lambda}}{< RMS_p >_{x,y,\lambda}} \frac{s_{ext}^2}{s_p^2} \times \mu_{lim,p} \tag{3.8}$$

where the subscript p and ext correspond to the parent cube, in which the source is present and the external one refers to other cubes. $< RMS >_{x,y,\lambda}$ is the median value over three axes of the MUSE cube, and s is the seeing value associated with observing condition. The final value of $V_{\max}$ is integrated over the individual layers of the 3D source plane masked cube, accounting for the condition of the limited magnification $\mu > \mu_{lim}$. At a given channel the value is estimated following the equation:

$$dV_k = N(\mu_{lim}, k) \times \omega \frac{c}{H_0} \int_{z_{min}(k)}^{z_{max}(k)} \frac{D_L^2(z')}{(1+z')^2 E(z')} dz' \tag{3.9}$$

where $E(z) = \sqrt{\Omega_m (1+z)^3 + (1-\Omega_m - \Omega_\Lambda)(1+z)^2 + \Omega_\Lambda}$, D_L is the luminosity distance following the function of redshift, ω is the angular size of the MUSE pixel, $z_{min}(k)$ and $z_{max}(k)$ are the redshift limits at k^{th} channel with respect to its spectral width, and

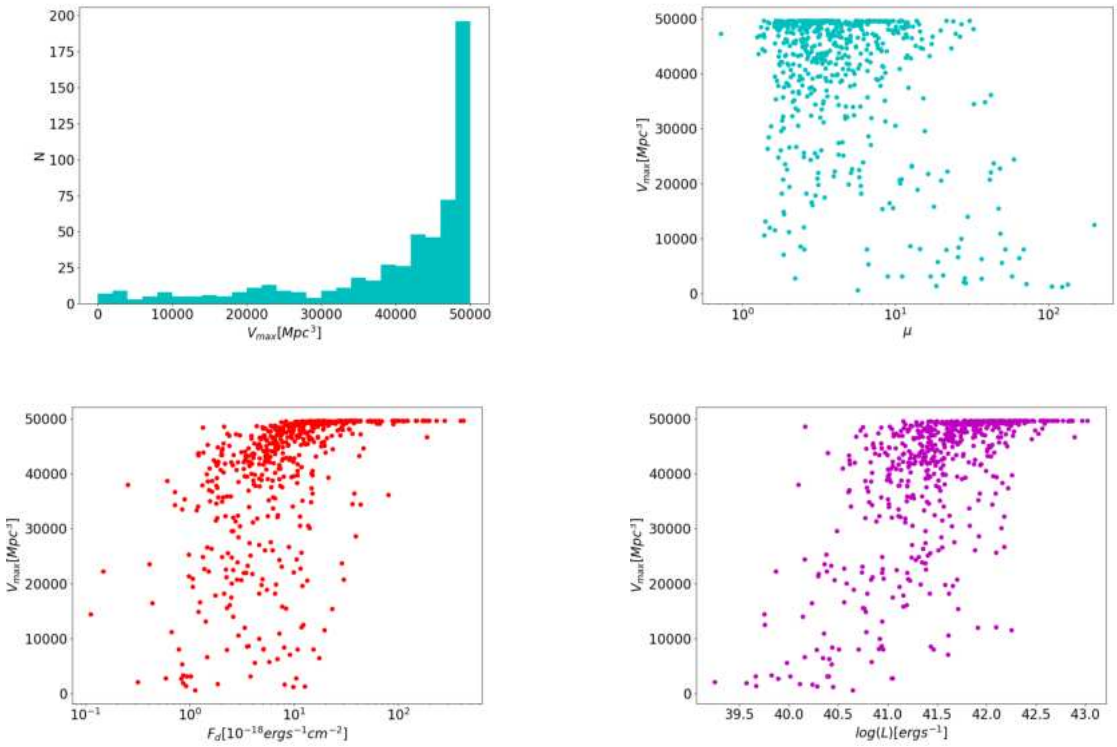

Figure 3.10: From left to right up to down: Total $V_{\max}$ distribution of LAEs in the present sample, the $V_{\max}$ versus magnification μ, $V_{\max}$ versus detected flux and $V_{\max}$ versus luminosity $\log(L)$.

$N(\mu_{lim}, k)$ is the number of unmasked pixels on the layer k associated with the condition of limited magnification. This function can be applied to compute $V_{\max}$ value for the full redshift range $2.9 < z < 6.7$, for the effective volume defining the region from the lowest redshift of the survey to the redshift value of the source.

From Fig. 3.10, most of the sources in the present work have been detected with a large value of the volume. However, several sources have a large magnification detected in a small volume. The $V_{\max}$ value tends to raise with the detection flux, this can be seen in the lower left panel of Fig. 3.10. This trend also can be seen on the lower right panel of that figure, which shows a weak correlation between luminosity and its $V_{\max}$ value.

The dependence of $V_{\max}$ on source magnification is shown in Figs. 3.11 and 3.12. For the highly magnified sources, that may be close to the caustic curve, its magnification deviation value varies largely when the source crosses the line, the uncertainties may reach up to 10% or more compared to its weighted value. When the magnification value is changed within its uncertainties, an exponential function can be used to describe this change. As the source has a modest magnification value, a linear function can be presented. This dependence of $V_{\max}$ on lensing magnification has been accounted for in the LF computation process.

The total co-moving volume computed following the procedure mentioned above is listed in Tab. 3.1.

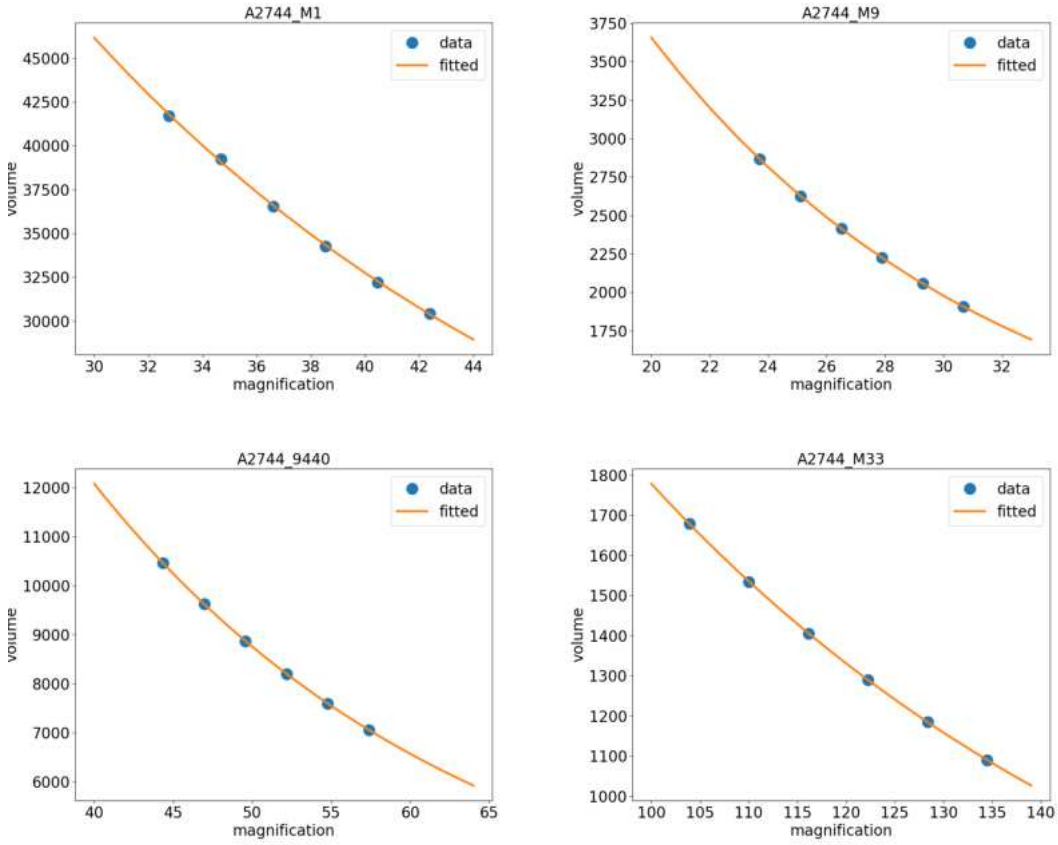

Figure 3.11: Dependence of $V_{\max}$ on the magnification value of the source, which has a highly magnified value when magnification is varied within its uncertainties $\pm 1\sigma$ and $\pm 2\sigma$. The blue points from left to right denote the $\mu - 2\sigma, \mu - 1\sigma, \mu, \mu + 1\sigma, \mu + 2\sigma, \mu + 3\sigma$, respectively. The orange solid line displays the best-fit exponential function.

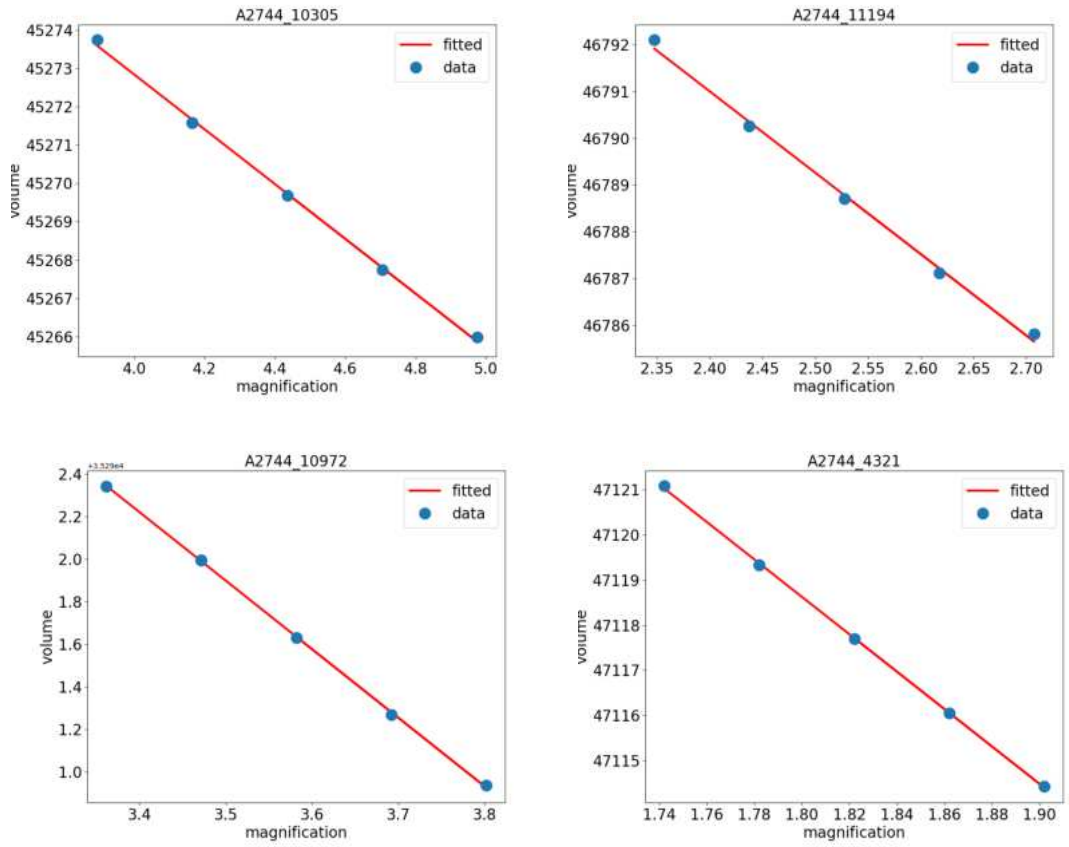

Figure 3.12: Dependence of $V_{\max}$ on magnification of the sources which have a low magnified value when magnification is varied within its uncertainties 1σ and 2σ. The blue points from left to right denote the $\mu-2\sigma, \mu-1\sigma, \mu, \mu+1\sigma, \mu+2\sigma$, respectively. The red solid line displays the best fit linear function of these blue points.

Cluster	Total co-volume [Mpc^3]
A2390	735
A2667	885
A2744	10500
A370	5350
AS1063	1970
BULLET	895
MACS0257	730
MACS0329	1225
MACS0416N	3420
MACS0416S	1670
MACS0451	1210
MACS0520	765
MACS0940	5760
MACS1206	2980
MACS2214	1100
RXJ1347	7920
SMACS2031	1675
SMACS2131	920
Total	49710

Table 3.1: Total co-volume of 17 clusters at redshift $2.9 < z < 6.7$.

4 Luminosity function

Contents

By definition, the LF is defined as the number of galaxies per a cosmic co-moving volume and a luminosity interval. However, not all the sources in the data sample can be 100% detectable, hence the requirement to correct for the actual probability of finding a source, which is called completeness. In this case, the (in)completeness is an additional correction which is needed to account for the detectability of a source in its parent MUSE cube. It is applied as a multiplicative factor to its previous contribution to the LF (see Sec. 4.2 and Eq. 4.1 below). In the following sub-sections, we present and discuss the determination of the completeness factors for each source, the determination of the LF values, and the fit of the LF points by a Schechter Function. We also discuss the comparison between our results and the previous ones in the literature.

4.1 Completeness determination

In a given noisy environment, the probability of successfully detecting the sources depends on their profiles both spatially and spectrally. This means that sources with too large of the noise are not detected. In this section, we introduce a parameter referring to this probability aiming to account for the noise effect. The process to estimate this parameter is conducted in the image plane and applied from source to source to retrieve the detection profile of each LAE and inject it into the masked detection layer. The final completeness value is estimated based on the number of successful outcomes divided by the total number of random injections of the source profile into a mock image.

4.1.1 Reconstruction of the source profile in image plane

The effect of noise on the probability of source detection will be investigated in the image plane where the source has been found first. In the previous steps, the source is always associated with a given channel in a MUSE cube corresponding to a given noise level. As a result, in this section, the probability that I mentioned before should be calculated in the plane where the Lyman alpha emission of the source reaches its peak, called the max-NB image. This image should not be tracked from the redshift of the source, because in some

Flag value	MIN_AREA	DETECT_THRESH	MATCHING_RADIUS
1	6	1.3	4
1	3	2.5	4
1	6	1.1	4
2	6	1.0	4
2	6	1.0	5
2	6	0.9	5
2	5	0.9	5
2	6	0.8	5
2	5	0.8	5
2	6	0.8	6
2	5	0.8	6
2	4	0.8	5
3	5	0.8	7
3	5	0.7	7
3	2	0.3	4

Table 4.1: Flag values based on a set of SExtractor parameters used for source recovery simulation.

cases there is an offset between the channel which is retrieved from redshift and the one found from the visual source inspection process. For several faint sources, with a complex morphology that varies from channel to channel, the difference in the selection NB layer could be the reason for the underestimation of the probability. The main difficulty is to properly model the light distribution both in the spatial and the spectra dimensions. To assess the quality of the detections, we use the same NB image which is extracted from the source inspection step. To have a more efficient accounting for the noise, the image of the individual source is sized by 80" × 80", to better account for the local noise in the source region. The source recovery is done based on two steps using the same criteria as the original source detection by using the same configuration/parameters of Source Extractor in the MUSELET package.

- From the max NB image of individual sources we run the Source Extractor using the same configuration of the MIN_AREA, DETECT_THRESHOLD, and MATCHING_RADIUS aiming to retrieve the segmentation image of the source. These parameters have been progressively loosened to make sure that the source has maximum opportunity to be detected.

- On the other side, we continue running the Source Extractor on the max NB image aiming to obtain the filtered image, that is background subtracted and convolved with different seeing values.

From the segmentation map, we have tried to match the positions in which the source has been detected (in the segmentation image) to the positions in the filtered image. Sometimes the Source Extractor does not work properly when creating the segmentation map image for faint sources. To compensate for this effect, we will search for the connected pixels in the filtered image. Finally, a sub-image containing all the pixels which have been assumed as a part of the source will be kept and matched to the object image to form the source profile in the image plane of individual sources.

The quality of the extraction process for individual sources has been quantified using a flag value. As shown in Table 4.1, trustworthy cases are assigned values Flag=1 or Flag=2, whereas a source denoted Flag=3 could be treated as a tentative detection. In the following steps, we keep only the good extractions (Flag=1,2) and ignore the dubious cases.

Applying these criteria to the data sample behind 17 lensing clusters, only 2% sources are marked Flag = 3, 5.5% cases are marked Flag = 2, and the rest are Flag = 1. The appearance of Flag = 3 could be explained by:

+ They are the faint sources, which have only a few pixels having a value above the given threshold to be considered as a part of the source.

+ There is a difference between the source position found in the catalog and the recovered source position. In practice, the morphology of the source varies from channel to channel, the difference in position between the recovered location and source position in the max-NB channel may be larger than in the other neighbor channels.

+ The size of the image is such that the exploration region is too small to provide a fair sampling of the background. In this work, we have faced several such cases, and for this reason, the size of the window has been enlarged from 30" × 30" used by DLV 2019 to 80" × 80". This results in a significant increase of the Flag=1,2 images with respect to the smaller window. For a source size of 30" × 30", 80% of the sources are marked Flag = 1,2 and the rest are Flag = 3. If we use this condition, we reject 20% of sources that belong to the faintest luminosity bins.

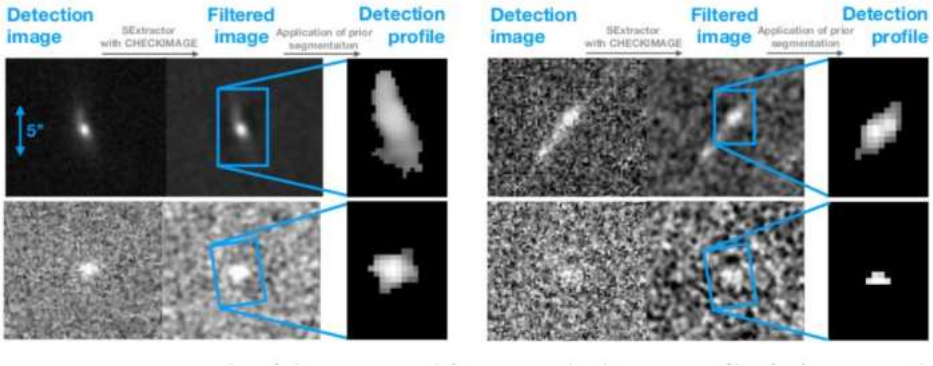

Figure 4.1: Detection profiles of four different LAEs. For each LAE case, from left to right, is the max-NB image, filtered image, and detection profile. A2390-96, a bright source (upper left), A2667-30, a bright but diffuse source (upper right), A2744-2956 (lower left), and A2744-12- 26, a faint source (lower right). All images are shown in the same spatial scale. Credit: Vieuville 2019.

4.1.2 Source recovery

In this section, I use the source profile found in the last subsection to obtain the simulated source profile in the image plane. The advantage of using the source profile is that it takes into account both the spectral profile and spatial profile of the LAE. To recover the source, we inject the source profile into a mocked image, which is built based on its max NB image (see Vieuville 2019 for details). We run Source Extractor on that image and count the number of successful detections. This is different from the previous steps when we ran the Source Extractor on the whole MUSE cube.

We have created a mock image for each LAE, which has been built based on its masked max NB image. This image is tracked following the previous steps using the SN value of the source in its detected layer in the MUSE cube. The injection is done only in pixels that are unmasked to make sure that the completeness value is properly taken into account.

The source profile is injected randomly 500 times on the mock image, each time the source is placed, the pixels are masked to avoid dominating too much at a given position or overlapping with other mock sources, and a new NB image will form. It asks Source Extractor to run using the same values of MIN_AREA and DETECT_THRESH. We match the detected source position in the catalog, which is created by Source Extractor to the input source position. If the distance between the two positions is less than 0.8", then the process is considered successful. The final completeness value is defined by the ratio between the number of recovered sources and the number of injected sources. The uncertainty in the completeness value of an individual source is estimated in the same way, the distribution of the recovered fraction provides the uncertainty value.

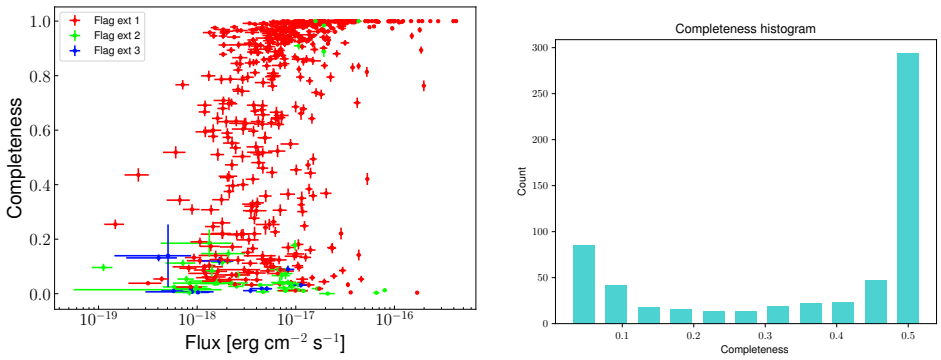

Figure 4.2: Left: Completeness vs. detection flux of LAEs from the present sample. Different colors indicate the quality of extraction from SExtractor. Only sources in the unmasked regions of the detection layer are considered here. Right: A completeness histogram for the sources used for the LF computation.

4.1.3 Discussion

Fig. 4.2 (left) displays the final values of completeness versus the detection flux of individual LAEs in the present data sample. The faintest sources have very low completeness and large uncertainty values, while the bright ones often have very high completeness and small uncertainty values. The appearance of Flag = 2 sources with low detection flux can be attributed, in part, to the population of faint extended sources. Although, the integrated flux of these sources in the max NB image is not high, a sufficient number of pixels meet the detection conditions. Consequently, these sources are still assigned of flag value of 2. I recall that for the rest of the work, we only use sources having Flag = 1,2. Fig. 4.2 (right) shows the completeness distribution. A large number of sources has completeness value greater than 50%. In most works dealing with the LF in lensing fields, all the images/sources are kept in the sample irrespective of their completeness values (that is, applying Equation 4.1 below without any restriction). For this reason, here we keep as many sources as possible by rejecting only sources having completeness values below 1%. This is discussed in more detail below. Note that DLV 2019 rejected sources with completeness below 10%, making this comparison more difficult.

Fig. 4.4 shows the measured fluxes of LAEs versus their redshift. Fig. 4.4 (left) displays the normal case of noise evolution, while Fig. 4.4 (right) shows an abnormal case of noise evolution with a clumpy appearance surrounding $z \sim 3.7$, corresponding to a wavelength of ~ 5500 Å. The low-completeness sources are the faintly detected flux ones, while the high-completeness sources seem to be detected with high signal-to-noise. These features are visible in the figure. However, some sources have high detection fluxes

and low completeness values, suggesting that source morphology is important, as already mentioned above.

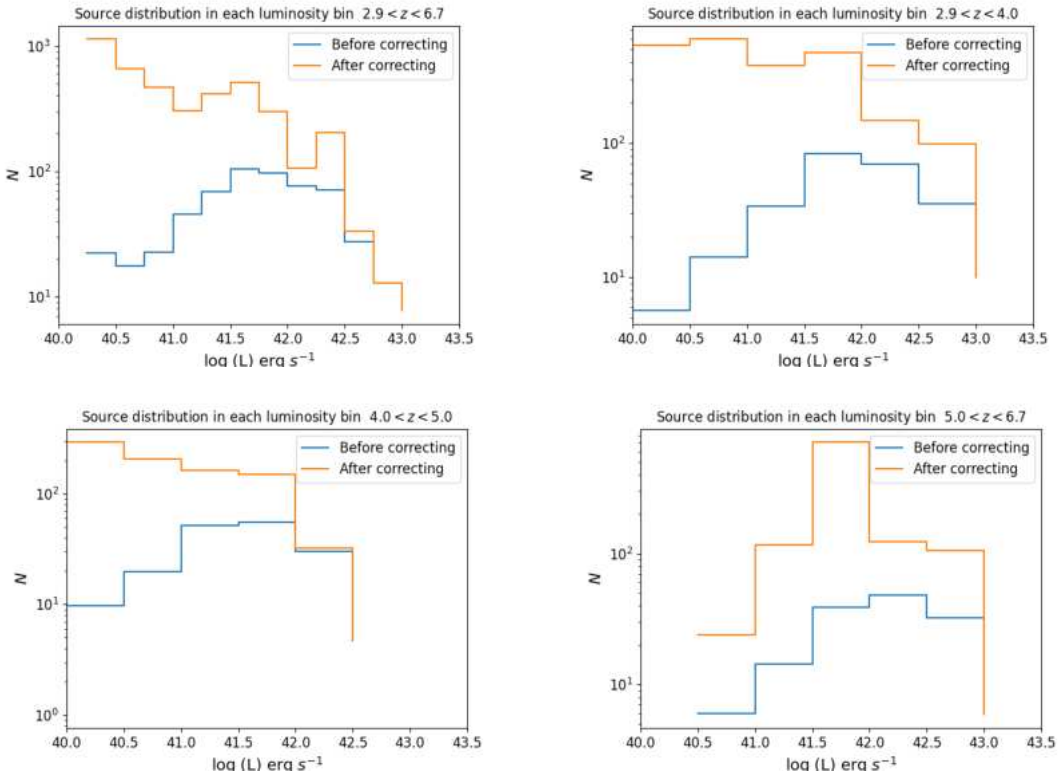

Figure 4.3: Source distribution in each luminosity bin before and after correction for the completeness value. From left to right, up to down is the distribution at redshift $2.9 < z < 6.7$, $2.9 < z < 4.0$, $4.0 < z < 5.0$, and $5.0 < z < 6.7$.

Fig. 4.3 displays the number of sources distributed in each luminosity bin before (blue line) and after (orange line) correction for the completeness values at 4 redshift ranges $2.9 < z < 6.7$, $2.9 < z < 4.0$, $4.0 < z < 5.0$, and $5.0 < z < 6.7$. At lower luminosity bins, most of the sources are faint ones with low completeness values. Therefore, when we correct for completeness, the number of sources should be detected in the cube increasing significantly. In contrast, the higher luminosity bins contain a large number of sources having a high completeness value, so the corrections do not have a strong impact.

4.2 LF computation

This section presents how to compute LF points in each luminosity bin after obtaining completeness and $V_{\rm max}$ of individual sources. In each luminosity bin, the value is defined as follows:

$$\Phi(L_i) = \frac{1}{\Delta \log L_i} \sum_j \frac{1}{C_j V_{\rm max,j}} \tag{4.1}$$

where the index i defines the luminosity bin i^{th}, index j corresponds to the source j in the data sample, C_j and $V_{\rm max,j}$ are the completeness and $V_{\rm max}$ of the j source, $\Delta\log(L_i)$ refers to the width of luminosity bin i^{th} in logarithmic scale. To check the possible evolution of LF with redshift, we use four redshift ranges: $2.9 < z < 6.7$, $2.9 < z < 4.0$, $4.0 < z < 5.0$, and $5.0 < z < 6.7$. We refer to these ranges as z_{all}, z_{35}, z_{45}, and z_{60}, respectively. The

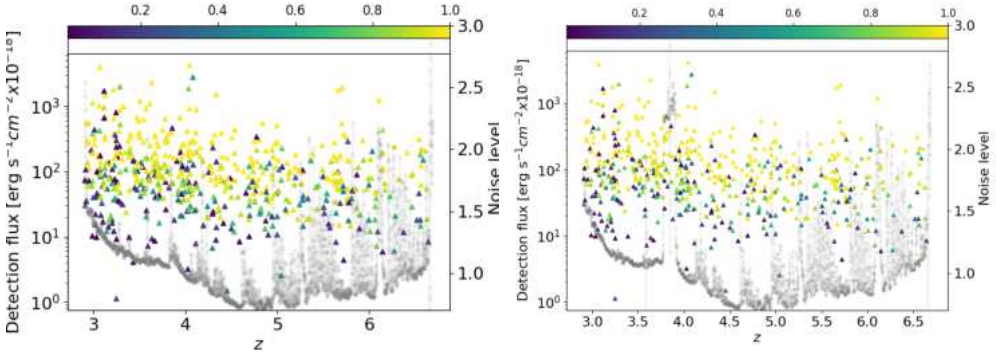

Figure 4.4: Detection flux vs redshift for all sources in the present sample. The color bar on the top shows the completeness value of each source in the sample. The grey points show the evolution of noise level as a function of wavelength/redshift or cluster A2667 on the left and AS1063 on the right.

luminosity bin width has been used as a normalization factor to study the density of the sources in a given co-moving volume and a given luminosity value. However, the number of sources in the faintest luminosity regime decreases quickly, so there may not be enough sources to populate the faintest luminosity bins. For this reason, in the global redshift interval, we divide the explored range into 12 luminosity bins with a width of 0.25, except for the faintest bin, which has a width of 1.25 to have a homogenous source distribution in each luminosity interval. This is applied to other redshift ranges with a larger width of 0.5 covering a luminosity range from 39.0 to 43.0, 39.0 to 43, and 40.0 to 43.0, with respect to the z_{35}, z_{45}, and z_{60}. To estimate the mean and the uncertainty of the LF values, we have employed an MCMC method that takes into account the contributions of completeness, flux measurement, and magnification of individual LAE in the data sample. We compute the LF for each of the 20,000 MCMC iterations. At each iteration, the value of completeness and flux are taken randomly within their error values while the magnification is collected from its magnification distribution in the image plane.

Faint sources are often highly magnified and have large magnification uncertainties. During each MCMC iteration, the luminosity of the source is recomputed based on the random input values of the source magnification, completeness, and flux, as described above. This means that the MCMC process may spread the contribution of a faint LAE source to several luminosity bins. On the other hand, bright sources with moderate magnifications only contribute to a given luminosity bin during this process. These features are illustrated in Fig. 4.5. Fig. 4.6 shows the LF results for each of the 12 luminosity bins after 20'000 MCMC iterations, together with the LF face value, which is computed directly based on the observed values of LAEs. The mean and statistical uncertainties of LF points are obtained from these histograms.

Apart from the statistical uncertainty obtained by MCMC process, there are two additional uncertainties that contribute to the total uncertainty of the LF points: cosmic variance, which accounts for the limited field of views of the survey and is derived from the calculations in Trenti et al. 2008, and the Poissonian representation of the source distribution within each luminosity bin. The final uncertainties are written under the form:

$$\Delta\Phi(L_i)^2 = \frac{1}{\Delta log L_i} \frac{N_{i,c}}{< V_{max} >} \sqrt{\delta_{CV}^2 + \left(\frac{1}{\sqrt{N}}\right)^2 + \delta_{MCMC}^2} \tag{4.2}$$

where δ_{CV} refers to the cosmic variance uncertainty, δ_{MCMC} is the MCMC uncertainty, $N_{i,c}$ is the number of LAEs after correcting for their completeness values in i^{th} bin,

$< V_{\max} >$ is the average value of $V_{\max}$ in i^{th} bin. The Poissonian uncertainty represents the bias of source distribution in each luminosity bin referred by $1/\sqrt{N_i}$.

Fig. 4.7 shows the total LF uncertainties for different luminosity bins and redshift ranges. It raises the important point that the LF face values obtained directly from observations are subject to large uncertainties, as they may not reflect the "true" values. This shows the importance of properly taking into account different sources of uncertainties when computing the LF.

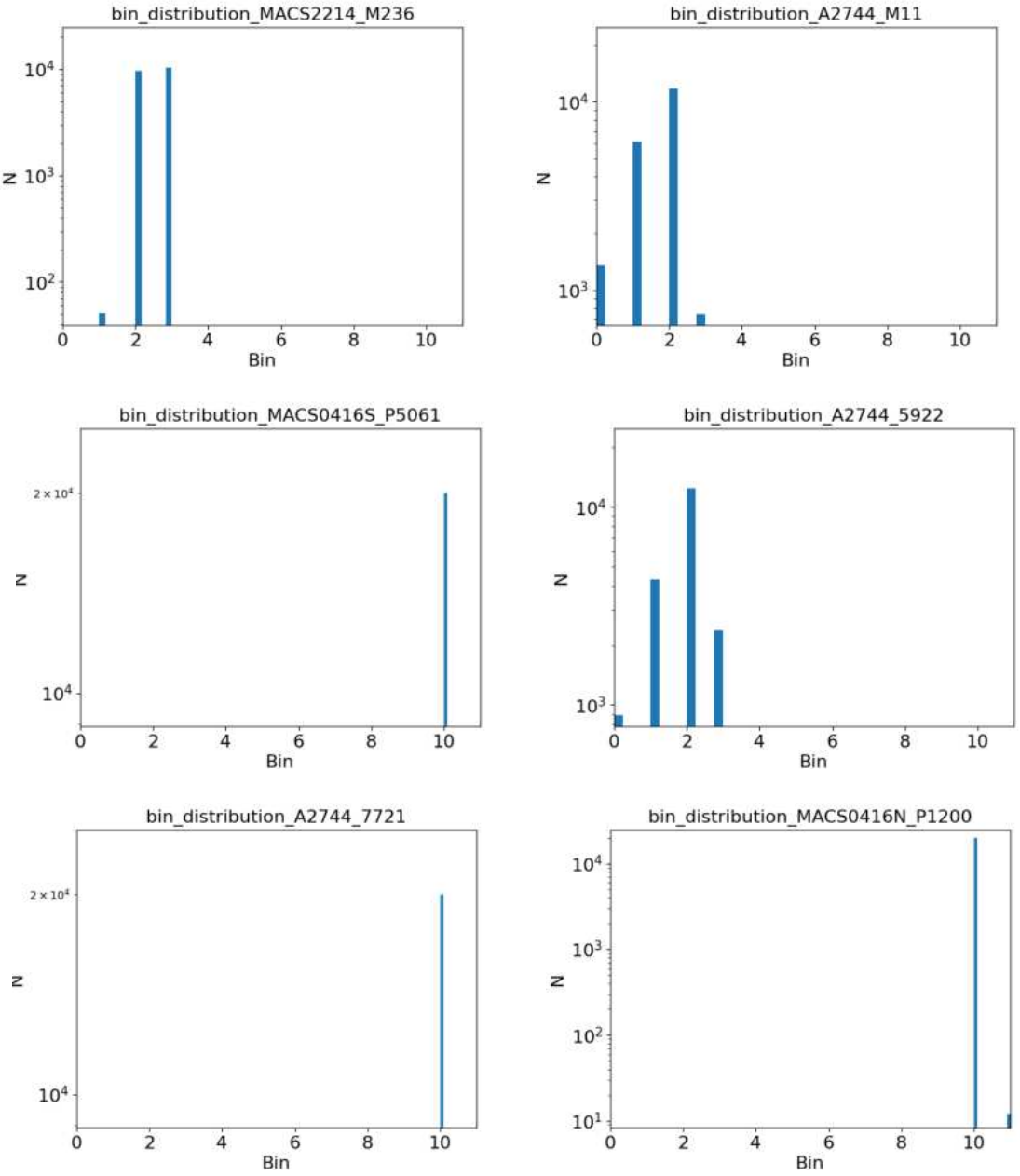

Figure 4.5: Illustration of the contribution of a given source to the luminosity bin during the MCMC process, when completeness, detected flux, and magnification are varied within $1-\sigma$. The ordinate shows the number of sources in the simulation (20'000 in total), and the abscissa shows i^{th} luminosity bins from the faintest bin (0) to the brightest bin (11). Each panel represents an individual source in one cluster field. Sources contributing to the brightest luminosity bins exhibit little dispersion, whereas sources contributing to the faintest bins are spread into several luminosity bins.

Table 4.2: Luminosity bins and LF points used for Fig. 4.13

log (L) [erg s^{-1}]	log $(\phi)(\Delta(\log(L))=1)^{-1}$[Mpc^{-3}]	$< N >$	$< N_{corr} >$	$< V_{\max} >$ [Mpc^3]
2.9<z<6.7				
39.00<39.63<40.25	$-0.68^{+0.04}_{-0.35}$	22.4	706.0	11827
40.25<40.38<40.50	$-0.40^{+0.04}_{-0.39}$	17.6	645.4	15074
40.50<40.63<40.75	$-0.17^{+0.16}_{-0.95}$	22.8	429.3	28457
40.75<40.88<41.00	$-0.71^{+0.06}_{-0.68}$	45.2	301.5	31613
41.00<41.13<41.25	$-0.83^{+0.19}_{-0.45}$	68.9	415.7	37344
41.25<41.38<41.50	$-0.96^{+0.03}_{-0.33}$	105.0	547.9	41321
41.50<41.63<41.75	$-1.17^{+0.07}_{-0.19}$	96.4	305.5	42227
41.75<41.88<42.00	$-1.88^{+0.09}_{-0.11}$	76.4	105.1	46139
42.00<42.13<42.25	$-1.51^{+0.07}_{-0.09}$	70.4	202.5	45795
42.25<42.38<42.50	$-2.43^{+0.24}_{-0.29}$	27.5	33.5	47554
42.50<42.63<42.75	$-2.98^{+0.13}_{-0.19}$	12.9	13.0	49295
42.75<42.88<43.00	$-3.20^{+0.15}_{-0.25}$	7.7	7.8	49258
2.9<z<4.0				
39.00<39.63<40.00	$-0.15^{+0.07}_{-0.52}$	6.64	415.33	1712
40.00<40.25<40.50	$-0.10^{+0.13}_{-0.62}$	14.19	920.22	6114
40.50<40.75<41.00	$-0.85^{+0.09}_{-0.22}$	34.0	396.17	11397
41.00<41.25<41.50	$-1.08^{+0.07}_{-0.10}$	83.7	473.6	14529
41.50<41.75<42.00	$-1.01^{+0.08}_{-0.14}$	69.5	148.0	15914
42.00<42.25<42.50	$-1.53^{+0.06}_{-0.11}$	35.6	101.55	16327
42.50<42.75<43.00	$-2.93^{+0.15}_{-0.23}$	10.0	10.0	17320
4.0<z<5.0				
39.00<39.25<39.50	$-0.93^{+0.30}_{-1.91}$	1.0	38.0	730
39.50<40.00<40.0	$-1.16^{+0.11}_{-0.22}$	2.4	48.3	4904
40.0<40.25<40.5	$-0.38^{+0.09}_{-0.50}$	7.4	311.4	3159
40.5<40.75<41.00	$-0.38^{+0.11}_{-0.88}$	19.6	205.1	7662
41.00<41.25<41.50	$-1.43^{+0.10}_{-0.14}$	51.4	161.2	11044
41.50<41.75<42.00	$-1.48^{+0.1}_{-0.15}$	55.0	148.5	12164
42.00<42.25<42.50	$-2.30^{+0.13}_{-0.18}$	30.0	32.2	13182
42.50<42.75<43.00	$-3.15^{+0.20}_{-0.42}$	4.7	4.8	13433
5.0<z<6.7				
40.00<40.25<40.50	$-1.55^{+0.20}_{-0.45}$	6.0	23.8	4725
40.50<40.75<41.00	$-0.89^{+0.24}_{-1.08}$	14.3	116.5	11105
41.00<41.25<41.50	$-0.66^{+0.15}_{-0.43}$	38.9	705.5	13545
41.50<41.75<42.00	$-1.52^{+0.19}_{-0.39}$	48.2	122.9	16190
42.00<42.25<42.50	$-1.63^{+0.09}_{-0.11}$	32.3	105.2	16705
42.50<42.75<43.00	$-3.19^{+0.2}_{-0.37}$	5.9	5.9	18542

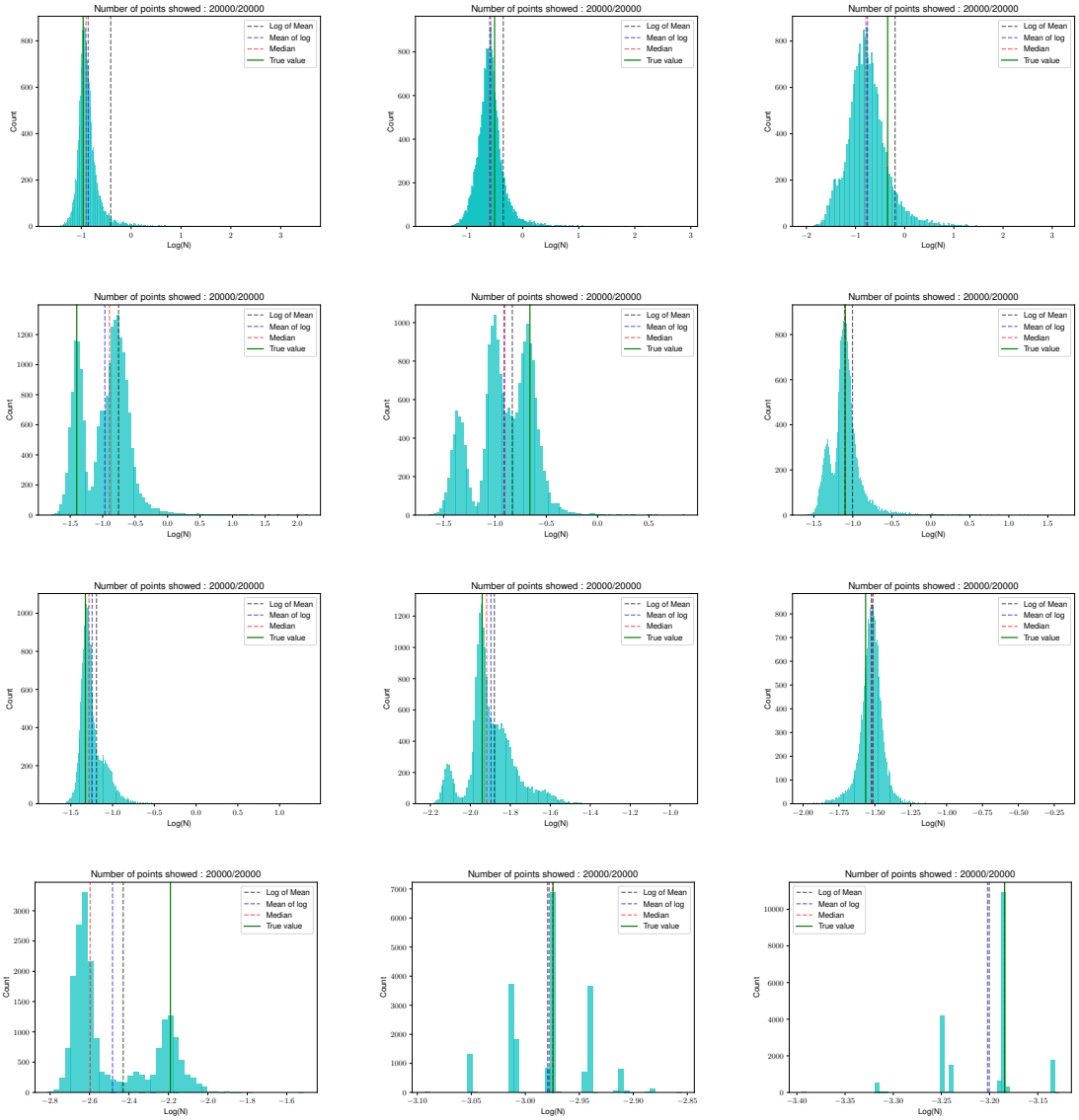

Figure 4.6: From left to right, up to down: LF histograms of each of the 12 luminosity bins (for the global redshift range) obtained from 20'000 MCMC iterations. Their median, median of log and log of the median are shown together with the face value.

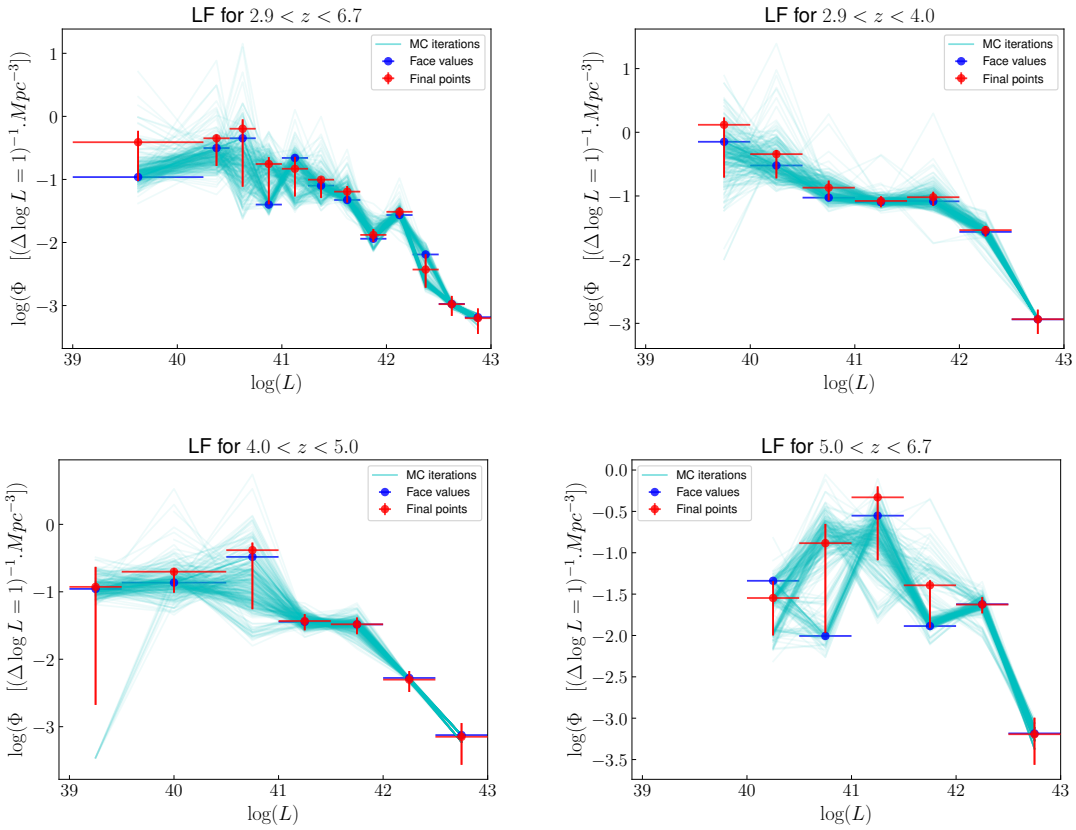

Figure 4.7: LF points in each luminosity bin at four redshift ranges obtained after 20'000 MCMC iterations are shown by the cyan lines together with face value LF found from all the Lyman alpha sources in the final data sample. The final uncertainties of LF points have already accounted for the statistical, Poissonian, and cosmic variance uncertainties.

4.2.1 Binning effect on the LF points

One factor that may affect the shape/evolution of LF at different redshift bins is the width of the luminosity bins, from that it may affect the source density measured in each bin. This can be tackled by testing the stability of the results obtained with different bin widths, as presented in this subsection.

Fig. 4.8 displays the effect of luminosity binning on the shape of the LF evolution. At redshift z_{all}, we have divided into six groups corresponding to six different bin sizes of luminosity and recompute LF values with respect to each bin. This also has been applied to other redshift ranges z_{35}, z_{45}, and z_{60}. The results show that the evolution of the LF does not significantly depend on the binning, as can be seen at low redshift ranges z_{all} and z_{35}. But in the higher redshift range, which contains fewer sources, the shape may vary a bit (Fig.4.8 bottom right). The figure also shows the changes in uncertainty values allocated in each luminosity bin during the tests. Independently of the binning tests, we find that the contribution of cosmic variance to the total uncertainty budget is about 15 to 20% at redshift z_{all} and 15 to 30% at other redshift ranges. The MCMC uncertainty significantly dominates at the lower luminosity bins, where the magnification and completeness uncertainties are larger compared to the bright luminosity bins. The Poissonian uncertainty becomes the main contributor at the highest luminosity bins with a smaller source density. There is a drop at $\log L = 42$ erg s^{-1}, this causes by an appearance of a low completeness source contributed to the previous luminosity bin.

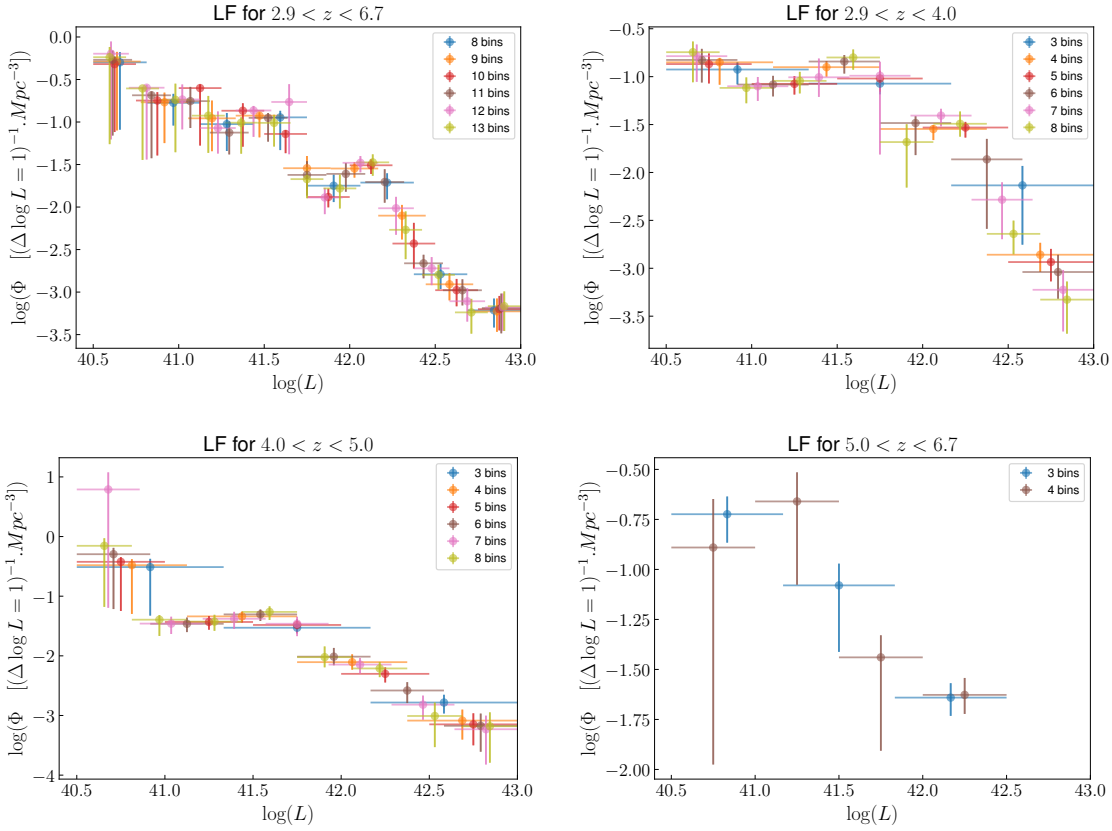

Figure 4.8: The LF points in each redshift range using different luminosity bin sizes.

4.2.2 Effect of source selection to the evolution of LF points

As I mentioned earlier, in this work we only use LAEs that have been identified with a high secure $zconf = 2,3$, and reject the ones having a lower rate $zconf = 1$. In this subsection, I include the sources which are treated as a lower quality to the final data sample and investigate their effect on the shape of the LF. It is worth noting that $zconf = 1$ objects have a tentative redshift assigned, with ~50% chances has been corrected. There are typically two different cases for $zconf = 1$ LAEs: faint detections with low SNR, or higher SNR detections with an ambiguous identification of a unique line. LAEs belonging to multiple imaged systems have $zconf = 1$ because of lensing considerations, making the redshift determination more secure.

Before including all of the $zconf = 1$ sources, we have made a small test on the sources observed from RXJ1347 to probe their effect and decide what we should do in the next steps. Indeed, there are 46 LAEs listed as $zconf = 1$ in this cluster observed with a shallower exposure time, that is two hours in the extended region and three hours in the central one. Most of these $zconf = 1$ LAEs are single-imaged, with a relatively small magnification value. Applying the same procedure and same criteria as the $zconf = 2,3$ sources we found that the completeness values of these sources are very small. The faintest sources are the ones having a poor extraction quality which are marked by Flag = 2, 3 in Fig. 4.9. In addition, we find that more than half of the sources have completeness below 10%. Combining these results with the information on the definition of $zconf = 1$ leading to a final decision, we don't have 100% confidence to say that they are real LAEs detected from the cube.

Based on the preliminary results, I have performed two tests to estimate the effect of source selection on the final results. One includes half of $zconf = 1$ and the other is adding

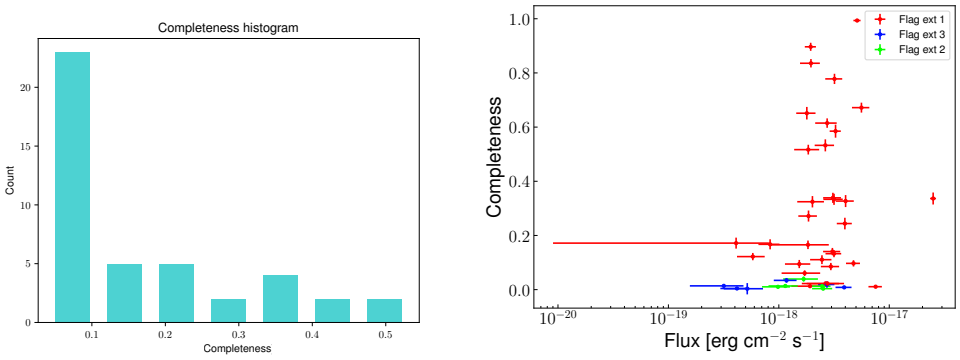

Figure 4.9: Left: Completeness histogram of LAEs ($zconf = 1$) behind RXJ1347. Right: Completeness versus the measured flux of $zconf = 1$ sources behind RXJ1347.

all the $zconf = 1$ to the final data sample. In both cases, when adding the $zconf = 1$ LAEs, the assigned values for the completeness and $V_{\rm max}$ in each luminosity bin were taken from the median values of $zconf = 2,3$ sources in the same bin. This was also applied for the uncertainty values of completeness and $V_{\rm max}$ of the $zconf = 1$ sources, meaning that these values of $zconf = 1$ sources were set equal to the $zconf = 2,3$ sources corresponding to that bin.

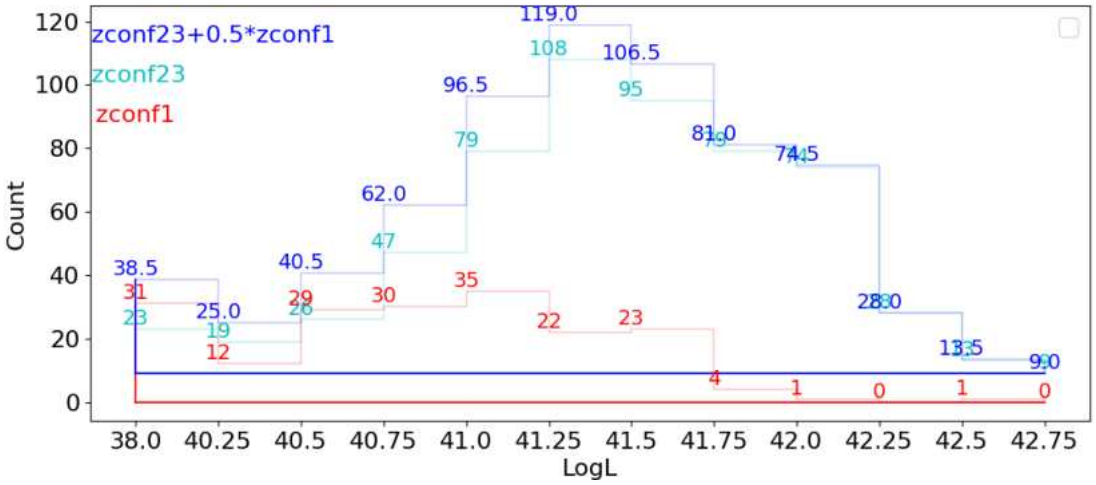

Figure 4.10: Source distribution in each luminosity bin when $zconf = 1$ sources are taken into account.

Fig. 4.10 shows the relative contribution of $zconf = 1$ sources to each luminosity bin. At the faint end ($\log L < 41.25$ [erg s^{-1}]), the number of $zconf = 1$ is similar to the number of the $zconf = 2,3$ whereas, the appearance of $zconf = 1$ sources at the bright end is almost zero. With the assumptions given above, we find that there is no effect of $zconf = 1$ sources on the shape of the LF and its uncertainty values at the bright end. On the contrary, there is a small variation towards the faint end. Fig. 4.11 shows the results of the LF points when incorporating half (blue) and all (red) $zconf = 1$ sources into the data sample. It again confirms that the source selection effect does not significantly affect the obtained LF shape, especially at the faint end. These results are later used to estimate the systematic uncertainties associated with the faint-end slope.

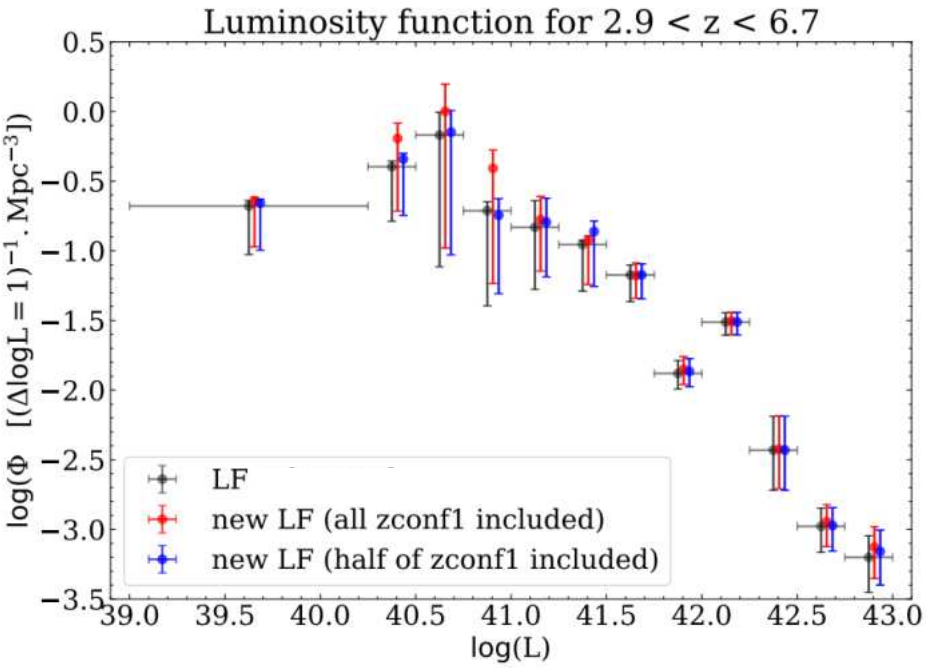

Figure 4.11: LF points in each luminosity bin when half and all the $zconf = 1$ sources have been included in the data sample.

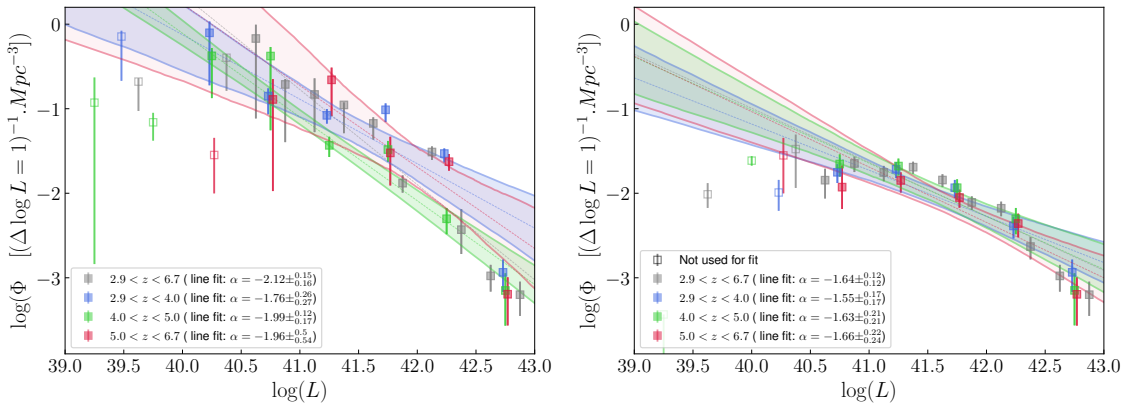

Figure 4.12: Faint end slope of LF at four redshift ranges $2.9 < z < 4.0$ (blue), $4.0 < z < 5.0$ (green), $5.0 < z < 6.7$ (red), and $2.9 < z < 6.7$ (black) when 1% completeness cut (left) and 10% completeness (right) cut have been applied. These fits use only our LF points constructed from the current sample. The open squares are not included in the fit.

4.3 LF results and comparison to the literature

To investigate the evolution of LF with redshift, we performed a simple linear fit to the slope on our LF value in four redshift ranges: one covers all the data sample and three others are sub-ranges corresponding to $2.9 < z < 4.0$, $4.0 < z < 5.0$ and $5.0 < z < 6.7$. These results are shown in Fig. 4.12. The open squares at the faint end are not included in the fit. They are often associated with sources that have low completeness, low luminosity, or too high magnification values. In these cases, they are considered less reliable for simple linear fitting. We will discuss the possibility of taking these points into account for Schechter fits later. The best-fit results are plotted in four redshift ranges with a 68% confidence region,

Redshift range	1% completeness cut	10% completeness cut
$2.9 < z < 6.7$	$-2.12^{+0.15}_{-0.16}$	$-1.64^{+0.12}_{-0.12}$
$2.9 < z < 4.0$	$-1.76^{+0.26}_{-0.27}$	$-1.55^{+0.17}_{-0.17}$
$4.0 < z < 5.0$	$-1.99^{+0.12}_{-0.17}$	$-1.63^{+0.21}_{-0.21}$
$5.0 < z < 6.7$	$-1.96^{+0.50}_{-0.54}$	$-1.66^{+0.22}_{-0.24}$

Table 4.3: Comparison slope values obtained from linear fitting using different completeness thresholds.

shown as a shaded region. It is worth mentioning that, due to lacking statistics in the faint luminosity bins, the width in such cases is larger compared to the others. The final slope values of the LF are $-2.12^{+0.15}_{-0.16}$, $-1.76^{+0.26}_{-0.27}$, $-1.99^{+0.12}_{-0.17}$ and $-1.96^{+0.5}_{-0.54}$, corresponding to the redshift range z_{all}, z_{35}, z_{45} and z_{60}. Our results confirmed that there is no evolution of the slope with the redshift, which has been mentioned in previous literature, specifically the work of DLV19, that focused on the LF at redshift $3 < z < 7$.

The work has been extended by applying the same completeness threshold (10%) as the one presented in DLV 2019 (Fig. 4.12 right). In both cases, a turnover at $\log L \sim 41$ [erg s^{-1}] is seen. Rejecting sources having completeness below 10% corresponds to repudiating 62 additional sources from the present sample, with 51 of them belonging to the six faintest luminosity bins. This significantly reduces the number of sources in these bins. Comparing the slope value in both cases, there is a noticeable decrease at a higher completeness threshold, i.e., 23%, 22%, 19%, and 16% with respect to the redshift z_{all}, z_{35}, z_{45} and z_{60}. The results are presented in Table 4.3.

4.4 Fitting with of a Schechter function

After having a general view of the linear fitting to the LF points, in this section, I present the procedure to fit our LF points using the Schechter function at four redshift ranges. I compare the results to the literature and discuss the findings. The data used in this work are from lensing clusters, which probe fainter luminosity bins compared to other observations in the blank field. However, the total co-moving volume in the present work is smaller due to being constrained by the magnification. To analyze the LF evolution we use the Schechter function, which is written under the form:

$$\Phi(L)dL = \Phi * \left(\frac{L}{L*}\right)^{\alpha} \exp\left(-\frac{L}{L*}\right)\frac{dL}{L*} \tag{4.3}$$

In the log form, this equation translates into:

$$\Phi(L)dL = \ln(10)\Phi * \left(\frac{L}{L*}\right)^{\alpha+1} \exp\left(-\frac{L}{L*}\right) d(\log L)$$

where $L*$ is the characteristic luminosity parameter when the Schechter function transfers from exponential law at the bright part to the power law at the faint part, α is the slope value of the Schechter function at the faint end, $\Phi*$ is the normalization parameter. The previous studies showed that the characteristic luminosity of the Schechter function is usually around $\log L* \sim 42$ [erg s^{-1}]. Our sample's maximum luminosity of ~ 43 [erg s^{-1}] means that our LF points are less efficient to probe the bright regime. To better constrain the bright part LF, we have used the results from the literature, which cover the same redshift and luminosity ranges as the present work. However, including such numerous data for the fitting could lead to bias that dominates the bright-end data. Therefore, these

data have been averaged with the same size of luminosity bin as in the present work.

We use the Python package $Lmfit$ (Newville et al. 2014) for the fitting process. $Lmfit$ makes use of the Levenberg-Marquardt algorithm to minimize the three Schechter parameters. There are several pieces of literature used as a constraint in the bright part such as:

+) Blanc et al. 2011 investigated the LF of 89 LAEs within a redshift range of $1.9 < z < 3.8$ observed by Hobby Eberly Telescope Dark Energy Experiment Pilot Survey (HETDEX) using the same $V_{\rm max}$ method.

+) Drake et al. 2017 constructed the LF of 604 LAEs covering the same redshift range compared to the present work in which the data were collected in the blank field by MUSE/VLT.

+) Cassata et al. 2011 used data from Vimos-VLT Deep Survey to study the LF of 217 LAEs at redshift $2 < z < 6.62$.

+) Sobral et al. 2018 presented the work with a large number of LAEs of ~ 4000 collected by the Subaru and Isaac Newton Telescope, observed in the ~ 2 deg^2 COSMOS field that covering a luminosity of $42.2 < \log L < 43.0$.

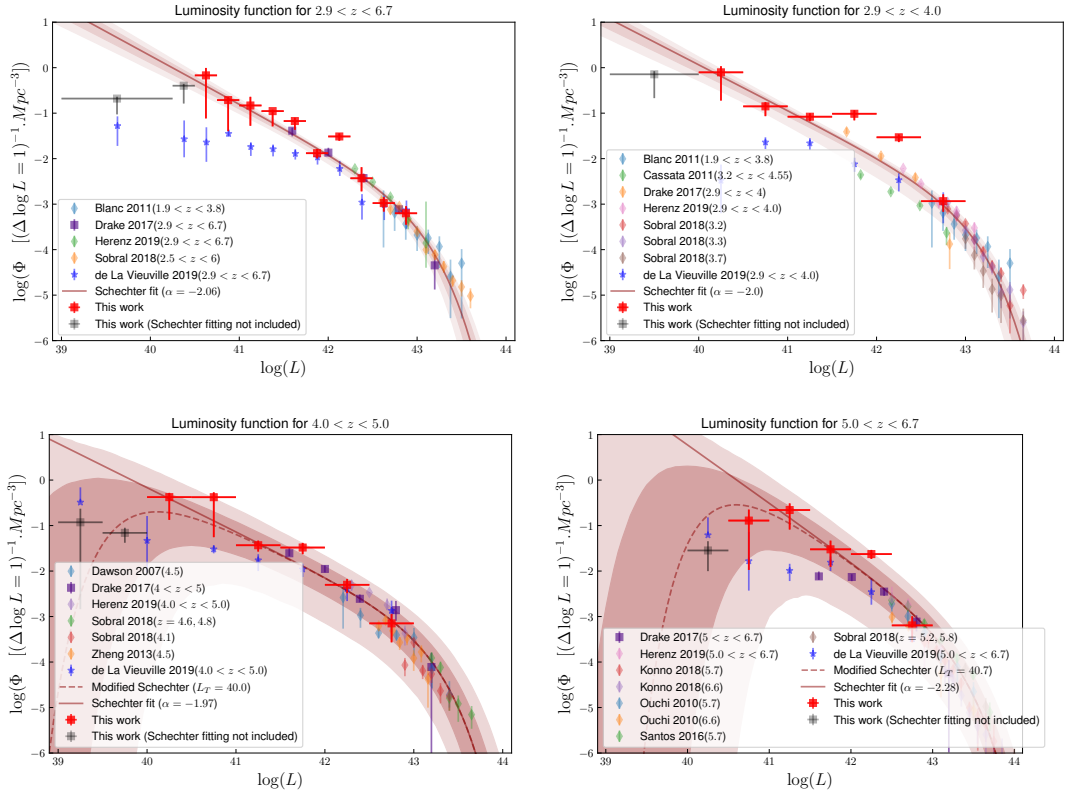

Figure 4.13: Evolution of LF with redshift in different redshift intervals, including previous literature data points. The red squares are the points from the present work. The literature points at the bright end of the LF: Ouchi, Shimasaku, Furusawa, et al. 2010, Sobral et al. 2018, Zheng et al. 2013, Herenz et al. 2019, and Drake et al. 2017 have been used for fitting. The blue points DLV 2019 are shown for comparison purposes only. The best-fit (Schechter function) are shown as solid lines and the 68% and 95% confidence areas as dark red shaded regions, respectively. The dashed lines shown in lower panels are modified Schechter functions to account for a possible turnover at the faintest luminosity bins.

The best-fit results of the Schechter function fitting in four redshift ranges are shown in Fig. 4.13. The best-fit parameters are shown in Table 4.4. The 68% and 95%

Table 4.4: Best fit parameter values for the Schechter function

Redshift	$\Phi*$ [10^{-4}Mpc^{-3}]	log $L*$ [erg s^{-1}]	α
$2.9 < z < 6.7$	$7.41^{+2.70}_{-2.20}$	$42.85^{+0.10}_{-0.10}$	$-2.06^{+0.07}_{-0.05}$
$2.9 < z < 4.0$	$6.56^{+3.20}_{-2.40}$	$42.87^{+0.11}_{-0.1}$	$-2.00^{+0.07}_{-0.07}$
$4.0 < z < 5.0$	$4.06^{+2.70}_{-1.70}$	$42.97^{+0.13}_{-0.11}$	$-1.97^{+0.09}_{-0.08}$
$5.0 < z < 6.7$	$3.49^{+2.11}_{-1.50}$	$43.09^{+0.10}_{-0.08}$	$-2.28^{+0.12}_{-0.12}$

confidence regions of the Schechter function fitting are shown in the dark red shaded area. As mentioned before, some open squares at the faintest bins have not been included in the traditional Schechter fit.

The luminosity log $L*$ found in this work is in line with DLV 2019, a few percent higher than the one obtained in Herenz et al. 2019 $42.20^{+0.22}_{-0.16}$ at global redshift range $2.9 < z < 6.7$. As mentioned in DLV 2019, the selection of data sets used for the Schechter fitting has an impact on the final results. This has been confirmed in the present work when we applied a different completeness threshold to decide which source would be kept for the LF computing. Even though the data are collected from the literature and used as a constraint at the bright part, a strong degeneracy between the parameters is still being seen. Consequently, we have to be careful to choose reasonable literature data, as performed here. From the present work, the log $L*$ parameter is well measured with different redshift bins. Within the uncertainty, this parameter displays a slight increase with the redshift.

The normalization factor $\Phi*$ of the Schechter function is in line with the results obtained from DLV 2019 and Sobral et al. 2018, but it shows a smaller value compared to the one from Herenz et al. 2019. This parameter is a normalization factor. It gives the number density of objects per unit volume and strongly depends on the literature data points used for the fitting.

While previous investigations, which lack data in the faint luminosity regime, usually fixed the slope value α at a fiducial value and tried to find the correlation between the two other parameters, the present work is able to find these parameters without any constraint. The final slope value α varies from $-2.0^{+0.07}_{-0.07}$ at redshift range $2.9 < z < 4.0$ to $-2.28^{+0.12}_{-0.12}$ at redshift $5.0 < z < 6.7$. At the global interval $2.9 < z < 6.7$, the slope value $-2.06^{+0.07}_{-0.05}$ is consistent with the values measured by Herenz et al. 2019 and Drake et al. 2017.

The sudden enhancement at the luminosity bin log $L \sim 42$ at redshift ranges z_{all} and z_{35} can be explained by the existence of very low completeness sources, which will contribute a large number of sources to the bin after correcting for completeness value. This may be related to the overdensity of background sources at redshift $z \sim 4$. Once again, this suggests that a larger cosmic variance than expected may happen in this bin.

The present work extends the work performed by DLV 2019, therefore it is worth comparing the results obtained from the two works. The best-fit parameter of the characteristic luminosity displays a consistency within $1-\sigma$ uncertainties in both different redshift bins. However, the slope value obtained in the present work is 20% steeper compared to previous published values. This could be explained by:

+ The difference in the data sample. The current study includes four times as many sources as those in DLV 2019.

+ The different completeness thresholds. Applying a lower limit in the present work to include as many sources as possible also affects the shape of the LF at the faint end. To illustrate this discussion, we have applied a completeness cut at 10% as performed in the work by DLV 2019. The results are displayed in Fig. 4.16. As expected, the number density of sources decreases significantly compared to those that are cut at 1%. In both cases, the

turnover/flattening trend at luminosity log$L \sim 41$ ergs^{-1} is observed.

+ The improved MCMC procedure (with respect to DLV 2019) better captures the relationship between magnification and $V_{\rm max}$ values of the sources.

- Effect of the literature data on the fitting of the linear function and the Schechter function.

As mentioned earlier, the data obtained from the lensing field are not sufficient to constrain the LF in the bright luminosity regime, i.e., above $L*$. Therefore, literature data from the bright end are needed for the fitting process. However, as the data in the bright end are numerous, including them for the fitting of the Schechter function may affect the final results. In this part, we investigate different combinations between our data points and those from the literature to study a possible impact. Specifically, at the bright end, above log(L) $\sim$ 43, we rely on literature data points and rely solely on our LF points at the faint end. By doing this, we want to illustrate the importance of the current data sets. For linear fitting, we made the fit in a luminosity interval of $40.5 <$ log L [erg s^{-1}] < 42.5 for $2.9 < z < 6.7$, $5.0 < z < 6.7$ and $40.0 <$ log L [erg s^{-1}] < 42.5 for two redshift bins $2.9 < z < 4.0$, $4.0 < z < 5.0$. The results are shown in Fig. 4.17. The faint-end slope values indicate a decrease when compared to the previous case involving a complete data sample (Fig. 4.12, left). The decreases are 16%, 18%, 7% and 23% with respect to the redshift interval z_{all}, z_{35}, z_{45}, and z_{60}. $L*$ is the parameter describing the "knee" of the Schechter function at the bright end. By removing the "knee" point, which is constrained by bright LF literature points, the faint-end slope decreases, as expected.

We performed the Schechter fitting, using LF data log(L) above 43 [erg s^{-1}] from the literature and below 43 [erg s^{-1}] from ours. The results are shown in Fig. 4.18. In general, the new results are in line with the original Schechter function fitting within their slope uncertainties. The slope value of the Schechter function when applying a different completeness threshold and including only literature data points that are above 43 [erg s^{-1}] to the fit are presented in Table 4.5.

- Effect of source selection

In the 17 lensing clusters, 190 LAEs (unique systems) have been classified as $zconf = 1$. However, due to the ambiguous nature of their detection line profiles, we have not included them in the computation of the LF presenting in the previous section. As mentioned earlier, at the faint-end,log $L<$ 41 [erg s^{-1}], $zconf = 1$ sources are just as numerous as $zconf = 2,3$ sources. They may contribute significantly to our faint LF points. To evaluate the impact of $zconf = 1$ sources on the final luminosity function (LF) points, we have incorporated them into our LAE sample. By adding two sub-datasets (half of $zconf = 1$ and all the $zconf = 1$) to the present data sample and employing the Schechter function fitting, the faint end slopes obtained from the two categories are -2.14 ± 0.08 and -2.29 ± 0.09, respectively. These values are steeper compared to the original sample (i.e., 5% steeper when half of $zconf = 1$ sources have been included, and 10% steeper for the case in which all the $zconf = 1$ sources have been added).

- Systematic uncertainties attached to the faint-end slope

+ Apart from the three types of uncertainties —statistical, cosmic variance, and Poissonian — one should also take into account the systematic uncertainty coming from lensing models, which constitutes another significant factor within the overall error estimation. The adoption of various lensing models might lead to distinct magnification factors for a given source, thereby amplifying the uncertainty associated with the obtained luminosity. This systematic uncertainty has been extensively documented in studies such as R. J. Bouwens, G. D. Illingworth, Oesch, H. Atek, et al. 2017; Hakim Atek, Johan Richard, et al. 2018; Priewe et al. 2017; Meneghetti et al. 2017. Its impact could be particularly notable within the faint end luminosity regime. As discussed in DLV 2019, its contribution

reaches approximately 15% at log(L) of 40.5 erg s^{-1}, particularly in the case of the lensing field A2744.

+ Another source of systematic uncertainties may come from the flux measurement. As mentioned in the previous section, source fluxes are obtained from two different methods. We mostly use fluxes from A. Claeyssens et al. 2022, which were obtained by fitting source spectra (first method). The remaining 1/3 of the sample was obtained from the second method using SExtractor. To assess the impact caused by the choice of using different methods, we recomputed the LF points by replacing all source fluxes obtained from the first method with those of the second one, i.e., using only detection fluxes. This computation further confirms the robustness of our results, as there is quite good agreement between the two. Using these new LF points, we obtain the Schechter's faint end slope value that is approximately 10% less than the previous slope. These results are useful to estimate the systematic uncertainties attached to the faint end slope.

Taking into account all possible effects that may affect the shape of the LF at the faint end, such as the completeness threshold, source selection, literature selection, and flux measurements, we estimate the uncertainty values of the slope at different redshift bins. The final slope values are -2.00 ± 0.50, -1.97 ± 0.50, -2.28 ± 0.50 and -2.06 ± 0.60 corresponding to the redshift ranges z_{35}, z_{45}, z_{60} and z_{all}. The final results are shown in Fig. 4.19 together with results from the literature. The horizontal error bars represent the redshift range of the survey. The results display a slight increase in the slope with redshift, but the uncertainties remain large. The results are presented in Table 4.6.

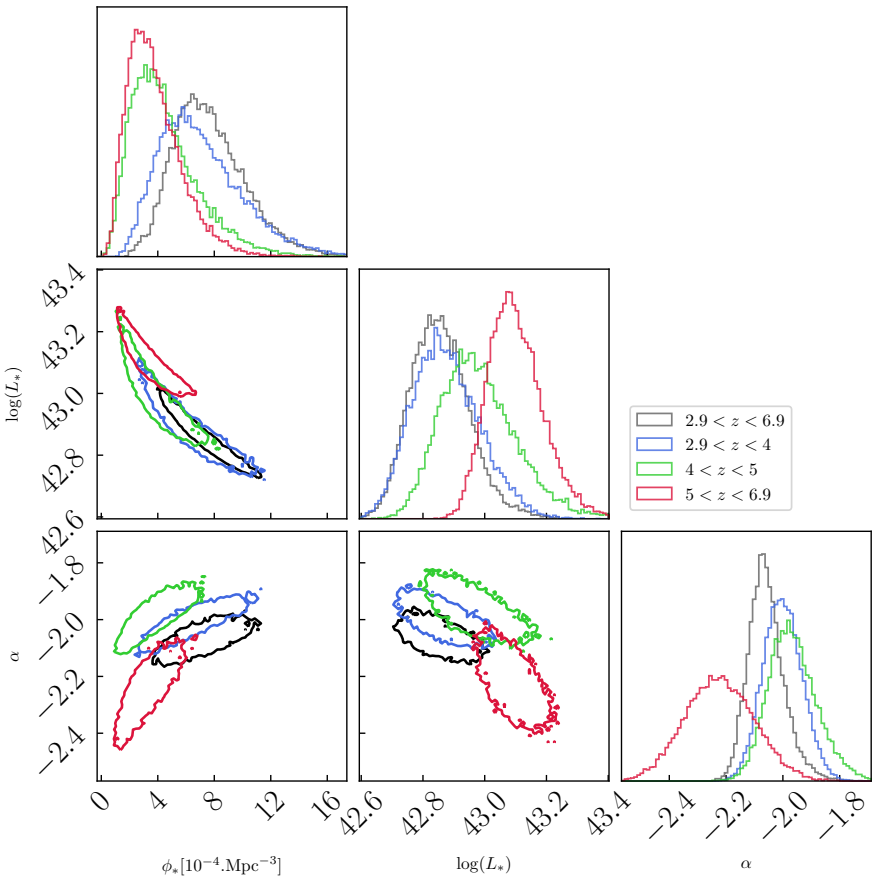

Figure 4.14: Correlation of three parameters of the Schechter function for four redshift intervals as indicated in the legends. Contours show the 68% confidence level of the fittings.

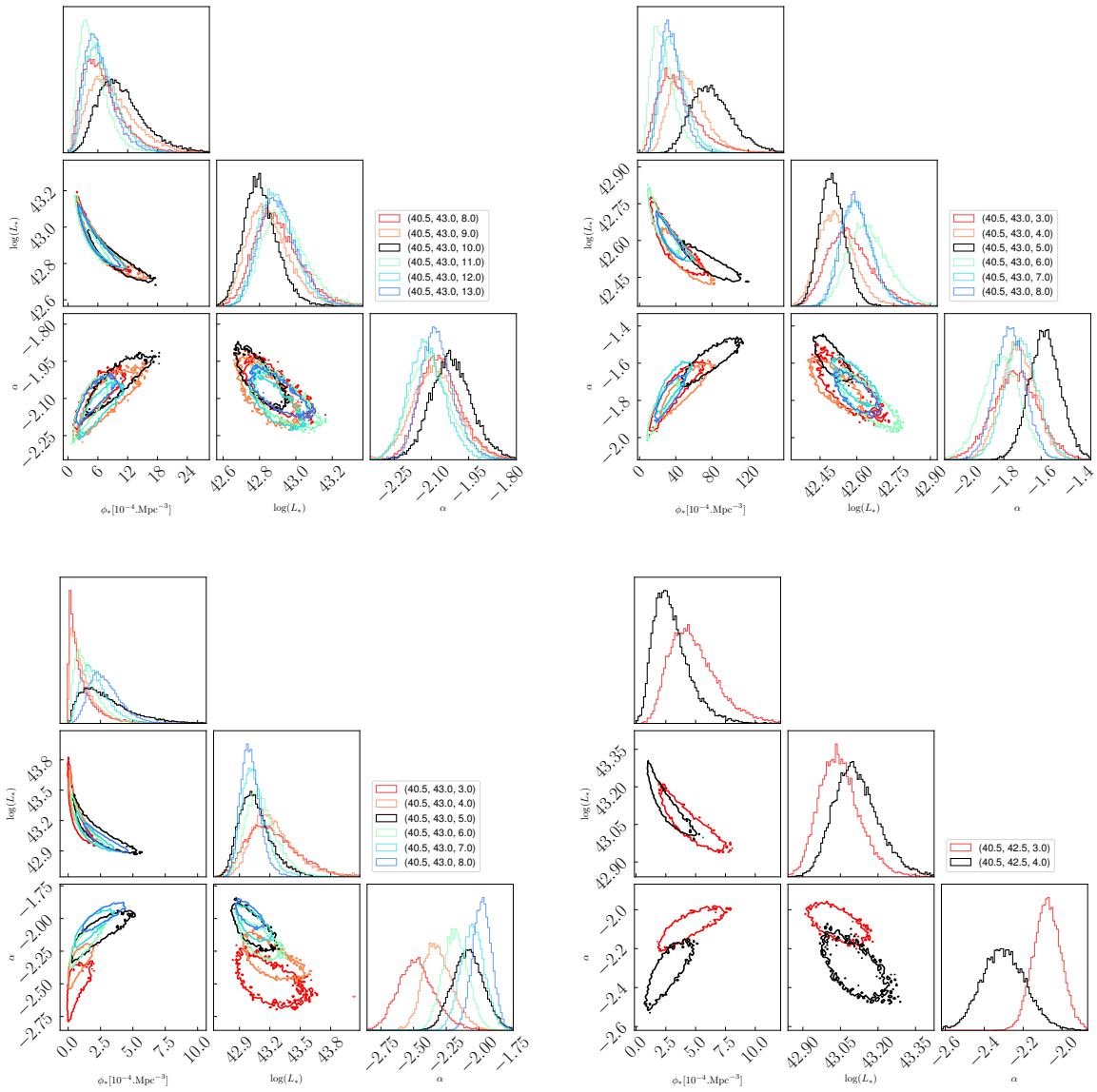

Figure 4.15: The correlation of three free parameters of the Schechter function within a 68% confidence level. From left to right, up to down corresponds to the redshift intervals $2.9 < z < 6.7$, $2.9 < z < 4.0$, $4.0 < z < 5.0$, and $5.0 < z < 6.7$, respectively. The tuples denote the lower and upper limits of the luminosity range with respect to the number of the bin.

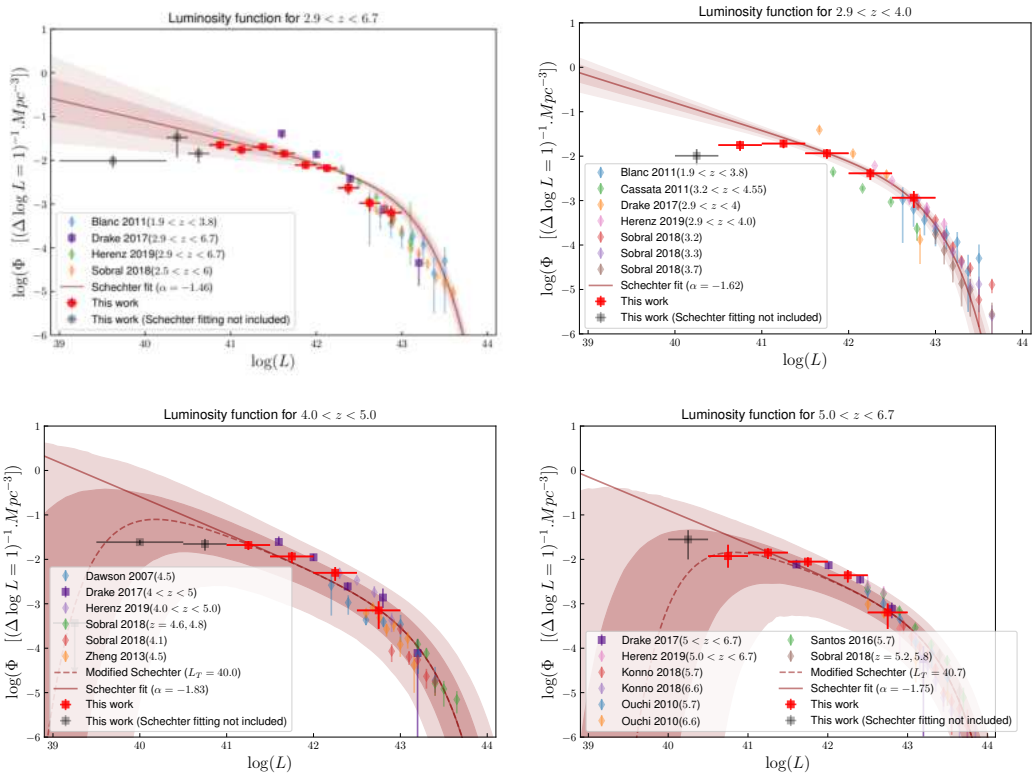

Figure 4.16: Same as Fig. 4.13 but applying a completeness cut at 10%.

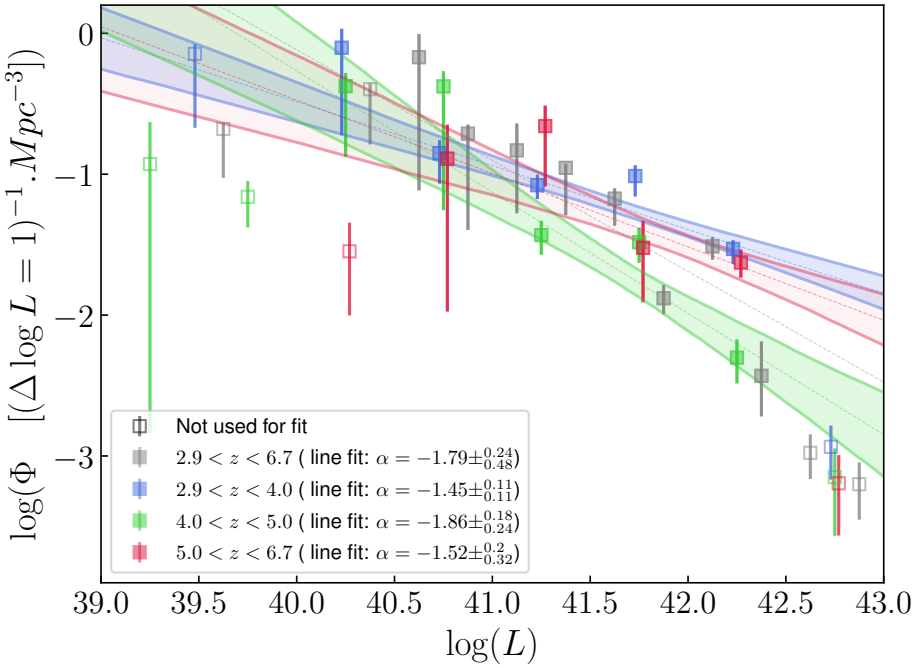

Figure 4.17: Faint end slope of the LF for four redshift intervals. The open squares at the faintest and brightest parts are not included in the fit.

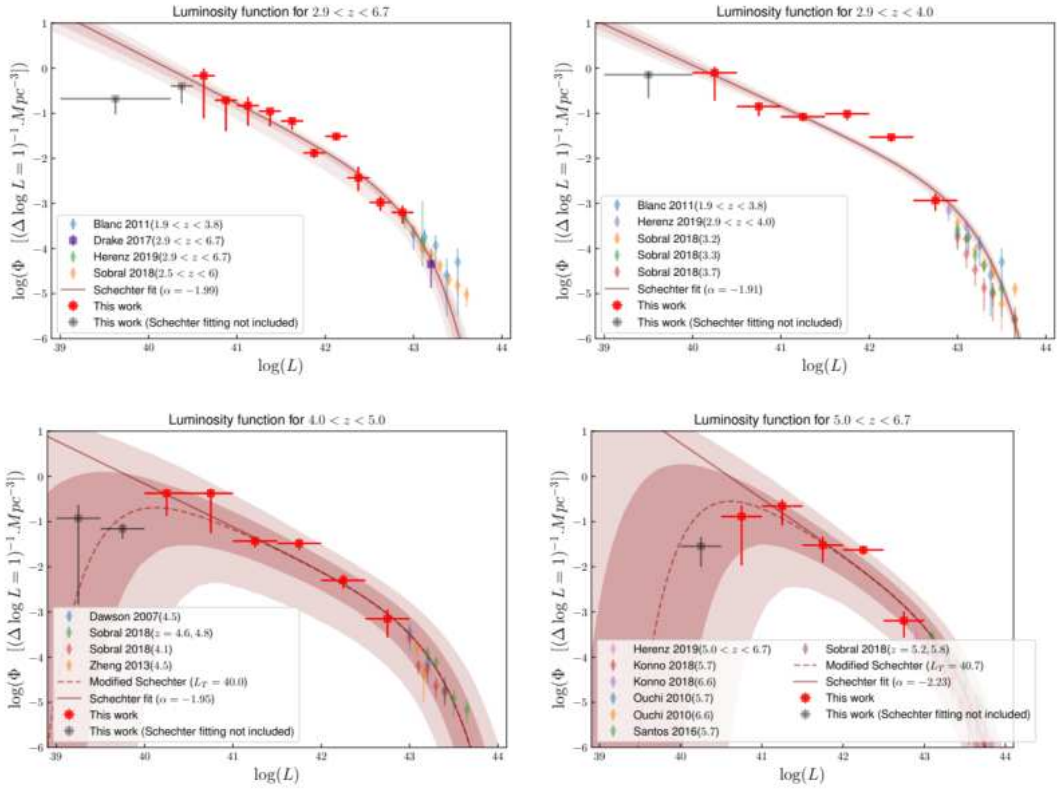

Figure 4.18: Schechter fits for the different redshift intervals, using the constraint that our LF points are at the faint end and literature data points are at logL > 43 erg s^{-1}. The red squares are the points from this work. The literature points are shown in the insert. The best fits of the Schechter function are shown as a solid line and the 68% and 95% confidence levels as dark red shaded areas, respectively.

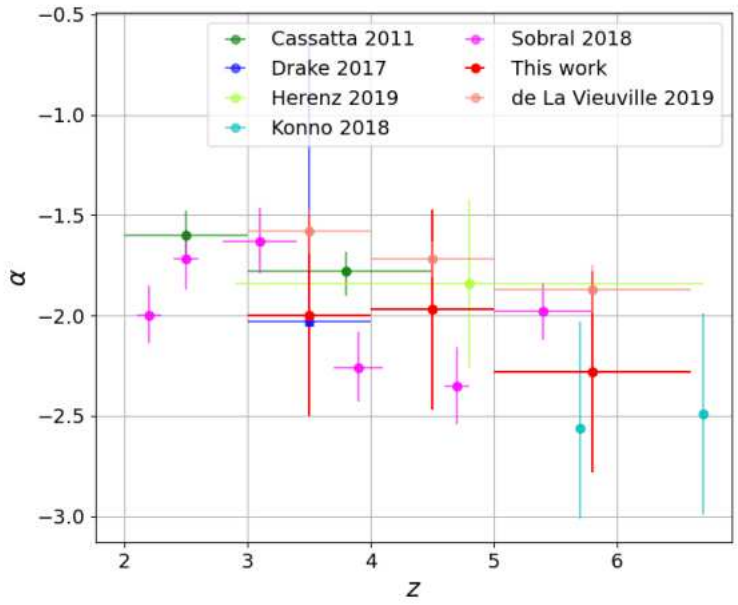

Figure 4.19: Faint end slope at different redshift ranges derived from the present work (red) and literature (other colors) as indicated in the legends. The horizontal error bars are the redshift range of the surveys.

Table 4.5: Summary of the best fit values of the faint end slope using different constraints

	Schechter fitting		Linear fitting	
Bins	Current result	Using literature log $L > 43$	Current result	Excluding LF values greater than 42.5
z_{all}	$-2.06^{+0.07}_{-0.05}$	-1.99 ± 0.08	$-2.12^{+0.15}_{-0.16}$	$-1.79^{+0.24}_{-0.48}$
z_{35}	$-2.00^{+0.07}_{-0.07}$	-1.91 ± 0.06	$-1.76^{+0.26}_{-0.27}$	$-1.45^{+0.11}_{-0.11}$
z_{45}	$-1.97^{+0.09}_{-0.08}$	-1.95 ± 0.09	$-1.99^{+0.12}_{-0.17}$	$-1.86^{+0.18}_{-0.24}$
z_{60}	$-2.28^{+0.12}_{-0.12}$	-2.23 ± 0.12	$-1.96^{+0.5}_{-0.54}$	$-1.52^{+0.20}_{-0.32}$

Table 4.6: Results of the faint end slope α from different tests

	z_{35}	z_{45}	z_{60}	z_{all}
Schechter fitting				
1% completeness cut	-2.00 ± 0.07	-1.97 ± 0.09	-2.28 ± 0.12	-2.06 ± 0.07
10% completeness cut	-1.78 ± 0.06	-1.83 ± 0.12	-1.75 ± 0.10	-1.46 ± 0.05
1% completeness cut, fluxes obtained from the second method	-2.10 ± 0.06	-1.97 ± 0.08	-2.24 ± 0.11	-1.82 ± 0.03
1% completeness cut zconf1 included	-1.83 ± 0.17	-1.92 ± 0.09	-1.94 ± 0.10	-2.29 ± 0.09
Linear fit				
1% completeness cut	-1.76 ± 0.27	-1.99 ± 0.17	-1.96 ± 0.54	-2.12 ± 0.16
10% completeness cut	-1.55 ± 0.17	-1.63 ± 0.21	-1.66 ± 0.24	-1.64 ± 0.12
Faint end slope retain	-2.00 ± 0.50	-1.97 ± 0.50	-2.28 ± 0.50	-2.06 ± 0.60

- The probability of a turnover in the faint-end at the higher redshift ranges.

Until now, the shape of the LF at the faintest luminosity/magnitude regime and the high redshift ranges is still not well known due to a lack of data. It is possible that there is a turnover, such as the one mentioned in R. J. Bouwens, G. D. Illingworth, Oesch, H. Atek, et al. 2017 at $M_{UV} > -15$ with a faint end slope of $\alpha = -1.91 \pm 0.04$. Hakim Atek, Johan Richard, et al. 2018 presents a probability of such a turnover at a faint end slope of $\alpha = -2.01^{+0.12}_{-0.14}$, a curvature parameter of $\beta = 0.48^{+0.49}_{-0.25}$ at a turnover magnitude $M_T = -14.93^{+0.61}_{-0.52}$. However, the recent paper by R. J. Bouwens, G. Illingworth, et al. 2022 ruled out this trend at redshift $z \sim 6$ when the magnitude reaches $M_{UV} = -14$. It is also possible that the faint-end slope continues to increase with magnitude, as suggested by Livermore et al. 2017 with a slope value of $\alpha = -2.10 \pm 0.03$ at magnitude $M_{UV} < -12.5$. Dawoodbhoy et al. 2023 used the CODA simulation to study the UV LF at redshift $z \sim 6$ and found strong evidence against a possible turnover at magnitude $M_{UV} = -12$. In the present work, we do not take the LF points at the faintest luminosity bins into account for the traditional Schechter fitting. We observe a possible turnover at the highest redshift intervals z_{45} and z_{60} (Fig. 4.13, lower panels). To account for this, we have introduced a modified Schechter function by multiplying the original function by an exponential term, which is now written in the form:

$$\Phi(L)\exp(-L_T/L)^m = \frac{\Phi*}{L*}\left(\frac{L}{L*}\right)^{\alpha} \exp(-L/L*)\exp(-L_T/L)^m \tag{4.4}$$

where: $\Phi(L)$ is the traditional Schechter function together with its three free parameters $(L*, \Phi*, \alpha)$, m is the curvature parameter defining a downward turnover if $m > 0$ and upward turnover if $m < 0$, L_T denotes the position of turnover, which is defined as the luminosity where the derivative $(d\Phi/d_L)_{L=L_T} = 0$. The shape of the modified Schechter function is shown in the lower panels of Fig. 4.13, 4.16, 4.17. Our data suggest that m is about unity and $log(L_T)$ are ~ 40 and ~ 40.7 erg s^{-1} for the redshift bins $4.0 < z < 5.0$ and $5.0 < z < 6.7$, respectively. The appearance of a turnover at the faintest luminosity bins is explained by star formation inefficiency in small dark matter halos (Jaacks et al. 2013; Gnedin 2016; Yue et al. 2016).

4.5 Comparison with theoretical predictions

Recently, two models have been developed by Garel et al. 2021 and Salvador-Solé et al. 2022 to predict the Lyman alpha LF at redshift $z \sim 6$. It is therefore necessary to compare the results of these models to that obtained in the present work for the highest redshift interval $5.0 < z < 6.7$. The first model, developed by Garel et al. 2021, applies the SPHINX radiation hydrodynamics cosmological simulation to predict the Lyman alpha LF at the EoR by estimating the radiative transfer of the sources from ISM to the IGM scales. The second model, developed by Salvador-Solé et al. 2022, uses the AMIGA (Analytic Model of Igm and GAlaxy evolution) model to predict the possible scenarios of single and double ionization, taking into account the impact of galaxy formation and its evolution within their feedback on the IGM. The former predicts a single hydrogen ionization stage at redshift $z \sim 6$, while the latter predicts two reionization stages at redshift $z \sim 6$ and ~ 10, with two separated phases defined by a short recombination episode. The results are shown in Fig. 4.20. At the luminosity range $40 < \log L[\text{ergs}^{-1}] < 42$, the prediction from AMIGA double ionization is in line with the one obtained from the SPHINX simulation after correction for the IGM. In general, the LF points are in good agreement with the two predictions without any normalization requirement. At the faintest luminosity bin, when $\log L < 41$, our LF point tends to depart from the SPHINX predictions but is still close to the single ionization model

from Salvador-Solé et al. 2022. However, at these redshift ranges, the uncertainty values are generally large, preventing us from evaluating the difference between the predictions. More observational data at the faint luminosity regime and at high redshift ranges are needed to solve this problem.

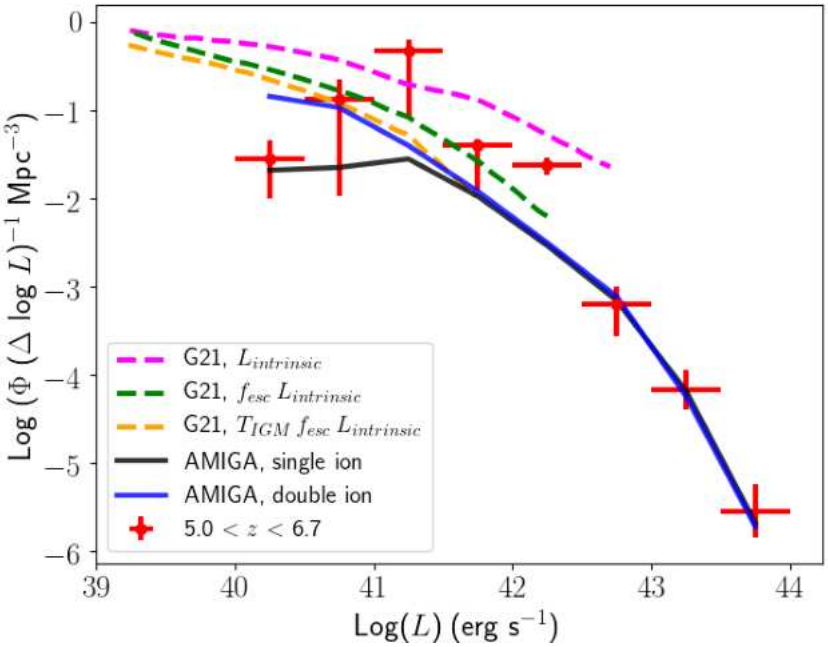

Figure 4.20: LF points obtained in the present work (red crosses) at the highest redshift range are compared to the model predictions (Garel et al. 2021) (dashed color lines) and AMIGA models (Salvador-Solé et al. 2022) (solid lines). The two LF points at the brightest part are taken from the literature by averaging their values in the same luminosity and redshift bin.

5 Star formation rate density and implications for the reionization

Contents

5.1 Star formation rate density

One of the greatest interests in the studies of galaxy evolution and reionization is understanding SFRD, which is a fundamental quantity of star formation occurring per unit time per unit volume at a specific redshift. Following the instruction proposed by Donald E Osterbrock et al. 2006, the quantity can be determined within a redshift range by integrating the LF to compute the luminosity density and be transformed using the following formula:

$$SFRD_{Lya}[\mathrm{M_\odot yr^{-1}Mpc^{-3}}] = \rho_{Lya}/1.05\times10^{42} \tag{5.1}$$

where ρ_{Lya} is Lyman alpha luminosity density in units of erg s^{-1} Mpc^{-3} given by this expression: $\rho_{Lya} = \int_{L_{inf}}^{L_{sup}} \Phi(L/L*)d(L/L*)$. The total star formation rate density (SFRD) shows a direct correlation with the density of luminosity and can be estimated by applying the calibration method established by Kennicutt 1998. This estimation involves assuming an intrinsic factor of 8.7 between the intrinsic fluxes of Lyα and Hα. Furthermore, the evaluation adheres to the case B recombination scenario, as outlined by Donald E. Osterbrock 1989, where the assumption is that all newly generated Lyman photons are re-absorbed by the neutral hydrogen atoms within the HII region. On the other hand, one converts the Lyα luminosity into Star Formation Rate (hereafter SFR) by assuming that the escape fraction for Lyman alpha photons is one, meaning that the SFRD above is a lower limit. From the luminosity distribution and the evolution of the LF at log L [erg s^{-1}] > 42, the shape of LF fits quite well with the Schechter function. This means that the final value of SFRD will not be affected by the upper limit of luminosity L_{supp} for the integration. On the contrary, the steep slope at the faint end makes the lower limit L_{inf} play an important role in estimating SFRD. This is illustrated in Figure 5.1. The red crosses show the SFRD for a luminosity interval of (39.5 < log L [erg s^{-1}] < 43), which covers the full range of present work. The brown-reddish crosses show the SFRD for high-narrower luminosity range of (41.0 < log L [erg s^{-1}] < 43.), whic corresponds to the limit ~ 0.03×log($L*$). This narrower range was chosen to include only the most secure determinations of the LF. It is clear that at a narrower range, the number of sources contributing to the budget is smaller than in the case of a wider luminosity range. The yellow region shows $1-\sigma$ and $2-\sigma$ confidence levels of the SFRD required to fully ionize the Universe, taken from the R. J. Bouwens, G. D. Illingworth, Oesch, Trenti, et al. 2015, assuming a clumping factor of 3 (see below) and the conversion to UV luminosity density with an assumption of log($\xi_{ion}f_{escp}$) = 24.5, where f_{escp} is the escape fraction of UV photons, ξ_{ion} is the production efficiency of Lyman-continuum photons per unit UV luminosity. The conversion to SFRD is then

calculated as, $SFRD_{Lya}[M_{\odot}\mathrm{yr}^{-1}\mathrm{Mpc}^{-3}] = \rho_{UV}/(8.0\times10^{27})$.

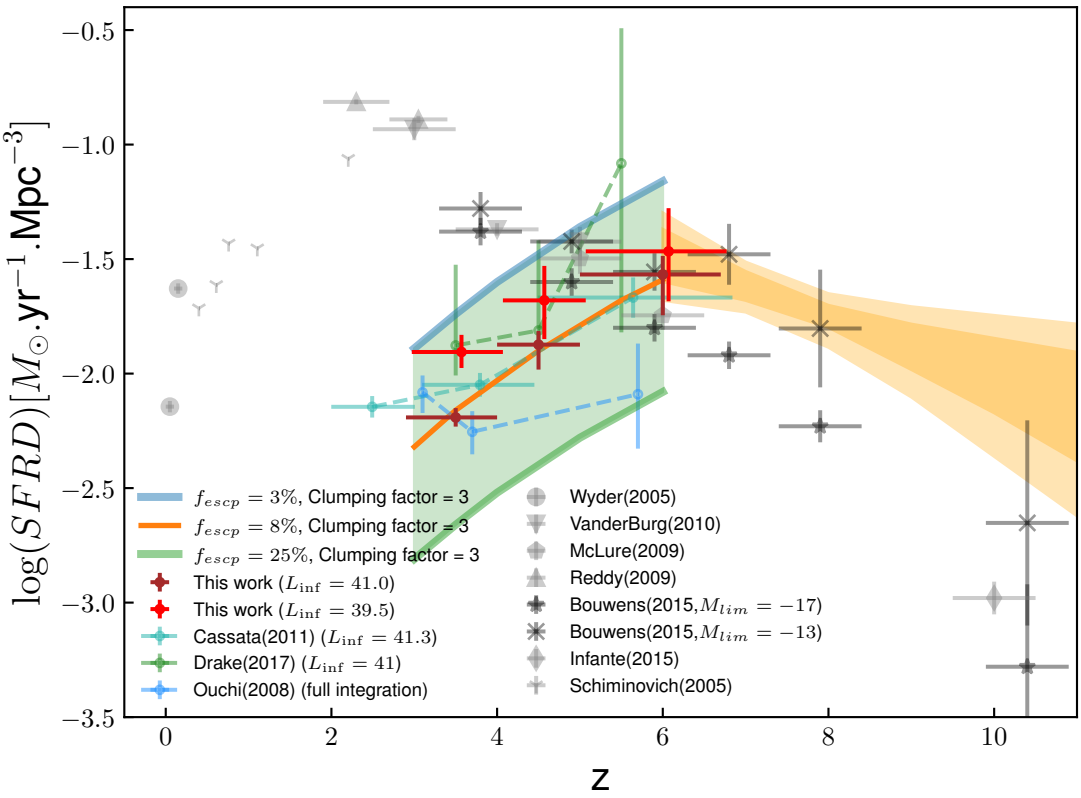

Figure 5.1: Cosmic evolution of the SFRD as a function of redshift. The data points are taken from the literature listed in the insert.

Figure 5.1 shows the evolution of the SFRD as a function of redshift, by comparing the results obtained in this work with previous results from the literature (see references in the legend). It is worth mentioning that Cassata et al. 2011 computed their SFRD by correcting for the influence of IGM absorption, assuming an escape fraction of ionizing photons that varies from 15% at redshift z=3 to 50% at redshift z=6, combining with a factor of radiative transfer as the one presented in Fan et al. 2006. Drake et al. 2017 used 604 LAEs in the blank field observed by MUSE/VLT to estimate the contribution of LAEs to the cosmic SFRD. It is clear that using data in the blank field will only help to detect bright sources, leading to a lack of data in the faint end. This means that the procedure to compute SFRD at the highest redshift will be associated with a large uncertainty. Ouchi, Shimasaku, Masayuki Akiyama, et al. 2008 integrated into the full range of their data to derive the SFRD. However, they fixed the slope value of $\alpha = -2$ due to the lack of observation towards the faint end. This is a very common situation when observations do not reach faint enough luminosity to compute the slope of the LF.

The ability of a population of sources to reionize the Universe is usually assessed by comparing its ionizing power to the critical value needed to maintain reionization at a given redshift. This critical value, which is the photon emission rate per unit cosmological comoving volume, was introduced by Madau, Haardt, and Rees 1999 as follows:

$$\dot{N} = (10^{51.2}\mathrm{s}^{-1}\mathrm{Mpc}^{-3})C_{30}\left(\frac{1+z}{6}\right)^3\left(\frac{\Omega_b h^2}{0.08}\right)^2 \tag{5.2}$$

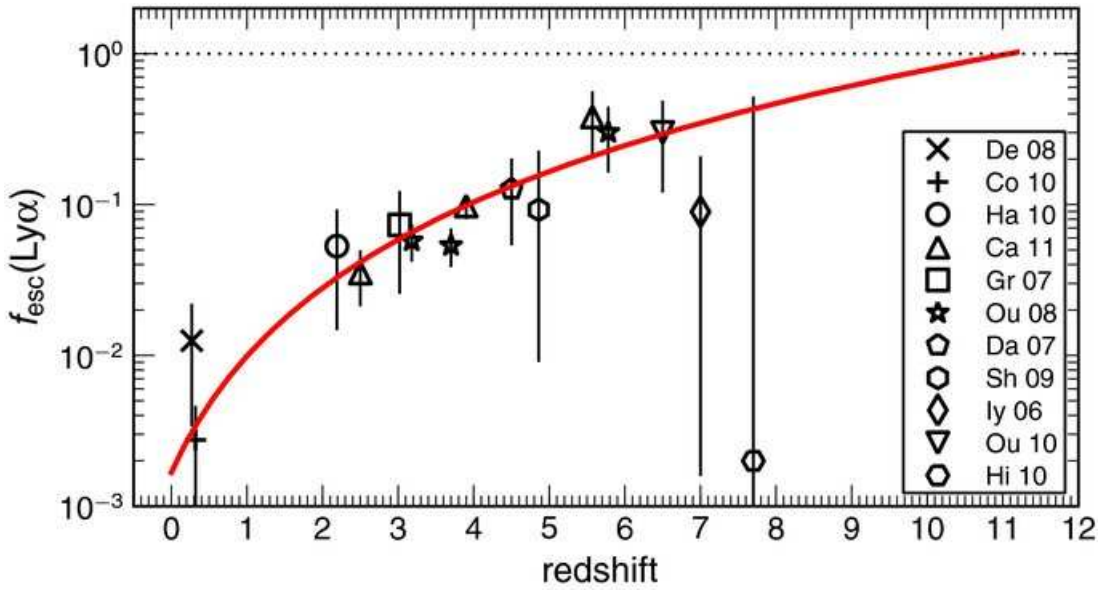

Figure 5.2: Evolution of f_{escp} as a function of redshift. The data points are taken from the literature listed in the insert. Credit: (M. Hayes, Daniel Schaerer, et al. 2011).

where C_{30} is the clumping factor C_{HII}=<n^2_{HII}>/<n_{HII}>^{2}, normalized to C_{HII}=30, n_{HII} is the mean comoving hydrogen density in the Universe. The clumping factor is a correction that takes into account the inhomogeneities in the IGM owing to the structure formation. It is a function of redshift and is used to estimate the amount of recombination that radiation must overcome to maintain the ionized state of the Universe (Gnedin and Ostriker 1997; Madau, Haardt, and Rees 1999; Fan et al. 2006). Shull et al. 2012 introduced a function to relate the clumping factor to redshift, $C_{HII} = 2.9 \times ((1+z)/6)^{-1.1}$. This includes the recombinations that occurr in gas that is a local domination candidate for ionization state. This clumping factor is around 4 at redshift $z = 3.5$, and decreases at higher redshifts. For example, it is 2.4 at $z = 6$ and falls between 1.2-1.4 at $z > 6$. This decrease can be explained by the increase in the neutral fraction of hydrogen in the environment. This clumping factor is even lower than 1 at redshift $z > 10$, as mentioned in the Finlator et al. 2012.

Assuming $C_{30} = 1$ and $\Omega_b h^2_{50} = 0.08$, the critical SFRD is written as:

$$SFRD_{crit} = \dot{N} \times 10^{-53.1} f^{-1}_{escp} \sim 0.013 f^{-1}_{escp} \times \left(\frac{1+z}{6}\right)^3 \tag{5.3}$$

where f_{escp} is the escape fraction of ionizing photon, which is defined as the fraction of ionizing photon that escape from the source galaxy to the IGM after correcting for recombination within its halo. If the escape fraction from the host galaxies is low, it is obvious that the star formation will be inefficient to reionize the Universe at high redshift. There are several ways to estimate the escape fraction of ionizing photons using the data collected from observations. One way is to use the HI covering fraction, dust attenuations, and column densities to compute the escape fraction. Another way is to use the Lyman alpha escape fraction. A third way is to compute the flux ratio of OIII/OII. These methods were described in detail by Chisholm, J. et al. 2018. Recent results show that the escape fraction of ionizing photon f_{escp}, typically falls within the range of 10 to 20%. This value remains consistent regardless of the mass or luminosity of the galaxy (Choudhury et al. 2015; Robertson, Ellis, et al. 2015). It is difficult to directly measure f_{escp} at high redshift ($z > 6$) due to the substantial opacity of the IGM towards ionizing photons (Inoue et al.

2014). However, computing the escape fraction of the ionizing photons is still a subject of debate, and more data is needed to constrain its value. In theory, this can be done by focusing on the absorption of the photons as they travel through the interstellar medium. Some recent results include: Wood et al. 2000 found a rough value of $f_{escp} < 1\%$ at redshift $z \sim 10$, suggesting that this value decreases with increasing redshift due to the increasing density of galactic discs. Razoumov et al. 2006 found that $f_{escp} \sim 1-2\%$ at $z = 2.39$ and $f_{escp} = 6-10\%$ at $z = 3.6$ using the galaxy formation simulations combined with 3D radiative transfer. In addition, hydrodynamical simulations suggest that f_{escp} is probably anisotropic and time-dependent (Cen et al. 2015; X. Ma et al. 2015). It depends on the characteristics of galaxies, such as a potentially higher f_{escp} for galaxies with lower mass, as demonstrated by J.-P. Paardekooper et al. 2015. This could impact the process of reionization Sharma et al. 2016.

The relationship between the Lyman alpha escape fraction and redshift is important for constraining the reionization history of the Universe. M. Hayes, Daniel Schaerer, et al. 2011 observed an evolution trend of $f_{escp}^{Ly\alpha}$ with redshift, described by $f_{escp}^{Ly\alpha} \propto (1+z)^{\xi}$, where $\xi = 2.57^{+0.19}_{-0.12}$ across an interval of redshift $0.3 < z < 6$ (see Figure 5.2). This evolution peaks at a value of unity at redshift $z = 11.1$. The increasing trend of $f_{escp}^{Ly\alpha}$ with the redshift corresponds to the changing of dust content within the galaxies up to $z \sim 6$. Beyond this point, there is an appearance of decline.

The quantities of $f_{escp}^{Ly\alpha}$ and f_{escp} are expected to be correlated. This was explored in Dijkstra et al. 2016; Izotov et al. 2019. Combining the results obtained from M. Hayes, Daniel Schaerer, et al. 2011, the order of magnitude expected for f_{escp} is $\sim 5\%$ at $z \sim 3$, and up to 25% at $z \sim 6$. Figure 5.1 shows the critical SFRD value obtained from these two extremes of f_{escp}, displayed as a shaded region using a typical value of the clumping factor of 3, which is mentioned in some studies, such as Pawlik et al. 2009; Robertson, Furlanetto, et al. 2013; Robertson, Ellis, et al. 2015; R. J. Bouwens, G. D. Illingworth, Oesch, Trenti, et al. 2015; Gorce, A. et al. 2018. The SFRD points obtained by integrating the luminosity in the range of $41 < \log L\ [\mathrm{erg\ s^{-1}}] < 44$ are consistent with the critical values obtained from an average value of $f_{escp} \sim 8\%$ and a typical clumping factor of 3 within a redshift range of $3 < z < 6.7$. This suggests that the contribution of LAEs to the ionizing flux in the given redshift range is sufficient to keep the hydrogen ionized. At redshift $z \sim 6$, this contribution is comparable to the one provided by LBGs.

Using LF face values as presented here implies that the role of the LAEs population in the cosmic reionization might exceed initial expectations. However, there are a few considerations to keep in mind. Firstly, the vast majority of past surveys have focused on the most luminous galaxies in the rest frame UV, which are ideal candidates for spectroscopic follow-up. However, these surveys can not probe the faint luminosity regime, down to 10^{39} [erg s^{-1}], as the present work does. Moreover, IFU observations can identify LAEs without any preselection. Secondly, the contribution to the SFRD is linked to the steepness of the faint-end slope being obtained, which is directly proportional to the Lyman alpha luminosity density. A slope that is 20% steeper significantly changes the contribution of LAEs to cosmic reionization. Thirdly, the lower boundary of the integration also affects the final contribution. Furthermore, there are significant uncertainties regarding the $f_{escp}^{Ly\alpha}$ and its evolution with redshift, which makes it difficult to compare this study to other studies that use different methodologies.

6 Conclusions and perspective futures

Contents

6.1 Summary and Conclusions

In this thesis, I have presented a study of LAEs LF using a large data sample of sources detected behind 17 lensing clusters observed with MUSE/VLT. Thanks to the lensing effect, the signal from distant galaxies has been magnified by a factor of 4 to 10 allowing us to blindly detect LAEs without any pre-selection and reaching to the faintest luminosity level compared to the blank field observations.

Because of the lensing effect, we usually observed multiple images of the same system. In this case, we have to choose one representative image for each system. The image should have a high signal to noise ratio and be more isolated than the other images of the same system. Finally, 600 LAEs have been selected behind 17 lensing clusters, covering four orders of magnitude in luminosity over $39 < \log L[\mathrm{erg\,s^{-1}}] < 43$, within a redshift interval of $2.9 < z < 6.7$. In the high redshift regime where they are one order of the magnitude fainter than those of current blank field surveys, in order to investigate a possible evolution of LF with redshift, and to estimate the associated contribution to the total cosmic reionization budget. Consequently, we probed the LF of LAEs over four redshift intervals. To deal with both the data obtained from lensing fields and from MUSE/VLT datacubes, we have adopted the approach described in DLV 2019, which uses the V_{max} method to compute the LF values. The main idea of the method is the creation a 3D detectability mask for each source in the MUSE cubes in the source plane, followed by an evolution of the cosmological volume obtained by integrating over the unmasked pixels in the 3D source plane mask. While maintaining the core framework, we made several changes to the original pipeline. These changes extended the previous sample to 17 lensing clusters and better accounted for the lensing magnification. The total co-moving volume in the global redshift range $2.9 < z < 6.7$ is $\sim$ 50'000 Mpc^3. This value is three times larger compared to the previous work of DLV 2019 that probed the LF of LAEs behind 4 lensing clusters (A1689, A2390, A2667, and A2777). However, it is much smaller than the value reported in blank field surveys. This is due to the lensing magnification effect.

To compute a luminosity function point, we must correct for the completeness of each source, in addition to its Vmax. The completeness value is calculated by injecting

the real source profile into a mock image and then counting the successful rate of this procedure. Aiming to include as many sources as possible for the LF computation, we used a 1% completeness threshold to reject faint sources. We computed the LF points in each luminosity bin and redshift range and fitted them with the Schechter function. The LF points at the faintest luminosity bins in the higher redshift ranges $4.0 < z < 5.0$ and $5.0 < z < 6.7$ were not included in the fit due to low completeness, and high magnification. They seem to suggest a flattening/turnover at the faintest luminosity regime in these two highest redshift ranges. To account for this, we have introduced a modified Schechter function: $\Phi(L)\exp(-L_T/L)^m = \frac{\Phi*}{L*}\left(\frac{L}{L*}\right)^{\alpha}\exp(-L/L*)\exp(-L_T/L)^m$ where L_T is turnover luminosity and m the curvature parameter defining the shape, downward or upward.

From the best-fit values of the Schechter function, we integrated the LF to compute the luminosity density and then converted it to the SFRD using an assuming an intrinsic factor between Lyman alpha and Hα fluxes and case B of the recombination (Donald E. Osterbrock 1989). The results showed that the LAEs contribute significantly to the reionization budget. At the critical value of photon emission rate per unit cosmological comoving volume, we estimate that the escape fraction of Lyman alpha photons is about 8% associated with a typical value of clumpy factor of 3.

In summary, we have presented a study on the LAEs LF using an extensive dataset consisting of 17 lensing clusters from the Lensed Lyman Alpha MUSE Arcs Sample observed with MUSE/VLT. From this dataset, we have selected 600 lensed LAEs behind these clusters within a redshift range of $2.9 < z < 6.7$ with a wide range of luminosity spanning four orders of magnitude $39.0 < \log L$ [erg s^{-1}] < 44.0, and effectively probing the faint luminosity regime, reaching down to 10^{40} [erg s^{-1}]. This data sample sets a strong constraint on the LF for faint luminosities and provides insight into the evolution of the slope as a function of redshift. The key outcome and conclusions are presented as follows:

- Regarding the methodology and processing pipeline, we have thoroughly investigated various effects, leading to improvements in the final results compared to the work of DLV 2019. We extended the previous sample to 17 lensing clusters and better accounted for the lensing magnification during the Vmax computation process.

- The evolution of LF with redshift has been investigated in four redshift intervals: $2.9 < z < 6.7$, $2.9 < z < 4.0$, $4.0 < z < 5.0$, and $5.0 < z < 6.7$. The total co-moving volume of the survey is ~ 50000 Mpc^3, largely dominated by A2744, as presented in DLV 2019.

- The best-fit value of the three parameters of the Schechter function in the redshift range of $2.9 < z < 6.7$ are: $\alpha = -2.06^{+0.07}_{-0.05}$, $\Phi*$ [10^{-4} Mpc^3] $= 7.41^{+2.70}_{-2.70}$, $\log L*$ [erg s^{-1}] $= 42.85^{+0.10}_{-0.10}$.

- Toward bright luminosity, $\log L$[erg s^{-1}] > 42, the present LF values are consistent with the results of the previous studies which is used the data from the MUSE-Wide observations, as well as with other published results using different observational techniques.

- Toward faint luminosity, the LF values are dominated by highly magnified and low completeness sources as expected. The source density is described by a steep slope of $\alpha \sim -2$, obtained from both linear fitting and fitting using the Schechter function. Our results are consistent with the slope values obtained by Drake et al. 2017 for all redshift intervals, by Herenz et al. 2019 for $2.9 < z < 6.7$, and 20% steeper than those obtained by DLV 2019. Taking into account various factors, such as different completeness thresholds, different flux measurements, varying fitting models, and source selection, the faint end slopes for four redshift ranges are -2.00 ± 0.50, -1.97 ± 0.50, -2.28 ± 0.50 and -2.06 ± 0.60. These values are consistent with other works within a $1-\sigma$ deviation.

- The faint end slope of the LF steepens with redshift, consistent with DLV19, although the uncertainties are large. There may be a turnover at luminosities fainter than log $L \sim 10^{41}$ [erg s^{-1}] for the two highest redshift intervals, yet the uncertainties remain large.

- The choice of the luminosity lower limit for the LF integration affects the SFRD value. The increase of SFRD with redshift implies that the LAEs play a major role for the cosmic reionization.

- The ionizing flux from LAEs seems to be sufficient to maintain the hydrogen ionized. At redshift $z \sim 6$, this value is comparable to the one provided by LBGs.

6.2 Future Perspectives

6.2.1 Luminosity function of line emissions observed with MUSE

The Lensed Lyman Alpha MUSE Arcs Sample (Lensed Lyman Alpha MUSE Arc Sample (LLAMAS)) has observed 25 massive clusters with an observing time of ~150 hours in total. It is expected to find more than 700 LAEs. This will be the largest data sample of lensed LAEs collected by MUSE/VLT at a redshift range $2.9 < z < 6.7$. The data from the project yields valuable insights into the luminosity distribution, enhancing the statistical representation of sources in the faintest luminosity regime.

In addition, the MUSE cube also includes information on other emission lines, such as Hα, OII, with good SNR. Using the same present method, we can look for the correlation between these emission lines and the total SFR. This will give us a unique opportunity to extend the results obtained in this thesis and improve our understanding of the LF and SFRD at a lower redshift, as well as their evolution with redshift.

6.2.2 Luminosity function using data from JWST and Euclid missions

Nearly 2 years since its launch, JWST has shown its power in collecting data at the EoR. Its observations of several gravitationally lensed clusters with its exquisitely sensitive NIR instruments (NIRSpec, NIRCam, NIRRISS) have provided the strongest constraint at the faintest end of the UV LFs. The galaxy density in such regimes can be estimated from the LF, suggesting that these galaxies may have played a significant role in the cosmic reionization. There are many first galaxies in the redshift range $7 < z < 15$ that have been confirmed on either Lyman alpha line emission with NIRSpec or the Gunn-Peterson Trough with deep photometry. I will pursue this topic by using the JWST data to study the evolution of the LF at the higher redshifts compared to the MUSE data.

Another opportunity is using Euclid data. Euclid is a space-based visible and near-infrared observatory with a primary mirror of 1.2 metres in diameter. The Euclid Deep Survey data will cover a region of 40 deg^2 with a limiting flux $\sim 5.10^{-17}$ erg s^{-1} cm^{-2} in the wavelength range of 920-1850 nm using the Euclid's blue and red grisms (Costille et al. 2016). This survey would be a great opportunity to study the Lyman alpha population at redshift $z \sim 6.5 - 9$ by constructing a blind flux-limited sample without any preselection. I will re-use and adapt some of the tools I have developed for this thesis to the Euclid survey to compute the LF of LAEs towards the bright end of the LF

6.2.3 Global escape fraction of Lyman alpha photons as a function of redshift

Using our LF of LAEs combined with the UV LF of all galaxies from R. J. Bouwens, G. D. Illingworth, Oesch, Trenti, et al. 2015, we can estimate the global evolution of the escape

fraction of Lyman alpha photons from 2.9 to the highest redshift in which we can find the galaxy based on JWST observations.

6.2.4 The ionizing photon production efficiency for LAEs using JWST and MUSE

The excellent combination of JWST and MUSE will open a new window to infer the ionizing photon budget of the Universe using a large data sample of LAEs. I will estimate this parameter's value in two cases: one without accounting for dust attenuation and another with dust attenuation corrections, using the assumption of a Calzetti attenuation law. This estimation will be based on the present MUSE data and the JWST Advanced Deep Extragalactic Survey.

Bibliography

[ABN02] Tom Abel et al. “The Formation of the First Star in the Universe”. In: *Science* 295.5552 (Jan. 2002), pp. 93–98. DOI: 10.1126/science.295.5552.93. arXiv: astro-ph/0112088 [astro-ph] (cit. on pp. 2, 3).

[Aki+08] M. Akiyama et al. In: *Panoramic Views of Galaxy Formation and Evolution*. Ed. by T. Kodama et al. Vol. 399. Astronomical Society of the Pacific Conference Series. Oct. 2008, p. 247 (cit. on p. 13).

[Ate+23] Hakim Atek, Ivo Labbé, et al. *First spectroscopic observations of the galaxies that reionized the Universe*. 2023. arXiv: 2308.08540 [astro-ph.GA] (cit. on p. 7).

[Ate+18] Hakim Atek, Johan Richard, et al. “The extreme faint end of the UV luminosity function at z 6 through gravitational telescopes: a comprehensive assessment of strong lensing uncertainties”. In: *Monthly Notices of the Royal Astronomical Society* 479.4 (July 2018), pp. 5184–5195. ISSN: 0035-8711. DOI: 10.1093/mnras/sty1820. eprint: https://academic.oup.com/mnras/article-pdf/479/4/5184/25207621/sty1820.pdf. URL: https://doi.org/10.1093/mnras/sty1820 (cit. on pp. 21, 49, 90, 96).

[Bac+10] R. Bacon, M. Accardo, et al. “The MUSE second-generation VLT instrument”. In: *Ground-based and Airborne Instrumentation for Astronomy III*. Ed. by Ian S. McLean et al. Vol. 7735. Society of Photo-Optical Instrumentation Engineers (SPIE) Conference Series. July 2010, 773508, p. 773508. DOI: 10.1117/12.856027. arXiv: 2211.16795 [astro-ph.IM] (cit. on p. 24).

[Bac+23] R. Bacon, J. Brinchmann, et al. “The MUSE Hubble Ultra Deep Field surveys: Data release II”. In: 670, A4 (Feb. 2023), A4. DOI: 10.1051/0004-6361/202244187. arXiv: 2211.08493 [astro-ph.GA] (cit. on pp. 26, 27, 48, 49, 59).

[Bac+21] R. Bacon, D. Mary, et al. “The MUSE Extremely Deep Field: The cosmic web in emission at high redshift”. In: 647, A107 (Mar. 2021), A107. DOI: 10.1051/0004-6361/202039887. arXiv: 2102.05516 [astro-ph.CO] (cit. on pp. 27, 29).

[Bac+17] Bacon, Roland et al. “The MUSE Hubble Ultra Deep Field Survey - I. Survey description, data reduction, and source detection”. In: *A&A* 608 (2017), A1. DOI: 10.1051/0004-6361/201730833. URL: https://doi.org/10.1051/0004-6361/201730833 (cit. on pp. 26, 27).

[Bah68] John N. Bahcall. “A Systematic Method for Identifying Absorption Lines as Applied to PKS 0237-23”. In: 153 (Aug. 1968), p. 679. DOI: 10.1086/149695 (cit. on p. 3).

[BS69] John N. Bahcall and Jr. Spitzer Lyman. “Absorption Lines Produced by Galactic Halos”. In: 156 (May 1969), p. L63. DOI: 10.1086/180350 (cit. on p. 3).

[Bal+16] I. Balestra et al. “CLASH-VLT: DISSECTING THE FRONTIER FIELDS GALAXY CLUSTER MACS J0416.1-2403 WITH 800 SPECTRA OF MEMBER GALAXIES”. In: *The Astrophysical Journal Supplement Series* 224.2 (June 2016), p. 33. DOI: 10.3847/0067-0049/224/2/33. URL: https://dx.doi.org/10.3847/0067-0049/224/2/33 (cit. on p. 36).

[BHO01] Rennan Barkana et al. “Constraints on Warm Dark Matter from Cosmological Reionization”. In: *The Astrophysical Journal* 558.2 (Sept. 2001), pp. 482–496. DOI: 10.1086/322393. URL: https://doi.org/10.1086%2F322393 (cit. on p. 2).

[Bec+15] George D. Becker, James S. Bolton, et al. In: 447.4 (Mar. 2015), pp. 3402–3419. DOI: 10.1093/mnras/stu2646. arXiv: 1407.4850 [astro-ph.CO] (cit. on pp. 7, 15).

[Bec+13] George D. Becker, Paul C. Hewett, et al. In: 430.3 (Apr. 2013), pp. 2067–2081. DOI: 10.1093/mnras/stt031. arXiv: 1208.2584 [astro-ph.CO] (cit. on p. 14).

[Bec+01] Robert H. Becker et al. In: *The Astronomical Journal* 122.6 (Dec. 2001), pp. 2850–2857. DOI: 10.1086/324231. URL: https://doi.org/10.1086%2F324231 (cit. on p. 2).

[Bec+06] Steven V. W. Beckwith et al. “The Hubble Ultra Deep Field”. In: 132.5 (Nov. 2006), pp. 1729–1755. DOI: 10.1086/507302. arXiv: astro-ph/0607632 [astro-ph] (cit. on p. 27).

[BA96] E. Bertin et al. “SExtractor: Software for source extraction.” In: 117 (June 1996), pp. 393–404. DOI: 10.1051/aas:1996164 (cit. on p. 48).

[Bin+16] Bina, D. et al. “MUSE observations of the lensing cluster Abell 1689”. In: *A&A* 590 (2016), A14. DOI: 10.1051/0004-6361/201527913. URL: https://doi.org/10.1051/0004-6361/201527913 (cit. on p. 44).

[Bla+11] Guillermo A. Blanc et al. “THE HETDEX PILOT SURVEY. II. THE EVOLUTION OF THE Lyα ESCAPE FRACTION FROM THE ULTRAVIOLET SLOPE AND LUMINOSITY FUNCTION OF 1.9 lt;zlt;3.8 LAEs”. In: *The Astrophysical Journal* 736.1 (July 2011), p. 31. DOI: 10.1088/0004-637X/736/1/31. URL: https://dx.doi.org/10.1088/0004-637X/736/1/31 (cit. on p. 88).

[Böh+01] H. Böhringer et al. “The ROSAT-ESO flux limited X-ray (REFLEX) galaxy cluster survey. I. The construction of the cluster sample”. In: 369 (Apr. 2001), pp. 826–850. DOI: 10.1051/0004-6361:20010240. arXiv: astro-ph/0012266 [astro-ph] (cit. on p. 38).

[BMP00] Micol Bolzonella et al. *Photometric Redshifts based on standard SED fitting procedures*. 2000. arXiv: astro-ph/0003380 [astro-ph] (cit. on pp. 17, 18).

[Bor+11] R. Bordoloi et al. In: 743.1, 10 (Dec. 2011), p. 10. DOI: 10.1088/0004-637X/743/1/10. arXiv: 1106.0616 [astro-ph.CO] (cit. on p. 5).

[Bou+22] R. J. Bouwens, G. Illingworth, et al. “z 2–9 Galaxies Magnified by the Hubble Frontier Field Clusters. II. Luminosity Functions and Constraints on a Faint-end Turnover”. In: *The Astrophysical Journal* 940.1 (Nov. 2022), p. 55. DOI: 10.3847/1538-4357/ac86d1. URL: https://dx.doi.org/10.3847/1538-4357/ac86d1 (cit. on pp. 21, 96).

[Bou+17] R. J. Bouwens, G. D. Illingworth, P. A. Oesch, H. Atek, et al. In: 843.1, 41 (July 2017), p. 41. DOI: 10.3847/1538-4357/aa74e4. arXiv: 1608.00966 [astro-ph.GA] (cit. on pp. 90, 96).

[Bou+15] R. J. Bouwens, G. D. Illingworth, P. A. Oesch, M. Trenti, et al. “UV Luminosity Functions at Redshifts z ∼ 4 to z ∼ 10: 10,000 Galaxies from HST Legacy Fields”. In: 803.1, 34 (Apr. 2015), p. 34. DOI: 10.1088/0004-637X/803/1/34. arXiv: 1403.4295 [astro-ph.CO] (cit. on pp. 98, 101, 104).

[BI06] Rychard Bouwens et al. “Luminosity functions and star formation rates at z6–10: Galaxy buildup in the reionization age”. In: *New Astronomy Reviews* 50.1 (2006). First Light and Reionization: Theoretical Study and Experimental Detection of First Luminous Sources in the Universe, pp. 152–156. ISSN: 1387-6473. DOI: https://doi.org/10.1016/j.newar.2005.11.027. URL: https://www.sciencedirect.com/science/article/pii/S138764730500165X (cit. on p. 13).

[Bra+06] Maruša Bradač, Douglas Clowe, et al. “Strong and Weak Lensing United. III. Measuring the Mass Distribution of the Merging Galaxy Cluster 1ES 0657–558*”. In: *The Astrophysical Journal* 652.2 (Dec. 2006), p. 937. DOI: 10.1086/508601. URL: https://dx.doi.org/10.1086/508601 (cit. on p. 34).

[Bra+09] Maruša Bradač, Tommaso Treu, et al. “Focusing Cosmic Telescopes: Exploring Redshift z ∼5-6 Galaxies with the Bullet Cluster 1E0657 - 56”. In: 706.2 (Dec. 2009), pp. 1201–1212. DOI: 10.1088/0004-637X/706/2/1201. arXiv: 0910.2708 [astro-ph.CO] (cit. on p. 34).

[Bri+17] J. Brinchmann et al. “The MUSE Hubble Ultra Deep Field Survey. III. Testing photometric redshifts to 30th magnitude”. In: 608, A3 (Nov. 2017), A3. DOI: 10.1051/0004-6361/201731351. arXiv: 1710.05062 [astro-ph.GA] (cit. on p. 27).

[Bro+01] V. Bromm et al. “The fragmentation of pre-enriched primordial objects”. In: 328.3 (Dec. 2001), pp. 969–976. DOI: 10.1046/j.1365-8711.2001.04915.x. arXiv: astro-ph/0104271 [astro-ph] (cit. on p. 2).

[BCL99] Volker Bromm et al. “Forming the First Stars in the Universe: The Fragmentation of Primordial Gas”. In: 527.1 (Dec. 1999), pp. L5–L8. DOI: 10.1086/312385. arXiv: astro-ph/9910224 [astro-ph] (cit. on p. 3).

[BB67] G. R. Burbidge et al. “Limits to the Distance of the Quasi-Stellar Objects Deduced from Their Absorption Line Spectra”. In: 148 (May 1967), p. L107. DOI: 10.1086/180026 (cit. on p. 3).

[Bur+06] Burgarella, D. et al. “Ultraviolet-to-far infrared properties of Lyman break galaxies and luminous infrared galaxies at z”. In: *A&A* 450.1 (2006), pp. 69–76. DOI: 10.1051/0004-6361:20054309. URL: https://doi.org/10.1051/0004-6361:20054309 (cit. on p. 17).

[Cam+17] Caminha, G. B., Grillo, C., et al. “A refined mass distribution of the cluster MACS J0416.1-2403 from a new large set of spectroscopic multiply lensed sources”. In: *A&A* 600 (2017), A90. DOI: 10.1051/0004-6361/201629297. URL: https://doi.org/10.1051/0004-6361/201629297 (cit. on pp. 36, 38).

[Cam+19] Caminha, G. B., Rosati, P., et al. “Strong lensing models of eight CLASH clusters from extensive spectroscopy: Accurate total mass reconstructions in the cores”. In: *A&A* 632 (2019), A36. DOI: 10.1051/0004-6361/201935454. URL: https://doi.org/10.1051/0004-6361/201935454 (cit. on pp. 35, 39).

[Can+14] Sebastiano Cantalupo et al. In: 506.7486 (Feb. 2014), pp. 63–66. DOI: 10.1038/nature12898. arXiv: 1401.4469 [astro-ph.CO] (cit. on p. 5).

[Cas+11] P. Cassata et al. In: 525, A143 (Jan. 2011), A143. DOI: 10.1051/0004-6361/201014410. arXiv: 1003.3480 [astro-ph.CO] (cit. on pp. 88, 99).

[CK15] Renyue Cen et al. "QUANTIFYING DISTRIBUTIONS OF THE LYMAN CONTINUUM ESCAPE FRACTION". In: *The Astrophysical Journal Letters* 801.2 (Mar. 2015), p. L25. DOI: 10.1088/2041-8205/801/2/L25. URL: https://dx.doi.org/10.1088/2041-8205/801/2/L25 (cit. on p. 101).

[CF93] Stephane Charlot et al. "Lyman-Alpha Emission from Galaxies". In: 415 (Oct. 1993), p. 580. DOI: 10.1086/173187 (cit. on pp. 9, 10).

[Chi+18] Chisholm, J. et al. "Accurately predicting the escape fraction of ionizing photons using rest-frame ultraviolet absorption lines". In: *A&A* 616 (2018), A30. DOI: 10.1051/0004-6361/201832758. URL: https://doi.org/10.1051/0004-6361/201832758 (cit. on p. 100).

[Cho+15] Tirthankar Roy Choudhury et al. "Lyman α emitters gone missing: evidence for late reionization?" In: 452.1 (Sept. 2015), pp. 261–277. DOI: 10.1093/mnras/stv1250. arXiv: 1412.4790 [astro-ph.CO] (cit. on p. 100).

[Cla21] Claeyssens. "L'émission Lyman-alpha du milieu circumgalactique des galaxies distantes zoomées par effet de lentille gravitationnelle et observées avec MUSE au VLT". PhD thesis. Université de Lyon, 2021 (cit. on pp. 39, 40, 52, 54).

[Cla+19] A Claeyssens et al. "Spectral variations of Lyman

$alpha$

emission within strongly lensed sources observed with MUSE". In: *Monthly Notices of the Royal Astronomical Society* 489.4 (Sept. 2019), pp. 5022–5029. ISSN: 0035-8711. DOI: 10.1093/mnras/stz2492. eprint: https://academic.oup.com/mnras/article-pdf/489/4/5022/30047592/stz2492.pdf. URL: https://doi.org/10.1093/mnras/stz2492 (cit. on p. 41).

[Cla+22] A. Claeyssens et al. "The Lensed Lyman-Alpha MUSE Arcs Sample (LLAMAS). I. Characterisation of extended Lyman-alpha halos and spatial offsets". In: 666, A78 (Oct. 2022), A78. DOI: 10.1051/0004-6361/202142320. arXiv: 2201.04674 [astro-ph.GA] (cit. on pp. 27, 53, 55, 91).

[CS16] Lauren Corlies et al. In: 827.2, 148 (Aug. 2016), p. 148. DOI: 10.3847/0004-637X/827/2/148. arXiv: 1607.08616 [astro-ph.GA] (cit. on p. 5).

[Cos+16] A. Costille et al. "Modeling effects of common molecular contaminants on the Euclid infrared detectors". In: *Space Telescopes and Instrumentation 2016: Optical, Infrared, and Millimeter Wave*. Vol. 9904. Edinburgh, United Kingdom, June 2016, 99042R. DOI: 10.1117/12.2233778. URL: https://hal.in2p3.fr/in2p3-01523543 (cit. on p. 104).

[CBT09] L. L. Cowie et al. "Measuring the Sources of the Intergalactic Ionizing Flux". In: 692.2 (Feb. 2009), pp. 1476–1488. DOI: 10.1088/0004-637X/692/2/1476. arXiv: 0811.1042 [astro-ph] (cit. on p. 7).

[CBH10] Lennox L. Cowie et al. In: *The Astrophysical Journal* 711.2 (Feb. 2010), p. 928. DOI: 10.1088/0004-637X/711/2/928. URL: https://dx.doi.org/10.1088/0004-637X/711/2/928 (cit. on p. 21).

[Daw+23] Taha Dawoodbhoy et al. “Cosmic Variance and the Inhomogeneous UV Luminosity Function of Galaxies During Reionization”. In: *arXiv e-prints*, arXiv:2302.08523 (Feb. 2023), arXiv:2302.08523. DOI: 10.48550/arXiv.2302.08523. arXiv: 2302.08523 [astro-ph.CO] (cit. on p. 96).

[DLV19] G. de la Vieuville et al. “Faint end of the z -7 luminosity function of Lyman-alpha emitters behind lensing clusters observed with MUSE”. In: *A&A* 628 (2019), A3. DOI: 10.1051/0004-6361/201834471. URL: https://doi.org/10.1051/0004-6361/201834471 (cit. on pp. 22, 23, 27, 31, 56–58, 62, 76, 77, 87–90, 102, 103).

[Deh+08] Jean-Michel Deharveng et al. “Lyα-Emitting Galaxies at 0.2 lt; z lt; 0.35 from GALEX Spectroscopy”. In: *The Astrophysical Journal* 680.2 (June 2008), p. 1072. DOI: 10.1086/587953. URL: https://dx.doi.org/10.1086/587953 (cit. on p. 21).

[DGV16] Mark Dijkstra et al. “THE Lyα–LyC CONNECTION: EVIDENCE FOR AN ENHANCED CONTRIBUTION OF UV-FAINT GALAXIES TO COSMIC REIONIZATION”. In: *The Astrophysical Journal* 828.2 (Sept. 2016), p. 71. DOI: 10.3847/0004-637X/828/2/71. URL: https://dx.doi.org/10.3847/0004-637X/828/2/71 (cit. on p. 101).

[Dow+07] C. C. Dow-Hygelund et al. In: *The Astrophysical Journal* 660.1 (May 2007), p. 47. DOI: 10.1086/512025. URL: https://dx.doi.org/10.1086/512025 (cit. on p. 19).

[Dra+17] Alyssa B. Drake et al. In: 471.1 (Oct. 2017), pp. 267–278. DOI: 10.1093/mnras/stx1515. arXiv: 1609.02920 [astro-ph.GA] (cit. on pp. 22, 27, 88, 89, 99, 103).

[Duv14] Florent Duval. “Lyman-α radiative transfer in Star- forming galaxies”. PhD thesis. Stockholm Uiversity, 2014 (cit. on p. 10).

[Ebe+07] H. Ebeling, E. Barrett, et al. “A Complete Sample of 12 Very X-Ray Luminous Galaxy Clusters at z > 0.5”. In: 661.1 (May 2007), pp. L33–L36. DOI: 10.1086/518603. arXiv: astro-ph/0703394 [astro-ph] (cit. on p. 30).

[EEH01] H. Ebeling, A. C. Edge, and J. P. Henry. “MACS: A Quest for the Most Massive Galaxy Clusters in the Universe”. In: 553.2 (June 2001), pp. 668–676. DOI: 10.1086/320958. arXiv: astro-ph/0009101 [astro-ph] (cit. on pp. 30, 35).

[Ebe+10] H. Ebeling, A. C. Edge, A. Mantz, et al. “The X-ray brightest clusters of galaxies from the Massive Cluster Survey”. In: *Monthly Notices of the Royal Astronomical Society* 407.1 (Aug. 2010), pp. 83–93. ISSN: 0035-8711. DOI: 10.1111/j.1365-2966.2010.16920.x. eprint: https://academic.oup.com/mnras/article-pdf/407/1/83/3065452/mnras0407-0083.pdf. URL: https://doi.org/10.1111/j.1365-2966.2010.16920.x (cit. on pp. 35, 36).

[Ebe+09] H. Ebeling, C. J. Ma, et al. “A spectacular giant arc in the massive cluster lens MACS J1206.20847*”. In: *Monthly Notices of the Royal Astronomical Society* 395.3 (May 2009), pp. 1213–1224. ISSN: 0035-8711. DOI: 10.1111/j.1365-2966.2009.14502.x. eprint: https://academic.oup.com/mnras/article-pdf/395/3/1213/18231618/mnras0395-1213.pdf. URL: https://doi.org/10.1111/j.1365-2966.2009.14502.x (cit. on p. 38).

[Eic+13] Thomas Eichner et al. “GALAXY HALO TRUNCATION AND GIANT ARC SURFACE BRIGHTNESS RECONSTRUCTION IN THE CLUSTER MACSJ1206.2-0847”. In: *The Astrophysical Journal* 774.2 (Aug. 2013), p. 124. DOI: 10.1088/0004-637X/774/2/124. URL: https://dx.doi.org/10.1088/0004-637X/774/2/124 (cit. on p. 38).

[EFH08] Elsner, F. et al. In: *A&A* 477.2 (2008), pp. 503–512. DOI: 10.1051/0004-6361:20078343. URL: https://doi.org/10.1051/0004-6361:20078343 (cit. on p. 13).

[Fan+06] Xiaohui Fan et al. In: 132.1 (July 2006), pp. 117–136. DOI: 10.1086/504836. arXiv: astro-ph/0512082 [astro-ph] (cit. on pp. 2, 15, 16, 99, 100).

[Fel+18] Anna Feltre, Roland Bacon, et al. “The MUSE Hubble Ultra Deep Field Survey. XII. Mg II emission and absorption in star-forming galaxies”. In: 617, A62 (Sept. 2018), A62. DOI: 10.1051/0004-6361/201833281. arXiv: 1806.01864 [astro-ph.GA] (cit. on p. 27).

[Fel+20] Anna Feltre, Michael V. Maseda, et al. In: 641, A118 (Sept. 2020), A118. DOI: 10.1051/0004-6361/202038133. arXiv: 2007.01878 [astro-ph.GA] (cit. on p. 12).

[FLY99] Alberto Fernández-Soto et al. In: 513.1 (Mar. 1999), pp. 34–50. DOI: 10.1086/306847. arXiv: astro-ph/9809126 [astro-ph] (cit. on p. 18).

[Fin+15] Steven L. Finkelstein et al. “The Evolution of the Galaxy Rest-frame Ultraviolet Luminosity Function over the First Two Billion Years”. In: 810.1, 71 (Sept. 2015), p. 71. DOI: 10.1088/0004-637X/810/1/71. arXiv: 1410.5439 [astro-ph.GA] (cit. on p. 7).

[Fin+12] Kristian Finlator et al. “Gas clumping in self-consistent reionization models”. In: *Monthly Notices of the Royal Astronomical Society* 427.3 (Dec. 2012), pp. 2464–2479. ISSN: 0035-8711. DOI: 10.1111/j.1365-2966.2012.22114.x. eprint: https://academic.oup.com/mnras/article-pdf/427/3/2464/3857876/427-3-2464.pdf. URL: https://doi.org/10.1111/j.1365-2966.2012.22114.x (cit. on p. 100).

[For+13] Amanda Brady Ford et al. “Hydrogen and metal line absorption around low-redshift galaxies in cosmological hydrodynamic simulations”. In: *Monthly Notices of the Royal Astronomical Society* 432.1 (Apr. 2013), pp. 89–112. DOI: 10.1093/mnras/stt393. URL: https://doi.org/10.1093%2Fmnras%2Fstt393 (cit. on p. 5).

[Gar+21] T. Garel et al. In: *Monthly Notices of the Royal Astronomical Society* 504.2 (Apr. 2021), pp. 1902–1926. DOI: 10.1093/mnras/stab990. URL: https://doi.org/10.1093%2Fmnras%2Fstab990 (cit. on pp. 96, 97).

[Gaw+07] Eric Gawiser, Harold Francke, et al. In: *The Astrophysical Journal* 671.1 (Dec. 2007), p. 278. DOI: 10.1086/522955. URL: https://dx.doi.org/10.1086/522955 (cit. on pp. 13, 19).

[Gaw+06] Eric Gawiser, Pieter G. van Dokkum, et al. “The Physical Nature of Lyα-emitting Galaxies at z=3.1”. In: 642.1 (May 2006), pp. L13–L16. DOI: 10.1086/504467. arXiv: astro-ph/0603244 [astro-ph] (cit. on p. 13).

[Gia+15] E. Giallongo et al. In: 578, A83 (June 2015), A83. DOI: 10.1051/0004-6361/201425334. arXiv: 1502.02562 [astro-ph.CO] (cit. on p. 7).

[GTF99] G. Giovannini et al. “Radio halo and relic candidates from the NRAO VLA Sky Survey”. In: 4.2 (Mar. 1999), pp. 141–155. DOI: 10.1016/S1384-1076(99)00018-4. arXiv: astro-ph/9904210 [astro-ph] (cit. on p. 31).

[Gne16] Nickolay Y. Gnedin. “COSMIC REIONIZATION ON COMPUTERS: THE FAINT END OF THE GALAXY LUMINOSITY FUNCTION”. In: *The Astrophysical Journal Letters* 825.2 (July 2016), p. L17. DOI: 10.3847/2041-8205/825/2/L17. URL: https://dx.doi.org/10.3847/2041-8205/825/2/L17 (cit. on p. 96).

[GO97] Nickolay Y. Gnedin and Jeremiah P. Ostriker. “Reionization of the Universe and the Early Production of Metals”. In: *The Astrophysical Journal* 486.2 (Sept. 1997), p. 581. DOI: 10.1086/304548. URL: https://dx.doi.org/10.1086/304548 (cit. on p. 100).

[Góm+12] P. L. Gómez et al. “OPTICAL AND X-RAY OBSERVATIONS OF THE MERGING CLUSTER AS1063”. In: *The Astronomical Journal* 144.3 (Aug. 2012), p. 79. DOI: 10.1088/0004-6256/144/3/79. URL: https://dx.doi.org/10.1088/0004-6256/144/3/79 (cit. on p. 33).

[Gon+10] Anthony H. Gonzalez et al. “Spectroscopic Confirmation of a z = 2.79 Multiply Imaged Luminous Infrared Galaxy Behind the Bullet Cluster”. In: 720.1 (Sept. 2010), pp. 245–251. DOI: 10.1088/0004-637X/720/1/245. arXiv: 1005.3817 [astro-ph.CO] (cit. on p. 34).

[Gor+18] Gorce, A. et al. “Observational constraints on key-parameters of cosmic reionisation history”. In: *A&A* 616 (2018), A113. DOI: 10.1051/0004-6361/201629661. URL: https://doi.org/10.1051/0004-6361/201629661 (cit. on p. 101).

[Gov+01a] F. Govoni, T. A. Enßlin, et al. “A comparison of radio and X-ray morphologies of four clusters of galaxies containing radio halos”. In: 369 (Apr. 2001), pp. 441–449. DOI: 10.1051/0004-6361:20010115. arXiv: astro-ph/0101418 [astro-ph] (cit. on p. 31).

[Gov+01b] F. Govoni, L. Feretti, et al. “Radio and X-ray diffuse emission in six clusters of galaxies”. In: 376 (Sept. 2001), pp. 803–819. DOI: 10.1051/0004-6361:20011016. arXiv: astro-ph/0107275 [astro-ph] (cit. on p. 31).

[Gra+18] A. Grazian et al. In: 613, A44 (May 2018), A44. DOI: 10.1051/0004-6361/201732385. arXiv: 1802.01953 [astro-ph.GA] (cit. on p. 7).

[Gre+17] Bradley Greig et al. In: 466.4 (Apr. 2017), pp. 4239–4249. DOI: 10.1093/mnras/stw3351. arXiv: 1606.00441 [astro-ph.CO] (cit. on p. 14).

[GP65] James E. Gunn et al. “On the Density of Neutral Hydrogen in Intergalactic Space.” In: 142 (Nov. 1965), pp. 1633–1636. DOI: 10.1086/148444 (cit. on pp. 13, 15).

[HM12] Francesco Haardt et al. “Radiative Transfer in a Clumpy Universe. IV. New Synthesis Models of the Cosmic UV/X-Ray Background”. In: 746.2, 125 (Feb. 2012), p. 125. DOI: 10.1088/0004-637X/746/2/125. arXiv: 1105.2039 [astro-ph.CO] (cit. on p. 8).

[Ham+87] F Hammer et al. *High Redshift and Primeval Galaxies*. 1987 (cit. on p. 32).

[Har+23] Yuichi Harikane et al. “A Comprehensive Study of Galaxies at z 9–16 Found in the Early JWST Data: Ultraviolet Luminosity Functions and Cosmic Star Formation History at the Pre-reionization Epoch”. In: *The Astrophysical Journal Supplement Series* 265.1 (Feb. 2023), p. 5. DOI: 10.3847/1538-4365/acaaa9. URL: https://dx.doi.org/10.3847/1538-4365/acaaa9 (cit. on p. 7).

[Has+17] T. Hashimoto et al. “The MUSE Hubble Ultra Deep Field Survey. X. Lyα equivalent widths at 2.9 < z < 6.6”. In: 608, A10 (Nov. 2017), A10. DOI: 10.1051/0004-6361/201731579. arXiv: 1711.01747 [astro-ph.GA] (cit. on p. 27).

[Hay+16] Matthew Hayes, Jens Melinder, et al. In: *The Astrophysical Journal* 828.1 (Aug. 2016), p. 49. DOI: 10.3847/0004-637X/828/1/49. URL: https://dx.doi.org/10.3847/0004-637X/828/1/49 (cit. on p. 5).

[Hay+11] Matthew Hayes, Daniel Schaerer, et al. In: *The Astrophysical Journal* 730.1 (Feb. 2011), p. 8. DOI: 10.1088/0004-637x/730/1/8. URL: https://doi.org/10.1088%2F0004-637x%2F730%2F1%2F8 (cit. on pp. 100, 101).

[Hay+21] Matthew J. Hayes et al. “Spectral Shapes of the Lyα Emission from Galaxies. I. Blueshifted Emission and Intrinsic Invariance with Redshift”. In: 908.1, 36 (Feb. 2021), p. 36. DOI: 10.3847/1538-4357/abd246. arXiv: 2006.03232 [astro-ph.GA] (cit. on p. 53).

[Hec+15] Timothy M. Heckman et al. “THE SYSTEMATIC PROPERTIES OF THE WARM PHASE OF STARBURST-DRIVEN GALACTIC WINDS”. In: *The Astrophysical Journal* 809.2 (Aug. 2015), p. 147. DOI: 10.1088/0004-637X/809/2/147. URL: https://dx.doi.org/10.1088/0004-637X/809/2/147 (cit. on p. 5).

[Hen+15] Alaina Henry et al. In: *The Astrophysical Journal* 809.1 (Aug. 2015), p. 19. DOI: 10.1088/0004-637x/809/1/19. URL: https://doi.org/10.1088%2F0004-637x%2F809%2F1%2F19 (cit. on p. 5).

[Her+19] Edmund Christian Herenz et al. In: 621, A107 (Jan. 2019), A107. DOI: 10.1051/0004-6361/201834164. arXiv: 1810.05037 [astro-ph.GA] (cit. on pp. 22, 27, 88, 89, 103).

[Hir+14] Shingo Hirano et al. “ONE HUNDRED FIRST STARS: PROTOSTELLAR EVOLUTION AND THE FINAL MASSES”. In: *The Astrophysical Journal* 781.2 (Jan. 2014), p. 60. DOI: 10.1088/0004-637X/781/2/60. URL: https://dx.doi.org/10.1088/0004-637X/781/2/60 (cit. on p. 3).

[HCM98] Esther M. Hu et al. In: 502.2 (Aug. 1998), pp. L99–L103. DOI: 10.1086/311506. arXiv: astro-ph/9803011 [astro-ph] (cit. on p. 19).

[Hum+13] Cameron B. Hummels et al. “Constraints on hydrodynamical subgrid models from quasar absorption line studies of the simulated circumgalactic medium”. In: *Monthly Notices of the Royal Astronomical Society* 430.3 (Feb. 2013), pp. 1548–1565. ISSN: 0035-8711. DOI: 10.1093/mnras/sts702. eprint: https://academic.oup.com/mnras/article-pdf/430/3/1548/4895446/sts702.pdf. URL: https://doi.org/10.1093/mnras/sts702 (cit. on p. 5).

[Ina+17] H. Inami et al. “The MUSE Hubble Ultra Deep Field Survey. II. Spectroscopic redshifts and comparisons to color selections of high-redshift galaxies”. In: 608, A2 (Dec. 2017), A2. DOI: 10.1051/0004-6361/201731195. arXiv: 1710.03773 [astro-ph.GA] (cit. on p. 27).

[Ino+14] Akio K. Inoue et al. “An updated analytic model for attenuation by the intergalactic medium”. In: 442.2 (Aug. 2014), pp. 1805–1820. DOI: 10.1093/mnras/stu936. arXiv: 1402.0677 [astro-ph.CO] (cit. on p. 100).

[Ito+18] Ryohei Itoh et al. In: *The Astrophysical Journal* 867.1 (Oct. 2018), p. 46. DOI: 10.3847/1538-4357/aadfe4. URL: https://dx.doi.org/10.3847/1538-4357/aadfe4 (cit. on p. 21).

[Iye+06] Masanori Iye et al. “A galaxy at a redshift z = 6.96”. In: *Nature* 443.7108 (Sept. 2006), pp. 186–188. DOI: 10.1038/nature05104. URL: https://doi.org/10.1038%2Fnature05104 (cit. on pp. 19, 20).

[Izo+19] Y I Izotov et al. “Diverse properties of Lyα emission in low-redshift compact star-forming galaxies with extremely high [Oiii]/[Oii] ratios”. In: *Monthly Notices of the Royal Astronomical Society* 491.1 (Oct. 2019), pp. 468–482. ISSN: 0035-8711. DOI: 10.1093/mnras/stz3041. eprint: https://academic.oup.com/mnras/article-pdf/491/1/468/31064386/stz3041.pdf. URL: https://doi.org/10.1093/mnras/stz3041 (cit. on p. 101).

[JTN13] Jason Jaacks et al. In: *The Astrophysical Journal* 766.2 (Mar. 2013), p. 94. DOI: 10.1088/0004-637X/766/2/94. URL: https://dx.doi.org/10.1088/0004-637X/766/2/94 (cit. on p. 96).

[Jau+16] M. Jauzac et al. “The extraordinary amount of substructure in the Hubble Frontier Fields cluster Abell 2744”. In: *Monthly Notices of the Royal Astronomical Society* 463.4 (Sept. 2016), pp. 3876–3893. ISSN: 0035-8711. DOI: 10.1093/mnras/stw2251. eprint: https://academic.oup.com/mnras/article-pdf/463/4/3876/18514327/stw2251.pdf. URL: https://doi.org/10.1093/mnras/stw2251 (cit. on p. 31).

[Joh+12] Ryan E. Johnson et al. “SLOSHING GAS IN THE CORE OF THE MOST LUMINOUS GALAXY CLUSTER RXJ1347.5-1145”. In: *The Astrophysical Journal* 751.2 (May 2012), p. 95. DOI: 10.1088/0004-637X/751/2/95. URL: https://dx.doi.org/10.1088/0004-637X/751/2/95 (cit. on p. 39).

[Joh+14] Sean D. Johnson et al. In: 438.4 (Mar. 2014), pp. 3039–3048. DOI: 10.1093/mnras/stt2409. arXiv: 1312.3944 [astro-ph.GA] (cit. on p. 5).

[Jon+10] T. A. Jones et al. “Resolved spectroscopy of gravitationally lensed galaxies: recovering coherent velocity fields in subluminous z ~2-3 galaxies”. In: 404.3 (May 2010), pp. 1247–1262. DOI: 10.1111/j.1365-2966.2010.16378.x. arXiv: 0910.4488 [astro-ph.CO] (cit. on p. 36).

[Jon+13] Tucker Jones et al. “THE ORIGIN AND EVOLUTION OF METALLICITY GRADIENTS: PROBING THE MODE OF MASS ASSEMBLY AT z $\simeq$ 2”. In: *The Astrophysical Journal* 765.1 (Feb. 2013), p. 48. DOI: 10.1088/0004-637X/765/1/48. URL: https://dx.doi.org/10.1088/0004-637X/765/1/48 (cit. on p. 36).

[Kar+15] Karman, W. et al. “MUSE integral-field spectroscopy towards the Frontier Fields cluster Abell S1063 - I. Data products and redshift identifications”. In: *A&A* 574 (2015), A11. DOI: 10.1051/0004-6361/201424962. URL: https://doi.org/10.1051/0004-6361/201424962 (cit. on p. 33).

[Kas+11] Nobunari Kashikawa et al. In: *The Astrophysical Journal* 734.2 (June 2011), p. 119. DOI: 10.1088/0004-637x/734/2/119. URL: https://doi.org/10.1088%2F0004-637x%2F734%2F2%2F119 (cit. on p. 21).

[KK93] Aggeliki Kassiola et al. “Elliptic Mass Distributions versus Elliptic Potentials in Gravitational Lenses”. In: 417 (Nov. 1993), p. 450. DOI: 10.1086/173325 (cit. on p. 44).

[KD04] Joshua C. Kempner et al. “A Chandra view of the multiple merger in Abell 2744”. In: *Monthly Notices of the Royal Astronomical Society* 349.2 (2004), pp. 385–392. DOI: 10.1111/j.1365-2966.2004.07534.x (cit. on p. 31).

[Ken98] Jr. Kennicutt Robert C. “The Global Schmidt Law in Star-forming Galaxies”. In: 498.2 (May 1998), pp. 541–552. DOI: 10.1086/305588. arXiv: astro-ph/9712213 [astro-ph] (cit. on p. 98).

[KC14] Taysun Kimm and Renyue Cen. “ESCAPE FRACTION OF IONIZING PHOTONS DURING REIONIZATION: EFFECTS DUE TO SUPERNOVA FEEDBACK AND RUNAWAY OB STARS”. In: *The Astrophysical Journal* 788.2 (May 2014), p. 121. DOI: 10.1088/0004-637X/788/2/121. URL: https://dx.doi.org/10.1088/0004-637X/788/2/121 (cit. on p. 3).

[Kim+17] Taysun Kimm, Harley Katz, et al. In: *Monthly Notices of the Royal Astronomical Society* 466.4 (Jan. 2017), pp. 4826–4846. ISSN: 0035-8711. DOI: 10.1093/mnras/stx052. eprint: https://academic.oup.com/mnras/article-pdf/466/4/4826/10873852/stx052.pdf. URL: https://doi.org/10.1093/mnras/stx052 (cit. on p. 3).

[KN11] Jean-Paul Kneib et al. “Cluster lenses”. In: *The Astronomy and Astrophysics Review* 19.1 (Nov. 2011). DOI: 10.1007/s00159-011-0047-3. URL: https://doi.org/10.1007%2Fs00159-011-0047-3 (cit. on pp. 27, 44).

[Koc+23] Dale D. Kocevski et al. “CEERS Key Paper. II. A First Look at the Resolved Host Properties of AGN at 3 lt; z lt; 5 with JWST”. In: *The Astrophysical Journal Letters* 946.1 (Mar. 2023), p. L14. DOI: 10.3847/2041-8213/acad00. URL: https://dx.doi.org/10.3847/2041-8213/acad00 (cit. on p. 7).

[Kon+16] Akira Konno, Masami Ouchi, Kimihiko Nakajima, et al. “BRIGHT AND FAINT ENDS OF Lyα LUMINOSITY FUNCTIONS AT z = 2 DETERMINED BY THE SUBARU SURVEY: IMPLICATIONS FOR AGNs, MAGNIFICATION BIAS, AND ISM H I EVOLUTION”. In: *The Astrophysical Journal* 823.1 (May 2016), p. 20. DOI: 10.3847/0004-637X/823/1/20. URL: https://dx.doi.org/10.3847/0004-637X/823/1/20 (cit. on p. 21).

[Kon+14] Akira Konno, Masami Ouchi, Yoshiaki Ono, et al. In: *The Astrophysical Journal* 797.1 (Nov. 2014), p. 16. DOI: 10.1088/0004-637X/797/1/16. URL: https://dx.doi.org/10.1088/0004-637X/797/1/16 (cit. on p. 21).

[Kon+18] Akira Konno, Masami Ouchi, Takatoshi Shibuya, et al. “SILVERRUSH. IV. Lyα luminosity functions at z = 5.7 and 6.6 studied with ~1300 Lyα emitters on the 14-21 deg^2 sky”. In: 70, S16 (Jan. 2018), S16. DOI: 10.1093/pasj/psx131. arXiv: 1705.01222 [astro-ph.GA] (cit. on p. 21).

[Kor+10] Katherine A. Kornei et al. In: *The Astrophysical Journal* 711.2 (Feb. 2010), p. 693. DOI: 10.1088/0004-637X/711/2/693. URL: https://dx.doi.org/10.1088/0004-637X/711/2/693 (cit. on p. 13).

[Kus+20] Haruka Kusakabe et al. “The MUSE Hubble Ultra Deep Field Survey. XIV. Evolution of the Lyα emitter fraction from z = 3 to z = 6”. In: 638, A12 (June 2020), A12. DOI: 10.1051/0004-6361/201937340. arXiv: 2003.12083 [astro-ph.GA] (cit. on p. 27).

[Lag+19] David J Lagattuta et al. “Probing 3D Structure with a Large MUSE Mosaic: Extending the Mass Model of Frontier Field Abell 370”. In: *Monthly Notices of the Royal Astronomical Society* (Mar. 2019). DOI: 10.1093/mnras/stz620. URL: https://doi.org/10.1093%2Fmnras%2Fstz620 (cit. on pp. 32, 44).

[LYF96] Kenneth M. Lanzetta et al. “Star-forming galaxies at very high redshifts”. In: 381.6585 (June 1996), pp. 759–763. DOI: 10.1038/381759a0. arXiv: astro-ph/9606171 [astro-ph] (cit. on p. 18).

[Lec+17] Leclercq, Floriane et al. “The MUSE Hubble Ultra Deep Field Survey - VIII. Extended Lyman-oes around high-z star-forming galaxies”. In: *A&A* 608 (2017), A8. DOI: 10.1051/0004-6361/201731480. URL: https://doi.org/10.1051/0004-6361/201731480 (cit. on pp. 11, 27, 28).

[LHW15] Nicolas Lehner et al. In: *The Astrophysical Journal* 804.2 (May 2015), p. 79. DOI: 10.1088/0004-637X/804/2/79. URL: https://dx.doi.org/10.1088/0004-637X/804/2/79 (cit. on p. 4).

[Liu+16] Chuanwu Liu et al. “Dark-ages reionization and galaxy formation simulation – IV. UV luminosity functions of high-redshift galaxies”. In: *Monthly Notices of the Royal Astronomical Society* 462.1 (July 2016), pp. 235–249. ISSN: 0035-8711. DOI: 10.1093/mnras/stw1015. eprint: https://academic.oup.com/mnras/article-pdf/462/1/235/18468542/stw1015.pdf. URL: https://doi.org/10.1093/mnras/stw1015 (cit. on p. 21).

[LFL17] R. C. Livermore et al. “Directly Observing the Galaxies Likely Responsible for Reionization”. In: *The Astrophysical Journal* 835.2 (Jan. 2017), p. 113. DOI: 10.3847/1538-4357/835/2/113. URL: https://dx.doi.org/10.3847/1538-4357/835/2/113 (cit. on p. 96).

[Lot+17] J. M. Lotz et al. “The Frontier Fields: Survey Design and Initial Results”. In: *The Astrophysical Journal* 837.1 (Mar. 2017), p. 97. DOI: 10.3847/1538-4357/837/1/97. URL: https://dx.doi.org/10.3847/1538-4357/837/1/97 (cit. on p. 18).

[Lov04] Jon Loveday. “Evolution of the galaxy luminosity function at z lt; 0.3”. In: *Monthly Notices of the Royal Astronomical Society* 347.2 (Jan. 2004), pp. 601–606. ISSN: 0035-8711. DOI: 10.1111/j.1365-2966.2004.07230.x. eprint: https://academic.oup.com/mnras/article-pdf/347/2/601/4882034/347-2-601.pdf. URL: https://doi.org/10.1111/j.1365-2966.2004.07230.x (cit. on p. 21).

[Lyn70] *IAU Symposium*. 1970 (cit. on p. 14).

[Ma+15] Xiangcheng Ma et al. “ The difficulty of getting high escape fractions of ionizing photons from high-redshift galaxies: a view from the FIRE cosmological simulations”. In: *Monthly Notices of the Royal Astronomical Society* 453.1 (Aug. 2015), pp. 960–975. ISSN: 0035-8711. DOI: 10.1093/mnras/stv1679. eprint: https://academic.oup.com/mnras/article-pdf/453/1/960/4935561/stv1679.pdf. URL: https://doi.org/10.1093/mnras/stv1679 (cit. on p. 101).

[MH15] Piero Madau and Francesco Haardt. “COSMIC REIONIZATION AFTER PLANCK: COULD QUASARS DO IT ALL?” In: *The Astrophysical Journal Letters* 813.1 (Oct. 2015), p. L8. DOI: 10.1088/2041-8205/813/1/L8. URL: https://dx.doi.org/10.1088/2041-8205/813/1/L8 (cit. on p. 7).

[MHR99] Piero Madau, Francesco Haardt, and Martin J. Rees. “Radiative Transfer in a Clumpy Universe. III. The Nature of Cosmological Ionizing Sources”. In: *The Astrophysical Journal* 514.2 (Apr. 1999), p. 648. DOI: 10.1086/306975. URL: https://dx.doi.org/10.1086/306975 (cit. on pp. 99, 100).

[Mah+18] G. Mahler et al. “Strong-lensing analysis of A2744 with MUSE and Hubble Frontier Fields images”. In: 473.1 (Jan. 2018), pp. 663–692. DOI: 10.1093/mnras/stx1971. arXiv: 1702.06962 [astro-ph.GA] (cit. on pp. 27, 29, 44).

[MR02] Sangeeta Malhotra et al. In: *The Astrophysical Journal* 565.2 (Jan. 2002), p. L71. DOI: 10.1086/338980. URL: https://dx.doi.org/10.1086/338980 (cit. on p. 9).

[ME12] Andrew W. Mann et al. “X-ray-optical classification of cluster mergers and the evolution of the cluster merger fraction”. In: 420.3 (Mar. 2012), pp. 2120–2138. DOI: 10.1111/j.1365-2966.2011.20170.x. arXiv: 1111.2396 [astro-ph.CO] (cit. on p. 36).

[Mas+18] Michael V. Maseda, Roland Bacon, et al. “MUSE Spectroscopic Identifications of Ultra-faint Emission Line Galaxies with M $_{UV}$ ∼ -15”. In: 865.1, L1 (Sept. 2018), p. L1. DOI: 10.3847/2041-8213/aade4b. arXiv: 1809.01142 [astro-ph.GA] (cit. on p. 27).

[Mas+17] Michael V. Maseda, Jarle Brinchmann, et al. “The MUSE Hubble Ultra Deep Field Survey. IV. Global properties of C III] emitters”. In: 608, A4 (Dec. 2017), A4. DOI: 10.1051/0004-6361/201730985. arXiv: 1710.06432 [astro-ph.GA] (cit. on p. 27).

[Mas+12] D. Masters et al. In: 755.2, 169 (Aug. 2012), p. 169. DOI: 10.1088/0004-637X/755/2/169. arXiv: 1207.2154 [astro-ph.CO] (cit. on p. 7).

[MB08] Chiara Mastropietro et al. “Simulating the Bullet Cluster”. In: *Monthly Notices of the Royal Astronomical Society* 389.2 (Sept. 2008), pp. 967–988. ISSN: 0035-8711. DOI: 10.1111/j.1365-2966.2008.13626.x. eprint: https://academic.oup.com/mnras/article-pdf/389/2/967/2970173/mnras0389-0967.pdf. URL: https://doi.org/10.1111/j.1365-2966.2008.13626.x (cit. on p. 34).

[Mat+18] Yoshiki Matsuoka et al. In: 70, S35 (Jan. 2018), S35. DOI: 10.1093/pasj/psx046. arXiv: 1704.05854 [astro-ph.GA] (cit. on p. 7).

[Mat+22] Jorryt Matthee et al. In: 660, A10 (Apr. 2022), A10. DOI: 10.1051/0004-6361/202142187. arXiv: 2111.14855 [astro-ph.GA] (cit. on p. 7).

[Mau+08] B. J. Maughan et al. “Images, Structural Properties, and Metal Abundances of Galaxy Clusters Observed with Chandra ACIS-I at 0.1 < z < 1.3”. In: 174.1 (Jan. 2008), pp. 117–135. DOI: 10.1086/521225. arXiv: astro-ph/0703156 [astro-ph] (cit. on p. 35).

[McG+13] Ian D. McGreer, Linhua Jiang, et al. “THE z = 5 QUASAR LUMINOSITY FUNCTION FROM SDSS STRIPE 82*”. In: *The Astrophysical Journal* 768.2 (Apr. 2013), p. 105. DOI: 10.1088/0004-637X/768/2/105. URL: https://dx.doi.org/10.1088/0004-637X/768/2/105 (cit. on p. 7).

[MMD14] Ian D. McGreer, Andrei Mesinger, et al. In: *Monthly Notices of the Royal Astronomical Society* 447.1 (Dec. 2014), pp. 499–505. ISSN: 0035-8711. DOI: 10.1093/mnras/stu2449. eprint: https://academic.oup.com/mnras/article-pdf/447/1/499/4933595/stu2449.pdf. URL: https://doi.org/10.1093/mnras/stu2449 (cit. on p. 15).

[MOF11] Matthew McQuinn et al. “ON LYMAN-LIMIT SYSTEMS AND THE EVOLUTION OF THE INTERGALACTIC IONIZING BACKGROUND”. In: *The Astrophysical Journal* 743.1 (Nov. 2011), p. 82. DOI: 10.1088/0004-637X/743/1/82. URL: https://dx.doi.org/10.1088/0004-637X/743/1/82 (cit. on p. 8).

[Meh+01] D. Mehlert et al. “Gravitationally lensed high redshift galaxies in the field of 1E0657-56”. In: 379 (Nov. 2001), pp. 96–106. DOI: 10.1051/0004-6361:20011286. arXiv: astro-ph/0109290 [astro-ph] (cit. on p. 34).

[Mel+88] Y Mellier et al. “Photometry, spectroscopy and content of the distant cluster of galaxies Abell 370”. In: *Astronomy and Astrophysics (ISSN 0004-6361), vol. 199, no. 1-2, June 1988, p. 13-28.* 199 (1988), pp. 13–28 (cit. on p. 32).

[Mén+10] Brice Ménard et al. “Measuring the galaxy–mass and galaxy–dust correlations through magnification and reddening”. In: *Monthly Notices of the Royal Astronomical Society* 405.2 (June 2010), pp. 1025–1039. ISSN: 0035-8711. DOI: 10.1111/j.1365-2966.2010.16486.x. eprint: https://academic.oup.com/mnras/article-pdf/405/2/1025/4001735/mnras0405-1025.pdf. URL: https://doi.org/10.1111/j.1365-2966.2010.16486.x (cit. on p. 5).

[Men+17] M. Meneghetti et al. “The Frontier Fields lens modelling comparison project”. In: *Monthly Notices of the Royal Astronomical Society* 472.3 (Aug. 2017), pp. 3177–3216. ISSN: 0035-8711. DOI: 10.1093/mnras/stx2064. eprint: https://academic.oup.com/mnras/article-pdf/472/3/3177/20133502/stx2064.pdf. URL: https://doi.org/10.1093/mnras/stx2064 (cit. on p. 90).

[Mer+11] J. Merten et al. “Creation of cosmic structure in the complex galaxy cluster merger Abell 2744”. In: 417.1 (Oct. 2011), pp. 333–347. DOI: 10.1111/j.1365-2966.2011.19266.x. arXiv: 1103.2772 [astro-ph.CO] (cit. on p. 31).

[Mes10] Andrei Mesinger. In: 407.2 (Sept. 2010), pp. 1328–1337. DOI: 10.1111/j.1365-2966.2010.16995.x. arXiv: 0910.4161 [astro-ph.CO] (cit. on p. 14).

[Mic+17] Genoveva Micheva et al. “Searching for candidates of Lyman continuum sources - revisiting the SSA22 field”. In: 465.1 (Feb. 2017), pp. 316–336. DOI: 10.1093/mnras/stw2700. arXiv: 1509.03996 [astro-ph.GA] (cit. on p. 7).

[Nai+22] Rohan P. Naidu et al. “Two Remarkably Luminous Galaxy Candidates at z ≈ 10–12 Revealed by JWST”. In: *The Astrophysical Journal Letters* 940.1 (Nov. 2022), p. L14. DOI: 10.3847/2041-8213/ac9b22. URL: https://dx.doi.org/10.3847/2041-8213/ac9b22 (cit. on p. 7).

[New+14] Matthew Newville et al. *LMFIT: Non-Linear Least-Square Minimization and Curve-Fitting for Python*. Zenodo. Version 0.8.0. Sept. 2014. DOI: 10.5281/zenodo.11813 (cit. on p. 88).

[Ono+17] Masafusa Onoue et al. In: 847.2, L15 (Oct. 2017), p. L15. DOI: 10.3847/2041-8213/aa8cc6. arXiv: 1709.04413 [astro-ph.GA] (cit. on p. 7).

[Opp+16] Benjamin D. Oppenheimer et al. In: 460.2 (Aug. 2016), pp. 2157–2179. DOI: 10.1093/mnras/stw1066. arXiv: 1603.05984 [astro-ph.GA] (cit. on p. 5).

[OGR10] François Orieux et al. “Bayesian estimation of regularization and point spread function parameters for Wiener–Hunt deconvolution”. In: *J. Opt. Soc. Am. A* 27.7 (July 2010), pp. 1593–1607. DOI: 10.1364/JOSAA.27.001593. URL: https://opg.optica.org/josaa/abstract.cfm?URI=josaa-27-7-1593 (cit. on p. 63).

[OF06] Donald E Osterbrock et al. “Book Review: Astrophysics of Gaseous Nebulae and Active Galactic Nuclei /University Science Books, 2005”. In: *Mercury* 35.1 (2006), p. 40 (cit. on p. 98).

[Ost89] Donald E. Osterbrock. *Astrophysics of gaseous nebulae and active galactic nuclei*. 1989 (cit. on pp. 9, 98, 103).

[OOS20] Masami Ouchi, Yoshiaki Ono, et al. In: *Annual Review of Astronomy and Astrophysics* 58.1 (Aug. 2020), pp. 617–659. DOI: 10.1146/annurev-astro-032620-021859. URL: https://doi.org/10.1146%2Fannurev-astro-032620-021859 (cit. on pp. 8, 10, 11).

[Ouc+08] Masami Ouchi, Kazuhiro Shimasaku, Masayuki Akiyama, et al. In: 176.2 (June 2008), pp. 301–330. DOI: 10.1086/527673. arXiv: 0707.3161 [astro-ph] (cit. on pp. 21, 99).

[Ouc+10] Masami Ouchi, Kazuhiro Shimasaku, Hisanori Furusawa, et al. In: 723.1 (Nov. 2010), pp. 869–894. DOI: 10.1088/0004-637X/723/1/869. arXiv: 1007.2961 [astro-ph.CO] (cit. on pp. 19, 88).

[PKD13] J. -P. Paardekooper et al. “The first billion years project: proto-galaxies reionizing the universe.” In: 429 (Feb. 2013), pp. L94–L98. DOI: 10.1093/mnrasl/sls032. arXiv: 1211.1670 [astro-ph.CO] (cit. on p. 7).

[PKD15] Jan-Pieter Paardekooper et al. “The First Billion Years project: the escape fraction of ionizing photons in the epoch of reionization”. In: *Monthly Notices of the Royal Astronomical Society* 451.3 (June 2015), pp. 2544–2563. ISSN: 0035-8711. DOI: 10.1093/mnras/stv1114. eprint: https://academic.oup.com/mnras/article-pdf/451/3/2544/4013769/stv1114.pdf. URL: https://doi.org/10.1093/mnras/stv1114 (cit. on p. 101).

[Pac+22] Fabio Pacucci et al. In: *Monthly Notices of the Royal Astronomical Society: Letters* 514.1 (Apr. 2022), pp. L6–L10. DOI: 10.1093/mnrasl/slac035. URL: https://doi.org/10.1093%2Fmnrasl%2Fslac035 (cit. on p. 16).

[Par+16] Paraficz, D. et al. “The Bullet cluster at its best: weighing stars, gas, and dark matter”. In: *A&A* 594 (2016), A121. DOI: 10.1051/0004-6361/201527959. URL: https://doi.org/10.1051/0004-6361/201527959 (cit. on p. 34).

[PP67] R. B. Partridge et al. In: 147 (Mar. 1967), p. 868. DOI: 10.1086/149079 (cit. on p. 9).

[Pat+18] V Patrício et al. “Kinematics, turbulence, and star formation of z 1 strongly lensed galaxies seen with MUSE”. In: *Monthly Notices of the Royal Astronomical Society* 477.1 (Mar. 2018), pp. 18–44. ISSN: 0035-8711. DOI: 10.1093/mnras/sty555. eprint: https://academic.oup.com/mnras/article-pdf/477/1/18/24615130/sty555.pdf. URL: https://doi.org/10.1093/mnras/sty555 (cit. on p. 32).

[Pat+16] Vera Patrício et al. “A young star-forming galaxy at z = 3.5 with an extended Lyman α halo seen with MUSE”. In: *Monthly Notices of the Royal Astronomical Society* 456.4 (Jan. 2016), pp. 4191–4208. ISSN: 0035-8711. DOI: 10.1093/mnras/stv2859. eprint: https://academic.oup.com/mnras/article-pdf/456/4/4191/9380736/stv2859.pdf. URL: https://doi.org/10.1093/mnras/stv2859 (cit. on pp. 39, 41).

[PSV09] Andreas H. Pawlik et al. “Keeping the Universe ionized: photoheating and the clumping factor of the high-redshift intergalactic medium”. In: *Monthly Notices of the Royal Astronomical Society* 394.4 (Apr. 2009), pp. 1812–1824. ISSN: 0035-8711. DOI: 10.1111/j.1365-2966.2009.14486.x. eprint: https://academic.oup.com/mnras/article-pdf/394/4/1812/4032564/mnras0394-1812.pdf. URL: https://doi.org/10.1111/j.1365-2966.2009.14486.x (cit. on p. 101).

[Pee93] P. J. E. Peebles. *Principles of Physical Cosmology*. 1993. DOI: 10.1515/9780691206721 (cit. on p. 1).

[PMC15] J. E. G. Peek et al. “Dust in the Circumgalactic Medium of Low-redshift Galaxies”. In: 813.1, 7 (Nov. 2015), p. 7. DOI: 10.1088/0004-637X/813/1/7. arXiv: 1411.3333 [astro-ph.GA] (cit. on p. 5).

[Piq+19] L. Piqueras et al. “MPDAF - A Python Package for the Analysis of VLT/MUSE Data”. In: *Astronomical Data Analysis Software and Systems XXVI*. Ed. by Marco Molinaro et al. Vol. 521. Astronomical Society of the Pacific Conference Series. Oct. 2019, p. 545 (cit. on p. 48).

[Pir+07] N. Pirzkal et al. In: *The Astrophysical Journal* 667.1 (Sept. 2007), p. 49. DOI: 10.1086/519485. URL: https://dx.doi.org/10.1086/519485 (cit. on p. 19).

[Pla+13] Planck Collaboration: et al. In: *A&A* 557 (2013), A52. DOI: 10.1051/0004-6361/201220941. URL: https://doi.org/10.1051/0004-6361/201220941 (cit. on p. 6).

[PG02] Cristiano Porciani et al. “The Clustering Properties of Lyman Break Galaxies at Redshift z 3”. In: *The Astrophysical Journal* 565.1 (Jan. 2002), p. 24. DOI: 10.1086/324198. URL: https://dx.doi.org/10.1086/324198 (cit. on p. 13).

[Pos+12] Marc Postman et al. “THE CLUSTER LENSING AND SUPERNOVA SURVEY WITH HUBBLE: AN OVERVIEW”. In: *The Astrophysical Journal Supplement Series* 199.2 (Mar. 2012), p. 25. DOI: 10.1088/0067-0049/199/2/25. URL: https://doi.org/10.1088%2F0067-0049%2F199%2F2%2F25 (cit. on p. 36).

[Pri+17] Jett Priewe et al. “Lens models under the microscope: comparison of Hubble Frontier Field cluster magnification maps”. In: 465.1 (Feb. 2017), pp. 1030–1045. DOI: 10.1093/mnras/stw2785. arXiv: 1605.07621 [astro-ph.CO] (cit. on p. 90).

[RH11] Michael Rauch et al. “Faint resonantly scattered Lyα emission from the absorption troughs of damped Lyα systems at z$\sim$ 3”. In: 412.1 (Mar. 2011), pp. L55–L57. DOI: 10.1111/j.1745-3933.2010.01004.x. arXiv: 1011.4061 [astro-ph.CO] (cit. on p. 4).

[RS06] Alexei O. Razoumov et al. “Escape of Ionizing Radiation from Star-forming Regions in Young Galaxies”. In: 651.2 (Nov. 2006), pp. L89–L92. DOI: 10.1086/509636. arXiv: astro-ph/0609545 [astro-ph] (cit. on p. 101).

[RER16] A. Repp et al. “A systematic search for lensed high-redshift galaxies in HST images of MACS clusters”. In: *Monthly Notices of the Royal Astronomical Society* 457.2 (Feb. 2016), pp. 1399–1409. ISSN: 0035-8711. DOI: 10.1093/mnras/stw002. eprint: https://academic.oup.com/mnras/article-pdf/457/2/1399/2894086/stw002.pdf. URL: https://doi.org/10.1093/mnras/stw002 (cit. on p. 30).

[Ric+15] J. Richard et al. “MUSE observations of the lensing cluster SMACSJ2031.8-4036: new constraints on the mass distribution in the cluster core.” In: 446 (Jan. 2015), pp. L16–L20. DOI: 10.1093/mnrasl/slu150. arXiv: 1409.2488 [astro-ph.CO] (cit. on pp. 39, 41, 44).

[Ric+21] Johan Richard, Adélaide Claeyssens, et al. “An atlas of MUSE observations towards twelve massive lensing clusters”. In: 646, A83 (Feb. 2021), A83. DOI: 10.1051/0004-6361/202039462. arXiv: 2009.09784 [astro-ph.GA] (cit. on pp. 27, 35–42, 48, 49).

[Ric+14] Johan Richard, Mathilde Jauzac, et al. “Mass and magnification maps for the Hubble Space Telescope Frontier Fields clusters: implications for high-redshift studies”. In: *Monthly Notices of the Royal Astronomical Society* 444.1 (Aug. 2014), pp. 268–289. ISSN: 0035-8711. DOI: 10.1093/mnras/stu1395. eprint: https://academic.oup.com/mnras/article-pdf/444/1/268/18502235/stu1395.pdf. URL: https://doi.org/10.1093/mnras/stu1395 (cit. on p. 32).

[Ric+10] Johan Richard, Graham P. Smith, et al. “LoCuSS: first results from strong-lensing analysis of 20 massive galaxy clusters at z= 0.2”. In: *Monthly Notices of the Royal Astronomical Society* 404.1 (Apr. 2010), pp. 325–349. ISSN: 0035-8711. DOI: 10.1111/j.1365-2966.2009.16274.x. eprint: https://academic.oup.com/mnras/article-pdf/404/1/325/11180369/mnras0404-0325.pdf. URL: https://doi.org/10.1111/j.1365-2966.2009.16274.x (cit. on p. 32).

[RO04a] M. Ricotti et al. “Reionization, chemical enrichment and seed black holes from the first stars: is Population III important?” In: 350.2 (May 2004), pp. 539–551. DOI: 10.1111/j.1365-2966.2004.07662.x. arXiv: astro-ph/0310331 [astro-ph] (cit. on p. 7).

[RO04b] Massimo Ricotti et al. “X-ray pre-ionization powered by accretion on the first black holes - I. A model for the WMAP polarization measurement”. In: 352.2 (Aug. 2004), pp. 547–562. DOI: 10.1111/j.1365-2966.2004.07942.x. arXiv: astro-ph/0311003 [astro-ph] (cit. on p. 7).

[Rob+15] Brant E. Robertson, Richard S. Ellis, et al. “COSMIC REIONIZATION AND EARLY STAR-FORMING GALAXIES: A JOINT ANALYSIS OF NEW CONSTRAINTS FROM PLANCK AND THE HUBBLE SPACE TELESCOPE”. In: *The Astrophysical Journal Letters* 802.2 (Apr. 2015), p. L19. DOI: 10.1088/2041-8205/802/2/L19. URL: https://dx.doi.org/10.1088/2041-8205/802/2/L19 (cit. on pp. 100, 101).

[Rob+13] Brant E. Robertson, Steven R. Furlanetto, et al. “NEW CONSTRAINTS ON COSMIC REIONIZATION FROM THE 2012 HUBBLE ULTRA DEEP FIELD CAMPAIGN”. In: *The Astrophysical Journal* 768.1 (Apr. 2013), p. 71. DOI: 10.1088/0004-637X/768/1/71. URL: https://dx.doi.org/10.1088/0004-637X/768/1/71 (cit. on pp. 7, 101).

[Rub+12] Kate H. R. Rubin et al. In: 747.2, L26 (Mar. 2012), p. L26. DOI: 10.1088/2041-8205/747/2/L26. arXiv: 1110.0837 [astro-ph.CO] (cit. on p. 5).

[Rub+15] Kate H. R. Rubin et al. “DISSECTING THE GASEOUS HALOS OF z 2 DAMPED Lyα SYSTEMS WITH CLOSE QUASAR PAIRS”. In: *The Astrophysical Journal* 808.1 (July 2015), p. 38. DOI: 10.1088/0004-637X/808/1/38. URL: https://dx.doi.org/10.1088/0004-637X/808/1/38 (cit. on p. 4).

[Rud+12] Gwen C. Rudie et al. In: *The Astrophysical Journal* 750.1 (Apr. 2012), p. 67. DOI: 10.1088/0004-637X/750/1/67. URL: https://dx.doi.org/10.1088/0004-637X/750/1/67 (cit. on p. 4).

[Sal+22] Eduard Salvador-Solé et al. In: *The Astrophysical Journal* 936.2 (Sept. 2022), p. 178. DOI: 10.3847/1538-4357/ac874c. URL: https://doi.org/10.3847%5C%2F1538-4357%5C%2Fac874c (cit. on pp. 96, 97).

[Sar+20] Sartoris, B. et al. “CLASH-VLT: a full dynamical reconstruction of the mass profile of Abell S1063 from 1 kpc out to the virial radius”. In: *A&A* 637 (2020), A34. DOI: 10.1051/0004-6361/202037521. URL: https://doi.org/10.1051/0004-6361/202037521 (cit. on p. 33).

[Sch02a] D. Schaerer. “On the properties of massive Population III stars and metal-free stellar populations”. In: 382 (Jan. 2002), pp. 28–42. DOI: 10.1051/0004-6361:20011619. arXiv: astro-ph/0110697 [astro-ph] (cit. on p. 3).

[Sch02b] D. Schaerer. “VizieR Online Data Catalog: Population Synthesis Models at very low metallicities (Schaerer, 2003)”. In: *VizieR Online Data Catalog*, VI/109 (Nov. 2002), pp. VI/109 (cit. on p. 9).

[SV08] Schaerer, D. et al. “3D Lyiation transfer - II. Fitting the Lyman break galaxy MS 1512-cB58 and implications for Lyission in high-z starbursts”. In: *A&A* 480.2 (2008), pp. 369–377. DOI: 10.1051/0004-6361:20078913. URL: https://doi.org/10.1051/0004-6361:20078913 (cit. on p. 11).

[Sch+00] Joop Schaye et al. In: 318.3 (Nov. 2000), pp. 817–826. DOI: 10.1046/j.1365-8711.2000.03815.x. arXiv: astro-ph/9912432 [astro-ph] (cit. on p. 14).

[Sch76] P. Schechter. “An analytic expression for the luminosity function for galaxies.” In: 203 (Jan. 1976), pp. 297–306. DOI: 10.1086/154079 (cit. on p. 20).

[Sch68] Maarten Schmidt. “Space Distribution and Luminosity Functions of Quasi-Stellar Radio Sources”. In: 151 (Feb. 1968), p. 393. DOI: 10.1086/149446 (cit. on p. 58).

[SEF92] Peter Schneider et al. *Gravitational Lenses*. 1992. DOI: 10.1007/978-3-662-03758-4 (cit. on p. 44).

[Sha+01] Alice E. Shapley, Charles C. Steidel, Kurt L. Adelberger, et al. “The Rest-Frame Optical Properties of z $\simeq$ 3 Galaxies*”. In: *The Astrophysical Journal* 562.1 (Nov. 2001), p. 95. DOI: 10.1086/323432. URL: https://dx.doi.org/10.1086/323432 (cit. on p. 13).

[Sha+06] Alice E. Shapley, Charles C. Steidel, Max Pettini, et al. In: 651.2 (Nov. 2006), pp. 688–703. DOI: 10.1086/507511. arXiv: astro-ph/0606635 [astro-ph] (cit. on p. 13).

[Sha+16] Mahavir Sharma et al. "The brighter galaxies reionized the Universe". In: *Monthly Notices of the Royal Astronomical Society: Letters* 458.1 (Feb. 2016), pp. L94–L98. ISSN: 1745-3925. DOI: 10.1093/mnrasl/slw021. eprint: https://academic.oup.com/mnrasl/article-pdf/458/1/L94/8010449/slw021.pdf. URL: https://doi.org/10.1093/mnrasl/slw021 (cit. on p. 101).

[Shi+14] Takatoshi Shibuya et al. In: *The Astrophysical Journal* 785.1 (Mar. 2014), p. 64. DOI: 10.1088/0004-637X/785/1/64. URL: https://dx.doi.org/10.1088/0004-637X/785/1/64 (cit. on p. 53).

[Shi+06] Kazuhiro Shimasaku et al. In: *Publications of the Astronomical Society of Japan* 58.2 (Apr. 2006), pp. 313–334. DOI: 10.1093/pasj/58.2.313. URL: https://doi.org/10.1093%2Fpasj%2F58.2.313 (cit. on p. 19).

[Shu+12] J. Michael Shull et al. "CRITICAL STAR FORMATION RATES FOR REIONIZATION: FULL REIONIZATION OCCURS AT REDSHIFT z ≈ 7". In: *The Astrophysical Journal* 747.2 (Feb. 2012), p. 100. DOI: 10.1088/0004-637X/747/2/100. URL: https://dx.doi.org/10.1088/0004-637X/747/2/100 (cit. on p. 100).

[Sob+18] David Sobral et al. In: 476.4 (June 2018), pp. 4725–4752. DOI: 10.1093/mnras/sty378. arXiv: 1712.04451 [astro-ph.GA] (cit. on pp. 88, 89).

[Sou+87] G. Soucail et al. "A blue ring-like structure in the center of the A 370 cluster of galaxies." In: 172 (Jan. 1987), pp. L14–L16 (cit. on p. 32).

[Spi+20] D Spinoso et al. In: *A&A* 643 (2020), A149. DOI: 10.1051/0004-6361/202038756. URL: https://doi.org/10.1051/0004-6361/202038756 (cit. on p. 21).

[Spi56] Jr. Spitzer Lyman. In: 124 (July 1956), p. 20. DOI: 10.1086/146200 (cit. on p. 3).

[Sta+14] Daniel P. Stark et al. "Ultraviolet emission lines in young low-mass galaxies at z ≃ 2: physical properties and implications for studies at z
gt; 7". In: *Monthly Notices of the Royal Astronomical Society* 445.3 (Oct. 2014), pp. 3200–3220. ISSN: 0035-8711. DOI: 10.1093/mnras/stu1618. eprint: https://academic.oup.com/mnras/article-pdf/445/3/3200/3477243/stu1618.pdf. URL: https://doi.org/10.1093/mnras/stu1618 (cit. on p. 36).

[Ste+10] Charles C. Steidel et al. In: 717.1 (July 2010), pp. 289–322. DOI: 10.1088/0004-637X/717/1/289. arXiv: 1003.0679 [astro-ph.CO] (cit. on p. 5).

[Sur+16] Joshua Suresh et al. "On the OVI abundance in the circumgalactic medium of low-redshift galaxies". In: *Monthly Notices of the Royal Astronomical Society* 465.3 (Oct. 2016), pp. 2966–2982. DOI: 10.1093/mnras/stw2499. URL: https://doi.org/10.1093%2Fmnras%2Fstw2499 (cit. on p. 5).

[Tan+09] Y. Taniguchi et al. "HUBBLE SPACE TELESCOPE/ADVANCED CAMERA FOR SURVEYS MORPHOLOGY OF Lyα EMITTERS AT REDSHIFT 5.7 IN THE COSMOS FIELD*". In: *The Astrophysical Journal* 701.2 (July 2009), p. 915. DOI: 10.1088/0004-637X/701/2/915. URL: https://dx.doi.org/10.1088/0004-637X/701/2/915 (cit. on p. 9).

[Tre+21] Maxime Trebitsch et al. In: 653, A154 (Sept. 2021), A154. DOI: 10.1051/0004-6361/202037698. arXiv: 2002.04045 [astro-ph.GA] (cit. on p. 7).

[TS08] M. Trenti et al. "Cosmic Variance and Its Effect on the Luminosity Function Determination in Deep High-z Surveys". In: *The Astrophysical Journal* 676.2 (Apr. 2008), p. 767. DOI: 10.1086/528674. URL: https://dx.doi.org/10.1086/528674 (cit. on p. 79).

[Tre+15] T. Treu et al. "THE GRISM LENS-AMPLIFIED SURVEY FROM SPACE (GLASS). I. SURVEY OVERVIEW AND FIRST DATA RELEASE". In: *The Astrophysical Journal* 812.2 (Oct. 2015), p. 114. DOI: 10.1088/0004-637x/812/2/114. URL: https://doi.org/10.1088%2F0004-637x%2F812%2F2%2F114 (cit. on p. 32).

[TH10] Dmitriy Tseliakhovich et al. "Relative velocity of dark matter and baryonic fluids and the formation of the first structures". In: *Phys. Rev. D* 82 (8 Oct. 2010), p. 083520. DOI: 10.1103/PhysRevD.82.083520. URL: https://link.aps.org/doi/10.1103/PhysRevD.82.083520 (cit. on p. 2).

[Tuc+98] W. Tucker et al. "1E 0657-56: A Contender for the Hottest Known Cluster of Galaxies". In: 496.1 (Mar. 1998), pp. L5–L8. DOI: 10.1086/311234. arXiv: astro-ph/9801120 [astro-ph] (cit. on p. 34).

[TPW17] Jason Tumlinson, Molly S. Peeples, et al. "The Circumgalactic Medium". In: *Annual Review of Astronomy and Astrophysics* 55.1 (2017), pp. 389–432. DOI: 10.1146/annurev-astro-091916-055240. eprint: https://doi.org/10.1146/annurev-astro-091916-055240. URL: https://doi.org/10.1146/annurev-astro-091916-055240 (cit. on p. 6).

[Tum+13] Jason Tumlinson, Christopher Thom, et al. In: 777.1, 59 (Nov. 2013), p. 59. DOI: 10.1088/0004-637X/777/1/59. arXiv: 1309.6317 [astro-ph.CO] (cit. on p. 5).

[Tur+14] Monica L. Turner et al. In: *Monthly Notices of the Royal Astronomical Society* 445.1 (Sept. 2014), pp. 794–822. ISSN: 0035-8711. DOI: 10.1093/mnras/stu1801. eprint: https://academic.oup.com/mnras/article-pdf/445/1/794/18753696/stu1801.pdf. URL: https://doi.org/10.1093/mnras/stu1801 (cit. on p. 4).

[Übl+23] Hannah Übler et al. *GA-NIFS: A massive black hole in a low-metallicity AGN at z ~ 5.55 revealed by JWST/NIRSpec IFS*. 2023. arXiv: 2302.06647 [astro-ph.GA] (cit. on p. 7).

[Ued+18] Shutaro Ueda et al. "A Cool Core Disturbed: Observational Evidence for the Coexistence of Subsonic Sloshing Gas and Stripped Shock-heated Gas around the Core of RX J1347.5–1145". In: *The Astrophysical Journal* 866.1 (Oct. 2018), p. 48. DOI: 10.3847/1538-4357/aadd9d. URL: https://dx.doi.org/10.3847/1538-4357/aadd9d (cit. on p. 39).

[Ume+12] Keiichi Umetsu et al. "CLASH: Mass Distribution in and around MACS J1206.2-0847 from a Full Cluster Lensing Analysis". In: 755.1, 56 (Aug. 2012), p. 56. DOI: 10.1088/0004-637X/755/1/56. arXiv: 1204.3630 [astro-ph.CO] (cit. on p. 38).

[Van+21] Vanzella, E. et al. "The MUSE Deep Lensed Field on the Hubble Frontier Field MACS J0416 - Star-forming complexes at cosmological distances". In: *A&A* 646 (2021), A57. DOI: 10.1051/0004-6361/202039466. URL: https://doi.org/10.1051/0004-6361/202039466 (cit. on p. 36).

[Ven+17] E. Ventou et al. “The MUSE Hubble Ultra Deep Field Survey. IX. Evolution of galaxy merger fraction since z ≈ 6”. In: 608, A9 (Dec. 2017), A9. DOI: 10.1051/0004-6361/201731586. arXiv: 1711.00423 [astro-ph.GA] (cit. on p. 27).

[Ver+18] A. Verhamme et al. “Recovering the systemic redshift of galaxies from their Lyman alpha line profile”. In: 478.1 (July 2018), pp. L60–L65. DOI: 10.1093/mnrasl/sly058. arXiv: 1804.01883 [astro-ph.GA] (cit. on p. 27).

[VSM06] Verhamme, A. et al. “3D Lyiation transfer - I. Understanding Lye profile morphologies”. In: *A&A* 460.2 (2006), pp. 397–413. DOI: 10.1051/0004-6361:20065554. URL: https://doi.org/10.1051/0004-6361:20065554 (cit. on p. 53).

[Vie19] G. de la Vieuville. “Le regard privilé’gié’ de MUSE sur les sources de la ré’ionisation cosmique”. PhD thesis. Toulouse University, 2019 (cit. on pp. 17, 18, 25, 76).

[Wal+14] Stéfan van der Walt et al. “scikit-image: image processing in Python”. In: *PeerJ* 2 (June 2014), e453. DOI: 10.7717/peerj.453. URL: https://doi.org/10.7717%2Fpeerj.453 (cit. on p. 63).

[WCS81] Ray J. Weymann et al. “Absorption Lines in the Spectra of Quasistellar Objects”. In: *Annual Review of Astronomy and Astrophysics* 19.1 (1981), pp. 41–76. DOI: 10.1146/annurev.aa.19.090181.000353. eprint: https://doi.org/10.1146/annurev.aa.19.090181.000353. URL: https://doi.org/10.1146/annurev.aa.19.090181.000353 (cit. on p. 14).

[WSS09] Robert P. C. Wiersma et al. In: 393.1 (Feb. 2009), pp. 99–107. DOI: 10.1111/j.1365-2966.2008.14191.x. arXiv: 0807.3748 [astro-ph] (cit. on p. 7).

[Wis+12] John H. Wise et al. “The birth of a galaxy – II. The role of radiation pressure”. In: *Monthly Notices of the Royal Astronomical Society* 427.1 (Nov. 2012), pp. 311–326. ISSN: 0035-8711. DOI: 10.1111/j.1365-2966.2012.21809.x. eprint: https://academic.oup.com/mnras/article-pdf/427/1/311/18233536/427-1-311.pdf. URL: https://doi.org/10.1111/j.1365-2966.2012.21809.x (cit. on p. 3).

[Wis+16a] L. Wisotzki et al. In: 587, A98 (Mar. 2016), A98. DOI: 10.1051/0004-6361/201527384. arXiv: 1509.05143 [astro-ph.GA] (cit. on p. 11).

[Wis+16b] L. Wisotzki et al. “Extended Lyman α haloes around individual high-redshift galaxies revealed by MUSE”. In: 587, A98 (Mar. 2016), A98. DOI: 10.1051/0004-6361/201527384. arXiv: 1509.05143 [astro-ph.GA] (cit. on p. 27).

[WL00] Kenneth Wood et al. “Escape of Ionizing Radiation from High-Redshift Galaxies”. In: *The Astrophysical Journal* 545.1 (Dec. 2000), p. 86. DOI: 10.1086/317775. URL: https://dx.doi.org/10.1086/317775 (cit. on p. 101).

[Xu+16] Dandan Xu et al. “Lens galaxies in the Illustris simulation: power-law models and the bias of the Hubble constant from time delays”. In: 456.1 (Feb. 2016), pp. 739–755. DOI: 10.1093/mnras/stv2708. arXiv: 1507.07937 [astro-ph.GA] (cit. on p. 3).

[YA00] Donald G. York and J. Adelman. In: 120.3 (Sept. 2000), pp. 1579–1587. DOI: 10.1086/301513 (cit. on p. 14).

[Yor+06] Donald G. York, Pushpa Khare, et al. In: 367.3 (Apr. 2006), pp. 945–978. DOI: 10.1111/j.1365-2966.2005.10018.x. arXiv: astro-ph/0601279 [astro-ph] (cit. on p. 5).

[YFX16] Bin Yue et al. “On the faint-end of the high-z galaxy luminosity function”. In: *Monthly Notices of the Royal Astronomical Society* 463.2 (Aug. 2016), pp. 1968–1979. ISSN: 0035-8711. DOI: 10.1093/mnras/stw2145. eprint: https://academic.oup.com/mnras/article-pdf/463/2/1968/9686521/stw2145.pdf. URL: https://doi.org/10.1093/mnras/stw2145 (cit. on p. 96).

[Zhe+13] Zhen-Ya Zheng et al. In: 431.4 (June 2013), pp. 3589–3607. DOI: 10.1093/mnras/stt440. arXiv: 1111.3386 [astro-ph.CO] (cit. on p. 88).

[ZM13] Guangtun Zhu et al. “The JHU-SDSS Metal Absorption Line Catalog: Redshift Evolution and Properties of Mg II Absorbers”. In: 770.2, 130 (June 2013), p. 130. DOI: 10.1088/0004-637X/770/2/130. arXiv: 1211.6215 [astro-ph.CO] (cit. on p. 4).

[Zit+12] A. Zitrin et al. “CLASH: Discovery of a Bright z ~= 6.2 Dwarf Galaxy Quadruply Lensed by MACS J0329.6-0211”. In: 747.1, L9 (Mar. 2012), p. L9. DOI: 10.1088/2041-8205/747/1/L9. arXiv: 1111.5006 [astro-ph.CO] (cit. on pp. 35, 38).

[Zit+10] Adi Zitrin et al. “Full lensing analysis of Abell 1703: comparison of independent lens-modelling techniques”. In: 408.3 (Nov. 2010), pp. 1916–1927. DOI: 10.1111/j.1365-2966.2010.17258.x. arXiv: 1004.4660 [astro-ph.CO] (cit. on p. 38).